

ARS

## JOURNAL

A PUBLICATION OF THE AMERICAN ROCKET SOCIETY

VOLUME 31 NUMBER 8

AUGUST 1961

## SURVEY ARTICLE

- Evolution of Upper Air Meteorology . . . . . H. J. aufm Kampe 1047

## CONTRIBUTED ARTICLES

- Winds and Circulations in the Mesosphere . . . . . Thomas J. Keegan 1060
- Lunar Impact Probe . . . . . Julian I. Palmore III 1066
- Inertial Sphere System for Complete Attitude Control of Earth Satellites  
. . . . . Karl W. Hering and Robert E. Hufnagel 1074
- Propulsion Requirements for Controllable Satellites  
. . . . . Theodore N. Edelbaum 1079
- Effects of Plane Librations on the Orbital Motion of a Dumbbell Satellite  
. . . . . John P. Moran 1089
- Controlled Rendezvous of Orbiting Space Stations . . . . . Norman S. Potter 1096
- Aerodynamic and Radiant Heat Input to Space Vehicles Which Re-Enter at  
Satellite and Escape Velocity . . . . . M. J. Brunner 1102
- A Simplified Model of Unstable Burning in Solid Propellants  
. . . . . M. Richard Denison and Eric Baum 1112
- Experimental Investigation of Detonation in Unconfined Gaseous Hydrogen-  
Oxygen-Nitrogen Mixtures . . . . . Leon H. Cassutt 1122
- Recent Hypersonic Studies of Wings and Bodies  
. . . . . Mitchel H. Bertram and Arthur Henderson Jr. 1129
- Approximate Solution of Isentropic Swirling Flow Through a Nozzle  
. . . . . Artur Mager 1140

## TECHNICAL NOTES

- Investigation of Rocket Flow Problems by Means of Short Duration Flow Devices  
. . . . . R. C. Weatherston and A. Hertzberg 1149
- Transport Properties of Dissociated Air . . . . . W. L. Bade, E. A. Mason and K. S. Yun 1151
- Lunar Landing Site Selection . . . . . Carl Trosc 1153
- Elementary Launch Guidance Methods for Deep Space Missions . . . . . Carl G. Pfeiffer 1155
- Experimental Performance of a Pulsed Gas Entry Coaxial Plasma Accelerator  
. . . . . F. Gloersen, B. Corowitz and W. Palm 1156
- Segmenting of Radiators for Meteoroid Protection  
. . . . . Robert E. English and Donald C. Quantert 1162
- Some Remarks on Solar Sail . . . . . A. Pozel and L. de Socio 1164

## DEPARTMENTS

- Book Notes . . . . . 1165
- Patents . . . . . 1167
- Technical Literature Digest . . . . . 1168

BLIND

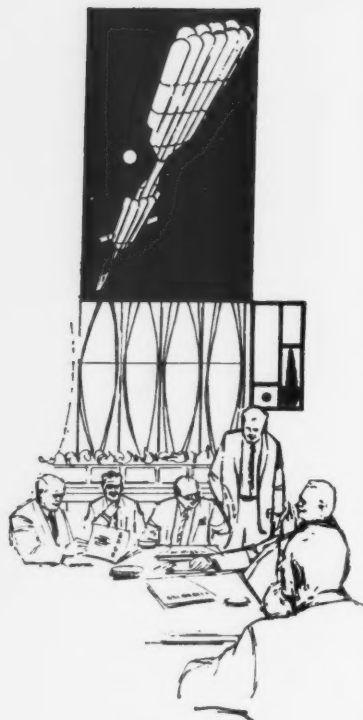
New York Coliseum

October 9-15, 1961

# AMERICAN ROCKET SOCIETY

## SPACE FLIGHT REPORT

TO THE NATION



**T**hrough the medium of the ARS SPACE FLIGHT REPORT TO THE NATION, the American Rocket Society, during the week of October 9-15, 1961, in New York Coliseum, will present a thorough and comprehensive review of the U. S. space program.

The SPACE FLIGHT REPORT TO THE NATION will present for the first time under one roof a complete review of the most significant work being done in each of the major technical disciplines contributing to current progress in rocketry, missiles, and space flight, and one of the largest and most extensive technical exhibits ever undertaken in these fields.

More than 300 technical papers will detail major space projects; will explore problems that must be solved to insure further, faster progress; and will stimulate penetrating discussions by outstanding authorities in the audience.

There will be three floors of technical exhibits and displays by more than 350 manufacturers, suppliers, engineering organizations, and governmental agencies, disclosing latest achievements, concepts, products, and ideas.



## ARS SPACE FLIGHT REPORT TO THE NATION will present:

- Under one roof, at one time, in one place the most comprehensive review of all the contributing technologies to the U. S. space effort.

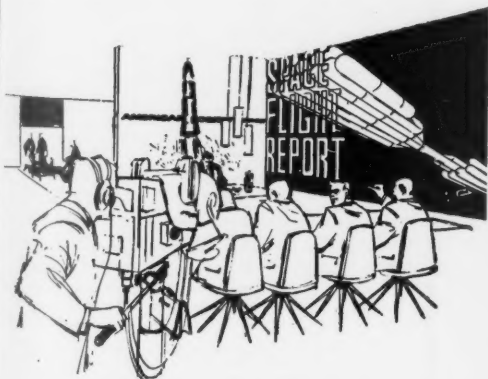
- Forty-two specialized technical sessions, all on the same floor with comfortable lounge areas and conference rooms for informal discussions.

- Three unique Space Flight Report panels that will explore and interpret space missions, space vehicles, and the global impact of space events for the technical community at large.

- A new exhibiting technique called "Exhibiting in Depth", permitting for the first time 3-dimensional displays with the main aisle running *through* the booths instead of by them.

- Main exhibit organized by NASA and DOD, representing U. S. space capability, which will be 88'x50' in floor area and will extend 60' into the air.

- The history, purposes, and plans of ARS graphically displayed in a booth designed by Raymond Loewy.



For further information about reservations, program information or exhibit space contact

## ARS SPACE FLIGHT REPORT TO THE NATION

**American Rocket Society**

500 Fifth Ave., New York 36, N. Y.

## Honorary Committee

Wernher von Braun, Chairman

Harold Boyer

Detlev W. Bronk

Overton Brooks

Milton U. Clauser

James R. Dempsey

Gen. James H. Doolittle

C. Stark Draper

Hugh L. Dryden

Trevor Gardner

Mrs. Robert H. Goddard

Harry F. Guggenheim

Willis M. Hawkins

Rear Adm. John T. Hayward

Samuel K. Hoffman

Robert H. Jewett

Arthur Kantrowitz

Dan A. Kimball

Maj. Gen. John B. Medaris

George F. Metcalf

Maj. Gen. Don R. Ostrander

William H. Pickering

Richard W. Porter

Simon Ramo

Harold W. Ritchey

Lt. Gen. Bernard A. Schriever

Howard S. Seifert

Abe Silverstein

Col. John P. Stapp

George P. Sutton

Maj. Gen. Holger N. Toftoy

George S. Trimble, Jr.

Lt. Gen. Arthur G. Trudeau

Harold Urey

Theodore von Karman

Alan Waterman

Elmer P. Wheaton

Herbert F. York

# ARS JOURNAL

A PUBLICATION OF THE AMERICAN ROCKET SOCIETY

**EDITOR** Martin Summerfield  
**ASSOCIATE TECHNICAL EDITOR** Irvin Glassman  
**MANAGING EDITOR** Margaret Sherman  
**STAFF EDITOR** Barbara Nowak  
**ART EDITOR** John Culin

## ASSOCIATE EDITORS

Igor Jurkevich, G. E. Space Sciences Laboratory, Russian Supplement;  
 George F. McLaughlin, Patents; Charles J. Mundo Jr., Raytheon Co.,  
 Guidance; Bernard H. Palewosky, Aeronautical Research Associates  
 of Princeton, Flight Mechanics; M. H. Smith, Princeton University,  
 Technical Literature Digest

## ASSISTANT EDITORS

Carol Falcetti, Eleanor Rosman, Carol Rubenstein

## DIRECTOR OF MARKETING

Owen A. Kean

## ADVERTISING PRODUCTION MANAGER

Walter Brunke

## ADVERTISING REPRESENTATIVES

### New York

D. C. Emery and Thomas Harford  
 400 Madison Ave., New York, N. Y.  
 Telephone: Plaza 9-7460

### Chicago

Thomas M. Byrne, Jr.  
 7116 North Greenview Ave., Chicago 26, Ill.  
 Telephone: 33-80-947

Atlanta  
 Joe H. Howell  
 1776 Peachtree Bldg., Atlanta 9, Ga.  
 Telephone: 873-2136

### Los Angeles

James C. Galloway and Co.  
 6535 Wilshire Blvd., Los Angeles, Calif.  
 Telephone: Olive 3-3223

### London

B. C. Nichols  
 151 Fleet St.  
 London E. C. 4, England

## American Rocket Society

500 Fifth Avenue, New York 36, N. Y.

Founded 1930

## OFFICERS

**President** Harold W. Ritchey  
**Vice-President** William H. Pickering  
**Executive Secretary** James J. Harford  
**Treasurer** Robert M. Lawrence  
**General Counsel** Andrew G. Haley  
**Director of Publications** Irwin Hersey

## BOARD OF DIRECTORS

(Terms expire on dates indicated)

Ali B. Cambel	1962	Samuel Herrick	1963
Richard B. Canright	1962	Arthur Kantrowitz	1963
William J. Cecka, Jr.	1963	A. K. Oppenheim	1961
James R. Dempsey	1961	Simon Ramo	1963
Herbert Friedman	1962	David G. Simons	1961
George Gerard	1961	John L. Sloop	1961
Robert A. Gross	1962	Martin Summerfield	1962
		Abe M. Zarem	1963

## TECHNICAL COMMITTEES AND CHAIRMEN

<b>Aerodynamics</b> , Robert M. L. Baker, Jr.	<b>Physics of the Atmosphere and Space</b> , Herbert Friedman
<b>Communications and Instrumentation</b> , Frank W. Lehan	<b>Power Systems</b> , John H. Huth
<b>Electric Propulsion</b> , Ernst Stuhlinger	<b>Propellants and Combustion</b> , Peter L. Nichols, Jr.
<b>Guidance and Control</b> , James S. Farrior	<b>Ramjets</b> , William H. Avery
<b>Human Factors and Bioastronautics</b> , Eugene B. Konecki	<b>Solid Propellant Rockets</b> , G. Daniel Brewer
<b>Hypersonics</b> , William H. Dorrance	<b>Space Law and Sociology</b> , Andrew G. Haley
<b>Liquid Rockets</b> , Martin Goldsmith	<b>Structures and Materials</b> , George Gerard
<b>Magnetohydrodynamics</b> , Milton M. Slawsky	<b>Test, Operations, and Support</b> , Eernhardt L. Dorman
<b>Missiles and Space Vehicles</b> , William M. Duke	<b>Underwater Propulsion</b> , Herman E. Sheets
<b>Nuclear Propulsion</b> , Robert W. Bussard	

## Scope of ARS JOURNAL

This Journal is devoted to the advancement of astronautics through the dissemination of original papers disclosing new scientific knowledge and basic applications of such knowledge. The sciences of astronautics are understood here to embrace selected aspects of jet and rocket propulsion, spacecraft mechanics, high speed aerodynamics, flight guidance, space communications, atmospheric and outer space physics, materials and structures, human engineering, overall system analysis and possibly certain other scientific areas. The selection of papers to be printed will be governed by the pertinence of the topic to the field of astronautics, by the current or probable future significance of the research, and by the importance of distributing the information to the members of the Society and to the profession at large.

## Information for Authors

Manuscript must be as brief as the proper presentation of the ideas will allow. Exclusion of dispensable material and conciseness of expression will influence the Editors' acceptance of a manuscript. In terms of standard-size double-spaced typed pages, a typical maximum length is 22 pages of text (including equations), 1 page of references, 1 page of abstract and 12 illustrations. Fewer illustrations permit more text, and vice versa. Greater length will be acceptable only in exceptional cases.

Short manuscripts, not more than one quarter of the maximum length stated for full articles, may qualify for publication as Technical Notes or Technical Comments. They may be devoted to new developments requiring prompt disclosure or to comments on previously published papers. Such manuscripts are published within a few months of the date of receipt.

Sponsored manuscripts are published occasionally as an ARS service to the industry. A manuscript that does not qualify for publication, according to the above-stated requirements as to subject, scope or length, but which nevertheless deserves widespread distribution among jet propulsion engineers, may be printed as an extra part of the Journal or as a special supplement, if the author or his sponsor will reimburse the Society for actual publication costs. Estimates are available on request. Acknowledgment of such financial sponsorship appears as a footnote on the first page of the article. Publication is prompt since such papers are not in the ordinary backlog.

Manuscripts must be double spaced on one side of paper only with wide margins to allow for instructions to printer. Include a 100 to 200 word abstract. State the author's positions and affiliations in a footnote on the first page. Equations and symbols may be handwritten or typewritten; clarity for the printer is essential. Greek letters and unusual symbols should be identified in the margin. If handwritten, distinguish between capital and lower case letters, and indicate subscripts and superscripts. References are to be grouped at the end of the manuscript and are to be given as follows. For journal articles: Authors first, then title, journal, volume, year, page numbers; for books: Authors first, then title, publisher, city, edition and page or chapter numbers. Line drawings must be clear and sharp to make clear engravings. Use black ink on white paper or tracing cloth. Lettering should be large enough to be legible after reduction. Photographs should be glossy prints, not matte or semi-matte. Each illustration must have a legend; legends should be listed in order on a separate sheet.

Manuscripts must be accompanied by written assurance as to security clearance in the event the subject matter lies in a classified area or if the paper originates under government sponsorship. Full responsibility rests with the author.

Preprints of papers presented at ARS meetings are automatically considered for publication.

Submit manuscripts in duplicate (original plus first carbon, with two sets of illustrations) to the Managing Editor, ARS JOURNAL, 500 Fifth Avenue, New York 36, N. Y.

ARS JOURNAL is published monthly by the American Rocket Society, Inc. and the American Interplanetary Society at 20th & Northampton Sts., Easton, Pa., U. S. A. Editorial offices: 500 Fifth Ave., New York 36, N. Y. Price: \$18.00 per year, \$3.00 per single copy. Second-class postage paid at Easton, Pa., with additional entry at New York, N. Y. This publication is authorized to be mailed at the special rates of postage prescribed by Section 132.122. Notice of change of address should be sent to the Secretary, ARS, at least 30 days prior to publication. Opinions expressed herein are the authors' and do not necessarily reflect the views of the editors or of the Society. © Copyright 1961 by the American Rocket Society, Inc.

# Evolution of Upper Air Meteorology

H. J. aufm Kampe

U. S. Army Signal Research and  
Development Lab.  
Fort Monmouth, New Jersey

**A**EROLGY, the science of the upper layers of the atmosphere, has greatly enhanced and contributed to the fields of meteorology, weather forecast, avionics and rocketry. Until about 1880 it was the general belief that low pressure systems, i.e., cyclones, are warm air-mass bodies; and high pressure systems, i.e., anticyclones, are cold air-mass bodies. However, the famous Austrian meteorologist Julius von Hann disproved this common view by making temperature measurements on mountains. These measurements clearly indicated that the main body of cyclones is cold, and the main body of anticyclones is warm. His investigations proved that aerological investigations are extremely important to our knowledge of the dynamics and thermodynamics of the atmosphere.

It was soon realized that aerological measurements should also be carried out synoptically, i.e., simultaneously, as was done with the ground observations. Kites, airplanes, and, in some instances, balloons were used at first as the vehicles to carry meteorological instruments aloft on a more or less routine basis. These measurements not only enhanced our knowledge of the structure of the atmosphere with regard to temperature, density, pressure and wind, but they also contributed tremendously to our knowledge of weather forecasting.

In 1936 the first 500-millebar (mb) maps were published on a daily basis,<sup>1</sup> and soon after it was evident that they offer an excellent tool for the forecast of the movement of low and high pressures as well as frontal systems. At the present time there is probably no forecaster making forecasts without the use of the so-called upper air contour maps.

With the development of weather balloons and radiosondes, the kite and airplane ascents were replaced by balloon ascents, since the balloon went much higher than the other vehicles. Again, more knowledge was added to our understanding of the atmosphere, and a feature extremely important not only to meteorology but also to avionics and rocketry was discovered: the westerly jet stream (Fig. 1), a relatively narrow current of very fast moving air masses with very strong vertical wind gradients, causing in special cases heavy turbulence.

With better balloons and instrumentation, higher and higher layers of the atmosphere were explored, and new discoveries were made. While it was found that the westerly jet occurs at higher latitudes and at about 8 to 10 km, an easterly jet was discovered at around 16 to 20 deg latitude and 30 to 35 km altitude (Fig. 2). Now, approximately 20 years after the first 500-mb charts covering a relatively small part of the world (Central and Western Europe) were published, upper air maps for temperature and wind up to 10 mb (30 km) are routinely plotted for the entire northern hemisphere, as can be seen in Fig. 3.

The most remarkable information that the high altitude balloon network yielded was the explosive warmings, which in most cases were strongest at the top of the ascents, and which occur mostly during the winter season (January and February). Fig. 4 shows such cases in 1957, in which the temperature within a few days rose very sharply by about 45 to 65 C. Such a tremendous temperature change in such a short time does not occur at any point on the surface of the Earth except perhaps on the Greenland icecap. Parallel to this phenomenon, the entire upper air pressure pattern changes completely, as can be seen in Figs. 5 through 8, which show a case of an explosive warming in 1958 that was analyzed by Dr. R. Scherhag and associates of the Free University, Berlin, Germany. The normal pressure pattern during the winter months shows a low pressure center near the pole, with more or less concentric contour lines from the pole to the subtropics as seen in Fig. 3. During such a disturbance as mentioned, this simple pattern is replaced by alternating high and low pressure systems, and instead of a low, a high is over the pole. After the disturbance, the winter pattern was gradually restored (Fig. 8).

The most surprising fact, however, is that this pattern was not drifting with the stratospheric winter westerlies, as one would expect, but from east to west. Two questions immediately arise: What was the temperature structure above the top of the balloon ascent, and, are there higher steering levels affecting the air masses around 30 km or even higher? To answer these questions data from higher levels are needed, and to collect these data rockets must be used as the vehicle.

The first attempts to measure the physical properties of the upper atmosphere were carried out with V-2 rockets,

Presented at the ARS 15th Annual Meeting, Washington, D. C., Dec. 5-8, 1960.

<sup>1</sup> This was carried out in Germany.

---

Hans Joachim aufm Kampe was born in Essen, Germany, on Dec. 10, 1912. He received M.S. and Ph.D. degrees in 1936 and 1941, respectively, from the Technical University, Darmstadt, Germany. From 1936 to 1945 he was with a research institute for aeronautics as atmospheric physicist, and he later directed the Meteorological Branch of this institute. From 1946 to 1948 he was with the Central Office of the German Weather Service for Northwest Germany in Hamburg, Germany. Since 1948 he has been with the U. S. Army Signal Research and Development Lab., Fort Monmouth, N. J., where he now serves as chief of the Atmospheric Physics Branch, Meteorological Div.

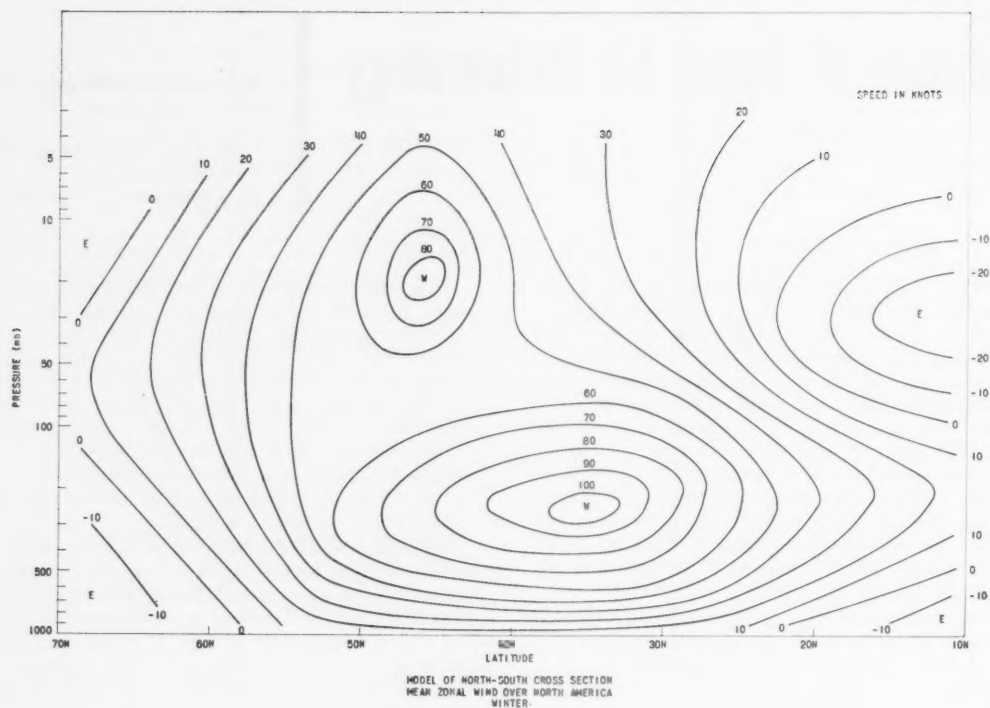


Fig. 1 Westerly jet stream

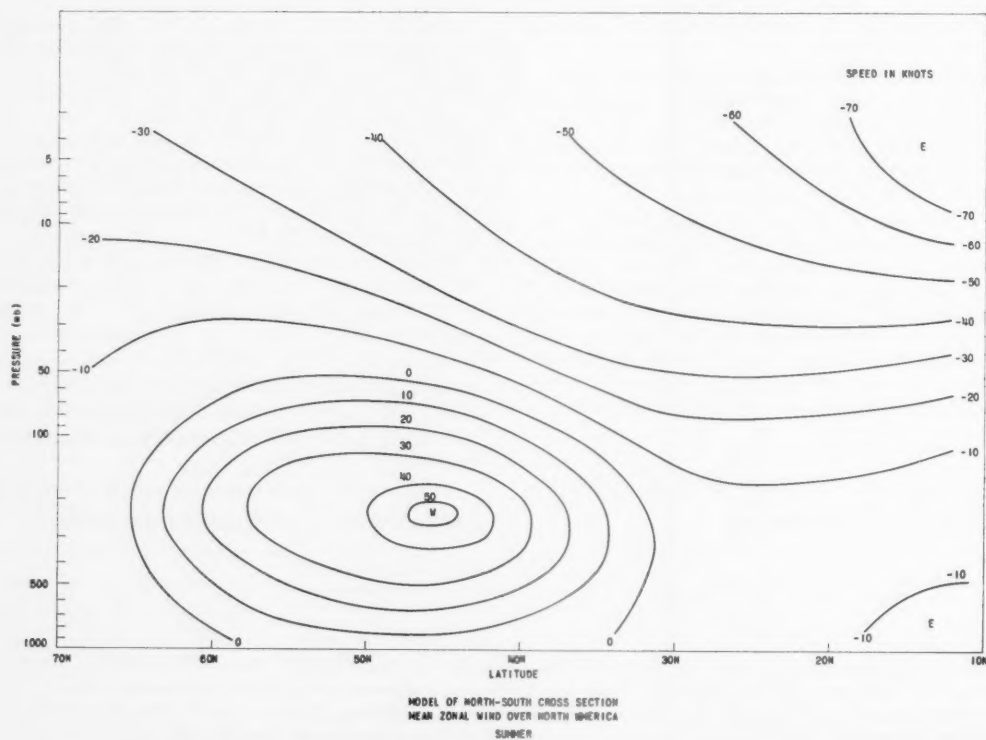


Fig. 2 Easterly jet stream



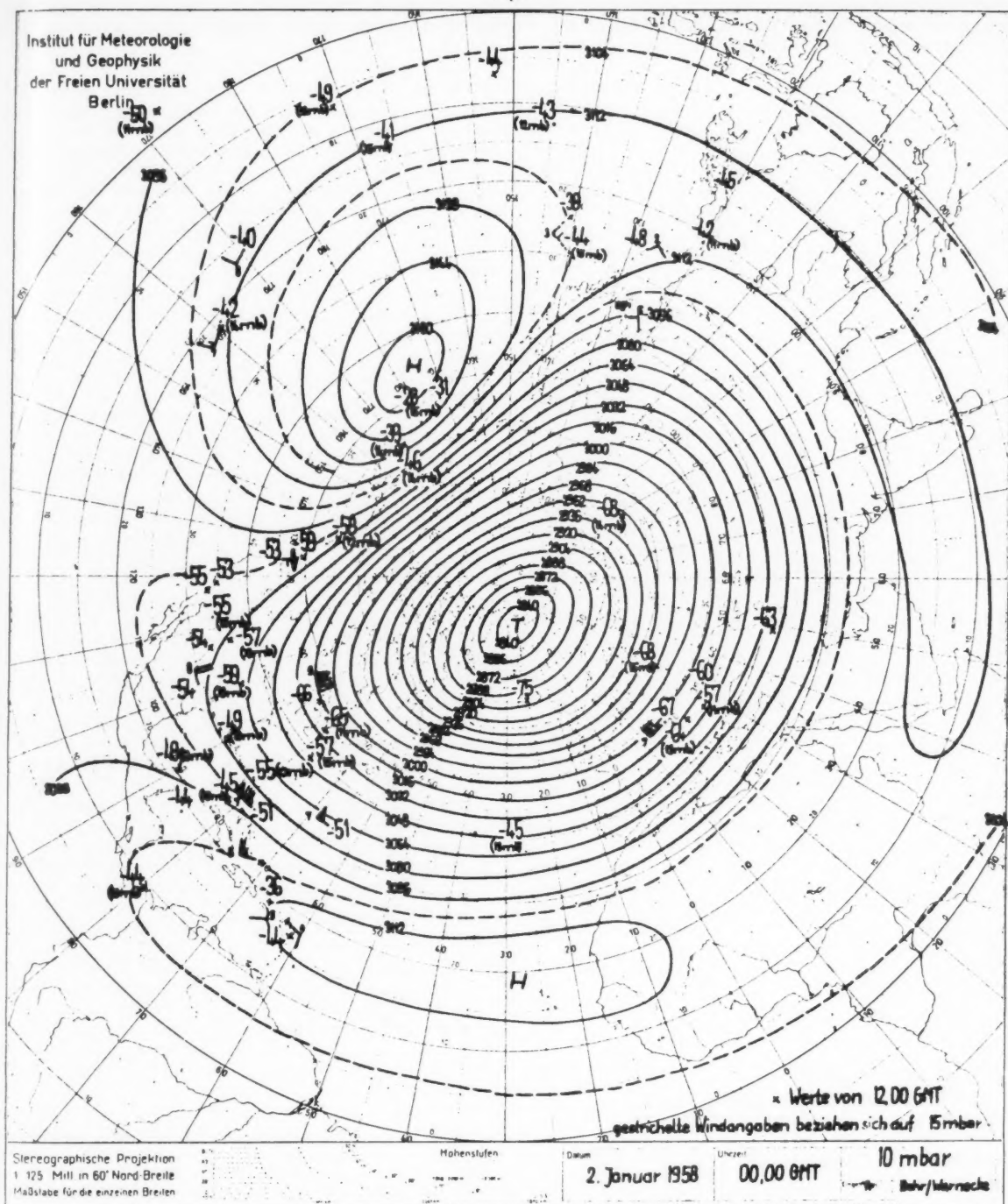


Fig. 3 Ten-millibar contour map for the northern hemisphere in winter

which actually were not built for this purpose. Therefore, a research rocket, the Aerobee, specifically designed for upper air research, was developed and used for, among other things, measurements of temperature, pressure, density and wind. These parameters were measured by different government agencies using different methods. The first flights were carried out at the White Sands Missile Range in the late 40's and early 50's. Results were published in 1952

(1)<sup>2</sup> by the Rocket Panel, which consists of scientists from government agencies and from universities. The big surprise of these results was that there were great differences between these measurements and the NACA standard atmosphere which was used for a long time by airplane and rocket designers as standard.

<sup>2</sup> Numbers in parentheses indicate References at end of paper.

In Fig. 9 one can see that at around 50 km the new results indicated a temperature approximately 70 C warmer than the standard atmosphere. This fact is rather significant. However, these results were obtained at one spot at about 30 deg N latitude. The question was whether the same results could be obtained in more northern areas. The IGY offered an excellent opportunity to answer this question, and a series of Aerobee firings was carried out at Fort Churchill, Canada.

One method of measuring the meteorological parameters, i.e., wind, temperature, density and pressure, was the so-called rocket-grenade experiment. Nineteen grenades were ejected at intervals of about 3 km, starting around 30 km from the Aerobee rocket and exploding 10 to 15 ft apart from the Aerobee. From the time of arrival and the angle of the wave front at the ground, temperature and wind of the 3-km layers were computed. The altitude of the rocket was determined by DOVAP. Finally, using the hydrostatic equation, pressure and density were computed.

Five rocket firings were carried out in the summer and five in the winter under the supervision of W. Stroud, W. Nordberg, L. Jones, and F. Bartmann (2). The first interesting result was the fact that the summer temperature data looked similar to the year-round data of the firings at White Sands Proving Ground (Fig. 10), indicating that during summer-time there is apparently not much difference in the temperature structure between a station at around 30 and one near 60 deg latitude, although the temperatures at 50 km and below at Fort Churchill were somewhat higher than at White Sands, and above 65 km the temperatures at Fort Churchill were lower.

The winter data, however, are quite different, as can be seen in Fig. 11. The most remarkable fact is that at around 80 km there is a temperature difference between winter and summer of about 60 to 70 C, the winter being warmer (Fig. 12). Because of this difference in temperature structure, the density during the winter between about 30 and 80 km is roughly half as low as during the summer (Fig. 13). The case is similar with regard to pressure. These results are important for meteorology as well as for aeronautics and rocketry. Another method, the so-called falling sphere method, devised by L. Jones and F. Bartmann (3) and based on the measurement of the drag acceleration of a sphere, yielded similar results, as did measurements based on still other principles, by LaGow et al. (4). In Summer the wind has an average speed above 25 km of about 100 mph, blowing from the east; and in winter it has a speed of about 200 mph and blows from the west.

The second remarkable result from these firings is that on

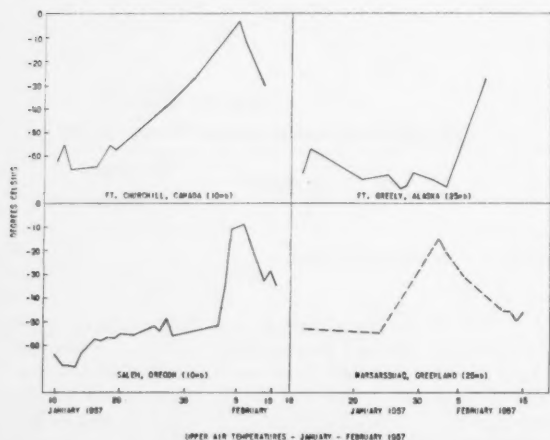


Fig. 4 Stratospheric temperature curves at different stations in January and February 1957

Jan. 27, 1958, shortly before a strong warming was observed at the top level of the balloon ascents (as mentioned before), the wind pattern changed completely, as can be seen in Fig. 14. According to L. Jones, et al. (5), the temperature at 45 km rose from about 240 C early on Jan. 26 to almost 290 K on Jan. 29, i.e., a few days earlier than at balloon level (Fig. 15). The exact mechanism causing the strong temperature increases starting at high levels and progressing to lower and lower levels is not known and can be determined only from daily synoptic measurements at different stations. The more or less sporadic rocket measurements already mentioned, and those by Stroud, Nordberg, and others, carried out at Guam, about 15 deg N, using the rocket-grenade method with the Nike-Cajun combination, prepared an excellent basis for planning such synoptic investigations.

In order to carry out synoptic rocket measurements with a network of stations, however, the cost of the rockets had to be reduced considerably. The trend of using progressively smaller rockets for meteorological measurements since the first V-2 flights is indicated in Fig. 16. The last two rockets shown in this figure are the Arcas and the Loki. These rockets are now being used in the synoptic meteorological rocket network (6), which is an undertaking supported jointly by the Army, Air Force, Navy NASA and Weather Bureau, as well as by Rand and Sandia Corps. Fig. 17 shows the stations at which firings are presently being carried out. We hope that other stations will be added in the U. S. and abroad. Presently, daily flights, except on weekends, are being carried out in the midmonth of each season. This schedule may change, depending on the results of the first year's operation, which started in October 1959. The results of the first year's measurements to 60 km have been analyzed and will be published in the near future. We hope that the synoptic rocket network firings will expand laterally, i.e., to other continents and possibly to the southern hemisphere, as well as upward to higher altitudes.

It is believed that the results of the analysis of network synoptic firings will add to and improve the picture we now have of the upper air circulation. The first such picture was produced by Kellogg and Schilling in 1951, Fig. 18, (7). Their presentation is the result of theoretical considerations based on few data. Quite different is the compilation of data published by Murgatroyd in 1957, Fig. 19, (8). It shows much more detail, and in some instances a west wind in Kellogg and Schilling's pictures becomes an east wind in the presentation of Murgatroyd. And yet the writer believes that even the average summer and winter presentation of winds and temperature as indicated by Murgatroyd is not the last word in this respect. This opinion is verified by a new look at the upper air meteorological picture by Batten (9) as the writer learned in private communications.

While Murgatroyd's data above 30 km were taken principally from abnormal sound propagation measurements as well as from meteor trails and ionospheric drifts, Batten made extensive use of rocket data, particularly those collected during IGY. In addition, he used some of the results yielded by the meteorological rocket network. Analyzing these data, he concluded that, particularly for the winter season when the upper atmosphere is in a status of unrest, there is a great need for more reliable upper air data, which he hopes will be obtained by the Meteorological Rocket Network.

One very important feature which became clear from Murgatroyd's and Batten's analyses is the astonishing fact (already mentioned in describing the results of the rocket firings during winter at Fort Churchill) that at the location where the energy flux from the sun is smallest, i.e., at the winter polar region, the temperature around 80 to 90 km is highest, and vice versa. This is a kind of paradox. Kellogg<sup>3</sup>

<sup>3</sup> Paper given at the joint session of the American Meteorological Society and the Institute of Aeronautical Sciences, Jan. 29, 1960.

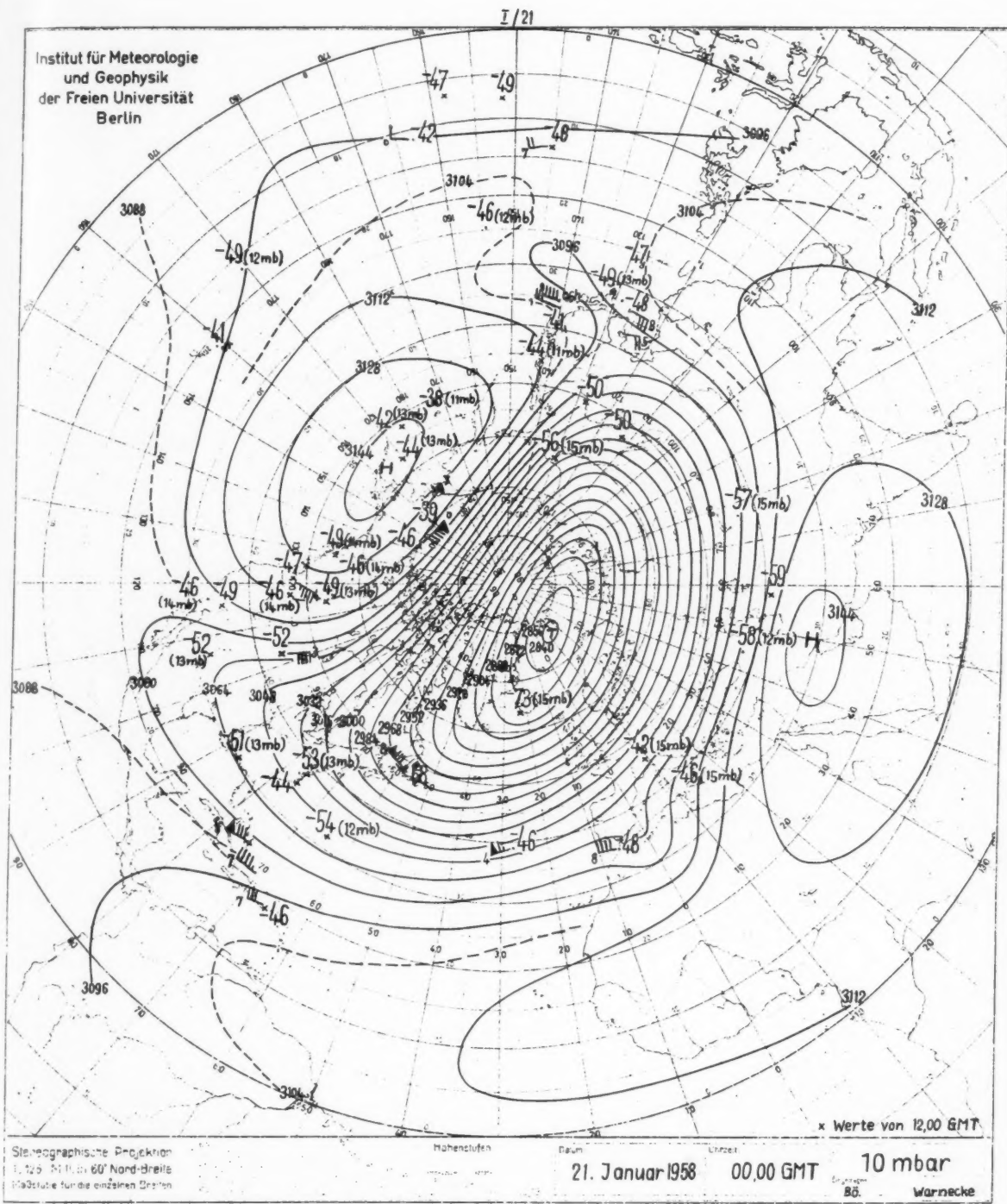


**Fig. 5** Pressure patterns at the beginning of a period of an "explosive warming"

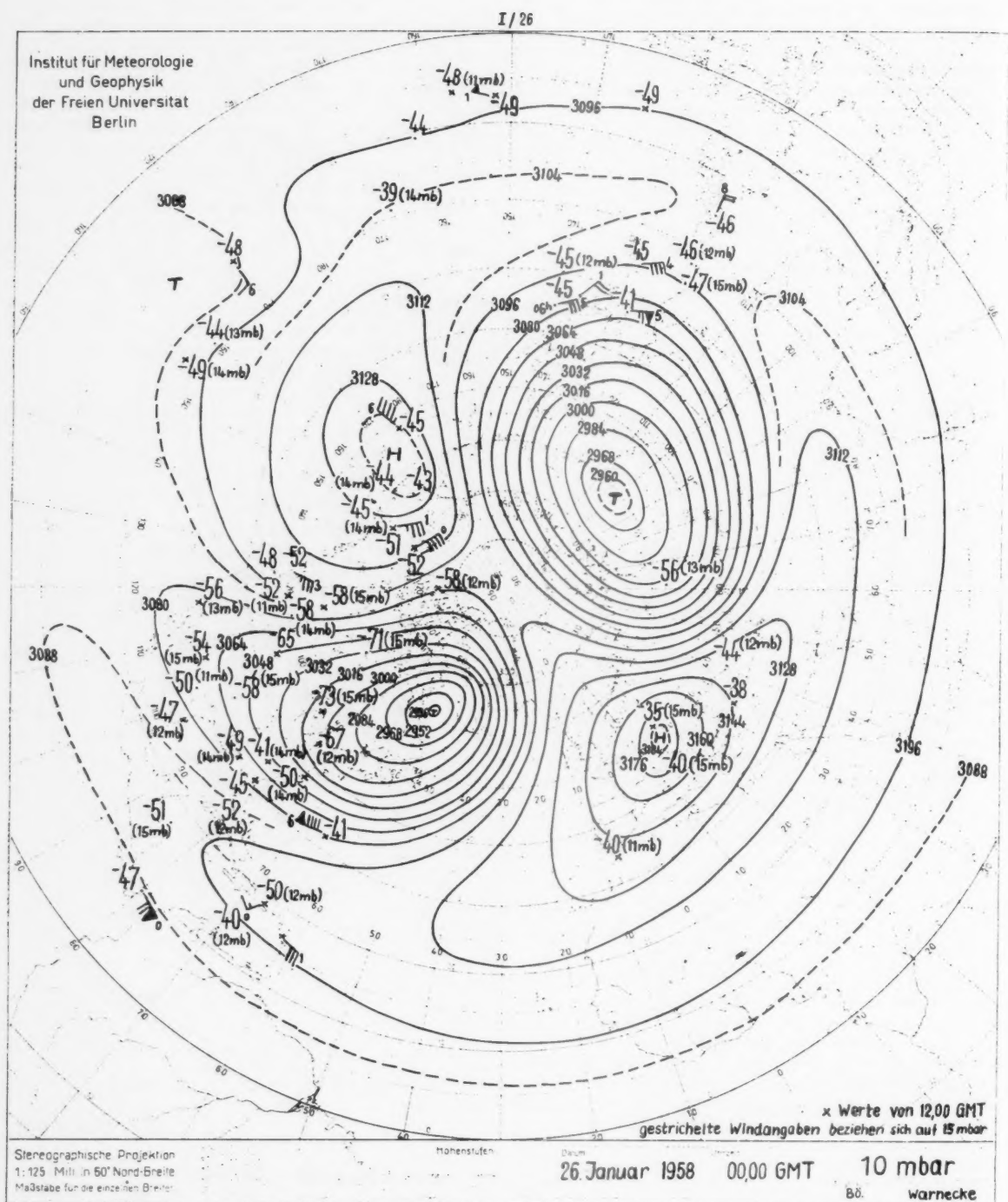


Fig. 6 Pressure patterns during the period of an "explosive warming"



I/30

Institut für Meteorologie  
und Geophysik  
der Freien Universität  
Berlin

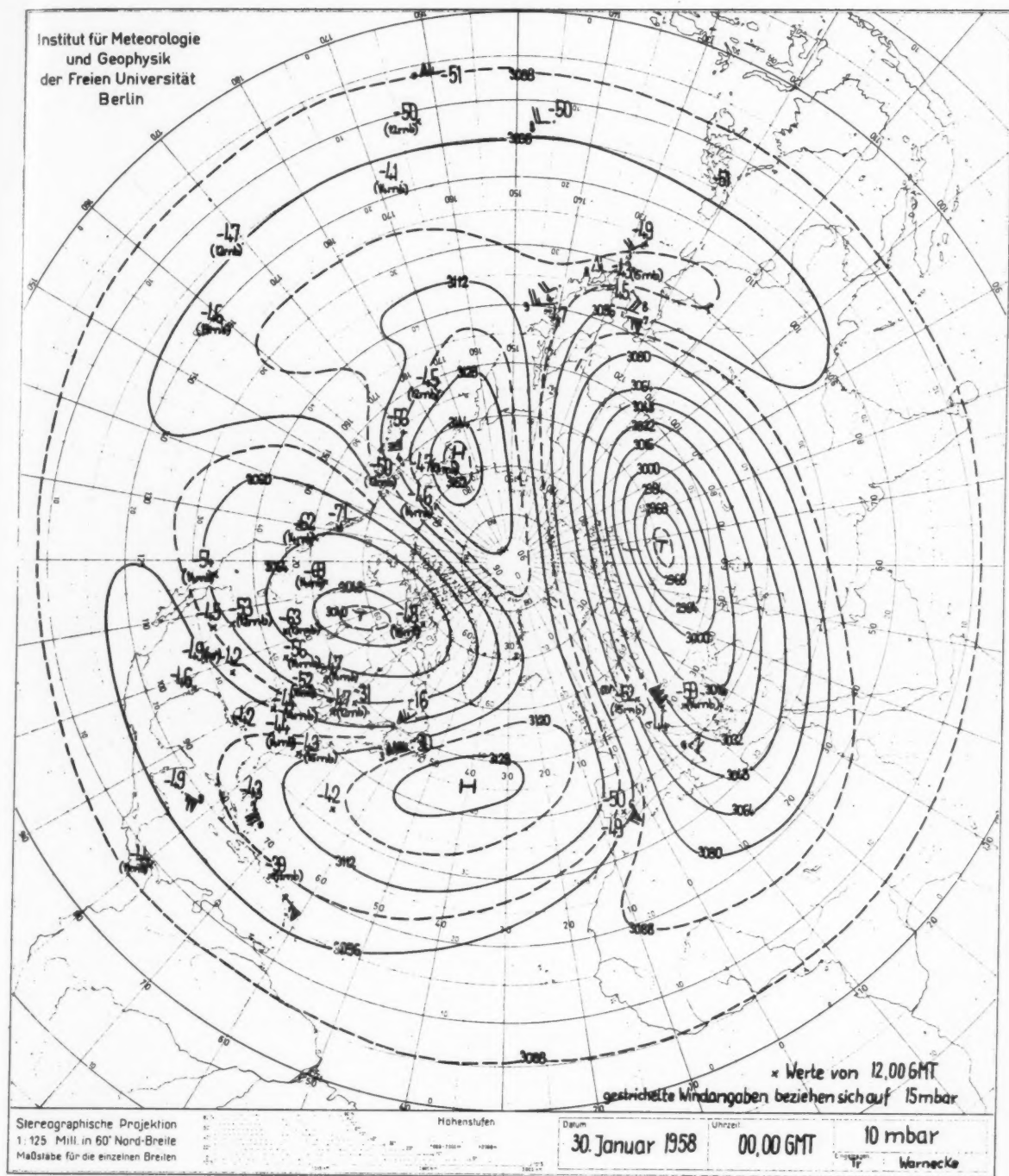


Fig. 7 Pressure patterns during the period of an "explosive warming"

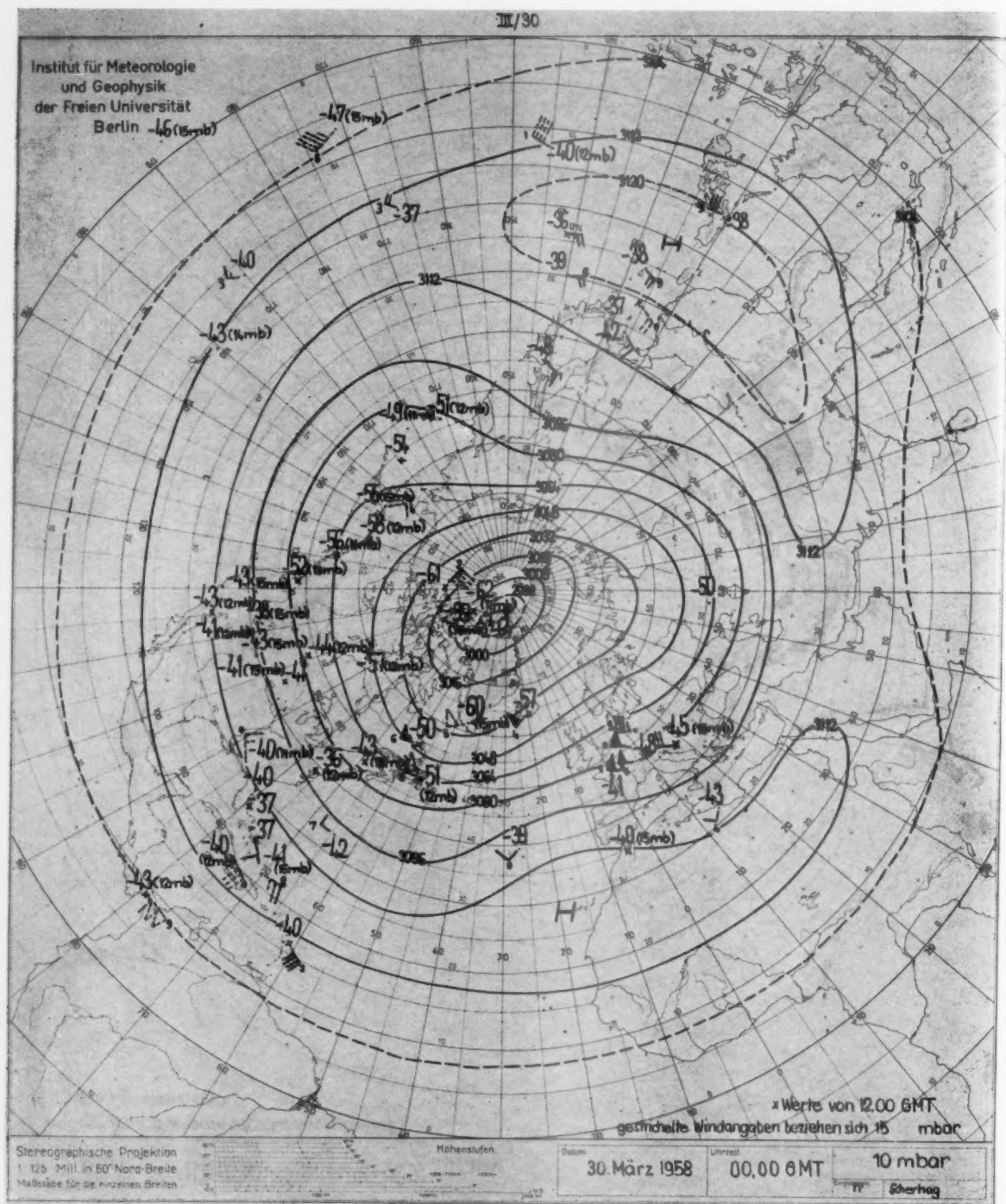


Fig. 8 Normal winter pressure pattern after period of an "explosive warming"

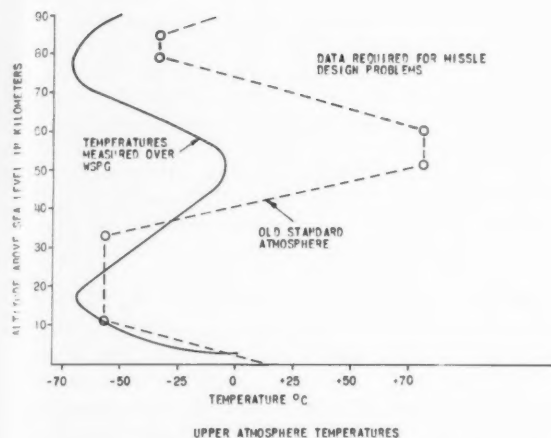


Fig. 9 Comparison between the old NACA Standard atmosphere and rocket data obtained by the rocket-grenade experiment at White Sands Missile Range

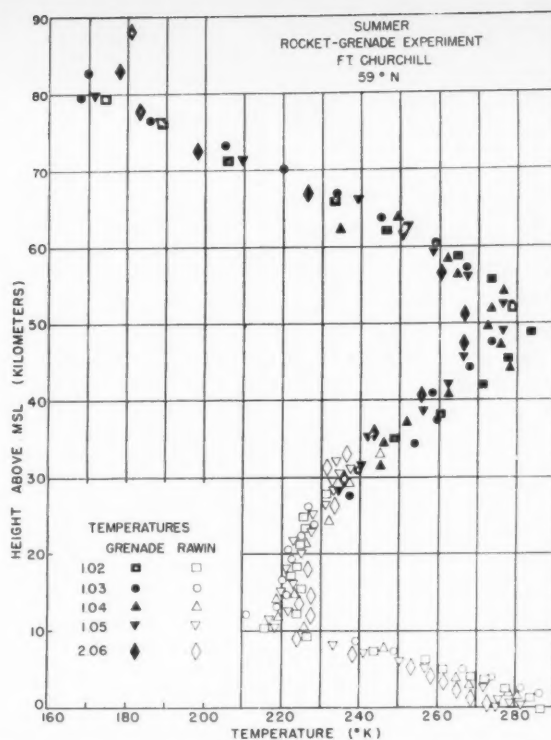


Fig. 10 Summer temperatures over Fort Churchill, Canada, as determined by the rocket-grenade experiment, according to Stroud et al.

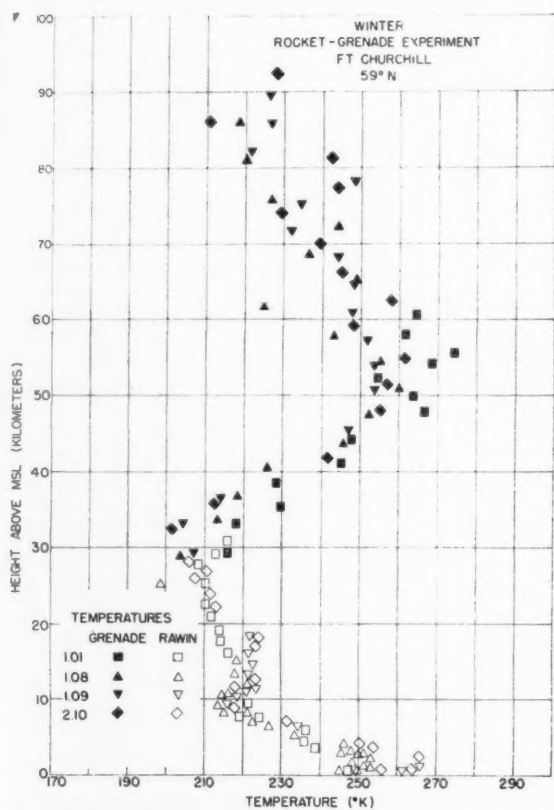


Fig. 11 Winter temperatures over Fort Churchill, Canada, as determined by the rocket-grenade experiment, according to Stroud et al.

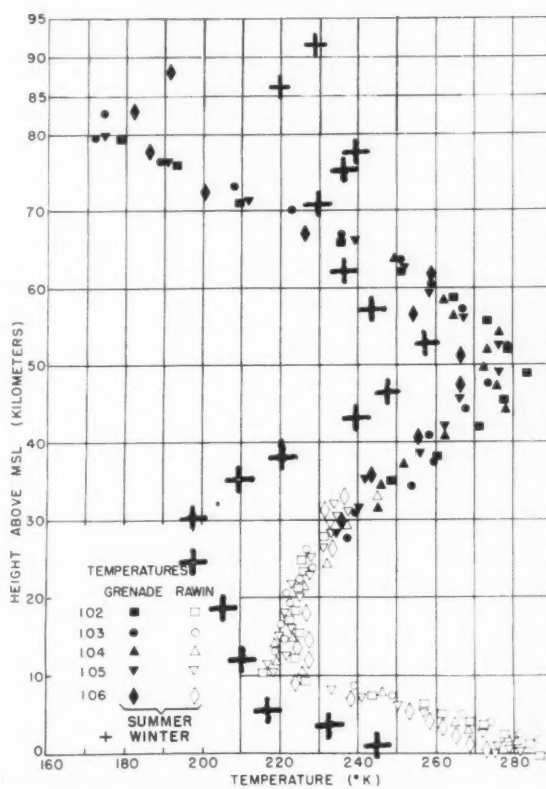


Fig. 12 Summer and approximate mean winter temperatures over Fort Churchill, Canada, as determined by the rocket-grenade experiment, according to Stroud et al.

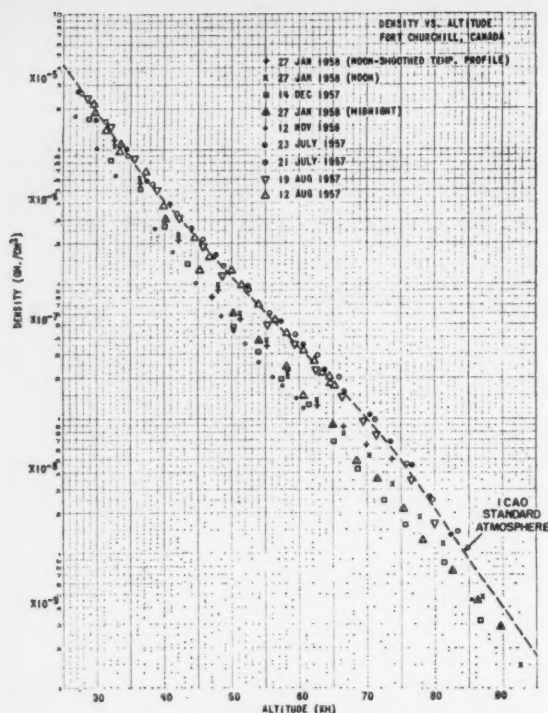


Fig. 13 Summer and winter density over Fort Churchill, Canada, as computed from data of the rocket-grenade experiment, according to R. Griffith (verbal communication)

has suggested that the high temperature over the northern region in winter could be readily explained by recombination of atomic oxygen to molecular oxygen, due to subsiding air over the polar region during wintertime.

Another point which should be realized by looking at Murgatroyd's as well as Batten's presentation is that they represent average conditions which may change from day to day as much or more than the conditions below 30 km shown before. In the higher layers, dramatic events are occurring. This may be seen in Fig. 20, which is a time exposure of the exhaust trail from the second-stage rocket of Project Shotput. Some results of the stereoscopic evaluation of the exhaust trail are shown in Fig. 21. As can be seen, there was a westerly wind at about 100 km of approximately 500 mph, and at about 115 km there was an easterly wind of approximately 220 mph with a tremendous wind shear of more than 200 mph per mile at 109 km.

Synoptic measurements at different locations should shed more light on this interesting phenomenon. Particularly, one should find out whether it is a part of a large scale circulation pattern or whether it has certain space and time limits as, e.g., the tidal winds, which in these altitudes are already very strong, as Fig. 22 shows. This figure is published in an article by Lovell in the book *The Earth and Its Atmosphere* edited by Bates (10) and gives the results of meteor-trail radio echo measurements carried out by personnel of the Jodrell Bank Experimental Station in England. The radio echo method is a very powerful tool for investigating the regions between about 80 and 110 km. The results obtained so far with this method (11) as well as those obtained by photographing meteor (12) and artificial

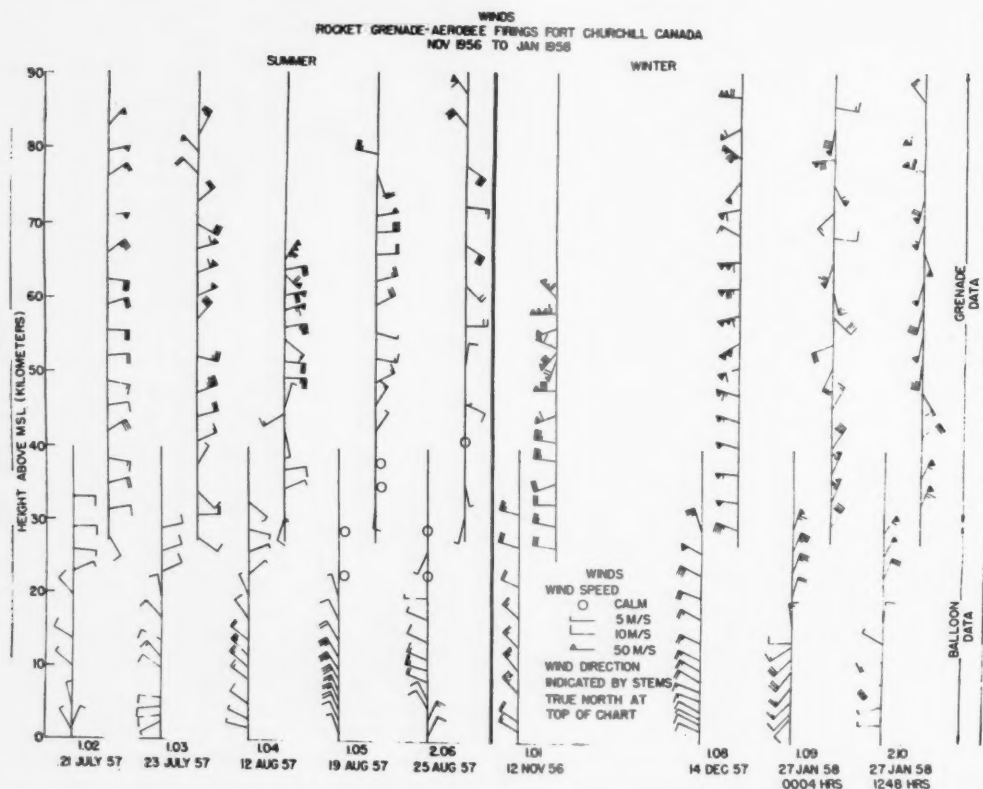


Fig. 14 Winds over Fort Churchill, Canada, as measured by the rocket-grenade technique during IGY, according to Stroud et al.



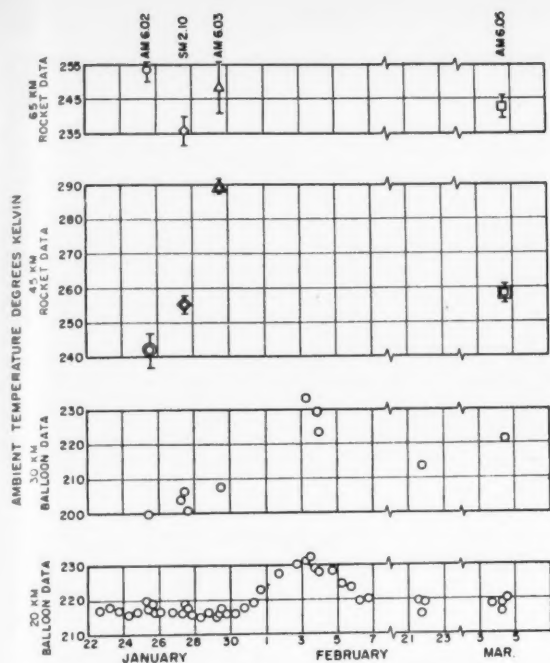


Fig. 15 Explosive warmings at high altitudes as determined with the "falling sphere" method and balloon ascents at Fort Churchill, Canada, winter 1958, according to Jones et al.

alkali vapor trails (13) also indicate strong wind shear and turbulence at the 100-km region. In order to study the tidal winds below 80 km, some of the Meteorological Rocket Network Stations, e.g., the White Sands Missile Range (located at about 5000 ft above sea level where Loki and Arcas rockets reach 80 km) will carry out several flights on certain days.

So far we have discussed only the determination of wind, temperature, density and pressure. But these parameters should by no means be the only ones measured. One of the most important constituents of the upper atmosphere is the ozone. It is because of the ozone that we have the meso-peak, i.e., the high temperatures around 50 km. It is obvious from this fact alone that great emphasis should be given to synoptic measurements of the ozone concentrations up to about 50 km. By doing this, a great deal can also be learned about the air-mass movements in the stratosphere and mesosphere, since ozone is a rather conservative property of the air in these altitudes. Some balloon measurements, particularly by Paetzold (14) and Brewer and Milford (15), are already available; but it is the opinion of the writer that synoptic rocket ascents to 60 km will yield the really interesting facts about the role of ozone in the heat budget of the upper atmosphere. A few special rocket measurements have already been carried out by Johnson (16), and another attempt in this direction will be made soon by Prof. Palmer of UCLA under Navy sponsorship.

Of similar importance as ozone measurements are water vapor measurements. In this connection, J. Brown, BRL<sup>2</sup> (17) has recently carried out successful balloon flights using a dew point hyrometer, and it is planned to also make water

<sup>2</sup> Army Ballistics Research Laboratory

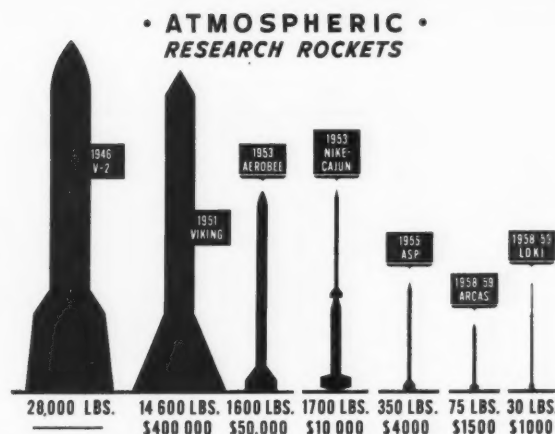


Fig. 16 Some of the upper atmosphere research rockets since 1946

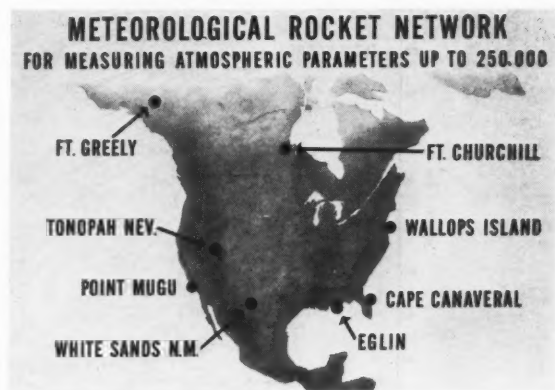


Fig. 17 Distribution of the present meteorological rocket network stations

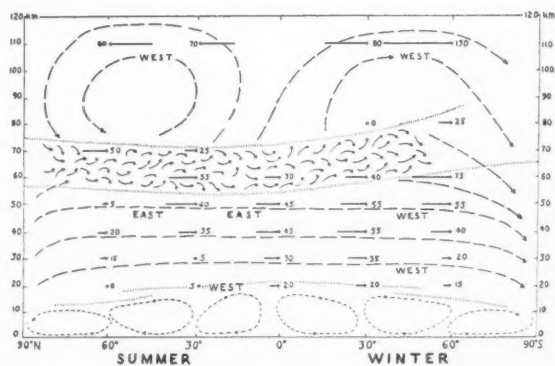


Fig. 18 Schematic representation of the general circulation in meridional cross section for northern summer, according to Kellogg and Schilling (1951)

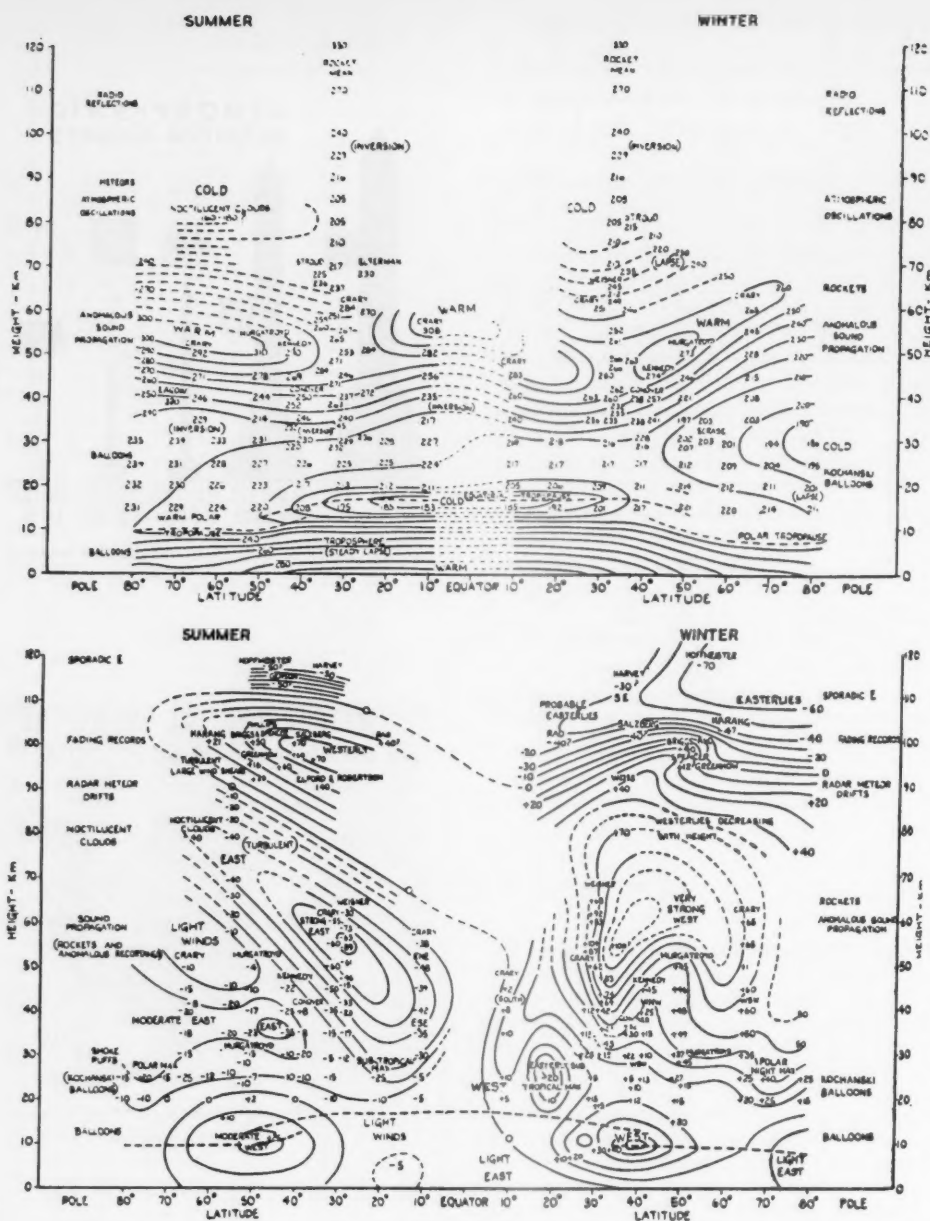


Fig. 19 Upper air temperature (a) and circulation (b), according to Murgatroyd (1957)

vapor measurements with rockets in the not too distant future.

It is the firm belief of the writer that extremely interesting tasks lie ahead with respect to the systematic synoptic exploration of the atmospheric layer between 30 and about 100 km which, by one well-known atmospheric physicist, has been named, appropriately, the "ignosphere."

## References

- 1 The Rocket Panel, "Pressures, Densities, and Temperatures in the Upper Atmosphere," *Phys. Rev.*, vol. 88, 1952, pp. 1027-1032.
- 2 Stroud, W. G., Nordberg, W., Bandeen, W. R., Bartmann, F. L. and Titus, P., "Rocket-Grenade Measurements of Temperature and Winds

in the Mesosphere over Churchill, Canada," *J. Geophys. Res.*, vol. 65, 1960, pp. 2307-2323.

3 Jones, L. M. and Bartmann, F. L., "A Simplified Falling-Sphere Method for Upper-Air Density," Univ. of Michigan Engng. Research Inst. Rep. 2215-10-T, 1956.

4 LaGow, H. E., Horowitz, R. and Ainsworth, J., "Rocket Measurements of the Arctic Upper Atmosphere," *Natl. Acad. Sci. IGY Rocket Rep. Ser. 1*, 27-37, 1958.

5 Jones, L. M., Peterson, J. W., Schaefer, E. J. and Schulte, H. F., "Upper-Air Density and Temperature, Some Variations and an Abrupt Warming in the Mesosphere," *J. Geophys. Res.*, vol. 64, 1959, pp. 2331-2340.

6 aufm Kampe, H. J., "The Meteorological Rocket Network," to be published in *Weatherwise*.

7 Kellogg, W. W. and Schilling, G. F., "A Proposed Model of the Circulation in the Upper Stratosphere," *J. Meteorol.*, vol. 8, 1951, pp. 222-230.

8 Murgatroyd, R. J., "Winds and Temperatures between 20 Km and 100 Km, A Review," *Quar. J. Royal Meteorol. Soc.*, vol. 83, 1957, pp. 417-458.

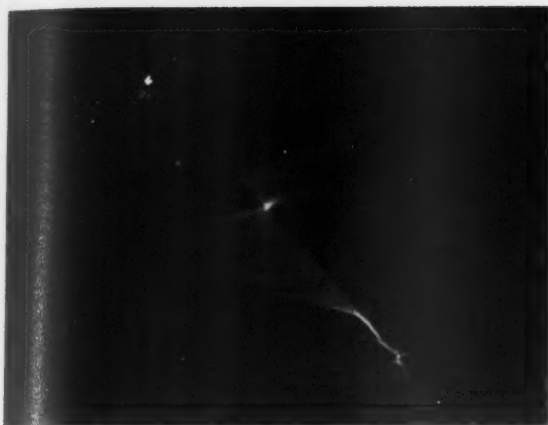
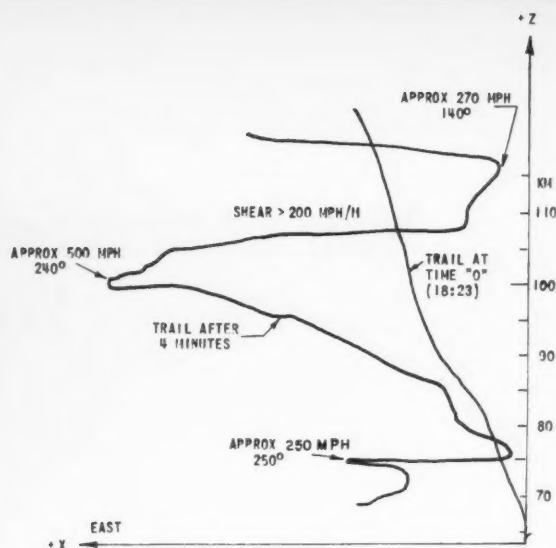


Fig. 20 Time exposure of the exhaust trail at about 60 to 120 km of the second stage of the Project Shotput rocket fired on Feb. 27, 1960 at Wallops Island, Va.



WALLOPS ISLAND ROCKET EXHAUST TRAILS  
27 FEB. 1960

Fig. 21 Winds between about 60 and 120 km as determined from the stereoscopic evaluation of the exhaust of the second stage of the Project Shotput rocket, fired on Feb. 27, 1960, 1820 hr

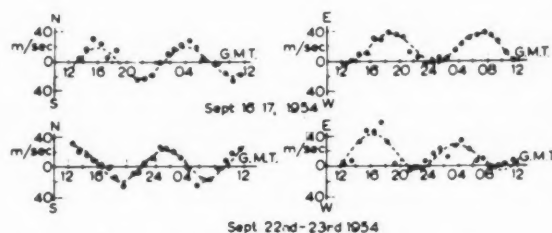


Fig. 22 Tidal winds according to meteor trail measurements made at Jodrell Bank, England

- 9 Batten, E. S., "Wind Systems in the Mesosphere and Lower Ionosphere," to be published.
- 10 *The Earth and Its Atmosphere*, D. R. Bates (ed.), Basic Books, Inc., N. Y., 1957.
- 11 Greenhow, J. S. and Neufeld, E. L., "Measurements of Turbulence in the 80- to 100 Km Region from the Radio Echo Observations of Meteors," *J. Geophys. Res.*, vol. 64, pp. 2129-2133.
- 12 Whipple, F. L., "Evidence for Winds in the Outer Atmosphere," *Proc. Natl. Acad. Sci. U. S.*, vol. 40, 1954, pp. 966-972.
- 13 Manning, E., Bedinger, J. F., Pettit, H. B. and Moore, C. B., "Some wind Determinations in the Upper Atmosphere using Artificially Generated Sodium Clouds," *J. Geophys. Res.*, vol. 64, 1959, pp. 587-591.
- 14 Paetzold, H. K., "Vertical Atmospheric Ozone Distributions," *Advances in Chem.*, Series No. 21, 209-220.
- 15 Brewer, A. W. and Milford, J. R., "The Oxford-Kew Ozone Sonde," *Proc. Royal Soc., Serial A, Math. and Phys.*, Serial 256, 1960, pp. 470-495.
- 16 Johnson, F. S., "High-Altitude Diurnal Temperature Changes Due to Ozone Absorption," *Bull. Amer. Meteorol. Soc.*, vol. 34, 1953, pp. 106-110.
- 17 Brown, J. A., "Distribution of Water Vapor in the Stratosphere," *Conf. on Stratospheric Meteorology*, Minneapolis, Minn., Sept. 1959.

### 1961 ARS Meeting Schedule

Date	Meeting	Location	Abstract Deadline
Aug. 7-9	Guidance and Control Conference	Palo Alto, Calif.	Past
Aug. 16-18	International Hypersonics Conference	Cambridge, Mass.	Past
Aug. 23-25	Biennial Gas Dynamics Symposium	Evanston, Ill.	Past
Oct. 2-7	XIIth International Astronautical Congress	Washington, D.C.	Past
Oct. 9-15	ARS SPACE FLIGHT REPORT TO THE NATION	New York, N.Y.	Past

Send all abstracts to Meetings Manager, ARS, 500 Fifth Ave., New York 36, N.Y.

# Winds and Circulations in the Mesosphere

THOMAS J. KEEGAN<sup>1</sup>

Air Force Cambridge Research  
Laboratories  
Bedford, Mass.

Some preliminary analyses are presented of winds and circulations in the mesosphere based upon the first year of data collected by the Meteorological Rocket Network. Differences between winds determined from radar targets released by rockets and those from the conventional balloon technique are discussed. The scale of seasonal, daily and vertical wind variations is illustrated by means of wind profiles and time cross sections. They demonstrate clearly the seasonal reversal of winds in the mesosphere and the existence of large variations in wind speed over periods of only several days. They also reveal that wind shears greater than  $0.030 \text{ sec}^{-1}$  exist near 180,000 ft. Examples are shown of the circulation over North America in spring and summer at heights up to 160,000 ft. Analysis of rocket wind data indicates that the technique is sound and that much can be learned by more intensive analysis.

**W**IND data to heights up to 220,000 ft have been collected on a semi-routine network basis since fall 1959. The initiation and development of this network and the equipment it utilizes have been described by Webb et al. (1)<sup>2</sup> and aufm Kampe (2). A general discussion of the available rockets and wind sensors, the techniques of collecting and reducing the data and some of the problems unique to a rocket network has been prepared by Keegan (3). The details of the data reduction and evaluation will be prepared by the Joint Scientific Advisory Group to the Meteorological Rocket Network.

The initial analyses presented herein demonstrate that meteorological rocket data are more than a scientific curiosity; they can be used to study the circulation and its variations. Furthermore, these variations are significant enough to make the study of the region scientifically interesting and potentially applicable to aerospace operations.

## Discussion of the Data

Some knowledge of how the data are collected and reduced is necessary in order to understand the differences between the familiar balloon and rocket soundings. The winds discussed in this paper were all determined from the horizontal displacement of a falling radar target over a period of 1 min. This displacement was determined graphically from a display which automatically and continuously recorded the position of the target in space. The 1-min mean winds thus derived were assumed to have occurred midway between the altitude of the target at the beginning and end of the minute. The targets used were radar-reflective chaff and parachutes.

The major difference between the balloon and rocket data is in the height interval over which the wind is averaged. In balloon soundings the custom is to average the winds over a

2 to 4-min interval. Since the balloon rises at almost constant rate, the winds represent essentially a constant time and space mean regardless of their altitude. The sensor or target used in a rocket sounding, however, is a falling body whose velocity decreases as the air density increases. This introduces a problem which does not arise in balloon soundings. Since the fall velocity varies considerably, the 1-min mean winds represent a much larger height mean at the top of a sounding than they do at the bottom. For a parachute with

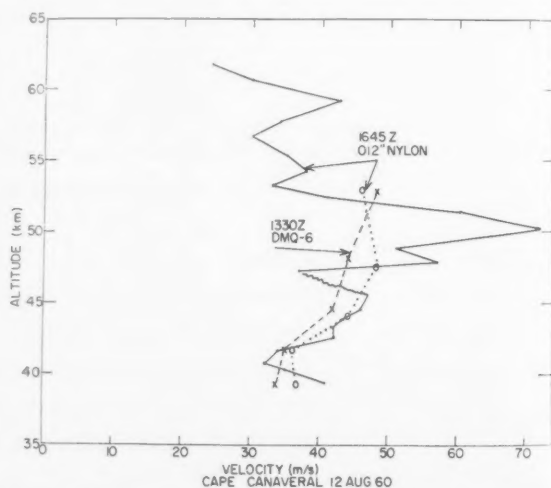


Fig. 1 Wind profiles at Cape Canaveral, Fla., 12 August 1960. Comparison of winds as computed from 1-min horizontal displacements of slow falling nylon chaff (solid line) and fast falling 15-ft parachute with DMQ-6 radiosonde attached (dashed line); dotted line is wind determined from nylon chaff when averaged over approximately the same height increment as was used for the parachute

Presented at the ARS Annual Meeting, Washington, D. C., Dec. 5-8, 1960; expanded.

<sup>1</sup> Research Scientist, Atmospheric Circulations Laboratory, Geophysics Research Directorate, Office of Aerospace Research, Laurence G. Hanscom Field.

<sup>2</sup> Numbers in parentheses indicate References at end of paper.



a temperature sensor attached, the fall rate may vary from around 25,000 fpm at 200,000 ft to 1000 fpm at 80,000 ft.

The characteristic of large fall velocities at high altitudes means that much detail in the wind profile may be smoothed out in a 1-min average. Fig. 1 illustrates two soundings taken about 3 hr apart. One sounding used light nylon chaff (solid line) and the other a heavier DMQ-6 radiosonde attached to a 15-ft parachute (dashed line) which had a fall velocity of about four to five times that of the chaff. The loss of wind detail sensed by the parachute is evident. If the nylon sounding is averaged over approximately the same height interval that the parachute fell in 1 min (dotted line), it becomes evident that the two soundings agree very well.

Greater detail could be obtained by averaging over a time interval of 10 to 15 sec instead of a minute, but this cannot be done from a graphical radar plot. Instead, digital data must be used. However, since the equipment to do this is not always available to the Rocket Network, initial reduction has been based upon the graphical output.

The initially rapid fall rate also introduces the problem

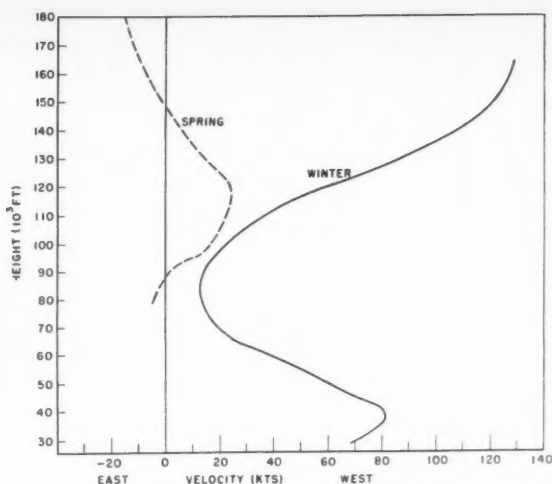


Fig. 2 Mean zonal wind profile at Wallops Island, Va., for winter (solid line) and spring (dashed line) 1960

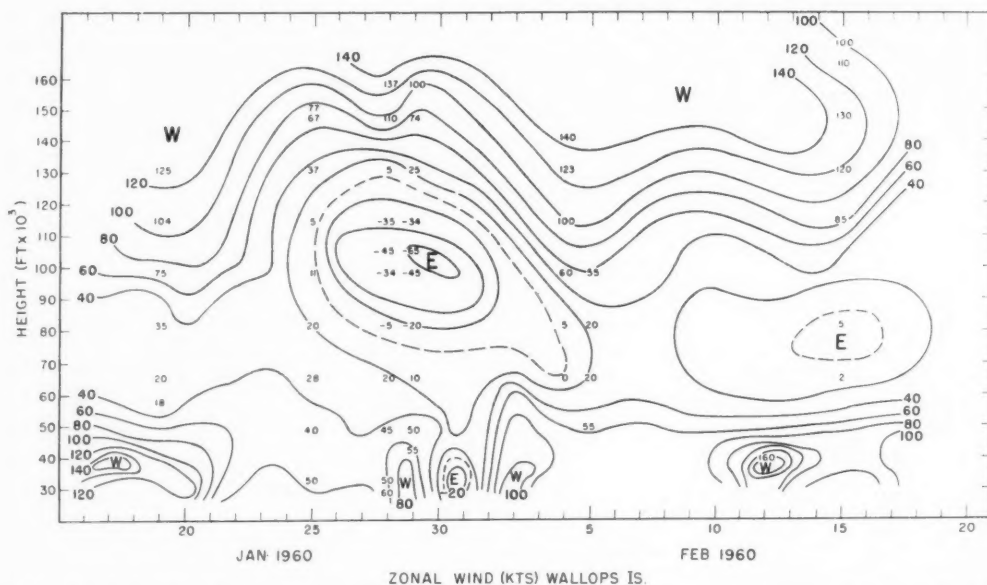


Fig. 3 Zonal wind (kts) time cross section Wallops Island, Va., January and February 1960; east winds are indicated as negative

of the time the sensor takes to respond to the wind. Barr (4) has made an intensive study of this lag as it applies to various types of chaff. Lally and Leviton (5) have investigated the wind tracking ability of a falling sphere, particularly in regard to the Robin balloon, and Keegan (6) discussed the practical application of these corrections. Here again, however, digital output is necessary in order to get the benefit of any corrections applied to the data.

To get around these difficulties, for the purposes of this paper, a judicious selection of data has been made. This resulted in the elimination of much data at the top of soundings, because of the possibility that the target was not responding well to the wind.

### Mesospheric Winds

The mesosphere is defined as the region in the standard atmosphere between approximately 90,000 and 250,000 ft. It is bounded on the bottom by the stratopause or the level at which the near isothermal lapse rate of the stratosphere

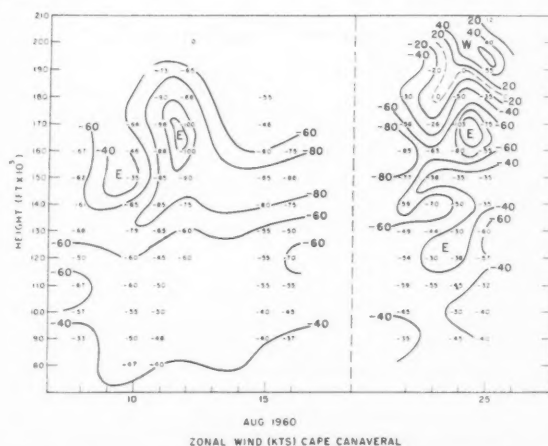
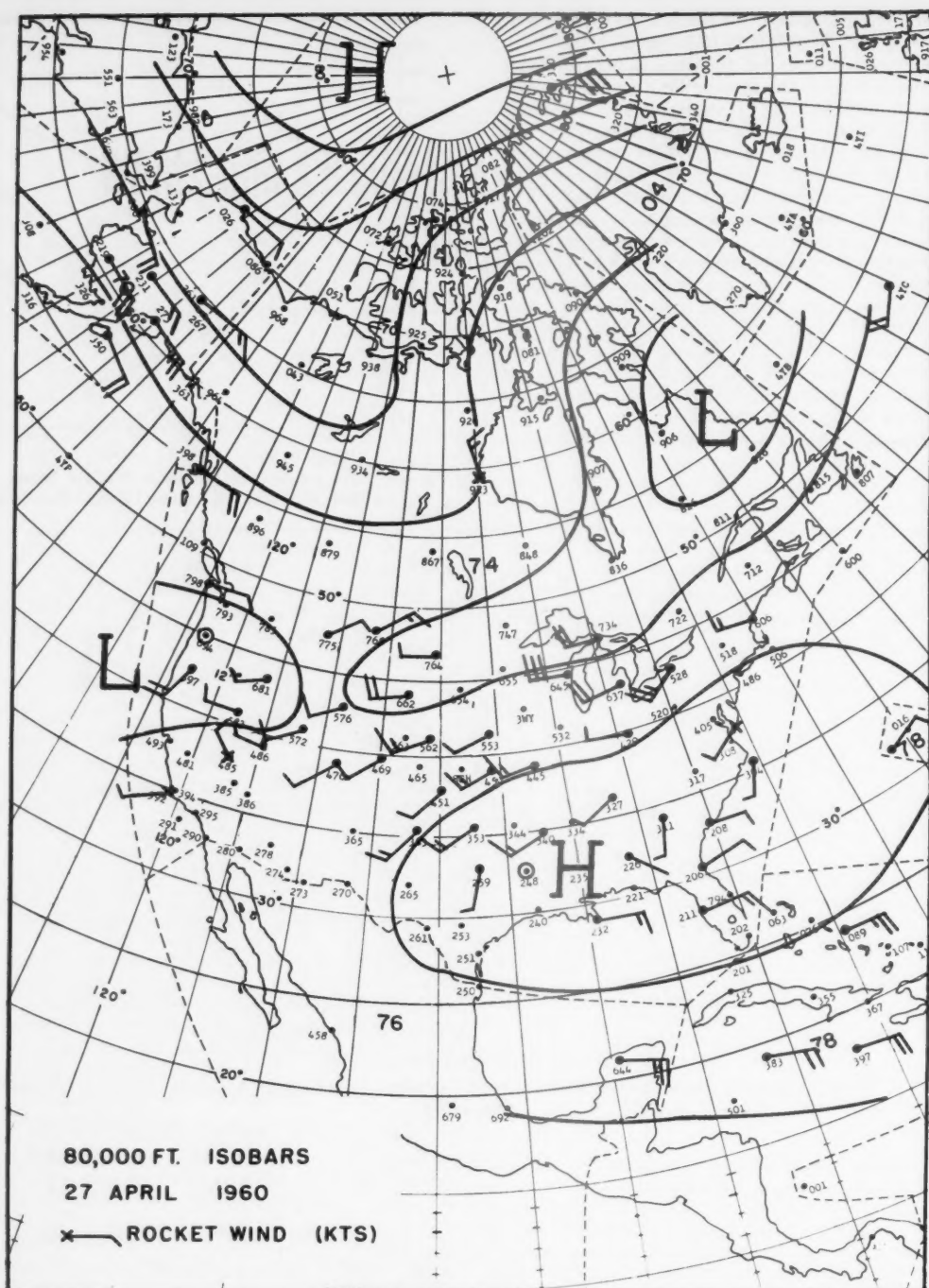


Fig. 4 Zonal wind (kts) time cross section Cape Canaveral, Fla., August 1960; east winds are indicated as negative



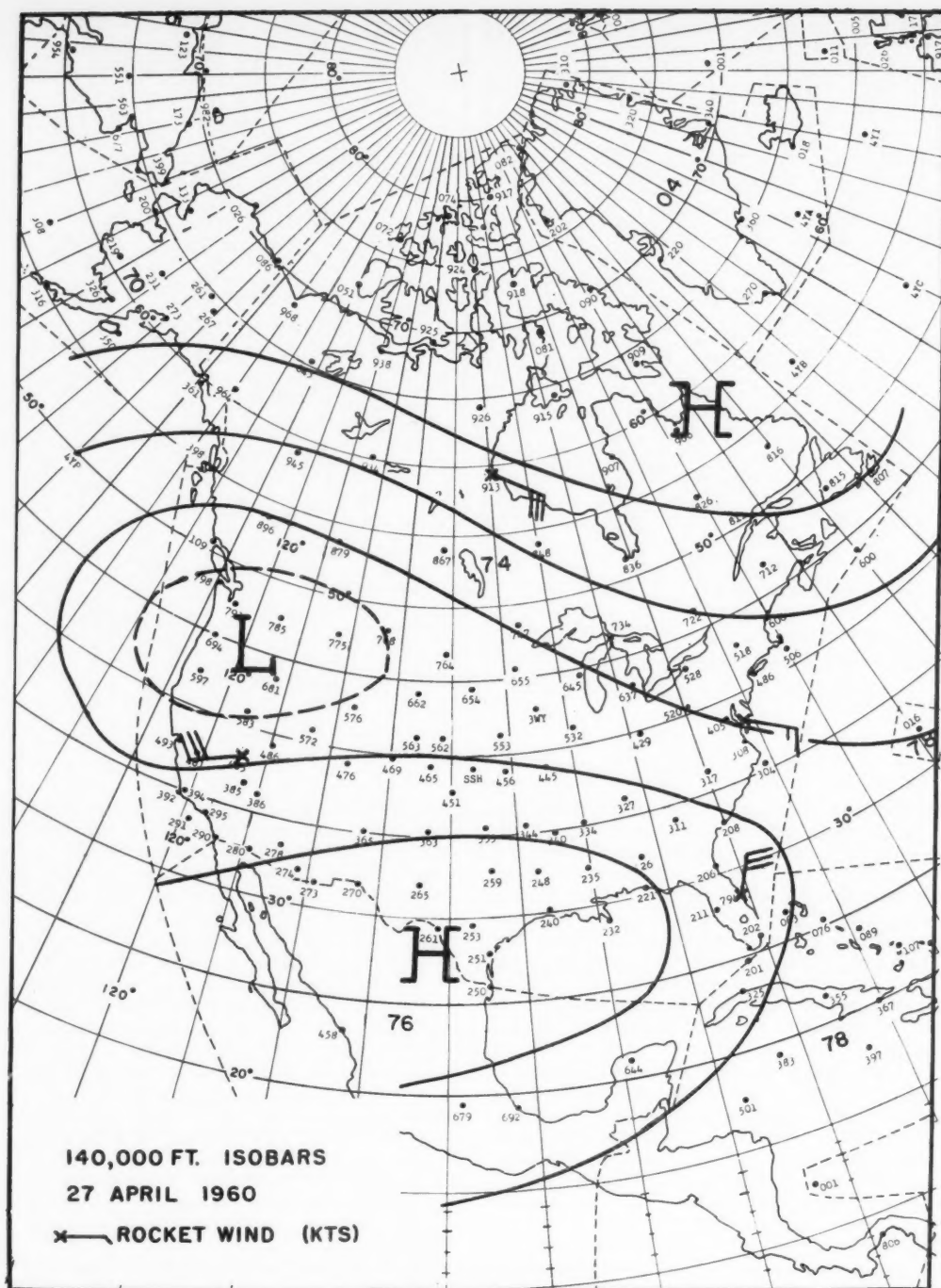


Fig. 6 140,000-ft isobars, 27 April 1960

tensity of the tropospheric wind maximum associated with the jet stream.

Above the winter tropospheric wind maximum, the wind speed decreases steadily with height up to about 90,000 ft. This decrease in speed is a consequence of the cold tropical stratosphere. With the colder air to the south, west winds will decrease with elevation. However, at 90,000 ft the west winds begin to increase with elevation because the air to the

north, circulating about the polar night vortex, is colder than that above the tropics at this level and for quite some distance above. The maximum wind in the mesosphere is over 120 knots (kts) and occurs some distance above the top of the data, probably near 200,000 ft. The wind profile agrees well with the mean winter zonal-wind cross section published by Murgatroyd (7).

The profile for the spring month shows that the meso-

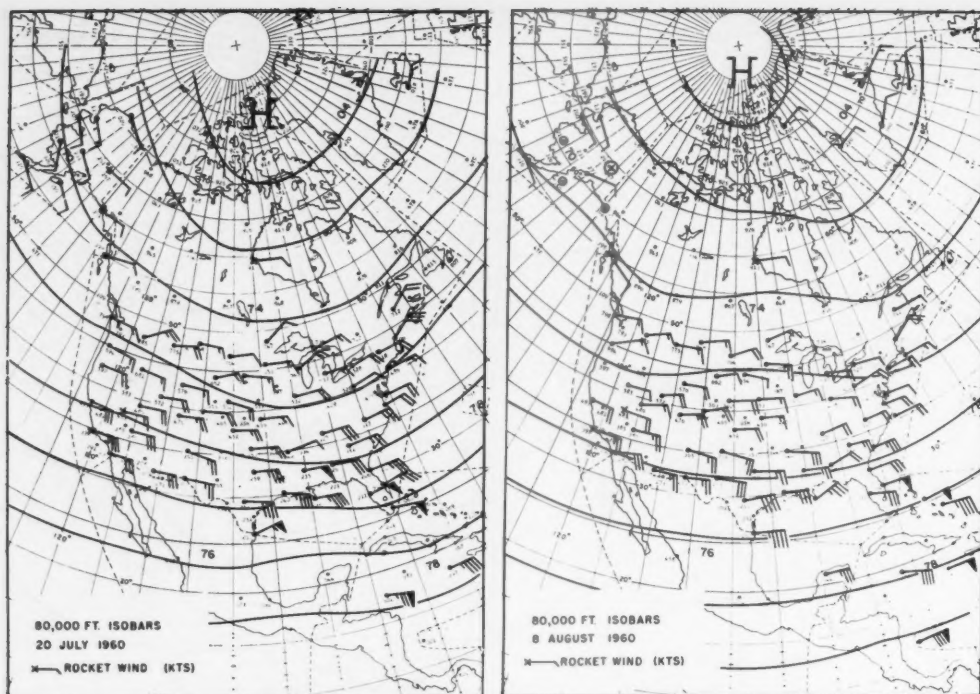


Fig. 7 80,000-ft isobars, 20 July 1960 (left) and 8 August 1960 (right)

sphere is undergoing a transition from the westerly circulation of winter to a summer easterly wind regime. The weak westerly wind maximum at about 120,000 ft results from the breakdown of the polar night vortex. It also shows up at Cape Canaveral, Fla., Tonopah, Nev., and Point Mugu, Calif., but is not in evidence at Fort Churchill, Canada, where easterly winds increased steadily with height. The reasons behind these profiles will be discussed in more detail in the section on mesospheric circulations. At Wallops Island, as at the other United States sites, the wind became easterly at about 150,000 ft and increased to the top of the available data.

The daily variability of the wind in winter is shown in Fig. 3. It is a time cross section at Wallops Island for the same mid January to mid February period from which the profile in Fig. 2 was constructed. Again rawinsonde data were used in the preparation of the diagram, but only rocket observations were plotted. Agreement was excellent between rocket and balloon winds at levels where there was an overlap.

Along the bottom of Fig. 3 are the tropospheric westerlies. The jet stream apparently passed over or very close to Wallops Island at the beginning and again near the end of the period, judging by the observations of 160-kt winds. Strangely, on one day the wind actually became easterly. The outstanding feature of Fig. 3 is the easterly maximum centered at about 100,000 ft on 30 January. This change in circulation produced a marked decrease in the west wind up to, at least, the mesopeak. The level of minimum west winds, which occurred at about 70,000 ft throughout most of the months, rose to 100,000 ft. There the winds reached easterly, speeds equivalent to the westerly speeds which occurred throughout most of the period.

It is interesting to speculate upon the relationship, if any, between this prolonged reversal of the circulation in the lower mesosphere and the appearance of easterly winds near the

tropopause on 30-31 January. The upper easterlies were the result of a large scale circulation change over the United States. The winds at Pt. Mugu show this same change to east winds at 100,000 ft. The easterly winds at 30,000 ft occurred when Wallops Island came under the influence of the circulation around a cold low which passed to the south. This low formed in a deep trough which developed several days earlier over the central United States. As the low moved slowly eastward it caused heavy precipitation over the southeastern states. Several stations reported from 4 to over 5 in. of rain in 3 to 4 days during the passage of this storm. Whether the development of the trough in the upper troposphere and the subsequent storminess was in any way connected with the preceding circulation changes in the upper stratosphere and lower mesosphere is not clear at this point. It would be worth investigating in greater detail.

The summertime mesosphere over Cape Canaveral (Fig. 4) continues to exhibit significant day to day variations. This is particularly noticeable during the periods from 10 to 12 August between 150,000 and 180,000 ft and from 22 to 25 August at all levels above 150,000 ft. But perhaps more interesting than the day to day variations are the vertical variations in wind velocity or the wind shear. On 25 August (a day on which three mutually consistent soundings were taken within 40 min) the zonal component of the wind went from E 75 kts at 170,000 ft to W 55 kts at 190,000 ft. This is a shear of about 6.5 kts per 1000 ft or 0.010 per sec. It increases to 9.0 kts per 1000 ft or 0.015 per sec between 180,000 and 190,000 ft. Over shorter height increments shears of at least 20 kts per 1000 ft or 0.030 per sec exist in the zonal component of the wind.

One must realize that the shear values given here do not represent an instantaneous picture of the atmosphere. They do represent the difference between 1-min average winds centered at different elevations which are separated in time by up to 7 min. Even the case of the 0.030 per sec shear, which



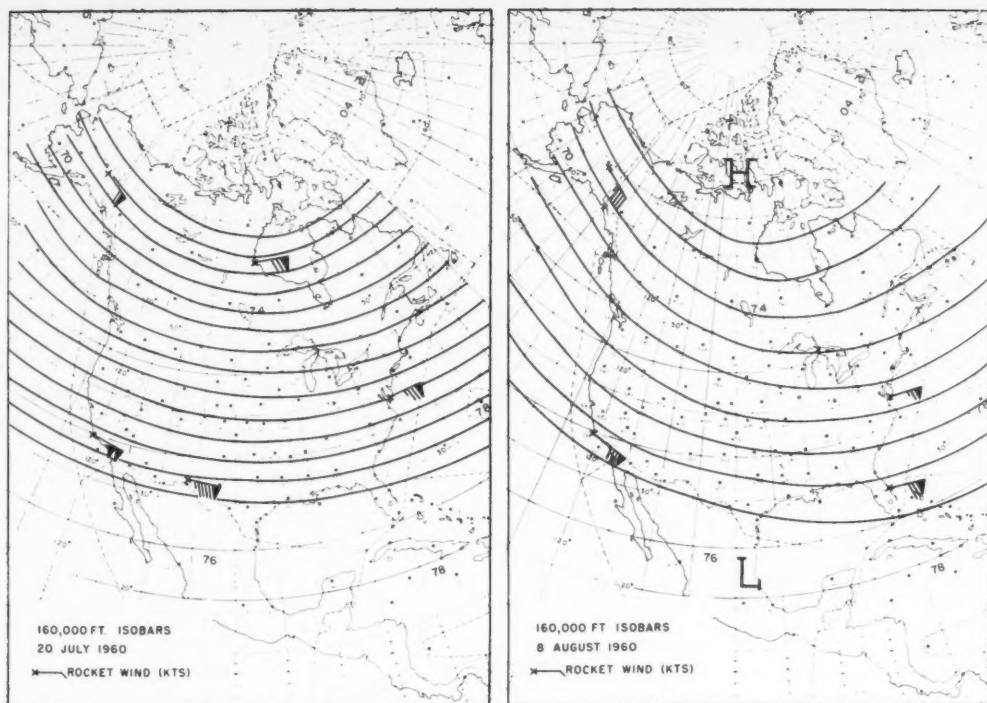


Fig. 8 160,000-ft isobars, 20 July (left) and 8 August 1960 (right)

was computed from the difference in two consecutive 1-min average wind speeds, is a mean value over a 2-min time and 4000-ft height interval. Undoubtedly, a representation of the wind profile with a higher resolution would show much greater values of wind shear.

The general features of this time cross section agree with Murgatroyd's values. The appearance of westerly winds at 200,000 ft near the end of August may be an indication of the onset of the transition period from summer to winter in the mesodecline. This reversal of direction occurs 50,000 ft lower than is indicated in Murgatroyd's summer cross section. Spot checks of autumn data indicate that westerly winds lowered to about 150,000 ft during September and occurred throughout the entire mesosphere by early October.

### Mesospheric Circulations

The rocket network has been operating on a seasonal basis. During one month each season an attempt was made to conduct firings on the same days at all the stations where rockets were available. Two stations participated in fall 1959, and seven stations were involved by summer 1960. This section gives examples of synoptic analyses which can be made with these data. On three days selected charts were analyzed for every 10,000 ft starting at 80,000 ft and using all available rocket and balloon winds. Only the charts for 80,000 ft and the top level for which a circulation pattern could be established are shown.

Fig. 5 illustrates the flow at 80,000 ft on 27 April 1960. A generally easterly circulation is established in the polar regions. Disturbances in the zonal flow at high latitudes still exist, as evidenced by the trough extending northwestward over the Canadian archipelago from the cyclone over Labrador. This cyclone and its major trough, which runs southwestward, are remnants of the cold polar night vortex which has been displaced to lower latitudes because of the rapidly

rising temperatures in the polar stratosphere. At 140,000 ft (Fig. 6) considerable change has taken place in the high latitude flow. The easterly circulation is here more firmly established. The cyclone over Labrador has been completely filled by the warm mesospheric air, and a ridge of the polar anticyclone extends over eastern Canada. Here again, as was noted in the discussion of the upper winds over Cape Canaveral in the summer, there is evidence that the seasonal transition is more advanced at the higher levels.

The cold belt responsible for the trough which lay along the Canadian-United States border at 80,000 ft is no longer present at 140,000 ft. The only vestige of it is a zone of cyclonic shear across the United States that weakens with elevation. Examination of data to higher levels on surrounding days suggests that at 160,000 ft the entire Western Hemisphere is experiencing easterly flow.

Referring back to the spring zonal-wind profile at Wallops Island in Fig. 2, the reason why the weak westerly maximum occurred at 120,000 ft now becomes obvious. It was, of course, due to the cold air belt across the northern United States. Fort Churchill, which was to the north of this belt, had steadily increasing east winds with height. Across the southern United States west winds reached a maximum at about 120,000 ft and moderated above that level where colder air occupied a position to the south.

Analysis of the charts one week earlier gives the same general picture of the circulation although many of the details are changed.

The summer-time flow at 80,000 ft (Fig. 7) displays the characteristically undistinguished easterly circumpolar current of the stratosphere in this season. Close examination of the charts indicates a slightly weaker flow on 8 August than on 20 July. At 160,000 ft (Fig. 8) the flow is obviously weaker on the later date. This further substantiates the speculation made earlier that seasonal changes are more advanced at high altitudes. It may be possible to demonstrate, when more data

are available, that the upper mesosphere responds more directly to the energy input of the sun than do the lower layers of the atmosphere.

The smooth zonal flow depicted on the summer charts seems to contradict the large variability of the zonal speeds shown on the time cross section at Cape Canaveral (Fig. 4). This need not so be, and one very obvious explanation of this seeming paradox is that an easterly wave type of disturbance propagates across the continent. This could cause variations in the zonal velocity at a station and yet escape detection in an analysis based on the thin network available today. More detailed analysis of the total wind field at individual stations may shed further light on this subject.

## Conclusions

Analysis of the Meteorological Rocket Network data demonstrates quite clearly that the mesosphere is a region of great meteorological interest. Aside from the presence of a westerly circulation in winter and an easterly circulation in summer, the only other generality which can be made at this time is that both winds and circulations exhibit great variability. Changes often occur over small space or short time intervals.

There is a strong suggestion that the circulation in the middle and upper mesosphere responds more rapidly than the lower levels to the seasonal variation in solar energy received by the atmosphere. Vertical wind shears observed in the mesodecline indicate that this is a layer of turbulent mixing analogous to the troposphere.

More intensive investigation of these features and others not discussed in this paper will certainly be scientifically rewarding in themselves, important contributions toward completing our understanding of how the atmosphere reacts to internal and external forces, and of importance to space programs, especially during critical phases of powered flight and during the soft re-entry of orbital and space vehicles.

## Acknowledgments

The author wishes to extend his thanks to W. Webb of the U. S. Army Signal Missile Support Agency, Chairman of the Meteorological Rocket Network Committee of IRIG, for providing most of the wind data used in this paper.

## References

- 1 Webb, W., Hubert, W., Miller, R. and Spurling, J., "Initiation of the Meteorological Rocket Network," presented at 187th National Meeting Amer. Meteorol. Soc., Eugene, Ore., June 14-16, 1960.
- 2 aufm Kampe, H., "The Meteorological Rocket Network," *Weatherwise*, vol. 13, no. 5, Oct. 1960, pp. 192-195.
- 3 Keegan, T., "Meteorological Rocketsonde Equipment and Techniques," *Bull. A.M.S.* (to appear in Spring 1961).
- 4 Barr, W., "Theoretical Evaluation of Cylindrical Chaff as a Wind Sensor at High Altitude," *USARL Tech. Rep. 2133*, U. S. Army Signal R & D Lab., 1960.
- 5 Lally, V., and R. Leviton, "Accuracy of Wind Determination from the Track of a Falling Object," *AF Surveys in Geophysics*, no. 93, AFCEC-TN-58-213, Geophysics Research Directorate, March 1958.
- 6 Keegan, T., "The Data Reduction Program of the Joint Scientific Advisory Group," 1961, contribution to *Meteor. Monograph on Rocket Network*, to be published by AMS.
- 7 Murgatroyd, R., "Winds and Temperatures between 20 km and 100 km—A Review," *Quar. J. Royal Meteorol. Soc.*, vol. 83, 1957, Oct. 1957, pp. 417-458.

# Lunar Impact Probe<sup>1</sup>

JULIAN I. PALMORE III<sup>2</sup>

George C. Marshall Space Flight Center (NASA) Huntsville, Ala.

The general need for, and the problems associated with, obtaining data pertaining to the moon's surface by the high velocity impact of a lunar probe are set forth in detail. The impact problem is investigated by first analyzing the origin of the forces resisting penetration, then adding these various forces to predict the resultant transient force response appearing as compression waves at a sensing station in the probe removed from the initial impact face. From this response, which is transmitted to Earth for analysis, detailed clues of the surface structure may be found. An analysis of possible lunar surfaces restricts the probe's design. Major restrictions are placed upon the probe shape because of the extremes involved in the impact at 7700 fps. A detailed discussion describes the suitability of cones and paraboloids in distinguishing different possible surfaces for impact velocities of this order. Computations from equations developed in the text are found throughout the report. Where appropriate, a discussion of the tabulated results is included.

**R**ADIO and thermal measurements have indicated the existence of at least a thin dust layer on the lunar sur-

Presented at the 15th Annual Meeting, Washington, D.C., Dec. 5-8, 1960; revised.

<sup>1</sup> Student paper (1959-60) Engineering Physics Dept., Cornell Univ. This paper received the ARS-Chrysler Corp. Undergraduate Student Award for 1960.

<sup>2</sup> Ensign, USN, attached to Research Projects Div. Member ARS.

face. This introduces the interesting possibility of exploring the depth of this layer by use of an impact probe.

Data relating to the strength and competence of the exposed surface are important to lunar vehicle designers and provide input for comparison with theoretical conclusions on the nature of this layer. Information is thereby provided to engineers and scientists investigating the structure of the visible surface.

There are two distinct types of surface layers proposed. One view, substantially supported by Gold (1)<sup>3</sup> is that the dust layer is much thicker locally than the data obtained from radio reflections indicate. Gold theorizes that local distributions of the dust deposited by micrometeorites and created by solar particles and thermal erosion may exceed several meters depth. The second idea, suggested by Baldwin (2) and others (3,4), is that the dust represents a very thin layer of possibly 2 cm thickness overlying a hard layer, which is generally conceded to be present at some depth beneath the dust layer. Gold suggests that the bonding and graduated strengthening of the dust with increased depth accounts for the solid subsurface.

Erosion of the highlands, that is, crater rims, ridges and faults, provides part of the dust deduced in Gold's examination of the surface. Meteoric influx to the surface, interpolated from present flux rates is presumed responsible for an accumulation of material which, when distributed over the entire lunar area, would result in dust depths on the order of 1 cm. It is likely (5), however, that in past eons the solar system was much more cluttered with micrometeorites, meteoroids and large chunks of matter than is presently indicated. Therefore, a greater rate of meteoric infall in the past would have increased meteoric dust to a layer several centimeters in depth.

Additional dust could have been created with the erosion of original lunar material by the above mechanisms, and possibly by action of solar plasma on the lunar surface.

After packing to a structure perhaps 0.1 times as dense as the material before erosion, the dust tends to bond together, producing a rigid but noncompetent structure, the dust grains being on the order of 10 to 100  $\mu$  diameter.

Table 1 lists the composition of stony meteorites, the principal constituent (90%) of present fluxes, and a composition possibly similar to that found in the near lunar subsurface (the first few feet of material beneath the surface). The maria are believed to hold frozen lava, which has a texture and composition similar to pumice (6).

One way in which this layer may be investigated is through the use of "hard landing" probes which fall to the surface with velocities on the order of the lunar escape velocity, 2.35 km/sec (7710 fps). Measurement of the penetration resistance of the lunar target material offers ample opportunity to evaluate its density, elasticity, compressive strength and other parameters. If relatively little resistance were offered to the probe's penetration, a thick dust layer might be suspected.

Upon impact, resistance information is relayed within the probe in the form of transient, elastic compressions. These waves are converted into electrical impulses by a sensing device and transmitted back by radio to a receiving station on Earth.

The impact may be analyzed by a few considerations. The primary energy absorbing mechanism in low speed impact is that associated with displacing surface material from the path of the incoming probe. Additional resistance to penetration occurs if the probe impacts a surface with a velocity substantially less than the surface sound speed. In this case, the probe must not only accelerate material in its immediate vicinity, but all material connected by sound compressions.

At very high incident velocities, on the order of 50 km/sec, impacts may be accompanied by large amounts of gasification and vaporization in both surface and probe. Energy is supplied at rates sufficient to break apart the solid state in both surface and target, shocks occur and an explosion results. At low impact speeds, on the order of the material's sound speed, vaporization cannot occur.

Before investigating the nature of the penetration forces at low speed impact, the overall penetration of a surface using an

Table 1 Principal composition of stony meteorites\*

Substance	Per cent
SiO	39
FeO	14 to 16
MgO	22 to 24
Fe	11.5 to 12.5
Other	10

\* See (10).

axially symmetric probe should be studied. The velocity vector is aligned with the probe axis, and is incident normal to the surface.

The time of penetration is a measure of the release of probe kinetic energy to the subsurface material. If this time is short, as when the resisting forces are high, then the surface absorbs the incoming kinetic energy except for the energy needed to destroy the probe. For deep penetration by shaped or pointed projectiles, it is assumed for the following brief discussion that the surface absorbs all of the projectile energy.

The depth and time of penetration, and energy lost to the surface per unit depth will be computed for the case in which the probe is small compared to the depth of penetration.

The equation of motion is written

$$m\dot{v} = R = \alpha + \beta kv^2 \quad [1]$$

in which  $R$  represents the surface resistance to penetration;  $\alpha$  is a constant resistance valued between 100 and 520 kg/cm;  $\beta$  and  $k$  are constants to be derived later;  $t$  is the time after impact;  $s$  is the depth of penetration measured downward from the surface;  $d/ds(v^2)$  is the energy lost to the surface per unit depth;  $A$  is the total cross sectional area of the probe; and  $m$  is the vehicle mass.

$$m \frac{dv}{dt} = \alpha + \beta kv^2 \quad m \int_{v_0}^v \frac{dv}{\alpha + \beta kv^2} = \int_0^t dt$$

Therefore

$$t = \frac{m}{(\alpha\beta k)^{1/2}} \arctan \left( \frac{\beta}{\alpha} k \right)^{1/2} V_0 \quad [2]$$

The crater depth is computed as

$$m v \frac{dv}{ds} = \alpha + \beta kv^2$$

Hence

$$\frac{m}{2\beta k} \ln \left( \frac{\alpha + \beta k V_0^2}{\alpha} \right) = S_0 \quad [3]$$

As the probe penetrates, surface material is crushed and removed ahead of the probe. The crater left by the probe is essentially a penetration crater and is not caused by the high release of energy and subsequent explosion.

Energy release at the surface from the initial impact is distributed in a thin disk-shaped volume, symmetric about the impact point.

The penetrating probe delivers energy to the subsurface outward from the probe path to a volume approximating a thin disk. At the stopping depth, the last bit of kinetic energy given to the surface is distributed over a hemispherical volume.

\* Numbers in parentheses indicate References at end of paper.

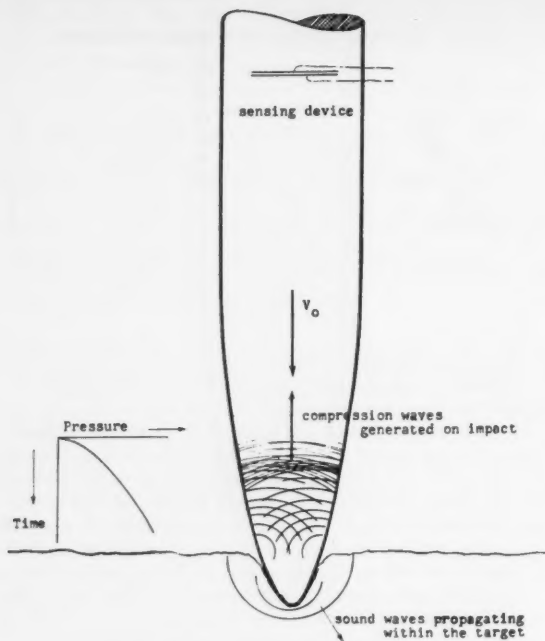


Fig. 1 Impact diagram

The surface damage per unit depth is proportional to the maximum energy released and as such varies as  $\Delta v^2$ . Assuming a constant maximum capacity of the subsurface material to absorb energy, the maximum radius  $R_m$  of the crater near the surface is proportional to  $(\Delta v^2)^{1/2}$ , and is proportional to  $(\Delta v^2)^{1/3}$  near the stopping depth.

To compute  $d/ds(v^2)$ , from the above

$$-ds = \frac{md(v^2)}{2(\alpha + \beta kv^2)}$$

Hence,  $d/ds(v^2) = -2(\alpha + \beta kv^2)/m$ .

Therefore

$$\begin{aligned} R_m &= [mA/2d/ds(v^2)]^{1/2} \\ R_m(s) &= [(\alpha + \beta kV_0^2)(A)]^{1/2} \exp[-\beta ks/m] \end{aligned} \quad [4]$$

The above solution represents  $R_m(s)$  near the surface, at which  $R_m \approx (\Delta v^2)^{1/2}$ .

The total volume is proportional to

$$\pi \frac{(\alpha + \beta kv^2)Am}{2k\beta}$$

The crater slope at the surface is

$$\text{slope} = f(\theta) = \frac{1}{dR_m/ds} = \frac{m}{[(\alpha + \beta kV_0^2)A]^{1/2}k\beta} \quad [5]$$

### Nature of the Impact Forces

The elastic compressions generated at the probe's shaped end and propagate rearward toward the sensing device in the stem. It is important to predict the time function of stress at the stem device associated with particular probe geometries and surface characteristics.

The maximum stress in the elastic signal is determined by the dynamic elastic properties of the probe material. However, the increase of stress as a function of time is governed by the surface properties and the probe's geometry. The

material characteristics determine the propagation speed  $c$  of an elastic compression. If the speed  $c$  is greater than  $V_0$ , the impact velocity, information may be obtained by the sensing device before the device penetrates the surface. Therefore,  $c$  is an important parameter in the following development.

A consideration of the nature of the impact leads to the development of the following three forces. The sum of these represents the entire impact force;  $F_1(t)$  describes the effect of probe geometry on change of momentum within the probe during impact (this force is independent of the surface properties);  $F_2(t)$  describes the reaction to the flow of displaced surface material around the probe;  $F_3(t)$  describes an effect associated with a characteristic impedance of the material in which  $V_0 < c$ , the sound speed in the surface.

**Assumptions:** The penetration properties of the shaped end of the probe are investigated.

In each of the following arguments,  $c > V_0$  is assumed,  $V_0$  being the impact velocity and  $c$  the speed of sound (elastic compressions) within the probe material. For  $F_2(t)$ , the surface is considered to possess no associated acoustic speed; for  $F_3(t)$ , an acoustic speed  $c_s$  is associated with the lunar surface material. The density in the surface and probe are represented by  $\rho_s$ ,  $\rho$ , respectively. Probe coordinates are  $(x, y)$ ,  $x$  being the axial coordinate, positive from the impacting end, and  $y$  the coordinate perpendicular to  $x$ , and positive upward.

The impact velocity  $V_0$  is coaxial and in the  $-x$  direction. By simply adding spherical waves assumed propagating from the probe's surface into the material, it is seen that no spherical wavelets are produced. Spherical waves from an apex disturbance are shown to satisfy the equations of motion of probe material in a conical probe; however, these equations are not satisfied by solutions of spherical waves propagating inward from the surface. To a first approximation, it is assumed that spherical waves do propagate into the medium of the probe for each stress increment (Fig. 1).

Speeds  $c_s$  and  $c$  are constant; at worst, they suffer several per cent variations due to their being functions of the respective density of the material in the elastic range.

**Forces:**  $F_1(t)$  is the rigid wall force, so named to describe the reaction between a perfectly elastic probe impacting normally on a rigid, immovable surface. In elementary theory the stress within an elastic cylinder resulting from the cylinder's collision with a rigid wall (defined:  $c_s \rightarrow \infty$ ) is just  $\rho c V_0$ . In the derivation of this stress, the force is a priori constant. It is easily shown to be constant by the following method:

The correct expression (impulse =  $\Delta$  momentum) is just

$$\int_0^t F_1(t) dt = 2mV_0 \quad [6]$$

in which  $V_0$  represents the impact velocity ( $-V_0$ , the rebound velocity) and  $m$ , the total mass contained within the bar, where  $m = \rho c A t/2$ ;  $t$  = the total time of impact;  $A$  = cross sectional area of the bar;  $\rho$  = density of the bar.

By differentiating Eq. 6 with respect to  $t$ ,  $F_1(t) = \rho c A V_0$ ; then  $\sigma_1(t)$  = stress on cylinder =  $\rho c V_0$  and  $\sigma_1(t)$  = const.

The method involves writing the mass of the symmetric probe as a function of distance from the impacting end,  $m = m(x) = \rho g(x)$ , where  $g(x)$  = volume of the probe.

We may represent  $dx$  as a velocity times a time or  $cdt$ ; therefore  $x_0 = cT_0$ . In general, the volume may be represented as a function of time with the substitution  $x = ct$ . Differentiating and equating yields  $F_1(t) \sim \rho g'(ct)\dot{x} = \rho c g'(ct)$ , in which the factor  $\rho c$  is the characteristic impedance. The result of this calculation for various geometries is listed in Table 2.

A physical argument may be formulated for the simple case of the elastic cone impact to deduce the time variation of the reaction force at the wall. The momentum carried within



the probe per unit length varies as the volume per unit length since, prior to impact, the probe moves initially with constant velocity. For a cone,  $g'(x)$ , in which the prime denotes the total derivative with respect to  $x$ , is proportional to  $x^2$ . Hence  $p'$  is proportional to  $x^2$  also. Assume  $c$  to be a constant. As the probe reaches the wall, the infinitesimal mass at the tip is stopped by an impulse  $dF_a$ . This impulse,  $dF_a$ , is transmitted in time  $dx/c$  to the next elemental volume containing more momentum. But  $dF_a$  cannot decelerate this infinitesimal slab to zero velocity, so the compression resulting from the initial incremental impulse is partially "reflected" to the origin, and again reflected as a compression. This reflection increases the wall reaction from  $dF_a$  to  $dF_b > dF_a$ . Since the volume of the cone increases continuously, so must the wall reaction.

The argument may be extended to any arbitrarily shaped object. Restrictions to this argument are as follows: When  $V_0 \rightarrow c$ , the assumption of elastic impact is seen to break down. Material compressed above its ultimate strength flows plastically. The possibility of shock wave formation is then present at high velocities.

The principal benefit of this argument is that it shows that stress is not discontinuous at the cone tip due to the existence of a signaling speed within the material. At impact velocities and times, on the order of the material's acoustic speed, the concept of rigid bodies is invalidated.

The displacement resistance of the surface is  $F_2(t)$ . It is the reaction resulting from the removal of surface material from the probe's path. It is assumed for this development that the shaped end is not appreciably deformed while penetrating the layers immediately beneath the surface. Another restriction is that the surface particles are given momentum in the direction normal to the probe surface. This implies that no shearing exists between lunar material and probe surface.

The velocity imparted in a direction normal to the probe surface is  $v \sin \theta$ ,  $\theta$  being the angle between the tangent to the surface and the probe axis ( $+x$  direction);  $\theta$  is constant for a cone but varies as  $\sin^{-1} dy/ds$  for an arbitrarily shaped solid of revolution.

The velocity change in the direction of the probe's velocity is  $v \sin^2 \theta$ . The differential force retarding the probe as a function of the distance  $x$  from the origin of the body-fixed coordinate system is equal to the differential mass swept per unit time  $\rho_s v dA$  times the velocity change  $v \sin^2 \theta$ . Therefore

$$dF_2(x)_{\text{normal}} = \rho_s v dA (v \sin \theta) \quad [7]$$

$$dF_2(x)_{\text{retard}} = \rho_s v dA (v \sin^2 \theta) \quad [8]$$

in which  $dA$ , the elemental area considered, is the area formed by projecting the increase in surface area per unit length onto a plane normal to the probe axis, this plane also being normal to the velocity vector;  $dA = \sin \theta dS$ ,  $dS$  being the increase in surface area per unit length.

In displacing surface material, the probe receives an impulse in the  $+x$  direction.

Now

$$dF_2(x)_{\text{retard}} = \rho_s v^2 \sin^2 \theta dA$$

Each particle offers continued resistance to the probe until it has been cleared from the vehicle's path. In essence, a flow of material around the shaped end of the probe is found. The total force is (see examples in Table 3)

$$F_2(x) = \int_{x=x_1}^{x=x} \sin^2 \theta \rho_s v^2 dA(x) \quad [9]$$

With the assumption that the velocity of the shaped end does not change appreciably as this portion of the probe penetrates, then  $v^2$  may be equated to  $V_0^2$  and  $x$  equated to  $V_0 t$ , thereby allowing  $F_2(x)$  to become  $F_2(V_0 t)$

$$F_2(V_0 t) = \int_{t=0}^{t=t} \sin^2 \theta \rho_s V_0^2 dA(V_0 t)$$

Table 2

$F_1(t)$  computed for plane wave propagation assumed

Solid of revolution	$F_1(t)$
Cylinder	$(\rho c A) V_0 = \text{const}$
Cone	$(2\rho\pi c^3 \tan^2 \theta) t^2$
Paraboloid	$(\rho\pi c^2) V_0 t$
Sphere	$\rho V_0 (-\pi c^3 t^2 + 2\pi A c^2 t)$

$F_1(t)$  computed assuming spherical wave propagation

Paraboloid	$2(c^2 t^2 + ct)^{1/2} (ct + 1) \rho V_0$
------------	---

Table 3  $F_2(V_0 t)$  computed for various geometries

Paraboloid	$\left( \frac{\pi}{4A^2} \rho_s V_0^2 \right) \ln(1 + 4A V_0 t)$
Cone	$\rho_s V_0^4 \sin^2 \theta \pi \tan^2 \theta$
Exponential	$\sim e^x$

Differentiating with respect to  $t$ , the rate of increase of  $F$  is found

$$\dot{F}_2(V_0 t) = \frac{d}{dt} \int_{t=0}^{t=t} \sin^2 \theta(t) \rho_s V_0^2 dA(V_0 t) \quad [10]$$

Note that  $F_2(V_0 t)$  is sufficient for the problem's solution, since the stress as a function of time at a sensing station is required. This stress contribution from  $F_2$  is

$$\sigma_2(V_0 t) = \frac{F_2(V_0 t)}{A_{\text{station}}} \quad [11]$$

After the shaped end has penetrated the surface, the probe slows down and invalidates the assumption of constant impact velocity. For the remaining penetration, an average value of  $\sin^2 \theta$  is defined:  $\overline{\sin^2 \theta}$ .

Having derived the equations of motion for entire penetration and crater formation in the previous section, the constants  $\beta$  and  $k$  are found to be

$$\beta \equiv \rho_s \text{ (different units)} \quad k = \overline{\sin^2 \theta}$$

To develop the equation for the force probe geometry as a function of force response, Eq. 9 is differentiated with respect to  $x$  to yield (in which  $dA = 2\pi y(x) dy(x)$ )

$$F_2'(x) = \frac{(y')^2}{1 + y'^2} \rho_s V_0^2 2\pi y(y') \quad [12]$$

$$F_2'(x) - \frac{(y')^3}{1 + y'^2} 2\pi y \rho_s V_0^2 = 0 \quad [13]$$

knowing  $F_2'(x) [\approx F_2'(t)]$  solve for  $y(x)$ , and thus determine the probe's shape.  $F_3$  is the force suggested to describe an impedance resistance associated with the elastic and semi-infinite character of the surface.

In the instance in which a shaped probe moves through a rigid dust ( $V_0 > c_s$  = the sound speed within the dust), compressions propagate laterally, and a region of higher density material is formed in a cone shape around the vehicle path. The absence of an impedance reaction accounts for the slow deceleration of the probe.

If the vehicle impacts at velocity  $V_0 < c_s$ , the material displaced consists not only of that adjacent to the vehicle, but all material "sensing" the penetration, or that material connected by sound compressions. Surface shear, rigidity, and resistance are pronounced in the penetration.

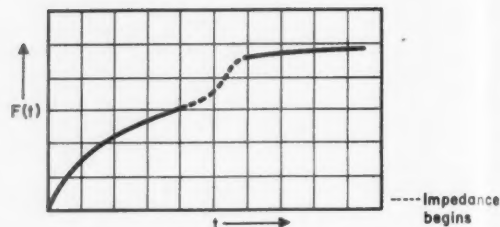
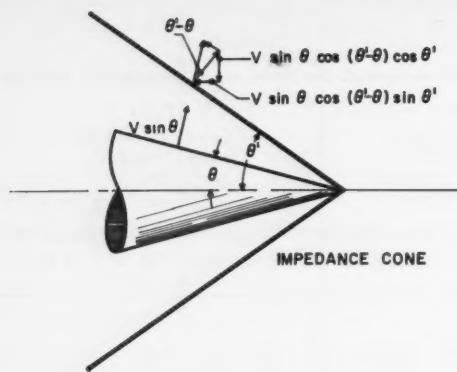


Fig. 2 At left, impedance resistance of the surface; at right, force response curve at a sensing station showing impedance effect beginning

The impedance to be described is discussed in relation to the shaped end of the probe. As the probe end begins penetration with the condition that  $c_s > V_0$ , material is compressed ahead of the probe as compressions propagate forward relative to the probe. Resistance increased above that due to the mass swept per unit time is observed. If the impact velocity  $V_0 > c_s$ , but  $\theta < \sin^{-1} c_s/V_0$ , then the surface material is compressed to the sides of the vehicle rather than ahead of it. The latter condition represents the normal velocity of the probe sides. The stress on the probe's shaped end is larger than is produced by impact with a surface of equal density without rigidity or with  $\theta > \sin^{-1} c_s/V_0$ . This increased stress results from the apparent penetration of a cone (e.g., of angle  $\theta' > \theta$ ) with velocity greater than the sound speed within the surface.

Upon examining the distribution of forces within the larger cone, then transmitting them back to the smaller probe cone to obtain the force reaction, one finds the force on the probe is proportional to  $\rho_s V_0^2 \sin \theta \sin \theta' \cos(\theta' - \theta) A'(t)$ , in which  $A'(t)$  is the maximum cross sectional area of the larger cone of compressed material as a function of time. When  $\theta' = \theta$ , the original values for  $F_2(t)$  are obtained. This effect should be noticeable if a geometry of varying surface slope impacts a surface with high velocity.

Consider the case in which a paraboloid impacts a material with a low sound speed. As the impact begins  $\theta = 90$  deg, and if  $V_0 > c_s$ , then there are no compressions propagating rapidly ahead of the vehicle. As the paraboloid slope lessens with further penetration, the normal velocity of the sides relative to the lunar surface decreases. After  $\theta = \theta_c = \sin^{-1} c_s/V_0$  is reached, surface compressions propagate away from the

sides of the vehicle. Therefore, a discontinuity in  $F_2$ , the rate of increase of force should occur, not a discontinuity in the force itself. This condition would be easily sensed at the sensing station (Fig. 2).

If a bonded dust layer were present on the lunar surface, an impacting probe would penetrate initially with velocity greater than the surface sound speed. When  $\theta = \sin^{-1} c_s/V_0$  is reached, the rate of increase in  $F_2(t)$ ,  $\dot{F}_2(t)$ , is coded into the compressions generated within the probe to be later recorded at the sensing station and subsequently relayed to the ground station. In this way, a rigid, light structure could be distinguished from a structure of low density.

## Impact Considerations

In developing the derivations, it becomes obvious that the parameters of the lunar material (such as density  $\rho_s$ , sound speed  $c_s$ ; hence, Young's modulus) are intimately connected with the penetration properties of the surface material. Information obtained from the impact consists essentially of 10 to 20 data, representing compression parameters measured at the sensing station.

To become familiar with many of the problems considered in designing the probe, it is necessary to compute the order of magnitude of the penetration force analyzed earlier in the paper.

Eq. 1, representing the entire subsurface penetration is initially limited by the term  $\beta k V_0^2$ . At impact speeds on the order of 8000 fps with a cone-shaped projectile,  $k < 1$ , and  $\beta \approx 60 \text{ #/ft}^3$ , therefore

$$\frac{\alpha}{\beta V_0^2} \approx 10^{-2} \ll 1 \quad [14]$$

Estimating values of  $\beta (\approx \rho_s)$  determines the analogous dynamic pressure breaking the vehicle.

Speculation concerning the lunar subsurface material has resulted in several theories. The presence of volcanic and meteoric materials is suspected in both eroded and noneroded forms. The more common materials suggested are basalts, and pumice-like textures. In Table 4 the densities of these materials are listed. The values are only approximate, since the geological nomenclature cannot be associated with unique densities and textures. Rather they should be used for order of magnitude calculations. One important fact is that the dust of any eroded material has a bulk density which cannot exceed that of the original material.

Table 4 Values of density and beta for lunar surface materials

Material	Weight density, lb/ft <sup>3</sup>	$\beta$ , (lb/in. <sup>2</sup> )(sec <sup>2</sup> /ft <sup>2</sup> ) = (slug/in. <sup>2</sup> ft)
Basalt	$\approx 182$	0.0392
Pitchstone	$\approx 143$	0.0308
Basaltic glass	$\approx 122$	0.0263
Pumice	$\approx 77.4$	0.0167
Pumice dust	$< 62.4$	0.0135
Basalt dust	$< 62.4$	0.0135
Iron powder*	$\approx 218.4$	0.0468

\* GAF carbonyl iron, 3- $\mu$  diameter

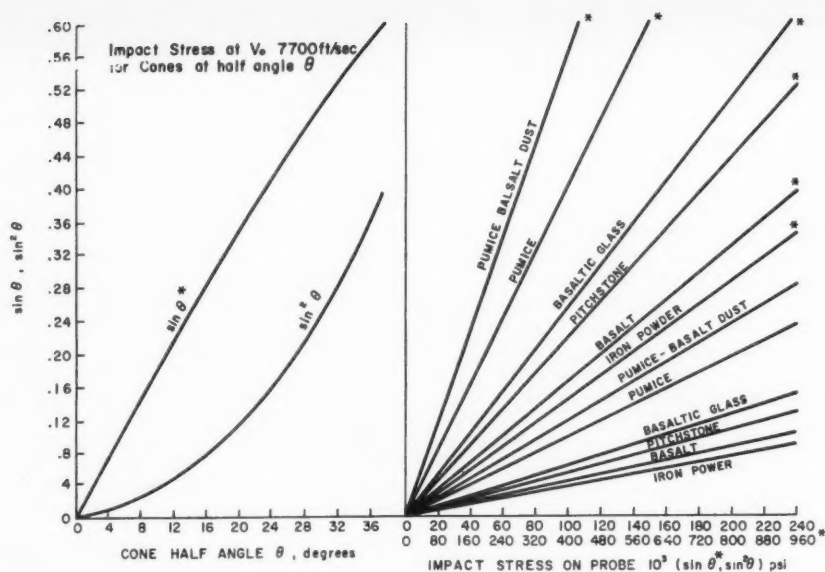


Fig. 3 At left, impact stress at  $V_0 = 7700$  fps for cones at half angle  $\theta$ ; at right, impact stress on probe  $10^3 (\sin \theta^*, \sin^2 \theta)$  psi

Basalts are dense to fine grained igneous rock usually consisting of a dark green mineral and magnetite. In contrast, pumice is a light but rigid structure full of minute cavities.

Any rigid material is capable of supporting sound waves. Dust sound speeds range in value from 1600 to 3000 fps, whereas rock transmits compressions at the speed of 7000 to  $2 \times 10^4$  fps.

Numerically,  $\beta$  is the mass density of the suggested material and has the units slug/in.<sup>2</sup>-ft; i.e.,  $\beta$  is measured mass-density per square inch cross section and foot depth.

Calculation of impact stresses may be abbreviated by use of the nomogram (Fig. 3). One enters this chart by selecting a maximum stress on impact, projecting this value onto the line corresponding to the surface selected as being representative, proceeding left to the  $\sin \theta$  or  $\sin^2 \theta$  curve, and then projecting downward to read the value of  $\theta$ , which results in the production of this stress. Any value of  $\theta$  lower than this, of course, corresponds to a lesser initial impact stress.

Further information on the suggested materials is found in Table 5.

It is apparent from the nomogram that as  $k \rightarrow 1$ , the value of the initial impact stress lies very close to the ultimate

strength of many materials. Some material properties are listed for comparison in Table 6. It should be recognized that within the elastic region of the stress-strain curve, the properties of metals are similar in both compression and tension.

However, in tension, the stress-strain curve increases to a maximum stress before the material parts; in compression, the form of the curve depends primarily on how the material is compressed. If a standard specimen (diameter  $> \frac{1}{2}$  length) is compressed in a testing machine, a curve similar to the tension curve is found; i.e.,  $d\sigma/d\epsilon$ , the slope of the real curve, decreases as the material deforms permanently (ductilely), then becomes constant as the material flows (plastically).

Contrarily, in hydrostatic compression the slope  $d\sigma/d\epsilon$  increases after the beginning of permanent deformation. The material is packed more closely, which tends to decrease sound speeds in this denser state. The increase in value of  $d\sigma/d\epsilon$  increases the speed  $c$  more rapidly than the density decreases it.

The slope  $d\sigma/d\epsilon$  in the elastic region is constant and is known as Young's modulus  $E$ . Some values are found in Table 7.

Table 5 Properties of various lunar surface materials

Material	Initial sound speed*		Bulk density		Grain density, g/cc	Equivalent porosity, %
	fps	m/sec	lb/ft <sup>3</sup>	g/cc		
Basalt	19,200	5840	182	2.84	2.96	4
Pitchstone	17,000	5180	143	2.24	2.31	3
Basaltic glass	12,500	3810	122	1.91	2.53	25
Pumice	7,400	2250	77.4	1.21	2.23	46
Pumice dust	2,400	730	< 62.4	< 1		
Basalt dust	2,000	610	< 62.4	< 1		
Iron powder**	1,300	400	< 218.4	< 3.5		
Soils (comparison)				1.0-2.0		40-50
Sand (comparison)				1.5		44

\* See (11).

\*\* GAF carbonyl iron powder (selected to represent cosmic infall material)—98.6% Fe, 3- $\mu$  diameter.

The sound speed  $c$  equals  $\sqrt{d\sigma/de}/\rho$ . As the density increases, the sound speed decreases for constant slope; however, when a material is compressed hydrostatically,  $d\sigma/de \rightarrow \infty$ ; hence, the sound speed increases drastically.

In the probe material,  $c > V_0$  must be fulfilled. This condition is seen to be easily satisfied by the materials listed in Table 7, and signifies that information may be obtained by the sensing station before it passes the surface level.

One calculation which confirms a suspicion that an improperly designed probe could be destroyed on impact is computing the ratio of the toughness of probe material to the specific energy available  $\Delta$ , the kinetic energy per unit volume carried by the probe. The specific energy is computed at a speed of 8000 fps. Toughness is defined as the work done per unit volume in plastically deforming a material. The results are shown in Table 8. This calculation is, by definition, independent of the probe geometry, but would apply to an impact in which  $\theta = 90$  deg.

The phenomena which occur on impact cannot be deduced from the value of  $\mathfrak{Z}/\Delta \ll 1$ . It does indicate that the energy needed to deform the probe is much less than the energy available.

As noted earlier in the paper, the rate of penetration, the rate at which the energy is transferred from probe to sub-surface, is important.

Three possibilities for probe deformation exist on initial penetration: (a) elastic compressions are generated within the probe; (b) plastic deformations occur; (c) shocks occur.

The force analysis shows that if  $\theta$  is small enough, the stress on impact does not exceed the yield strength of the probe material. It is also noted that  $c_e$ , the speed of elastic compressions, has the value  $c_e \approx 2V_0$ .

The retarding force  $\beta V_0^2 \sin^2 \theta$  is not the stress which compresses the probe, but the value  $\beta V_0^2 \sin \theta$ . The probe should

be designed such that  $\beta V_0^2 \sin \theta$  is less than the material's ultimate strength to insure that the probe material does not reach the state of plastic flow.

Shock phenomena discussed in (7,8) are completely ruled out since the strength of the material is approximately equal to the impact stresses and  $c_e > V_0$ .

In order to investigate the phenomena of plastic flow more thoroughly, several ideas must be considered. The first is that a general stress-strain curve is composed of three regions: in the first  $d\sigma/de$  is constant and has the maximum value  $d\sigma/de = E$ , Young's modulus; the second is that in which permanent deformations in tension occur with stresses below the value of ultimate yield; the third is the region of plastic deformation or flow of material. In the first and third range  $d\sigma/de$  is constant and approximately defines the velocity of elastic and plastic deformation, respectively. The value of  $d\sigma/de$  is variable within the ductile region and, as such, defines a variable wave velocity. In hydrostatic compression, the ductile and plastic regions are combined into a general region in which the material becomes more dense and  $d\sigma/de$  increases, thereby increasing the propagation speed of waves. The probe is compressed dynamically, rather than hydrostatically.

The velocities of elastic waves in steel are on the order of 18,000 fps, and the velocity of plastic waves is  $<1000$  fps. Fig. 4 shows that as the impact stress is increased, the velocity of plastic waves increases until elastic and plastic waves proceed with equal velocity. Shock phenomena then occur with additional stress increases.

If the ultimate strength of the material were exceeded by the normal impact stress  $\beta V_0^2 \sin \theta$ , the probe would deform plastically, and the speed of plastic deformation would be equal to the impact velocity  $V_0$ . The reason for this is that as the probe flows and is blunted on impact, the stress immediately increases to much higher values, thereby destroying the probe's shaped end as it enters the surface.

As the shaped end initially penetrates, the total force is small, even though the stress is high. The stress signal received by a sensing station after a suitable time is much below that of the original plastic stress due to the area increase along the probe. Therefore, the original plastic stress must have decreased to an elastic value in some area between the impacting surface

Table 6 Material properties (in tension)

Material	Yield strength (elongated after 2% permanent set), psi	Ultimate strength, psi
Steel, 1095	$\approx 89,000$	$\approx 110,000$
Steel, 3140	$\approx 260,000$	$\approx 291,000$
Cast iron	too low for use in probe	
Aluminum	$< 50,000$	$< 70,000$
Glass	compressive strengths $\approx$ 100,000 psi; tensile strength very low	

Table 7 Material properties

Material	Young's modulus $E$ , psi	$\rho$ , g/cm <sup>3</sup>	$c$ , fps
Aluminum	$10 \times 10^6$	2.7	16,900
Steel	$30 \times 10^6$	7.7	17,900
Magnesium	$6 \times 10^6$	1.74	15,200
Fused quartz	$0.1 \times 10^6$	2.2	1,860

Table 8 Values of toughness to energy available

Material	Toughness ( $\mathfrak{Z}$ ), lb/in. <sup>3</sup>	Ratio $\mathfrak{Z}/\Delta$
3140	$\approx 22,400$	0.0073
Aluminum	$\approx 9,500$	0.0078
Brass	$\approx 22,400$	0.0070

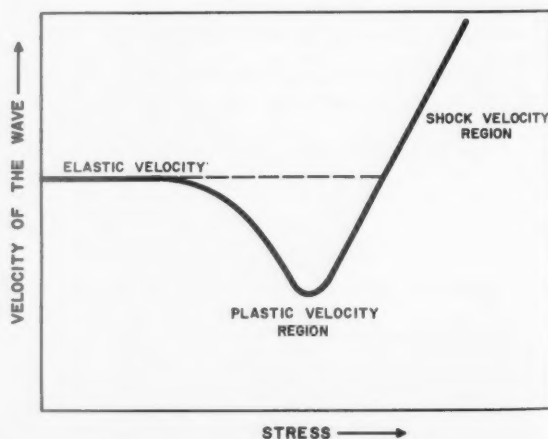


Fig. 4 Velocity of wave disturbances in a material is double valued as plastic flow occurs in the material. An elastic signal is propagated ahead of the plastic flow wave. As the stress is increased this plastic propagation velocity increases until shock phenomena occur. Shock propagation speed exceeds elastic speed



and the sensing station. When this occurs, the wave velocity increases, and the wave propagates as an elastic wave.

From (9), dynamic compressive yield strengths greater than static yield strengths have been measured and are listed as approximately two to three times as great as the static values. Therefore, more leeway is given in probe design; however, values of stress should be kept small by suitable design.

Dispersion is one possible way in which the wave shape may be distorted. Since the time of impact is on the order of milliseconds, the dispersion is much less than that found in propagating detonation waves produced in microseconds.

The probe sensing device may be a capacitor with vacuum between plates. The displacement of one face results in a current proportional to the rate of displacement and stress increase. Using this device, the entire wave shape including plastic flow can be measured. Care must be taken in the selection of the sensing station location so that reflected waves do not interfere with the compressions being produced at the shaped end. Since the signal  $F(t)$  acts as if it originates at a station of a constant distance, special precautions need not be taken.

## Conclusions

The most important measurement is that of determining the depth of the dust layer. This depth may be any distance between zero and several feet, depending upon the particular area in which the probe lands and the dust forming and transport processes on the lunar surface.

The probe, therefore, must be able to distinguish between a solid surface, a solid surface with an overlying dust layer, or a layer of dust with continuously increasing density and rigidity.

One way in which to determine the difference is to assume that a dust is present, then build into the probe enough geometry to distinguish an encounter with a solid surface or layered medium.

A method of detecting a surface sound speed is suggested by  $F_3(t)$ . The probe is designed to penetrate the surface of a dust layer with associated sound speed  $c_s$ . The penetration is by a cone in which  $\theta > \sin^{-1} c_s/V_0$ . Therefore, no surface impedance effects are initially recorded. The cone rides atop a solid of revolution of varying surface slope so that impedance effects are first detected when the critical slope is reached,  $\theta = \sin^{-1} c_s/V_0$ . For this geometry, a paraboloid is chosen. The slope of the cone and paraboloid are matched at their junction.

If, as the probe penetrates a solid layer is encountered, the cone is designed to flow plastically, thereby destroying the remaining section of the probe as it penetrates the solid interface. This destruction will be recorded at the sensing station as a large discontinuous increase in the stress rate.

A slight ambiguity is present in that a very dense medium may cause the same reaction as a less dense but more rigid medium. This ambiguity is present only at the interface and not during penetration of the dust layer. Table 9 incorporates these conclusions. Fig. 5 illustrates the stress recorded at the sensing station.

## Acknowledgment

I wish to thank Thomas Gold of Cornell University for suggesting the study of the lunar surface high velocity impact probe and for his help and guidance.

## References

- 1 Gold, T., "The Lunar Surface," *Monthly Notices Royal Astronom. Soc.*, 115, 1958, pp. 585-604.
- 2 Baldwin, R., *The Face of the Moon*, Chap. 2, Univ. Chicago Press, 1958.
- 3 Bensko, J., "Selenology," *Handbook of Astronautical Engineering*, McGraw-Hill, N. Y., 1961.

**Table 9** Determination of various surfaces with shaped probe (cone mounted on a paraboloid)

Determination of:

- |                |  |
|----------------|--|
| (a) Dust       | The probe survives the impact. Impedance effects are recorded after the critical angle of slope of the probe surface is reached.   |
| (b) Solid      | With the same, or higher, bulk density and high sound speed, the probe is destroyed on impact, the velocity of the plastic deformation being equal to the velocity of initial impact. If the probe is not destroyed, the transient wave is represented by $F_1, F_2, F_3$ . Impedance is detected. |
| (c) Dust layer | Combination of (a) and (b) with impedance noted.   |
| (d)            | Other combination are possible.  |

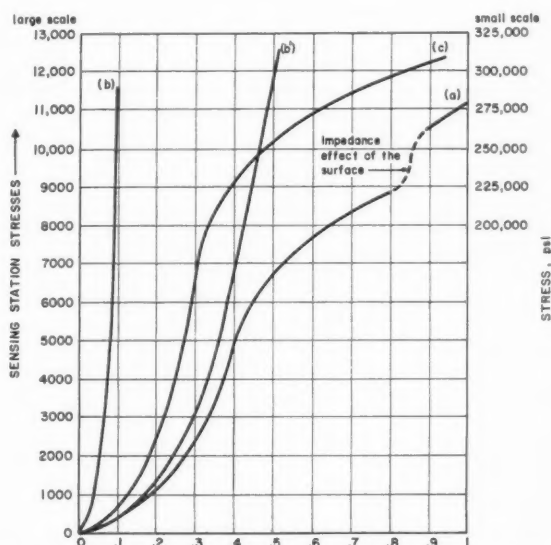


**Fig. 5** Schematic representation of conclusions, curves (a, b, b', c)

$t$  = time  
 $L$  = length of the probe's shaped end  
 $V_0$  = initial impact velocity  
 $a, b, c$  = large scale  
 $b'$  = small scale

- 4 Whipple, F., *Earth, Moon and Planets*, Harvard Univ. Press Cambridge, 1958, pp. 152-153.
- 5 YuLevin, B., "Origin and Composition of the Earth," translated by A. Henn from *Izv. Akad. Nauk SSR*, ser. geofiz. no. 11, 1958, pp. 1323-1331.
- 6 Kuiper, G., "The Moon," *J. Geophys. Res.*, vol. 64, 1959, pp. 1713-1719.
- 7 Bjork, R., "Effects of a Meteoroid Impact on Steel and Aluminum in Space," Rand Corp., Santa Monica, Calif., P-1662, pp. 4-9.
- 8 Rice, M., McQueen, R. and Walsh, J., "Compression of Solids by Strong Shock Waves," *Solid State Physics*, 6, Academic Press, N. Y., pp. 1-4.
- 9 Duvall, G., "Some Properties and Applications of Shock Waves," Stanford Research Inst. Rpt. 006-60, p. 31.
- 10 *Handbook of Physical Constants*, by F. Birch (ed.), Geological Soc., 1942, Tables 2-4.
- 11 "Sonic Velocity in Possible Lunar Surface Materials," Proc. of the Lunar and Planetary Exploration Colloquium, vol. 1, no. 4, Pub. 513 W 4, North American Aviation, Calif., 1959.

# Inertial Sphere System for Complete Attitude Control of Earth Satellites

KARL W. HERING<sup>1</sup> and  
ROBERT E. HUFNAGEL<sup>2</sup>

Electro-Optical Division,  
The Perkin-Elmer Corp.  
Norwalk, Conn.

An electrically conducting sphere placed in a rotating magnetic field will experience a torque about the axis of rotation. This torque arises from eddy current drag between the field and the sphere and can be used to control satellite attitude. Accumulated satellite angular momentum will appear as rotation of the sphere and will be automatically dumped by eddy current interaction with the Earth's magnetic field. The sphere can be positioned without mechanical contact with the satellite by high frequency alternating magnetic fields. Very precise attitude guidance as well as slewing operations and momentum dumping can all be achieved with one device. Three axis control with one sphere eliminates gyroscopic interaction. Electrical efficiency compares favorably with other system types.

**I**N THIS paper we present a system concept for generating the torques for attitude control of Earth satellites. The system described would be particularly useful where long life and very precise (fractional arc-second) control are important.

Fundamentally, we proposed to produce the torques necessary for attitude control by magnetic interaction with a freely suspended sphere. This basic concept has been previously suggested independently by Spitzer (1), Ormsby (2), Haeussermann (3),<sup>3</sup> and possibly others. Because of the free suspension, friction and vibration, problems normally associated with some other systems are eliminated. Because the sphere is symmetrical, only one sphere need be used for attitude control about all three satellite axes. Gyroscopic interaction is eliminated.

The particular system described here, as first conceived by Spitzer (1), differs from the inertial sphere systems described by others in that accumulated angular momentum is passively dumped by eddy current interaction with the Earth's magnetic field. Unless some means for dumping angular momentum is provided, an attitude control system can eventually saturate and lose control. Although for this system effective momentum dumping is confined to altitudes where the Earth's magnetic field strength is relatively high, an advantage is gained through the elimination of jets or other auxiliary momentum dumping devices. Since no material is expelled in this dumping process, the useful life of a satellite employing this system is limited only by the reliability of its components.

## Basic Description

To accelerate the satellite about some arbitrary axis it is necessary to generate, by means of three sets of coils surrounding the sphere, a magnetic field which rotates relative to the sphere about the desired acceleration axis in the direction

opposite to the desired satellite acceleration. Eddy current will be induced in the conducting spherical shell which will interact with the applied magnetic field so as to accelerate the sphere about the axis of magnetic field rotation. By conservation of momentum, the satellite will turn in the desired direction. Since it is the relative rotation between the sphere and the magnetic field which causes the acceleration, the sphere can never go faster than the maximum magnetic field rotation speed.

When the satellite is guided to a fixed attitude, all net angular momentum accumulated by the satellite will appear as rotation of the inertial sphere. Angular momentum will be dumped by eddy current drag between the Earth's magnetic field and the spinning sphere if there is a component of the local magnetic field which is normal to the axis of spin. Although this condition may not be satisfied for all times during the course of one orbit pass about the Earth, it will be satisfied for some times, unless the plane of the orbit were along the Earth's magnetic Equator.<sup>4</sup> High inclination orbits are best for magnetic dumping of momentum, but orbits with inclinations as low as 30 deg are still compatible with this scheme.

It is necessary to keep the sphere freely suspended without touching the torquing coils which surround it. This is relatively easy to achieve, since in orbit the sphere experiences almost no apparent forces. Suspension can be obtained with the aid of a spatially nonuniform, high frequency alternating magnetic field which acts as a loose "spring" to keep the sphere centered between its coils. As before, the interaction is between the applied magnetic field and the eddy currents induced in the sphere.

With all these magnetic fields about, there are bound to be interactions and secondary effects. Detailed analyses of these effects are difficult, but preliminary results show that the secondary effects can either be ignored or that they are easily accommodated by compensation elsewhere.

Presented at the ARS 13th Annual Meeting, Washington, D. C., Dec. 5-8, 1960.

<sup>1</sup> Senior Staff Systems Engineer.

<sup>2</sup> Senior Staff Physicist.

<sup>3</sup> Numbers in parentheses indicate References at end of paper.

<sup>4</sup> As long as the Earth's magnetic dipole is not aligned with the Earth's spin axis, a free orbit of this type is impossible.

## Production of Torque

Smythe (4) has shown that a uniform magnetic field of magnitude  $B$ , rotating with a velocity  $\tilde{\omega}$  relative to a thin shelled electrically conducting sphere, will exert a torque  $\tilde{T}$  on the sphere equal (in cgs units) to

$$\tilde{T} = \frac{2\pi\delta\tilde{\omega}a^4B^2 \times 10^{-9}}{3\eta \left[ 1 + \left( \frac{4\pi a\delta\omega}{3 \times 10^9\eta} \right)^2 \right]} \quad [1]$$

where the sphere has radius  $a$ , shell thickness  $\delta$ , and is made of material of resistivity  $\eta$ . This torque is maximized when  $\omega = \omega_m$  where

$$\omega_m = \frac{3 \times 10^9\eta}{4\pi a\delta} \quad [2]$$

Using  $\omega_m$  we find that Eq. 1 may be expressed in the more simple form

$$\tilde{T} = \frac{B^2a^3}{4} \left[ \frac{2(\tilde{\omega}/\omega_m)}{1 + (\omega/\omega_m)^2} \right] \quad [3]$$

Since the term inside the brackets in Eq. 3 reaches a maximum value of 1 when  $\omega = \omega_m$ , it is clear that the maximum torque possible depends only on  $B$  and  $a$ .

This is significant when one wishes to dissipate accumulated angular momentum by interaction with the Earth's magnetic field. The maximum torque developed by the Earth's field must be greater than the time average of all the external torques tending to perturb the satellite. If this condition is not satisfied, the accumulation of angular momentum by the satellite will eventually saturate the attitude control system. For a 400 mile orbit at an inclination of 45 deg the minimum rms magnetic field strength for any spin axis orientation is about 0.25 gauss.

Fig. 1 shows a plot of torque developed by interaction with the Earth's magnetic field, taken here to be 0.25 gauss. For the purpose of the example we have assumed a  $\frac{1}{2}$  cm thick aluminum shell for the sphere.

Since the maximum expected average perturbing torque for a well designed satellite is about 100 to 300 dyne-cm it is clear that the sphere must have a 20 to 30 cm radius if it is to be capable of dissipating all accumulated angular momentum. At first this may seem to be large, but one must remember that this sphere could replace three flywheels and a year's supply of jet fuel. For the purpose of an example we will choose  $a = 25$  cm.

A typical satellite capable of utilizing the fine degree of attitude control available would have a moment of inertia of about  $10^{10}$  gm-cm<sup>2</sup> or more. In order to slew this satellite at a rate of  $10^{-2}$  radians/sec, the inertial sphere must be capable of developing a peak angular momentum of  $10^8$  dyne-cm-sec in about 100 sec, which corresponds to a torque of  $10^6$  dyne-cm.

In order to attain highest system efficiency yet maintain the potential capabilities of this device, we rotate the servo controlled magnetic field at a speed of about  $1.2 \omega_m$ , and require that the speed of the sphere be less than  $\omega_m$  when it has its peak slewing angular momentum. Since the moment of inertia of the spherical shell is

$$J = \frac{8\pi}{3} a^4 \delta \rho \quad [4]$$

where  $\rho$  is the density of the sphere material, we find that when  $\omega = \omega_m$ , the angular momentum is (in cgs units)

$$J\omega_m = 2 \times 10^9 a^3 \eta \rho \quad [5]$$

which is independent of the skin thickness.

If  $J\omega_m$  is to be greater than  $10^8$  dyne-cm-sec we must have

$$\rho\eta > \frac{1}{20a^3} = 3.2 \times 10^{-6} \text{ ohm-gm-cm}^{-2} \quad [6]$$

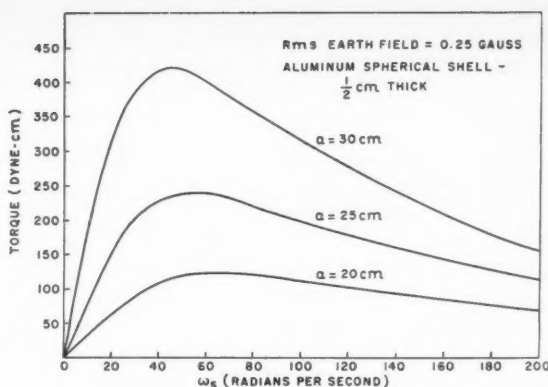


Fig. 1 Torque on spherical shell by Earth's magnetic field as a function of angular velocity  $\omega$ , and sphere radius  $a$

where we recall that  $a$  was chosen to be 25 cm. If we choose the material to be aluminum for its low density ( $\rho = 2.7$  gm/cm<sup>3</sup>) we find that its resistivity ( $\eta = 2.8 \times 10^{-6}$  ohm-cm at 20 C) is more than sufficient to satisfy Eq. 6. In this case the angular speed corresponding to  $10^8$  dyne-cm-sec would be

$$\omega = \omega_m \frac{3.2 \times 10^{-6}}{\eta \rho} = 0.44\omega_m \quad [7]$$

Using the results above, we find with Eq. 3 that a rotating magnetic field of 20 gauss strength is sufficient to develop an average slewing torque of  $10^6$  dyne-cm. In finding this, one must recall that it is the difference between the magnetic field speed and the ball speed that should be used in Eq. 3.

To choose the shell thickness  $\delta$ , we note that the shell must be thick enough to be rigid at the speed  $\omega_m$ . Also  $\delta$  should be large enough to allow efficient generation of the rotating magnetic field at the frequency  $1.2\omega_m$ . On the other hand the weight of the sphere is proportional to  $\delta$ , and thus  $\delta$  should be small. A reasonable compromise seems, for this example, to be  $\delta = 0.5$  cm.

For this case we find that the sphere mass is 10.6 kg, that  $\omega_m = 54$  radians/sec and that the magnetic field angular speed is 65 radians/sec = 10 cps.

## Generation and Control of the Rotating Magnetic Field

It was shown in the previous discussion that to produce a torque about any axis, one must generate a magnetic field rotating about that axis.

In a practical system it is convenient to produce torque in any given direction by properly exciting a set of coils fixed to the satellite. For example, torques may be produced about X, Y or Z Cartesian coordinates by simultaneous production of magnetic fields in the X, Y and Z directions as follows

Direction of torque	X field,	Y field	Z field
$\pm X$	0	$A \cos \omega t$	$\pm A \sin \omega t$
$\pm Y$	$\pm A \sin \omega t$	0	$A \cos \omega t$
$\pm Z$	$A \cos \omega t$	$\pm A \sin \omega t$	0

For applications where sequential torque control about X, Y and Z axis suffice, control may be obtained by switching the excitation of the three sets of coils in accordance with the aforementioned equations.

For many applications, however, greater flexibility of control may be required. For example, a narrow field telescope assigned to photograph stars having its optical axis along the

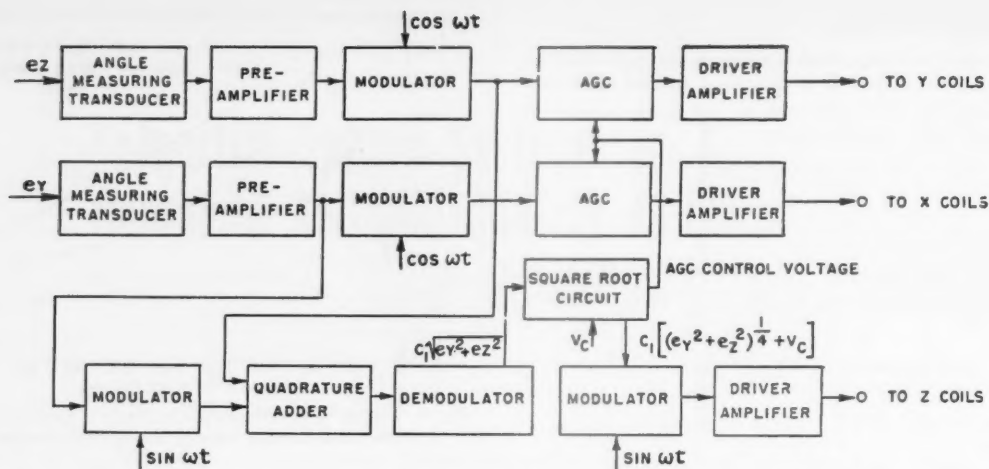


Fig. 2 Block diagram of magnetic field rotational control for production of torques about any axis perpendicular to  $X$  axis

$X$  axis of the satellite may be required to have very tight angular position tolerances against rotational errors about the  $Y$  and  $Z$  axes. On the other hand, for a narrow field of view, the rotational tolerance about the  $X$  axis will be considerably larger. Here a control system will be capable of maximum accuracy when a torque can be applied which will simultaneously compensate for combined  $Y$  and  $Z$  rotational errors. On the other hand, control need be applied only occasionally to compensate for angular error about the  $X$  axis. If  $e_Y$  and  $e_Z$  are components of pointing error along the  $Y$  and  $Z$  axis, then the components of the field required to produce a compensation torque in the desired direction are

$$\begin{aligned} B_X &= K\sqrt{e_Z^2 + e_Y^2} \sin \omega t \\ B_Y &= K e_Z \cos \omega t \quad B_Z = K e_Y \cos \omega t \end{aligned} \quad [8]$$

The torque is proportional to the square of the magnitude of the field. In order to produce linear control, the multiplier  $K$  in Eqs. 8 should be

$$K = C(e_Y^2 + e_Z^2)^{-1/4} \quad [9]$$

where  $C$  is a constant. Fig. 2 shows a block diagram of a possible mechanization of these equations for linear torque control. The angle measuring transducers are assumed to be linear. The error signals are amplified and modulated to produce voltages proportional to  $e_Y \cos \omega t$  and  $e_Z \cos \omega t$ . The quantity

$$\sqrt{e_Z^2 + e_Y^2}$$

is produced by quadrature addition of  $e_Z$  and  $e_Y$ . A simple diode square root circuit is used to approximately produce the quantity

$$\sqrt{e_Z^2 + e_Y^2}$$

In order to prevent the possibility of division by zero, it is desirable to make the square root circuit imperfect so as to give an output more closely approximating

$$\sqrt{e_Z^2 + e_Y^2} + V_c$$

where  $V_c$  is a small fixed bias voltage. The output of this imperfect square root circuit is modulated by  $\sin \omega t$  to produce the  $X$  axis coil excitation. The factor  $K$  is introduced into the  $Y$  and  $Z$  axes channels by means of automatic gain control

amplifiers. The introduction of the bias voltage  $V_c$  insures proper control for small  $e_Y$  and  $e_Z$  with very crude nonlinear circuit elements. When rotation about the  $X$  axis is desired, switching circuits (not shown) may be employed to properly excite the  $Y$  and  $Z$  coils.

Simultaneous three axis control is more difficult to achieve and will not be discussed here.

The coils required to produce the rotating magnetic field will next be considered. In order to minimize forces tending to translate the spherical shell, a uniform magnetic field is desired along each Cartesian coordinate. An efficient coil configuration producing a unidirectional field consists of windings on a sphere with the current flowing along parallels of latitude, so that the winding density is proportional to  $\sin \theta$ , where  $\theta$  is the angle between the polar axis of the sphere and a radius vector. It can be shown that for a single layer spherical coil close packed at the Equator

$$B = \frac{2I}{3d} \quad [10]$$

where  $I$  is the current in the coil and  $d$  is the diameter of the wire; the resulting field  $B$  is directed along the polar axis of the windings. Using this relationship, it can readily be shown that for a single layer coil

$$WM = 35B^2 r^4 \eta_c \rho_c \quad [11]$$

where  $W$  is the d-c  $I^2R$  coil loss (w),  $M$  is the mass of coil (gm),  $B$  is the required field amplitude (gauss),  $r$  is the radius of spherical coil (cm),  $\eta_c$  is the coil resistivity (ohm-cm) and  $\rho_c$  is the coil density (gm/cm<sup>3</sup>). For an aluminum coil with  $r = 30$  cm and  $B = 20$  gauss,  $WM = 8.7 \times 10^4$ ; or for  $M = 10$  kg, 8.7 w per coil will be dissipated. The wattage dissipation is based on the d-c resistance of the coil. The product  $WM$  will actually be larger because of skin effect. However, the use of low frequencies and, if necessary, hollow conductors will minimize this increase. For the production of the rotating field, it is conceivable that three mutually perpendicular coils can be wound on a spherical form in such a manner that interaction is minimized. The total coil assembly capable of producing a rotating field of 20 gauss would have a mass of 30 kg and dissipate approximately 17.4 w. This field reacting against a 25 cm radius,  $\frac{1}{2}$  cm thick aluminum sphere will produce a maximum torque of  $1.4 \times 10^6$  dyne-cm.



## Suspension of Inertial Sphere

A means of suspending the spherical shell within the confines of the coils producing the rotational magnetic field is to utilize a spatially nonuniform rapidly oscillating magnetic field. This method of suspension will effectively isolate the satellite from undesired torque or vibrational disturbances from the spinning sphere.

The magnitude of the required positioning forces are small for a satellite in stable orbit because all force perturbations will be small. Usually the worst perturbation occurs during slewing if the spherical shell is not located at the satellite's center of mass. For maximum slewing requirements of 180 deg in 2 min, the satellite will be accelerated through 90 deg in 1 min, requiring an angular acceleration of  $1.74 \times 10^{-3}$  radians/sec<sup>2</sup>. When a  $\frac{1}{2}$  cm thick, 25 cm radius aluminum shell (weighing 10.6 kg) is located a distance  $l$  (cm) from the center of mass of the satellite, the force required to keep the spherical shell positioned within the coil system is then  $18.5 l$  dynes. It is seen that  $l$  may be large before appreciable positioning forces are required. Successive applications of angular positioning torques, however, can induce relatively large amplitudes of oscillation in the suspension system. It is reasonable to assume that the effective spring constant required to maintain small amplitudes under conditions of successive applications of maximum torques need be no greater than about 1000 dyne/cm. The period of oscillation for this value of spring constant will be approximately 20 sec, which is relatively small.

In order to obtain approximate relationships between positioning forces and operating parameters, a simple model will be considered. Fig. 3 shows a magnetic shell of radius  $a$  suspended between two Helmholtz coils, each of radius  $b$ , arranged to produce opposing fields. The alternating magnetic field induces eddy currents in the spherical shell. The net effect of these eddy currents is to produce a field equivalent to that of a magnetic dipole whose magnitude is a function of  $Z$  and which interacts with the field gradient to produce a restoring force. Assuming that the induced magnetic dipole moment is approximately equal to that induced by the

average value of the field produced by the coils, and also assuming that each coil produces a magnetic field identical to that of a single current loop, the force along the  $Z$  axis is given by the following approximate relationships

$$F_z(\text{dynes}) = \frac{3\pi^2}{200} \left(\frac{a}{b}\right)^3 (nI)^2 \cos^2 \Psi \times \left[ \frac{1}{(1 + Y_1^2)^{3/2}} - \frac{1}{(1 + Y_2^2)^{3/2}} \right] \left[ \frac{Y_1}{(1 + Y_1^2)^{5/2}} + \frac{Y_2}{(1 + Y_2^2)^{5/2}} \right] \quad [12]$$

where  $I$  is the rms value of sinusoidal current (amp),  $n$  is the number of turns per coil,  $Z$  is the displacement of the spherical shell along the  $Z$  axis, (cm),  $S$  is the separation between coils (cm), and  $\sigma$  is the area resistivity (ohm)

$$Y_1 = \frac{S/2 + Z}{b} \quad Y_2 = \frac{S/2 - Z}{b} \quad \cos^2 \Psi = \frac{(\mu a \omega_p)^2}{(\mu a \omega_p)^2 + (3\sigma)^2} \quad [13]$$

For  $\omega_p$  greater than 300 radians/sec,  $\cos^2 \Psi$  approaches unity. These formulas assume that magnetic skin depth penetration is not a limiting factor. Using the classical skin depth penetration formula

$$\text{penetration} = \sqrt{2\eta/\mu\omega} \quad [14]$$

where  $\eta$  = resistivity (ohm-cm), a  $\frac{1}{2}$  cm thick aluminum spherical shell will have the maximum value of effective spring constant for frequencies above 1800 radians/sec. Since the wattage dissipated increases with frequency, it is not advantageous to operate at higher than this frequency.

A plot of  $F_z/(nI)^2$  vs. displacement  $Z$  is shown in Fig. 4.

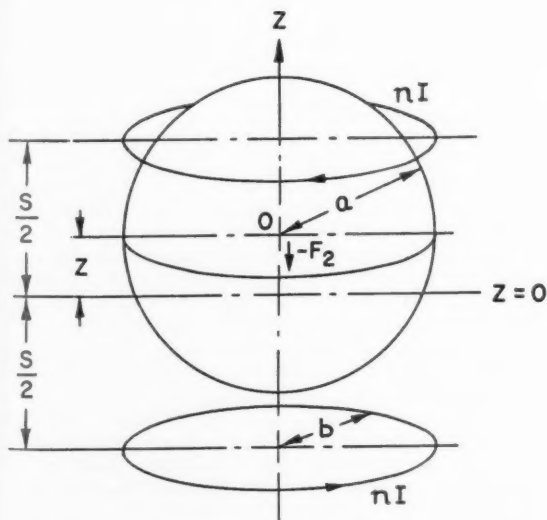


Fig. 3 Geometry of suspension coils

$S = 50$  cm,  $a = b = 25$  cm

$nI$  = rms value of ampere turns in each coil

Current varying sinusoidally with  $\omega > 300$  radians/sec

Spherical shell = aluminum

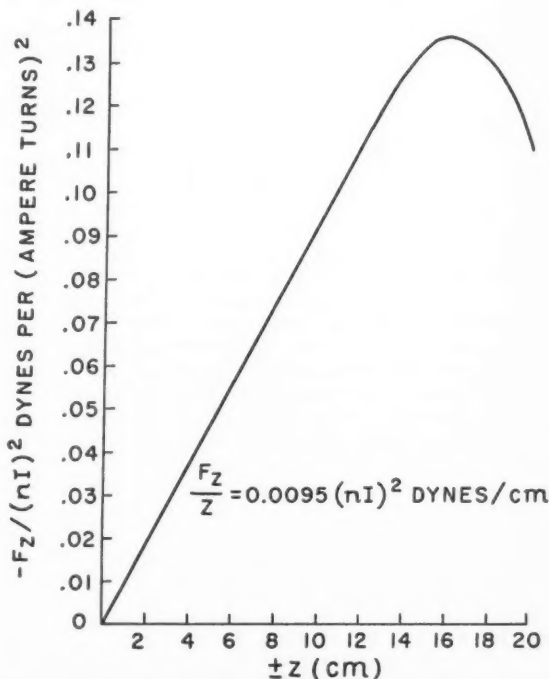


Fig. 4 Restoring force per (amp-turn)<sup>2</sup> vs. displacement of spherical shell (see Fig. 3 for geometry)

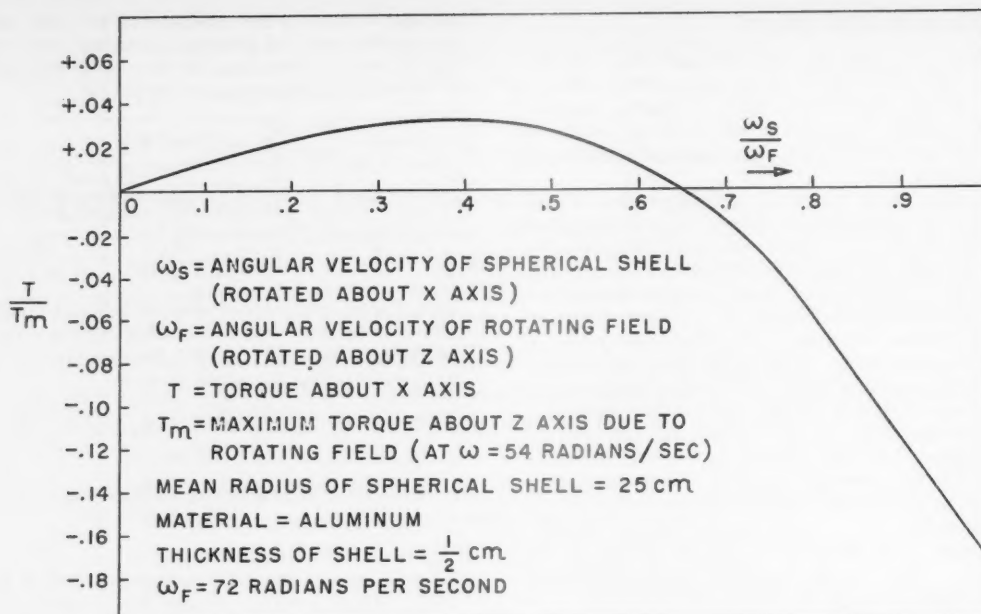


Fig. 5 Cross coupling torques vs. angular velocity of magnetic field and spherical shell

Over a large range of  $Z$ , the curve is linear and the effective spring constant is 0.0095 dynes per cm per (amp-turn)<sup>2</sup>. In order to obtain 1000 dynes cm<sup>-1</sup>, 325 amp-turns per coil would be required.

In order to obtain the required field, it is desired to minimize the mass of the coil assembly as well as the wattage dissipated. For the coils, the product  $WM$  (wattage times mass) is proportional to resistivity  $\eta_c$  times the density  $\rho_c$  of the coil conductors. The material having the lowest value of  $\eta_c \rho_c$  is aluminum. For the above example

$$WM = 20 \frac{F}{Z} \text{ watt-gm per coil}$$

where the coil material is aluminum.

For  $F/Z = 1000$  dynes/cm,  $WM$  is 20 w-kg; or for a mass per coil of 5 kg, approximately 8 watts would be dissipated in both coils when maximum forces are required.

This calculation assumes that the resistance of the coils is equal to the d-c resistance. In an actual coil design, the skin effect on the conductors will increase the effective resistance of the coil. The additional wattage times mass requirement due to skin effect can, however, be minimized by proper design of the coils. Additional power dissipated due to eddy currents in the spherical shell is in the order of 0.1 w. Except when the satellite is being rotated, the power requirement would certainly be reduced by at least an order of magnitude.

It is desirable to provide a means for damping the position oscillations of the spherical shell. Several methods may be employed to produce the required damping. For example, additional coils could be used to provide damping forces. The currents in these coils could be controlled by spherical shell position sensor signals transformed by suitable networks. Position sensing signals may be obtained, for example, by capacitor bridge techniques.

In the above example of magnetic positioning, motion along the  $Z$  axis only has been considered. It can be shown that the configuration of Fig. 3 will also provide comparable forces opposing motion of the spherical shell in the  $X$  and  $Y$  directions. The example serves to demonstrate that the order of

magnitude of power and weight required to produce the desired amount of positioning force is reasonably small and that interacting torques are negligible. In designing a magnetic positioning system, alternate configurations would probably be used. One possible arrangement would involve the use of coils having cylindrical symmetry placed equidistant from the surface of the spherical shell. This arrangement has been suggested by Spitzer (1).

### Interactions

Rotation of the spherical shell in the presence of the positioning field about an axis perpendicular to that field produces a torque. It can be shown from the torque equation (Eq. 3) that the ratio of this torque to that produced by rotation in the Earth's magnetic field has a maximum value approximately equal to  $2[\omega_s \bar{B}_p / \omega_F B_E]^2$ , where  $\bar{B}_p$  is the rms value of the positioning field.

For the above example,  $\bar{B}_p$  has a maximum value in the order of 3 gauss so that the torque on the sphere will be only 0.4 times that of the torque due to the Earth's magnetic field. This small value of interacting torque is easily offset by the driving field.

Another interaction occurs during the generation of torques. When the rotational axis of the spherical shell is not aligned with the rotational axis of the magnetic field, the resultant torque is not produced about the axis of field rotation. However, the component of torque normal to the desired torquing direction is small. Fig. 5 shows that when the spherical shell is rotating about an axis  $X$  perpendicular to the desired torquing direction  $Z$  the maximum amount of torque in the  $X$  direction is only 3% of the maximum torque in the desired  $Z$  direction.

During automatic pointing where position signals are continuously measured, the effect of these small torquing errors will be negligible.

### Summary

The discussion in this paper has demonstrated that very precise attitude control by means of a magnetically suspended

and magnetically actuated spherical shell is feasible and that the mass, size, and wattage requirements are reasonable when compared with other systems. This method of attitude control offers the advantages of large range of control, lack of frictional effects, negligible interacting torques (no gyroscopic effects), and ability to passively dump undesired cumulative angular momentum into the Earth's magnetic field.

The parameters for the example discussed in the text are summarized in Table 1.

### Acknowledgments

The work reported here is the outgrowth of a study (5) performed for Lyman Spitzer Jr. of Princeton University. Many of the concepts and ideas expressed here are Professor Spitzer's.

Roderic Scott of Perkin-Elmer contributed significantly to this program during its conceptual phases. We wish also to thank Robert Noble of Perkin-Elmer for his help during this program and for his aid in reviewing the manuscript.

### References

1. Spitzer, L., "Space Telescopes and Components," *Astronom. J.*, vol. 65, no. 5, June 1960, pp. 242-263. Also presented orally at the 104th meeting of the Amer. Astronom. Soc., Cleveland, Ohio, Dec. 1959.
2. Ormsby, R. D., "A Free Reaction Sphere Satellite Attitude Control System," Proc. of the National Specialists Meeting on Guidance of Aero-Space Vehicles, Boston, May 1960.
3. Haeussermann, W., "Comparison of Some Actuation Methods for Attitude Control of Space Vehicles," *Aero/Space Engng.*, May 1960, pp. 64-65.

Table 1 Summary of parameters

Radius of spherical shell	25 cm
Shell thickness	0.5 cm
Shell material	aluminum
Shell mass	10.6 kg
$\omega_m$ = relative angular speed at maximum torque	54 radians/sec
Minimum average torque in Earth's magnetic field <sup>a</sup> when $\omega = \omega_m$	240 dyne-cm
Maximum slewing torque	$1.4 \times 10^6$ dyne-cm
Driving field intensity for maximum slewing torque	20 gauss
Driving field frequency = $1.2\omega_m$	10 cps
Power required for maximum torque	18 w
Mass of torquing coils	30 kg
Peak suspension field strength	5 gauss
Suspension field frequency	288 cps
Effective suspension "spring constant"	1000 dynes/cm
Total power for sphere suspension <sup>b</sup>	8.4 w
Mass of suspension coils <sup>b</sup>	5 kg

<sup>a</sup> For 400 mile orbit at 45 deg inclination.

<sup>b</sup> Not counting damping coils if added.

4. Smythe, W. R., *Static and Dynamic Electricity*, 2nd edit., McGraw-Hill, N. Y., 1950.

5. Perkin-Elmer Tech. Rep. no. 5584, March 1960.

## Propulsion Requirements for Controllable Satellites

THEODORE N. EDELBAUM<sup>1</sup>

United Aircraft Corp.  
East Hartford, Conn.

Propulsion requirements are determined for several controllable satellite missions. Both high thrust propulsion systems such as chemical rockets and low thrust propulsion systems such as ion rockets are considered. Rendezvous missions are treated by determining minimum fuel maneuvers for small, simultaneous changes in the elements of quasi-circular orbits. Orbit transfer missions are treated by determining minimum fuel maneuvers for large changes in the elements of circular orbits. Orbit maintenance missions are treated by determining the propulsion necessary to cancel perturbations due to the atmosphere, the Earth's bulge, and the sun and moon. Among the results of the study is a closed-form analytic solution for the optimum low thrust transfer between inclined circular orbits of different radii.

THIS paper is an outgrowth of a presentation on controllable satellite propulsion given at the ARS Controllable Satellites Conference in April 1959. The material for that presentation was prepared jointly by the Pratt & Whitney Aircraft Division and the Research Laboratories of United

Presented at the ARS Semi-Annual Meeting, Los Angeles, Calif., May 9-12, 1960.

<sup>1</sup> Senior Research Engineer, Research Laboratories. Member ARS.

Aircraft Corp. The present paper includes that portion of the original study that dealt with propulsion requirements as well as extensions to the orbit transfer analyses.

### Scope of Study

Fig. 1 illustrates a typical elliptical satellite orbit which can be described in terms of various sets of orbital elements. In this report, the following elements are considered: length

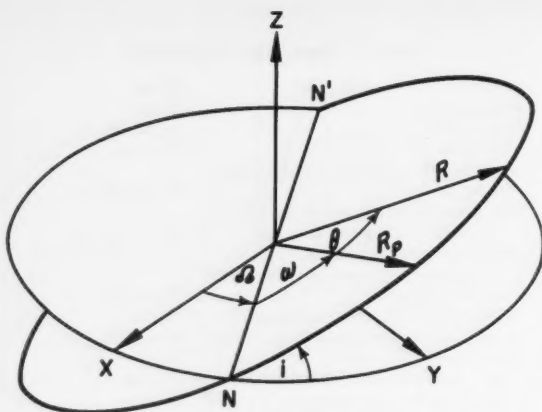


Fig. 1 Satellite orbit

of the semimajor axis  $a$ , eccentricity  $e$ , inclination to the equatorial plane  $i$ , and angle between the line of nodes and the line of apsides  $\omega$ . The semimajor axis is half the distance between the point of closest approach to the Earth (perigee) and the point of furthest retreat from the Earth (apogee). The line connecting these two points (the major axis) is known as the line of apsides. The eccentricity represents the percentage difference between the semimajor axis and either the perigee or the apogee distance. The inclination is the angle between the orbital plane and the  $X, Y$  reference plane. The intersection of the orbital plane and the reference plane is known as the line of nodes (the line  $N-N'$  in Fig. 1). Angular position in the orbit is measured from either the perigee  $\theta$  or a fixed reference point  $\theta'$ .

This study is concerned with the propulsion requirements for varying these orbital elements. Several representative missions are treated under the following headings: (a) Precision Orbit Establishment (b) Modification of Circular Orbits (c) Orbit Maintenance.

Typical missions in the section on precision orbit establishment include the placement of a 24-hr satellite directly above a given point on the Earth's Equator and rendezvous with other vehicles in orbit. Circular orbits have been considered because they are simple to analyze and because they are desirable for many satellite missions. In all cases, the initial departure of the orbit from the desired circular orbit is assumed to be small so that the changes may be considered as linear.

In the section on modification of circular orbits, the use of propulsion to produce gross changes in the orbit is considered. Here also only circular orbits are considered. Typical missions under this heading include the establishment of equatorial orbits from nonequatorial parking orbits, changes in orbit altitude, and changes in the position in the orbit.

The section on orbit maintenance deals with cases where a perturbed orbit is controlled so as to cancel the effects of the perturbations. As particular examples, the maintenance of an orbit in the atmosphere and of a 24-hr satellite orbit in the presence of solar, lunar and bulge perturbations are considered.

Some of these missions can be accomplished either with systems (such as chemical rockets) having high thrust-weight ratios or with systems having low thrust-weight ratios (such as ion rockets or plasma jets). The proposed devices can give accelerations of from less than  $10^{-4}$  gm to greater than  $10^2$  gm. These accelerations can result in corrections being made during many revolutions of the satellite or at essentially a single point in the orbit. Most of the available propulsion systems tend to result in maneuver times

that are either much shorter or much longer than the time for one revolution. Only these cases are treated herein because they constitute the primary interest and because the intermediate cases do give intermediate results. Generally, a high thrust system is taken as having a vehicle thrust-weight ratio of  $\frac{1}{2}$  or greater, while a low thrust system is assumed to have a vehicle thrust-weight ratio of  $10^{-2}$  or less. A further restriction on the low thrust system is that the maneuver must require many revolutions of the satellite. If the required maneuver becomes very small, the low thrust system need be used during only a fraction of a revolution and will behave as a high thrust system. With typical electrical propulsion systems having thrust-weight ratios on the order of  $10^{-4}$ , this latter circumstance corresponds to minute corrections.

The high thrust systems are normally characterized by low specific impulse and high fuel consumption. The maneuvers for this system are optimized so as to minimize fuel consumption. On the other hand, the low thrust systems tend to have high specific impulse and low fuel consumption but very long maneuver times. For these systems the engine is assumed to run continuously and maneuver time is minimized. As long as the engine runs continuously, minimum-time maneuvers are also minimum-fuel maneuvers and vice versa. One unusual system is the energy storage system described in (1).<sup>2</sup> This system uses an electric generator to charge an energy storage unit over many revolutions of the satellite and then releases the energy in short impulses. Here, the interest is in minimizing both fuel consumption and energy consumption in order to minimize charging time as well as fuel. However, since energy minimization is equivalent to fuel minimization in this case, the high thrust system results are directly applicable to this system.

The control systems examined are not required to have variable thrust magnitude. Only burning time and thrust direction are varied. In general, the engines are assumed to be fully controllable in direction. This could be realized in practice by gimbaling the nozzles or by turning the whole satellite. Some attitude control system is probably required but is not discussed.

All the results of the mission analyses are expressed in terms of a required characteristic velocity. Characteristic velocity is a useful parameter because it is independent of both specific impulse and thrust-weight ratio for either high or low thrust systems. All propulsion systems are assumed to operate at constant specific impulse so that the mass ratio required for any maneuver is equal to the exponential of the required characteristic velocity divided by the exhaust velocity.

## Precision Orbit Establishment

### Small Changes of Individual Elements of Orbit

**Optimum High Thrust Corrections:** Optimum methods of making both large and small changes in the individual elements of circular satellite orbits with high thrust have been treated in the literature, e.g., (1 through 10). For changes in the semimajor axis or eccentricity, the well-known Hohmann transfer ellipse is optimum. For small changes in inclination, the optimum maneuver is a single impulse at the line of nodes directed normal to the plane of the orbit. Changes in position in the orbit are accomplished by transferring to a larger or a smaller orbit and revolving in this orbit until the original orbit can be re-entered at the desired point. Reference (3) shows that tangential impulses are essentially indistinguishable from the true optimum for this case. For this case the characteristic velocity requirements are inversely proportional to the number of revolutions in the intermediate orbit.

<sup>2</sup> Numbers in parentheses indicate References at end of paper.



**Optimum Low Thrust Corrections:** The optimum low thrust correction maneuvers for each of these elements are derived in the Appendix. Derivations of the first three of these are also given in (11) and the fourth is derived in (1). For changes in the semimajor axis, the optimum maneuver requires directing the thrust so that it is always tangent to the velocity vector. For changes in eccentricity, the optimum maneuver closely approximates directing the thrust in one direction normal to the line of apsides. This program is more than twice as efficient as the radial thrust programs for changes in eccentricity suggested in the literature. Changes in inclination are accomplished by directing the thrust normal to the plane of the orbit for half a cycle and then reversing the direction for the other half. Rider has recently treated low thrust changes in inclination for elliptic orbits of any eccentricity (12). Changes in position in the orbit are made by applying tangential thrust in one direction until half the correction is made and then applying tangential thrust in the other direction until the original orbit is re-established. As with high thrust, the characteristic velocity is reduced by increasing the number of revolutions required for the maneuver. The characteristic velocity requirements for these maneuvers with both high and low thrust are given in Table 1. Changes in the major axis can be accomplished with the same characteristic velocity with either type of system, but changes in eccentricity with low thrust require a 30% higher characteristic velocity than with high thrust, changes in inclination require 57% more, and changes in position with the same number of revolutions, 100% more. This difference in characteristic velocity for changes in position is probably not significant because the low thrust system will normally require a large number of revolutions to make the correction, and even for only one revolution the characteristic velocity requirement for changing position is an order of magnitude smaller than that required for other changes. It is necessary to perform a complete mission analysis to determine the significance of these differences in characteristic velocity. Low thrust systems and high thrust systems are fundamentally different and cannot be compared on this basis alone.

#### Combination Maneuvers

**High Thrust:** Small changes in both the semimajor axis and the eccentricity can be made simultaneously with a total velocity increment which is equal to that for the larger correction alone. The reason for this is that whatever must be added to one of the impulses must be subtracted from the other, and the sum of the impulses remains the same. Changes in position can also be obtained free by splitting one of the impulses into two parts. For example, not quite all of the required velocity increment is applied in the second impulse, and the rest is applied in a third impulse. Several recent papers have used this concept for changes in position (13 through 15).

Analysis of the optimum maneuvers for the general three-dimensional case is quite complex even for the quasi-circular orbits considered herein (16). It is believed that the optimum maneuver generally requires three impulses for changes in major axis, eccentricity, and inclination; four impulses are required if orbital position is to be changed also. Because of the large number of variables and the complex equations needed to analyze this general maneuver, the general case is not treated herein. Instead, a simplified case is analyzed where the optimum planar maneuver is combined with a change in inclination without changing the planar maneuver. The results of this analysis, which is contained in the Appendix, are given in Fig. 2. This figure shows the combinations of planar and nonplanar changes that can be obtained for a given characteristic velocity. The planar change in semimajor axis or eccentricity per unit characteristic velocity is plotted against the nonplanar change in inclination that can

Table 1 Characteristic velocity requirements for small changes of quasi-circular orbits

High thrust	Low thrust
$\frac{\Delta V}{V_0} = 0.5 \frac{\Delta a}{a_0}$	$\frac{\Delta V}{V_0} = 0.5 \frac{\Delta a}{a_0}$
$\frac{\Delta V}{V_0} = 0.5 \Delta e$	$\frac{\Delta V}{V_0} = 0.649 \Delta e$
$\frac{\Delta V}{V_0} = 1.0 \Delta i$	$\frac{\Delta V}{V_0} = 1.571 \Delta i$
$\frac{\Delta V}{V_0} = 0.106 \frac{\Delta \theta'}{n}$	$\frac{\Delta V}{V_0} = 0.212 \frac{\Delta \theta'}{n}$

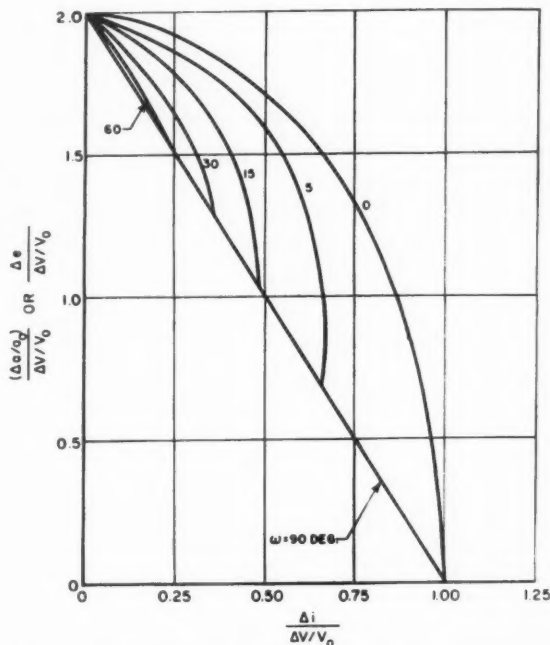


Fig. 2 Combination maneuvers for quasi-circular orbits: high thrust

be obtained with the same unit characteristic velocity. As in the planar case, small changes in both the semimajor axis and the eccentricity can be made simultaneously with a total velocity increment which is equal to that for the larger correction alone. The total characteristic velocity required for a maneuver always lies between the algebraic sum and the vector sum of the planar and nonplanar velocity impulses. For cases where the line of nodes is not coincident with the lines of apsides, it should be possible to improve these results by allowing for some variation of the planar maneuver.

**Low Thrust:** The optimum steering programs for combinations of changes in the semimajor axis, eccentricity and inclination are derived in the Appendix. Changes in orbital position can also be made with these programs because such variations require an alternation of period, which is equivalent to changes in semimajor axis. Some special cases of this optimum steering program for planar maneuvers are illustrated in Fig. 3. The figure shows the variation in the angle

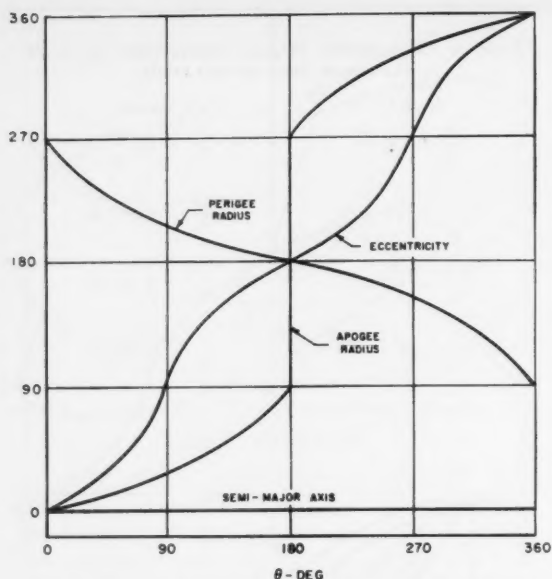


Fig. 3 Some optimum steering programs with low thrust

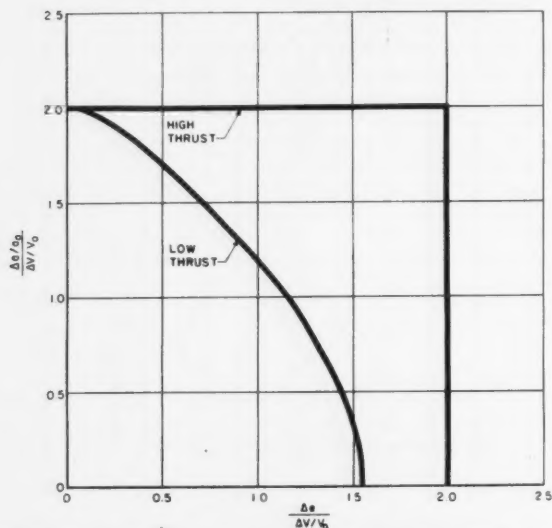


Fig. 4 Characteristic velocity requirements for planar maneuvers

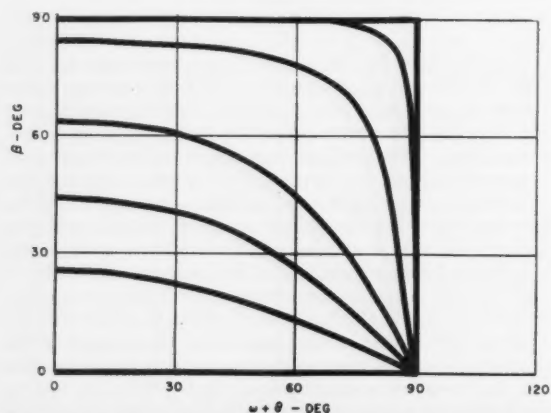


Fig. 5 Optimum steering programs for changing semimajor axis and inclination

between the thrust vector and the velocity vector required for optimum combinations of changes in semimajor axis and eccentricity. The particular programs shown in this figure maximize the semimajor axis, the eccentricity, and the apogee radius, or minimize the perigee radius. The results of these programs are shown in Fig. 4, where they are compared with the corresponding high thrust results. As in Fig. 2, the curves represent the changes that can be obtained with given characteristic velocities. The intersection of the curves with the axis represents individual maneuvers while all other points on the curves represent combination maneuvers. The steering program that maximizes semimajor axis produces no change in eccentricity while the steering program that maximizes eccentricity produces no change in semimajor axis. If the size of the changes that can be obtained with low thrust is compared to those obtainable with high thrust, it can be seen that the disparity is greater for combination maneuvers than for the individual maneuvers. This shows that planar maneuvers with high thrust can be combined more efficiently than planar maneuvers with low thrust.

The steering programs for a number of different combinations of changes in semimajor axis and inclination are shown in Fig. 5. The angle  $\beta$  is the angle between the thrust vector and the plane of the orbit. The results of these programs are illustrated in Fig. 6, where they are compared with the results for high thrust systems. Also shown is the result of keeping the angle between the thrust line and the orbit plane constant in magnitude. This latter steering program gives near-optimum results which can be analyzed simply in terms of trigonometric functions rather than in terms of the elliptic integrals that result from the optimum program. In contrast with the planar results, nonplanar combination maneuvers with low thrust can be combined at least as efficiently as can the maneuver with high thrust. In many cases the characteristic velocity advantage of the high thrust system will be smaller for nonplanar combination maneuvers than for individual maneuvers.

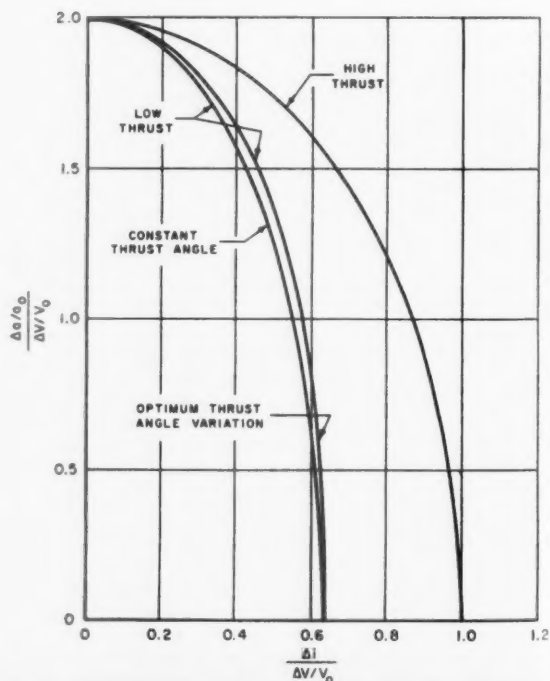


Fig. 6 Characteristic velocity requirements for changes in semimajor axis and inclination

## Modification of Circular Orbits

Large changes in the individual elements of circular satellite orbits are considered in this section. The small-change assumption of the last section is dropped, but the quasi-circular assumption is retained. Because of this latter assumption, large changes in eccentricity are not considered, although changes in orbit altitude and inclination are considered. The allowance of large changes complicates the analysis because the possible fuel savings of various intermediate orbits may be larger than the amount of fuel required to enter the intermediate orbits. It becomes necessary to consider many different possibilities.

### Changes in Radius

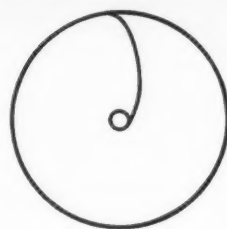
In 1925 Hohmann (2) demonstrated his now classic result that the optimum way to transfer from one circular orbit to another is via an ellipse which is tangent to both orbits. This two-impulse maneuver represents the absolute minimum fuel consumption for most cases of practical interest (5). However, for transfer to circular orbits which are more than twelve times larger (or smaller) than the original orbit, it is possible to save fuel by going to a three-impulse transfer. The three-impulse bi-elliptic transfer is illustrated in Fig. 7. It starts as a conventional Hohmann transfer except that a larger initial impulse is used to transfer beyond the radius of the final orbit. At the apogee of this transfer orbit a second impulse is used to bring the perigee of the transfer ellipse to the radius of the final orbit. The final circular orbit is then entered at the perigee of this second ellipse by means of a third impulse. The farther away the apogee of the transfer ellipse is located, the greater is the fuel saving. The absolute minimum fuel consumption represents going to infinity and applying an infinitesimal impulse there to return along a parabola which is tangent to the final orbit. The characteristic velocity savings of this high thrust maneuver are shown in Fig. 8. Going to twice the radius of the final orbit produces about half the characteristic velocity savings of going to infinity. Since the maximum possible saving in characteristic velocity is about 8%, these savings probably do not justify the increased complexity and transfer times of these maneuvers. This maneuver was apparently first derived by Shternfeld (8). Independent descriptions of this maneuver appear in (9) and (10). A comparison of the Hohmann transfer and the bi-elliptic transfer for co-apse elliptic orbits is contained in (6).

Also shown in Fig. 8 are the characteristic velocity requirements for low thrust transfer between circular orbits. It is demonstrated in (17) that the optimum thrust direction for escape with low thrust is halfway between the tangent to the orbit and the normal to the radius vector. This result is also largely applicable to transfer between circular orbits. For the purposes of this report, the difference between this program and tangential thrust can be considered negligible. In transferring between circular orbits with tangential thrust, the vehicle will quickly approach a mean path whose slope is twice the local thrust-weight ratio and whose velocity is equal to local circular velocity (18). As a result, the satellite will arrive at the final orbit with an eccentricity of twice the local thrust-weight ratio. This is a very small eccentricity and can be cancelled by a high thrust type maneuver after the final orbit radius has been reached, or it can be cancelled by a combination maneuver during the final cycle or cycles. In either case, the characteristic velocity requirement is very small.

### Changes in Inclination

To change the inclination of a satellite orbit it is necessary to change the direction of the velocity vector. The smaller this velocity vector, the smaller the required characteristic velocity. This is a case in which it is desirable to use fuel to

HOHMANN TRANSFER



BI-ELLIPTIC TRANSFER

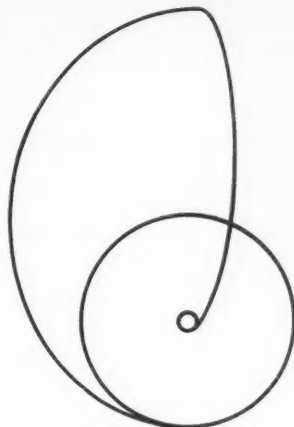


Fig. 7 Minimum fuel transfers

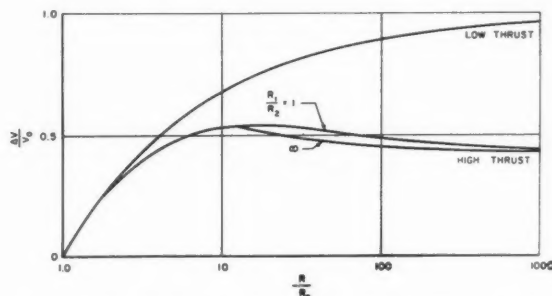


Fig. 8 Characteristic velocities for transfer between circular orbits

establish an intermediate orbit which will have a low velocity so that the change in inclination can be made economically. In (7), it is shown that for large changes in inclination, a tangential impulse which establishes an elliptic orbit, followed by a normal impulse at the apogee of this ellipse and a tangential impulse at perigee to re-establish a circular orbit, can produce fuel savings over a single normal impulse. In the Appendix it is shown that it is advantageous to do part of the change in inclination when entering and leaving the elliptic orbit. The optimum distribution of inclination changes has been treated in several papers (13,14,19,20). Distributing the inclination change produces a small saving in characteristic velocity, usually less than 5% of circular velocity (20), and makes the three-impulse maneuver optimum for all angles rather than for large angles only. The characteristic velocity requirements of these maneuvers are shown in Fig. 9. For small changes in inclination, there is an optimum period for each inclination, while for large changes, the optimum period is infinite. As a consequence, the theoretical optimum is to escape to infinity along a parabolic orbit, change the inclination of the parabolic orbit with an infinitesimal impulse at infinity, and then return and re-enter a circular orbit. Although this maneuver is clearly impractical, it is possible to save fuel by taking longer and longer times to make the maneuver. The curves of Fig. 9 show the maneuver times in terms of the initial orbital periods ( $P_0$ ) that are required for various characteristic velocities. Although not shown, the optimum three-impulse maneuvers for small changes produce only small improvements over the one-impulse maneuver.

With low thrust it is also advantageous to expend some fuel in reducing velocity as well as in changing inclination. For this case the inclination is changed continuously while the satellite revolves in its orbit, so that it is necessary to reduce the velocity throughout the orbit rather than just at one point. This is done by maintaining the orbit as a circle and changing inclination while this circle is first expanded and then shrunk. Two optimum methods of doing this are discussed in the Appendix. The first represents the true optimum where thrust angle is varied through each cycle and also as a function of the size of the orbit. In the second case, thrust angle is maintained constant through each cycle, although it is still varied as a function of the size of the orbit. For the latter case, all the results can be expressed in closed form. The difference in characteristic velocity between the two cases varies between zero and a maximum of 3%. If large changes in inclination are required, it is once again desirable to escape to "infinity," change the inclination at

"infinity," and then return. Because the motor is run continuously, this is a minimum-time as well as a minimum-fuel maneuver. It is not possible to trade these two quantities by changing the maneuver as with the high thrust case.

#### Changes in Inclination and Radius

Rider has recently published an excellent survey of high thrust transfer between inclined circular orbits of different radii (20). He compares two- and three-impulse transfers with and without distribution of the change in inclination.

The optimum low thrust transfer between inclined circular orbits of arbitrary radius is derived in the Appendix in the course of deriving the optimum maneuver for large changes in inclination only. The variational formulation of the inclination problem is necessarily identical to the variational formulation of the more general problem. Every one of the optimum trajectories for producing changes in inclination alone is also an optimum way of getting to every combination of radius and inclination along that trajectory. This is illustrated in Fig. 10 where the trajectories corresponding to various values of the initial steering angle  $\beta_0$  are plotted vs. inclination and velocity. Velocity can be used as a variable instead of radius because the orbit always remains quasi-circular so that the square of the velocity is inversely proportional to the radius. It is used in preference to radius because it does not become infinite. Fig. 10 also shows the characteristic velocity requirements for any desired change in both inclination and velocity.

#### Orbit Maintenance

The orbit of any real satellite will not be a precise Keplerian ellipse. Various natural forces will tend to perturb the orbit. For many applications these perturbations will be acceptable, but there are other applications for which it will be necessary to use propulsion to cancel the effects of perturbations. The most important of these perturbing forces are due to atmospheric drag, the gravitational field of the Earth's equatorial bulge, and the gravitational field of the sun and moon. Radiation pressure will be important only if the satellite has an unusually low density.

Atmospheric drag tends to decrease both the semimajor axis and the eccentricity of any elliptic orbit. The perigee altitude of the satellite will decrease at an increasing rate with time until the satellite re-enters the dense part of the atmosphere and either burns up or impacts the surface of the Earth. For altitudes above approximately 300 miles this effect is negligible. However, thrust will be required to maintain satellites at altitudes of the order of 100 miles for more than a day or so. A satellite of standard density can be maintained at about this altitude by continuous application of thrusts of from  $10^{-5}$  to  $10^{-4}$  times the vehicle weight.

The most important effects of the Earth's equatorial bulge are to cause a small change in the period of the satellite, a continuous rotation of the orbital plane around the polar axis of the Earth, and a continuous rotation of the line of apsides in the plane of the orbit. The sun and the moon cause similar effects except that in these cases the satellite orbital plane rotates with respect to the polar axis of the ecliptic and the moon's orbital plane.

One mission for which these perturbations are important is the stationary 24-hr equatorial satellite. If such a satellite were put precisely over a given point on the Earth's Equator, the combined effect of the equatorial bulge, the sun, and the moon would be to cause a slow rotation of the plane of the orbit in space. As seen from Earth, the satellite would appear to gradually develop a figure 8 motion with a period of one day. This motion would grow in amplitude until it reached about 15 deg north and south of the equator after 25 years. After another 25 years the amplitude would have decreased back to zero, and the cycle would repeat itself.

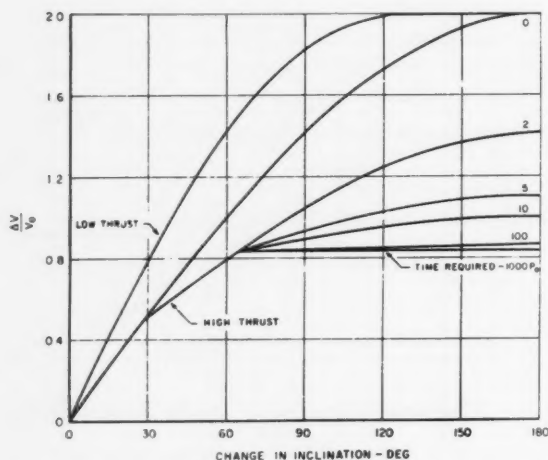


Fig. 9 Minimum characteristic velocity for orbital plane rotation of a circular orbit

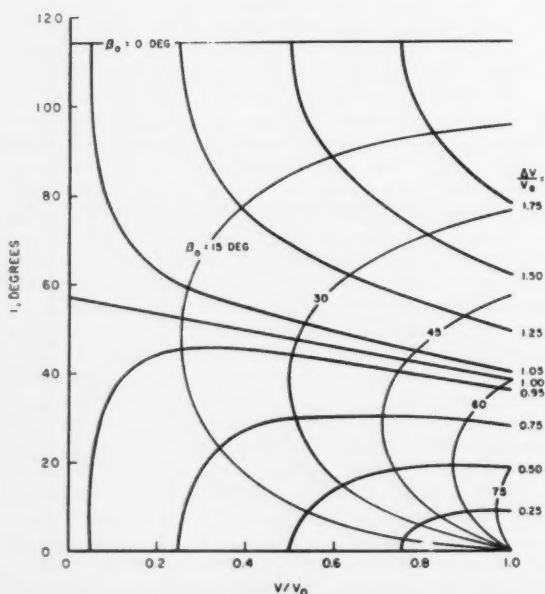


Fig. 10 Characteristic velocities for transfer between inclined circular orbits



In the first year the maximum excursion would be about a degree. This motion could be suppressed by changing the orbital inclination when it grew too large or by continuous application of thrust. A continuous thrust of 2.5 times  $10^{-7}$  times the weight of the satellite would suppress the motion if the direction were changed by 180 deg every half day. Alternately, thrusts of larger magnitude with characteristic velocities of 165 fps per year could be used. Because of the small amount of thrust required, even an ion rocket with a thrust-weight ratio as low as  $10^{-5}$  could be considered a high thrust system for this application.

## Appendix: Derivation of Optimum Maneuvers

### Equations of Motion of Orbit Elements

The analyses of this appendix are carried out in terms of the elements of the elliptic orbit. The rates of change of each of these elements have been derived by following the techniques presented in (21). The thrust force is broken down into three mutually perpendicular components: a tangential component which is tangent to the velocity vector, an orthogonal component which is normal to the plane of the orbit, and a normal component which is normal to the other two. These components are expressed in terms of two angles, the angle between the velocity vector and the component of the thrust vector in the plane of the orbit  $\alpha$ , and the angle between the thrust vector and the plane of the orbit  $\beta$ .

$$F_T = F \cos \beta \cos \alpha \quad F_N = F \cos \beta \sin \alpha \quad F_z = F \sin \beta \quad [1]$$

For almost circular orbits where the eccentricity and inclination are small, the equations of motion are

$$\begin{aligned} \frac{di}{dt} &= \frac{\cos(\omega + \theta) F_z}{V_0 m} \\ \frac{d\Omega}{dt} &= \frac{\sin(\omega + \theta) F_z}{i V_0 m} \\ \frac{da}{dt} &= \frac{2a F_T}{V_0 m} \\ \frac{de}{dt} &= \frac{2 \cos \theta F_T}{V_0 m} + \frac{\sin \theta F_N}{V_0 m} \\ \frac{d\omega}{dt} &= \frac{2 \sin \theta F_T}{e V_0 m} + \frac{\cos \theta F_N}{e V_0 m} - \frac{\sin(\omega + \theta) F_z}{i V_0 m} \end{aligned} \quad [2]$$

### Optimum High Thrust Maneuvers

#### Large Changes in Inclination

An efficient maneuver for effecting large changes in inclination is discussed in (7). This maneuver consists of applying a tangential impulse to change the original circular orbit to an ellipse, changing inclination at the apogee of the ellipse, and re-establishing a circular orbit with a tangential retrothrust at perigee. The following analysis is intended to show that this maneuver can be improved slightly by combining part of the change in inclination with the initial and final impulses.

The characteristic velocity required for finite changes in inclination with high thrust is simply the vector difference between the initial and final velocity vectors. For the present problem, the required characteristic velocity is given by

$$\frac{\Delta V}{V_0} = 2 \frac{V}{V_0} \sin i/2 \quad [3]$$

The perigee velocity required to establish a specific apogee

radius is given by

$$\frac{V_1}{V_0} = \sqrt{\frac{2Ra}{Ra + R_0}} \quad [4]$$

The characteristic velocity required to produce an initial (or final) change in inclination is

$$\frac{\Delta V_1}{V_0} = \sqrt{\frac{V_1^2}{V_0^2} - \frac{2V_1}{V_0} \cos i_1 + 1} \quad [5]$$

The total characteristic velocity for the maneuver is given by

$$\begin{aligned} \frac{\Delta V}{V_0} &= 2 \sqrt{\frac{V_1^2}{V_0^2} - \frac{2V_1}{V_0} \cos i_1 + 1} \\ &\quad + 2 \left( \frac{2V_0}{V_1} - \frac{V_1}{V_0} \right) \sin \left( \frac{i}{2} - i_1 \right) \end{aligned} \quad [6]$$

The time of the maneuver depends only upon the choice of apogee radius. The required characteristic velocity for a given maneuver time can be minimized by optimizing the initial change in inclination. An explicit expression for the optimum value of this angle can be derived by assuming that this angle is small. More exact calculations have shown that this assumption is justified in all cases of interest

$$\begin{aligned} \frac{\Delta V}{V_0} &\approx 2 \sqrt{\left( \frac{V_1}{V_0} - 1 \right)^2 + \frac{V_1}{V_0} i_1^2} + \\ &\quad + 2 \left( \frac{2V_0}{V_1} - \frac{V_1}{V_0} \right) \left( \sin \frac{i}{2} - i_1 \cos \frac{i}{2} \right) \end{aligned} \quad [7]$$

Differentiating Eq. 7 with respect to the initial change in inclination and setting the result equal to zero produces the following expression for the optimum initial angle

$$i_{1opt} \approx \frac{1 - \frac{V_0}{V_1}}{\sqrt{\left( \frac{\sec i/2}{2 \frac{V_0}{V_1} - \frac{V_1}{V_0}} \right)^2 - \frac{V_0}{V_1}}} \quad [8]$$

This optimum initial angle was used with Eq. 6 to draw up the curves of Fig. 9. The optimum initial angle given by Eq. 8 approaches zero as the inclination becomes large. As this is the case considered in (7), the results of Fig. 9 become identical with the results in (7) for large changes in inclination.

### Combination of Small Planar Maneuvers with Small Changes in Inclination

As mentioned in the body of the report, the optimum combination maneuvers for high thrust systems are difficult to derive because of the large number of variables involved. A simplified approach will be considered herein, where a given planar maneuver is combined with a change in inclination. The planar components of the initial and final impulses are assumed to be tangent to the velocity vector, applied at apogee or perigee, and fixed in magnitude. The magnitude of the orthogonal components of the initial and final impulses, and the magnitude and point of application of an intermediate orthogonal impulse, are allowed to vary. These four variables are interconnected so that only two may be considered as independent. The two independent variables are optimized to produce the results shown in Fig. 2.

The derivation starts with the first and last of Eqs. 2. The first describes the rate of change of inclination due to an orthogonal force, while the last describes the rate of change of the angle between the line of apsides and the line of nodes.

Examination of these two equations shows that the rate of change of the angle between the line of nodes and the line of apsides depends upon the inclination and that the rate of change of inclination depends on this angle. These equations must be solved simultaneously to determine the effect of small finite impulses. This determination is simplified by the assumption of tangential impulses at the apsides, because such impulses have no effect on the position of the line of apsides. Using this assumption, the first and last of Eqs. 2 can be combined to yield

$$\frac{d\omega}{\tan(\omega + \theta)} = -\frac{di}{i} \quad [9]$$

This equation can be integrated directly

$$\ln \frac{\sin(\omega + \theta)_2}{\sin(\omega + \theta)_1} = \ln \frac{i_1}{i_2} \quad i \sin(\omega + \theta) = \text{const.} \quad [10]$$

Eq. 10 has a simple physical interpretation: the distance of the satellite from the reference plane does not change during the impulsive maneuver. This means that the final impulse that reduces the inclination of the satellite to zero must be given at the line of nodes. Since it has also been assumed that the last impulse takes place at the line of apsides, the second of the three impulses must make the line of apsides coincident with the line of nodes. The two remaining independent variables which will be optimized are taken as the point of application of this second impulse ( $\theta$ ) and the inclination after this second impulse ( $i$ ). The impulse required to produce a given change in inclination or in position of the line of nodes is found by combining Eq. 10 with the last of Eqs. 2 and integrating

$$\begin{aligned} d\omega &= -\frac{\sin^2(\omega + \theta)}{i \sin(\omega + \theta)_1} \frac{F_x dt}{V_0 m} \\ \frac{1}{V_0} \int \frac{F_x dt}{m} &= -i_1 \sin(\omega + \theta)_1 \int \frac{d\omega}{\sin^2(\omega + \theta)} \\ \frac{\Delta V_x}{V_0} &= i_1 \sin(\omega + \theta)_1 [\cot(\omega + \theta)_2 - \cot(\omega + \theta)_1] \end{aligned} \quad [11]$$

The sum of the required velocity impulse is given by

$$\Sigma \frac{\Delta V}{V_0} = \sqrt{\left(\frac{\Delta V_{T1}}{V_0}\right)^2 + [i_0(\cos \omega_0 + \sin \omega_0 \cot \theta) - i]^2 + \frac{i_0 \sin \omega_0}{\sin \theta} + \sqrt{\left(\frac{\Delta V_{T2}}{V_0}\right)^2 + i^2}} \quad [12]$$

Differentiating this equation with respect to  $\theta$  and setting the result equal to zero results in the following expression for the optimum value of  $\theta$

$$\cot \theta_{\text{opt}} = \frac{i_0 \cos \omega_0 - i}{\frac{\Delta V_{T1}}{V_0} - i_0 \sin \omega_0} \quad [13]$$

Differentiating Eq. 12 with respect to  $i$  and setting the result equal to zero results in the following expression for the optimum value of  $i$

$$i_{\text{opt}} = \frac{\frac{\Delta V_{T2}}{V_0} i_0 (\cos \omega_0 + \sin \omega_0 \cot \theta)}{\frac{\Delta V_{T1}}{V_0} + \frac{\Delta V_{T2}}{V_0}} \quad [14]$$

Combining Eqs. 13 and 14 leads, after some reduction, to

$$\cot \theta_{\text{opt}} = \frac{i_0 \cos \omega_0}{\frac{\Delta V_{T1}}{V_0} + \frac{\Delta V_{T2}}{V_0} - i_0 \sin \omega_0} \quad [15]$$

$$i_{\text{opt}} = \frac{\Delta V_{T2}}{V_0} \cot \theta_{\text{opt}} \quad [16]$$

Introducing these equations into Eq. 12 and simplifying leads to the final result

$$\Sigma \frac{\Delta V}{V_0} = \left( \frac{\Delta V_{T1}}{V_0} + \frac{\Delta V_{T2}}{V_0} + i_0 \sin \omega_0 \right) \times \sqrt{1 + \left( \frac{i_0 \cos \omega_0}{\frac{\Delta V_{T1}}{V_0} + \frac{\Delta V_{T2}}{V_0} - i_0 \sin \omega_0} \right)^2} \quad [17]$$

One of the interesting characteristics of this equation is that the required velocity impulse depends only upon the total magnitude of the planar velocity impulse and not upon its distribution. This means that in both the three-dimensional and two-dimensional cases, a change in eccentricity or orbital position can be obtained free if the required change in major axis is large enough. The velocity increment required for the planar part of the maneuver depends only upon the largest single planar correction that must be made.

### Optimum Low Thrust Maneuvers

#### Steering Programs for Small Changes in Elements of Orbit

The optimum steering program for small changes in the elements of almost circular orbits can be easily derived by using the ordinary theory of maxima and minima. The general theory of the calculus of variations can offer improvements over this simple theory only when the changes are large, as in the inclination problem considered at the end of this appendix.

The problem is to optimize the steering angles of the thrust vector as a function of orbital position. Combination of Eqs. 1 and 2 yields

$$\begin{aligned} \frac{da/a_0}{dt} &= \frac{F}{mV_0} [2 \cos \alpha \cos \beta] \\ \frac{de}{dt} &= \frac{F}{mV_0} [2 \cos \theta \cos \alpha \cos \beta + \sin \theta \sin \alpha \cos \beta] \\ \frac{di}{dt} &= \frac{F}{mV_0} [\cos(\omega + \theta) \sin \beta] \end{aligned} \quad [18]$$

The optimum steering program is found by combining Eqs. 18 by means of Lagrange multipliers and setting the partial derivatives of this expression with respect to the steering angles equal to zero

$$\frac{\partial}{\partial \alpha} \frac{\partial}{\partial \beta} \left[ \frac{da/a_0}{dt} + \lambda_1 \frac{de}{dt} + \lambda_2 \frac{di}{dt} \right] = 0 \quad [19]$$

Substituting the expression of Eqs. 18 into Eqs. 19 and carrying out the indicated operations result in the following expressions for the optimum steering angles

$$\begin{aligned} \tan \alpha_{\text{opt}} &= \frac{\lambda_1 \sin \theta}{2(1 + \lambda_1 \cos \theta)} \\ \tan \beta_{\text{opt}} &= \frac{\lambda_2 \cos(\omega + \theta)}{\sqrt{4(1 + \lambda_1 \cos \theta)^2 + \lambda_1^2 \sin^2 \theta}} \end{aligned} \quad [20]$$

#### Planar Maneuvers

When the required maneuver is a planar one, the second Lagrange multiplier of Eqs. 19 and 20 becomes zero and the thrust line always lies in the plane of the orbit. Only the first of Eqs. 20 need then be considered. This section will consider some special cases of this equation. The first case is a change in major axis only. The Lagrange multiplier is

then zero and the thrust should always be tangent to the orbit

$$\frac{da}{a_0} = 2 \frac{F}{mV_0} dt \quad \frac{\Delta V}{V_0} = \frac{1}{2} \frac{\Delta a}{a_0} \quad [21]$$

If it is desired to change the eccentricity without changing the major axis, then the Lagrange multiplier should be taken as infinite and the steering program is given by

$$\tan \alpha_{opt} = 1/2 \tan \theta \quad [22]$$

This equation is plotted in Fig. 3. The thrust direction comes close to representing a constant direction in space and this latter program gives very close to optimum results.

The characteristic velocity for changes in eccentricity is found by substituting Eq. 22 into the second of Eqs. 18 and integrating

$$\begin{aligned} \frac{de}{d\theta} &= \frac{F}{mV_0} \left[ \frac{4 \cos \theta}{\sqrt{4 + \tan^2 \theta}} + \frac{\tan \theta \sin \theta}{\sqrt{4 + \tan^2 \theta}} \right] \\ \frac{de}{d\theta} &= \frac{FR}{mV_0^2} \frac{4 \cos^2 \theta + \sin^2 \theta}{\sqrt{4 \cos^2 \theta + \sin^2 \theta}} \\ \frac{de}{d\theta} &= \frac{FR}{mV_0^2} 2\sqrt{1 - 3/4 \sin^2 \theta} \end{aligned}$$

The change in eccentricity per revolution is given by a complete elliptic integral of the second kind

$$\begin{aligned} \Delta e &= \frac{FR}{mV_0^2} 8 \int_0^{\pi/2} \sqrt{1 - 3/4 \sin^2 \theta} d\theta \\ \Delta e &= \frac{8FR}{mV_0^2} E(\sqrt{3/4}) = \frac{8FR}{mV_0^2} (1.2111) \end{aligned} \quad [23]$$

The characteristic velocity for the change in eccentricity per cycle is given by

$$\frac{\Delta V}{V_0} = \frac{F}{m} \frac{R_0}{V_0^2} 2\pi \quad \frac{\Delta V}{V_0} = 0.649 \Delta e \quad [24]$$

There are several other values of the Lagrange multiplier where the optimum steering program can be substituted in Eqs. 18 and integrated analytically. The details of these will not be given here as the integrations are straightforward and the results are shown as the low thrust curve in Fig. 4. The steering program for two of the more important cases, maximizing the rates of change of apogee or perigee radius, is shown in Fig. 3. For these cases the values of the Lagrange multipliers are plus and minus one, respectively.

### Nonplanar Maneuvers

Nonplanar maneuvers can be treated exactly as were the planar maneuvers of the last section. For simplicity, only the cases where the eccentricity does not change will be considered. With this assumption, Eq. 20 reduces to

$$\tan \alpha_{opt} = 0 \quad \tan \beta_{opt} = \frac{\lambda_2}{2} \cos(\omega + \theta) \quad [25]$$

The second equation is plotted in Fig. 5 for various values of the Lagrange multiplier. Changing the notation of the second of Eqs. 25 and substituting into Eq. 18 yields

$$\begin{aligned} \tan \beta &= k' \cos \theta \\ \frac{mV_0^2}{FR_0} di &= \frac{k' \cos^2 \theta}{\sqrt{1 + k'^2 \cos^2 \theta}} d\theta = \frac{k' - k' \sin^2 \theta}{\sqrt{1 + k'^2 - k'^2 \sin^2 \theta}} d\theta \\ \frac{mV_0^2}{FR_0} \frac{da}{a_0} &= \frac{2}{\sqrt{1 + k'^2 \cos^2 \theta}} d\theta = \frac{2}{\sqrt{1 + k'^2 - k'^2 \sin^2 \theta}} d\theta \end{aligned} \quad [26]$$

The following standard substitution

$$k = \frac{k'}{\sqrt{1 + k'^2}} \quad [27]$$

changes Eqs. 26 to

$$\begin{aligned} \frac{mV_0^2}{FR_0} di &= \frac{k - k \sin^2 \theta}{\sqrt{1 - k^2 \sin^2 \theta}} d\theta \\ &= \frac{k^2 - 1}{k\sqrt{1 - k^2 \sin^2 \theta}} d\theta + \frac{\sqrt{1 - k^2 \sin^2 \theta}}{k} d\theta \\ \frac{mV_0^2}{FR_0} \frac{da}{a_0} &= \frac{2\sqrt{1 - k^2}}{\sqrt{1 - k^2 \sin^2 \theta}} d\theta \end{aligned} \quad [28]$$

Integrating Eqs. 28 over a complete cycle results in complete elliptic integrals of the first and second kind

$$\begin{aligned} \frac{mV_0^2}{FR_0} \Delta i &= 4 \left[ \frac{k^2 - 1}{k} K + \frac{E}{k} \right] \\ \frac{mV_0^2}{FR_0} \frac{\Delta a}{a_0} &= 8\sqrt{1 - k^2} K \end{aligned} \quad [29]$$

Expressing these in terms of required characteristic velocity results in

$$\frac{\Delta V}{V_0} = \frac{\Delta i}{\frac{2}{\pi} \left[ \frac{k^2 - 1}{k} K + \frac{E}{k} \right]} \quad \frac{\Delta V}{V_0} = \frac{\Delta a/a_0}{\frac{4}{\pi} \sqrt{1 - k^2} K} \quad [30]$$

The characteristic velocity requirements given by Eqs. 30 are plotted in Fig. 6. Also shown in Fig. 6 is the result of keeping the thrust angle  $\beta$  constant. This can be seen to give near optimum results.

Where only a change in inclination is desired,  $k$  should be taken as unity, and where only a change in major axis is desired  $k$  should be taken as zero. The results of these two cases are given by

$$\frac{\Delta V}{V_0} = \frac{\pi}{2} \Delta i \quad \frac{\Delta V}{V_0} = \frac{1}{2} \frac{\Delta a}{a_0} \quad [31]$$

The second of these equations checks with Eq. 21, as it should.

### Changes in Position in Orbit

The only method of producing changes in orbital position with a continuous small thrust is to change the period of the orbit. The most economical way of doing this is to use tangential thrust in one direction until half the desired change in position is accomplished, and then to reverse the thrust direction until the original orbit is re-established.

For small changes in period, the change in period for a given change in major axis is given by

$$\frac{\Delta P}{P_0} = \frac{3}{2} \frac{\Delta a}{a_0} \quad [32]$$

The change in period produced by a given characteristic velocity is found by substituting Eq. 21 into Eq. 32, as follows

$$\frac{\Delta P}{P_0} = 3 \frac{\Delta V}{V_0} = \frac{3FP_0}{mV_0} n \quad [33]$$

The change in position per cycle is given by

$$\frac{\Delta \theta'}{\Delta n} = 2\pi \frac{\Delta P}{P_0} = 6\pi \frac{FP_0}{mV_0} n \quad [34]$$

Integrating Eq. 34 over  $n$  cycles yields

$$\Delta\theta' = 3\pi \frac{FP_0}{mV_0} n^2 = 3\pi \frac{\Delta V}{V_0} n \quad [35]$$

Eq. 35 applies to only one segment of the maneuver. For the total maneuver where the period is first increased (or decreased) and then decreased (or increased), the change in  $\theta'$  is given by

$$\Delta\theta' = 2 \left[ 3\pi \frac{\Delta V}{2V_0} n \right] \quad [36]$$

The required characteristic velocity is

$$\frac{\Delta V}{V_0} = \frac{4}{3} \frac{\Delta\theta'}{2\pi n} \quad [37]$$

Eq. 37 agrees with the result obtained in (1).

### Large Changes in Inclination

This section will consider the derivation of the optimum steering program for producing large changes in inclination with low thrust devices. This is a problem which can be solved exactly by the general methods of the calculus of variations. However this solution cannot be carried out in a closed form and would require very extensive numerical calculations. The problem will be simplified by making two assumptions which allow a closed form solution within the framework of the general theory of the calculus of variations. The first assumption is that the orbits always remain quasi-circular. It can be shown that this should be the case for very small changes, as well as for very large changes in inclination. It will be assumed that the orbits should remain quasi-circular for all intermediate changes as well. This assumption allows the use of the previous results on small changes in inclination and major axis for the individual revolutions of the satellite. The problem is basically one of how rapidly the orbit should enlarge and shrink while the inclination is being changed.

The second assumption is that the thrust angle will be held constant during each revolution. Fig. 6 shows that there is little difference between this case and the true optimum for each cycle. The more general case can be developed in exactly the manner presented here, but it leads to complicated expressions having no closed form solution. The present solution produces near optimum results having a surprisingly simple form.

When the thrust angle is kept constant, the change in inclination can be expressed by

$$di = \frac{2}{\pi} \frac{F \sin \beta}{mV} dt \quad [38]$$

As the orbits will remain quasi-circular if the thrust angle is held constant over each revolution, the velocity will decrease as the major axis increases

$$dV = -\frac{F}{m} \cos \beta dt \quad [39]$$

The variational problem is formulated using velocity as the independent variable. This is merely an artifice to simplify the analysis and does not affect the results. The variational integral to be optimized is given by

$$-\int \left( \frac{di}{dV} + \lambda \frac{dt}{dV} \right) dV = \int \left( \frac{2 \tan \beta}{\pi V} + \frac{\lambda m}{F \cos \beta} \right) dV \quad [40]$$

The Euler equation of this problem is simply that the partial derivative of the integrand with respect to the thrust angle

should be zero

$$\frac{\partial}{\partial \beta} \left( \frac{2 \tan \beta}{\pi V} + \frac{\lambda m}{F \cos \beta} \right) = 0$$

This reduces to

$$V \sin \beta = \frac{2F}{m\pi\lambda} = \text{const} = V_0 \sin \beta_0 \quad [41]$$

Eqs. 39 and 38 can now be integrated with this steering program

$$\frac{F}{m} dt = -\frac{dV}{\cos \beta} = -\frac{dV}{\sqrt{1 - \sin^2 \beta} \frac{V_0^2}{V^2}}$$

$$\frac{F}{m} dt = -\frac{dV}{2 \sqrt{V^2 - V_0^2 \sin^2 \beta_0}}$$

$$ft = \Delta V = V_0 \cos \beta_0 - \sqrt{V^2 - V_0^2 \sin^2 \beta_0}$$

$$V = \sqrt{V_0^2 - 2V_0\Delta V \cos \beta_0 + \Delta V^2} \quad [42]$$

$$di = -\frac{2 \tan \beta}{\pi V} dV \quad di = -\frac{2}{\pi V} \frac{V_0 \sin \beta dV}{\sqrt{V^2 - V_0^2 \sin^2 \beta_0}}$$

$$i = \frac{2}{\pi} \sin^{-1} \frac{V_0 \sin \beta_0}{V} - \frac{2\beta_0}{\pi} \quad [43]$$

Eqs. 42 and 43 can be combined to give:

$$(a) \text{ For } \frac{\Delta V}{V_0} \leq \cos \beta_0:$$

$$i = \frac{2}{\pi} \sin^{-1} \frac{V_0 \sin \beta_0}{\sqrt{V_0^2 - 2V_0\Delta V \cos \beta_0 + \Delta V^2}} - \frac{2\beta_0}{\pi} \quad [44a]$$

$$(b) \text{ For } \frac{\Delta V}{V_0} \geq \cos \beta_0:$$

$$i = 114.6^\circ - \frac{2}{\pi} \sin^{-1} \frac{V_0 \sin \beta_0}{\sqrt{V_0^2 - 2V_0\Delta V \cos \beta_0 + \Delta V^2}} - \frac{2\beta_0}{\pi} \quad [44b]$$

Eqs. 42 and 44 represent the changes in velocity and inclination that can be obtained with a given characteristic velocity as the initial steering angle is changed. These equations may be solved simultaneously to determine the characteristic velocity requirements directly in terms of the orbital velocities and the inclination

$$\Delta V = \sqrt{V_0^2 - 2VV_0 \cos \frac{\pi}{2} i + V^2} \quad [45]$$

### Nomenclature

- $a$  = semimajor axis of orbit
- $e$  = eccentricity of orbit
- $E$  = energy per unit mass, complete elliptic integral of the second kind
- $F$  = thrust force
- $i$  = inclination of orbit to a reference plane
- $k, k'$  = constants which represent the moduli of elliptic integrals
- $K$  = complete elliptic integral of the first kind
- $L$  = angular momentum per unit mass
- $m$  = mass
- $n$  = number of revolutions
- $P$  = period of orbit



- $R$  = radius  
 $t$  = time  
 $V$  = velocity  
 $\Delta V$  = characteristic velocity  
 $\Omega$  = position angle of the line of nodes (see Fig. 1)  
 $\alpha$  = angle between the velocity vector and the component of the thrust vector in the plane of the orbit  
 $\beta$  = angle between the thrust line and the plane of the orbit  
 $\theta$  = position angle in the orbit measured from perigee  
 $\theta'$  = position angle in the orbit measured from a fixed reference  
 $\lambda$  = Lagrange multiplier  
 $\phi$  = flight path angle with the horizontal  
 $\omega$  = angle between the line of nodes and the line of apsides

#### Subscripts

- $a$  = apogee  
 $N$  = normal component  
 $opt$  = optimum  
 $p$  = perigee  
 $T$  = tangential component  
 $z$  = orthogonal component  
 $0$  = initial; circular  
 $1$  = intermediate  
 $2$  = final

#### References

- 1 Camac, M., "Reduction of Flight Time and Propulsion Requirements of Satellites with Electric Propulsion by the Use of Stored Electrical Energy," *ARS JOURNAL*, vol. 30, no. 1, Jan. 1960.
- 2 Hohmann, W., *Die Erreichbarkeit der Himmelskörper*, Oldenbourg Publ., Munich, 1925.
- 3 Berman, L. J., "Correction of Epoch Error in Circular Orbits," AFOSR TN 59-62, April 1959.
- 4 Lawden, D. F., "Interplanetary Rocket Trajectories," *Advances in Space Science*, vol. 1, Academic Press, N. Y., 1959.
- 5 Munick, H., McGill, R. and Taylor, G. E., "Analytic Solutions to Several Optimum Orbit Transfer Problems," *J. Astronaut. Sci.*, vol. 7, no. 4, Winter 1960.
- 6 Ting, L., "Optimum Orbital Transfer by Several Impulses," *Astronautica Acta*, vol. 6, fasc. 5, 1960.
- 7 Rider, L., "Characteristic Velocity for Changing the Inclination of a Circular Orbit to the Equator," *ARS JOURNAL*, vol. 29, no. 1, Jan. 1959.
- 8 Shternfeld, A., *Soviet Space Science*, Basic Books, Inc., N. Y., 1959.
- 9 Hoelker, R. F. and Silber, R., "The Bi-Elliptic Transfer Between Circular Co-Planar Orbits," Army Ballistic Missile Agency, DA Technical Memo 2-59, Jan. 1959.
- 10 Edelbaum, T. N., "Some Extensions of the Hohmann Transfer Maneuver," *ARS JOURNAL*, vol. 29, no. 11, Nov. 1959.
- 11 Brown, H. and Nelson, J. R., "Thrust Orientation Patterns for Orbit Adjustment of Low Thrust Vehicles," *ARS JOURNAL*, vol. 30, no. 7, July 1960.
- 12 Rider, L., "Low Thrust Correction of Orbital Orientation," *ARS JOURNAL*, vol. 30, no. 7, July 1960.
- 13 Fiul, A. and Braham, H., "Optimization of Vehicles and Trajectories for the Twenty-Four Hour Equatorial Satellite Mission," *ARS preprint* 1120-60, presented at the ARS Semi-Annual Meeting and Astronaut. Exposition, Los Angeles, Calif., May 9-12, 1960.
- 14 Hoelker, R. and Silber, R., "Analysis of Injection Schemes for Obtaining a Twenty-Four Hour Orbit," IAS paper 60-75, June 1960.
- 15 Van Gelder, A., Beltrami, E. and Munick, H., "On Minimum Time Minimum Fuel Rendezvous," presented at the Nov. 1960 meeting of the Soc. for Industrial and Appl. Math.
- 16 Long, R. S., "Transfer Between Non Co-Planar Elliptical Orbits," *Astronautica Acta*, vol. 6, fasc. 2-3, 1960.
- 17 Lawden, D. F., "Optimal Escape from a Circular Orbit," *Astronautica Acta*, vol. 41, fasc. 3, 1958.
- 18 Perkins, F. M., "Flight Mechanics of Low-Thrust Spacecraft," *J. Aero/Space Sci.*, vol. 26, no. 5, May 1959.
- 19 Horner, J. M. and Silber, R., "Impulse Minimization for Hohmann Transfer Between Inclined Circular Orbits of Different Radii," Army Ballistic Missile Agency, DA Tech. Rep. 70-59, Dec. 1959.
- 20 Rider, L., "Characteristic Velocity Requirements for Impulsive Thrust Transfers Between Non Co-Planar Circular Orbits," *ARS JOURNAL*, vol. 31, no. 3, March 1961.
- 21 Moulton, F. R., *An Introduction to Celestial Mechanics*, Mac-Millan, N. Y., 1914.

## Effects of Plane Librations on the Orbital Motion of a Dumbbell Satellite

JOHN P. MORAN<sup>1</sup>

THERM, Inc.  
Ithaca, N. Y.

The equations of motion of a dumbbell satellite oscillating or tumbling in the plane of its orbit are treated by a perturbation technique which assumes the satellite's length to be small with respect to its orbital radius. The unperturbed orbital motion is that of a point mass at the mass center of the satellite, while the equations for the perturbed motion are essentially decoupled. Analytic solutions are obtained under initial conditions which would have yielded a circular orbit were the satellite a point mass. Although the disturbances induced in the orbital motion by the librations are usually quite small, for certain frequencies of the librations a resonance phenomenon occurs; i.e., the perturbation quantities contain secular terms, so that they grow indefinitely with increasing time.

THE MOTION of a satellite about its mass center is a problem of prime importance in connection with many satellite missions, the more exciting of which necessitate the directional stabilization of the vehicle. An important factor in this motion is the variation of the gravitational force on a

mass particle in the satellite with its distance from the body about which the vehicle is orbiting. As a result, the point at which the net force acts—the center of gravity of the satellite—does not, in general, coincide with its center of mass. It is then possible for the line between the gravitational and mass centers to be noncoincident with the line of action of the gravitational force, so that a torque is exerted about the mass center of the satellite.

The existence of a gravitational torque was first noted over 150 years ago in connection with the longitudinal oscillations

Presented at the ARS 15th Annual Meeting, Washington, D. C., Dec. 5-8, 1960.

<sup>1</sup> Associate Research Scientist, Therm Advanced Research, Member ARS.

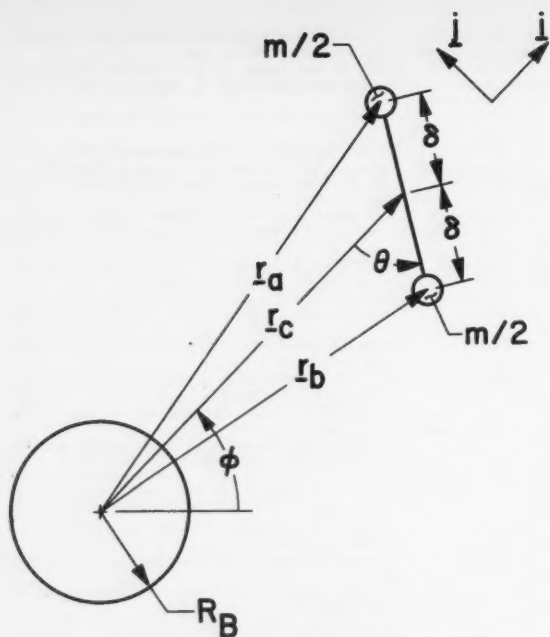


Fig. 1 Dumbbell satellite in planar motion

of the moon. The name given this motion, *lunar librations*, has been carried over into some of the more modern analyses of the motion of artificial satellites (1 through 17).<sup>2</sup> That is, the motion of the satellite's mass center is distinguished from its motion about that point by referring to the former as the *orbital motion* and the latter as the *librational motion*.

In the formulation of most of these analyses, the distinction between the two motions is carried somewhat deeper than nomenclature. That is, the orbital motion is assumed to be unaffected by the librations, so that the shape of the orbit may be specified a priori. This specification is then used in conjunction with the equation of the motion about the satellite's mass center to determine the history of the librations.

Strictly speaking, such a simplification is incorrect. A noticeable coupling is exhibited between the orbital and librational motions in the equations of motion as derived by D. E. Ordway (1) for a dumbbell satellite and by R. H. Frick and T. B. Garber (2) for a satellite of arbitrary shape. The physical origin of this coupling may be traced to the fact that the position of the gravitational center of the vehicle relative to its center of mass varies with the satellite's orientation. Since the force accelerating the mass center depends on the radius vector to the center of gravity, the orientation of the satellite is seen to be a factor in the motion of its mass center.

In the present paper, we examine the interaction between the coupled orbital and librational motions by studying the planar motion of an idealized dumbbell satellite. The equations of the motion are treated by a perturbation technique which considers the length of the satellite to be small in comparison with the radius of the orbit. After a system of successive approximations is set up, the first-order effects of the "dumbbellness" of the satellite are studied in detail for the special case where the unperturbed orbit is circular. No restriction is placed on the amplitude of the librations a priori; indeed, a solution is found for the case where the satellite is executing a tumbling motion.

<sup>2</sup> Numbers in parentheses indicate References at end of paper.

## Equations of the Planar Motion of a Dumbbell Satellite

Let us consider the planar motion of an idealized dumbbell satellite—formed by two point masses of mass  $m/2$  connected by a rigid weightless rod of length  $2\delta$ —about a nearly spherical and homogeneous body of mean radius  $R_B$ , as shown in Fig. 1. So as to simplify our nomenclature, we shall refer to this body as Earth, although the analysis is by no means restricted to Earth satellites.

In the Earth-fixed coordinates shown in Fig. 1,  $r_a$  and  $r_b$  define the locations of the two point masses, while  $r_c$  is the radius vector to the satellite's mass center. By symmetry this point is located at the midpoint of the rod joining the masses. We denote the angle between  $r_c$  and the rod by  $\theta$ , while  $\phi$  defines the sweep of the  $r_c$  vector in the plane of the orbit. Unit vectors  $i$  and  $j$  are defined in the directions of increasing  $r_c$  and  $\phi$ , respectively. We may relate  $r_a$  and  $r_b$  to  $r_c$  and  $\delta$  by

$$\underline{r}_a = (r_c \pm \delta \cos \theta) \underline{i} \pm \delta \sin \theta \underline{j} \quad [1]$$

In developing the equations of the motion, we make the following assumptions:

1 The gravitational attractions of all other heavenly bodies are neglected, and the mass of Earth is supposed to be much greater than  $m$ . We may then regard the Earth-fixed coordinate system as an inertial frame of reference.

2 The lengths characterizing the oblatenesses both of Earth and of the satellite are assumed to be small with respect to  $R_B$ . The effects of the two oblatenesses may then be considered separately (3). That is, for the purposes of this analysis, it is permissible to assume that Earth is spherically symmetric and homogeneous.

3 The orbit is assumed to be high enough above the surface of Earth so that atmospheric drag is negligible. Further, the influences of solar pressure and other extraneous effects are ignored.

Within these assumptions, the only external forces acting on the satellite are the gravitational attractions of Earth on the two point masses. The acceleration of the satellite's mass center is related to the sum of these two forces by Newton's law

$$m \ddot{\underline{r}}_c = -(1/2)GMm \{ \underline{r}_a/r_a^3 + \underline{r}_b/r_b^3 \} \quad [2]$$

where  $G$  is the gravitational constant and  $M$  the mass of Earth. Substituting Eqs. 1 into Eq. 2 and resolving the resultant equation along the  $i$  and  $j$  axes, we obtain

$$\ddot{r}_c - r_c \dot{\phi}^2 = -(1/2)GM \left[ \frac{r_c + \delta \cos \theta}{r_a^3} + \frac{r_c - \delta \cos \theta}{r_b^3} \right] \quad [3]$$

$$r_c \ddot{\phi} + 2\dot{r}_c \dot{\phi} = -(1/2)GM \delta \sin \theta \{ r_a^{-3} - r_b^{-3} \} \quad [4]$$

It is evident from these equations that the orbital and librational motions of the satellite are indeed coupled, as was noted previously.

Since the gravitational attractions are centrally directed, the moment exerted on the satellite about the center of Earth is zero. Thus the angular momentum of the satellite about that point,  $\underline{H}_B$  say, is a constant. We then have, making use of Eqs. 1

$$\begin{aligned} \underline{H}_B &= (1/2)m \{ (\underline{r}_a \times \dot{\underline{r}}_a) + (\underline{r}_b \times \dot{\underline{r}}_b) \} \\ &= m \{ r_c^2 \dot{\phi} + \delta^2 (\dot{\phi} + \dot{\theta}) \} (\underline{i} \times \underline{j}) \end{aligned} \quad [5]$$

Designating conditions at  $t = 0$  by the subscript  $i$ , we thus require

$$r_{ci}^2 \dot{\phi} + \delta^2 (\dot{\phi} + \dot{\theta}) = r_{ci}^2 \dot{\phi}_i + \delta^2 (\dot{\phi}_i + \dot{\theta}_i) \quad [6]$$

It is convenient to differentiate Eq. 6 and combine it with

Eq. 4 to yield

$$\delta^2 \left[ \ddot{\phi} + \ddot{\theta} - \frac{GM}{2} \frac{r_c}{\delta} \sin \theta (r_a^{-3} - r_b^{-3}) \right] = 0 \quad [7]$$

The system of equations of which we seek a solution then comprises Eqs. 3, 6, and 7. Since this set is of fifth order in the variables  $r_c$ ,  $\phi$  and  $\theta$ , we require initial conditions to be given as follows

$$r_c(0) = r_{ci}, \dot{r}_c(0) = \dot{r}_{ci}, \phi(0) = \phi_i, \dot{\phi}(0) = \dot{\phi}_i, \theta(0) = \theta_i, \dot{\theta}(0) = \dot{\theta}_i \quad [8]$$

Up until now the analysis has closely followed that of Ordway (1), who went on to study the stability of certain orientations of the satellite.<sup>3</sup> Here we are instead concerned with the response of the satellite to rather arbitrary initial conditions over long periods of time. This objective is incompatible with the small-disturbance-from-equilibrium assumptions used in (1).

### Small-Perturbation Approach

The nonlinear character of the set of equations derived above makes an exact solution improbable. However, we have not yet fully exploited the assumption that

$$\delta \ll R_B < r_c \quad [9]$$

In this section, Eqs. 3, 6 and 7 will be reduced to a more tractable set by the introduction of this restriction.

We first note that if we substitute Eq. 1 into Eqs. 3 and 7 and expand  $r_a$  and  $r_b$  about  $r_c$ , we obtain

$$\ddot{r}_c - r_c \dot{\phi}^2 = - \frac{GM}{r_c^2} \left[ 1 + \frac{3}{2} \left( \frac{\delta}{r_c} \right)^2 (3 \cos^2 \theta - 1) + O[(\delta/r_c)^4] \right] \quad [10]$$

$$\delta^2 \left[ \ddot{\phi} + \ddot{\theta} + 3 \frac{GM}{r_c^3} \sin \theta \{ \cos \theta + O[(\delta/r_c)^2] \} \right] = 0 \quad [11]$$

The forms of Eqs. 6 and 10 reveal that the "dumbbellness" of the satellite affects the motion of its mass center by the introduction of terms which are of the order of  $(\delta/r_c)^2$ ; i.e., the terms of zeroth order in this quantity describe the orbit of a point mass at the mass center of the satellite. We thus assume that

$$r_c(t) = \sum_{n=0}^{\infty} r_n(t) \delta^{2n} \\ \phi(t) = \sum_{n=0}^{\infty} \phi_n(t) \delta^{2n} \quad [12]$$

where

$$\delta \equiv \delta/R_B \quad [13]$$

A system of successive approximations may now be set up by assuming the  $r_n$ 's and  $\phi_n$ 's to be all of the same order of magnitude, substituting Eqs. 12 into the equations of motion and the boundary conditions, and equating terms of like order in  $\delta^2$ . So treating Eqs. 6 and 10, we obtain for the zeroth-order set of equations

$$r_0^2 \dot{\phi}_0 = r_{ci}^2 \dot{\phi}_i \quad [14]$$

$$\ddot{r}_0 - r_0 \dot{\phi}_0^2 = -GM/r_0^2 \quad [15]$$

<sup>3</sup> The stability problem has more recently been considered independently by H. R. Rosner (21) and G. M. Schindler (22), who, as did Ordway (1), also take into account the coupling between the orbital and librational motions.

These equations describe the Keplerian orbit of a point mass located at the mass center of the dumbbell.

Similarly, the first-order set of equations is found from Eqs. 6, 10 and 11 to be

$$r_0^2 \dot{\phi}_1 + 2r_0 \dot{\phi}_0 r_1 + R_B^2 (\dot{\phi}_0 + \dot{\theta}) = R_B^2 (\dot{\phi}_i + \dot{\theta}_i) \quad [16]$$

$$\ddot{r}_1 - \dot{\phi}_0^2 r_1 - 2r_0 \dot{\phi}_0 \dot{\phi}_1 =$$

$$\frac{GM}{r_0^3} \left[ 2r_1 - \frac{3}{2} \frac{R_B^2}{r_0} (3 \cos^2 \theta - 1) \right] \quad [17]$$

$$\ddot{\theta} + 3 \frac{GM}{r_0^3} \sin \theta \cos \theta = -\ddot{\phi}_0 \quad [18]$$

In writing Eq. 16, we have noted that the initial conditions on  $r_c$  and  $\phi$ , Eqs. 8, are independent of  $\delta$ , so that

$$r_n(0) = \dot{r}_n(0) = \dot{\phi}_n(0) = 0 \quad [n > 0] \quad [19]$$

It is noteworthy that the equation describing the librational motion, Eq. 18, is completely independent of the perturbations that motion induces in  $r_c$  and  $\phi$ . Thus, if, as in (2 through 9) and in (11 through 17),  $r_c(t)$  and  $\phi(t)$  are specified a priori as the orbital radius and angular velocity of a point mass [in the present nomenclature, as  $r_0(t)$  and  $\dot{\phi}_0(t)$ ], then the solution for  $\theta(t)$  is correct to the order of  $\delta^2$ .

Not only does Eq. 18 decouple from Eqs. 16 and 17, but these latter equations may be rearranged so that the entire first-order set is essentially decoupled. To do so, we multiply Eq. 16 by  $2\dot{\phi}_0/r_0$  and add the resultant relation to Eq. 17, obtaining

$$\ddot{r}_1 + S(\dot{\phi}_0, r_0) r_1 = T(r_0, \dot{\phi}_0, \theta) \quad [20]$$

where

$$S(\dot{\phi}_0, r_0) \equiv 3\dot{\phi}_0^2 - 2GM/r_0^3 \quad [21]$$

$$T(r_0, \dot{\phi}_0, \theta) \equiv - \frac{R_B^2}{r_0} \left[ 2\dot{\phi}_0 [\dot{\theta} - \dot{\phi}_i + \dot{\phi}_0 - \dot{\phi}_i] + \frac{3}{2} \frac{GM}{r_0^3} (3 \cos^2 \theta - 1) \right] \quad [22]$$

Thus, in principle, the problem may be solved sequentially as follows:

1 First, select the initial conditions in accordance with Eqs. 8 and solve Eqs. 14 and 15 for  $r_0(t)$  and  $\dot{\phi}_0(t)$ ; i.e., choose the shape of the unperturbed orbit.

2 Substituting the solution of Eqs. 14 and 15 into Eq. 18, solve for  $\theta(t)$ .

3 Using these results, determine  $r_1$  from Eq. 20. This step is facilitated by the fact that Eq. 20 is linear.

4 Finally, by a simple algebraic manipulation of Eq. 16, solve for  $\dot{\phi}_1$ .

### Special Case: Perturbations of a Circular Orbit

The procedure outlined above underscores the importance of the role played by Eq. 18 in the solution. Before the effects of the dumbbellness of the satellite on its orbit can be calculated, we must determine its librational motion. Unfortunately, except when the unperturbed orbit is circular (4,5) or when the eccentricity of the orbit and the amplitude of the librations are small (2,4,6), it has not been possible to obtain a solution of Eq. 18 in closed form. Otherwise, recourse must be made to numerical techniques (2,7,8).

To be sure, the essential decoupling of the equations of the perturbed motion would simplify the solution in such cases. Nevertheless, the analyticity of the solution for  $\theta$  for arbitrary magnitudes of the librations in the special case where  $r_0$  and  $\dot{\phi}_0$  describe a circular orbit makes a study of that particular situation quite attractive. Thus the remainder

of our analysis will be devoted to a detailed examination of the planar motion of a dumbbell satellite under initial condition which would yield a circular orbit except for the mass separation.

For this case,  $r_0$  is a constant, and, from Eq. 14, so is  $\dot{\varphi}_0$ . For simplicity, let

$$\begin{aligned} r_0(t) &= R \equiv r_{ci} \\ \dot{\varphi}_0(t) &= \Omega \equiv \dot{\phi}_i \end{aligned} \quad [23]$$

Then, from Eq. 15

$$\Omega^2 = GM/R^3 \quad [24]$$

Noting that  $\varphi_0 = \Omega t$ , we shall use this quantity as a dimensionless time variable, denoting derivatives with respect to  $\varphi_0$  by primes; i.e.

$$(\quad)' \equiv d(\quad)/d\varphi_0 \quad [25]$$

### Librational Motion

We must first consider the motion of the satellite about its mass center. In view of Eqs. 23, 24 and 25, Eq. 18 now simplifies to

$$\theta'' + 3 \sin \theta \cos \theta = 0 \quad [26]$$

Multiplying through by  $2\theta'$  and integrating, we obtain

$$\theta'^2 + 3 \sin^2 \theta = \theta_o'^2 \quad [27]$$

where  $\theta_o'$  is the value of  $\theta'$  at  $\theta = 0$ .

The solution of Eq. 27 is expressible in terms of elliptic functions (18), the exact form of the solution depending on  $\theta_o'$ . If we arrange our time scale so that  $\theta_i = 0$  and  $\theta_o' = \theta_i'$ , we have

$$\begin{aligned} \sin \theta &= (\theta_i' \sqrt{3}) \operatorname{sn} \sqrt{3} \varphi_0 & [|\theta_i'| < \sqrt{3}] \\ &= \operatorname{sn} \theta_i' \varphi_0 & [|\theta_i'| > \sqrt{3}] \end{aligned} \quad [28]$$

Here the modulus  $k$  of the elliptic functions is given by

$$\begin{aligned} k &= |\theta_i'|/\sqrt{3} & [|\theta_i'| < \sqrt{3}] \\ &= \sqrt{3}/|\theta_i'| & [|\theta_i'| > \sqrt{3}] \end{aligned} \quad [29]$$

In Fig. 2, time histories of the librational motion of the satellite have been plotted for various values of  $|\theta_i'|$ . When this parameter is less than  $\sqrt{3}$ , the motion of the satellite is oscillatory about  $\theta = 0$ ; while for  $|\theta_i'| > \sqrt{3}$ , the dumbbell tumbles end over end. In either case, the motion is periodic, with the period  $T$  being

$$\begin{aligned} T &= (4/\sqrt{3} \Omega) K(k) & [|\theta_i'| < \sqrt{3}] \\ &= (4/\theta_i' \Omega) K(k) & [|\theta_i'| > \sqrt{3}] \end{aligned} \quad [30]$$

where  $K(k)$  is the complete elliptic integral of the first kind. This period is equal to the orbital period,  $2\pi/\Omega$ , for two values of  $|\theta_i'|$ ; viz., 1.66675 and 1.78794.

In the degenerate case  $\theta_i' = \pm\sqrt{3}$ , the period of the motion is infinite, so that the dumbbell asymptotically approaches the horizontal position,  $\theta = \pm\pi/2$ . Taking the limit of Eqs. 28 and 29, we may write for this case

$$\sin \theta = \tanh \theta_i' \varphi_0 \quad [|\theta_i'| = \sqrt{3}] \quad [31]$$

Curves similar to those presented in Fig. 2 were plotted previously by W. B. Klemperer (5). In his discussion of the equations governing these curves, however, there appears to be a misprint. Specifically, for  $|\theta_i'| > \sqrt{3}$ ,  $\theta_i t$  is related to

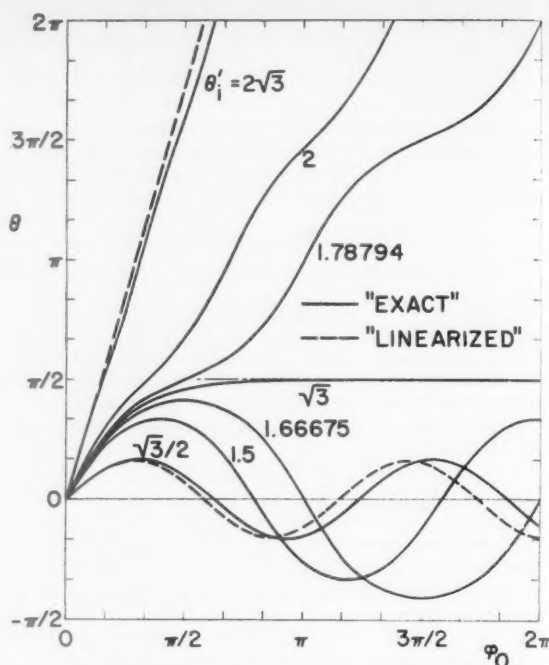


Fig. 2 Time histories of planar librational motion of dumbbell satellite in nearly circular orbit

$\theta$  with the complete elliptic integral; viz.

$$\theta_i' \varphi_0 = F(\pi/2, \sqrt{3}/|\theta_i'|) \quad [32]$$

To correct the discussion, it is necessary to replace the argument  $\pi/2$  by  $\theta$ . Eqs. 32 and 28 are then equivalent (19).

When  $\theta_i'$  is very small or very large, Eq. 28 may be approximated by

$$\begin{aligned} \theta &\approx (\theta_i'/\sqrt{3}) \sin \sqrt{3} \varphi_0 & [|\theta_i'| \ll \sqrt{3}] \\ &\approx \theta_i' \varphi_0 & [|\theta_i'| \gg \sqrt{3}] \end{aligned} \quad [33]$$

These approximate ("linearized") formulas are compared in Fig. 2 with the exact relations given by Eq. 28 for appropriately large or small values of  $\theta_i'$ . It is seen that although the shapes of the exact and approximate curves are quite close, there is a small discrepancy in the period of the motion, which would lead to rather large cumulative errors after a few revolutions of the satellite.

### Perturbations Induced in the Motion of the Mass Center

We now turn to the determination of the influence of the librations of the satellite on the motion of its mass center. As pointed out previously, we must first solve Eq. 20 for  $r_1$ , and then use that result to determine  $\varphi_1'$  from Eq. 16; which, in view of Eqs. 23, 25, and 27, may be written

$$(R/R_B)^2 \varphi_1' = \theta_i' \{1 - [1 - (3/\theta_i'^2) \sin^2 \theta]^{1/2}\} - 2(Rr_1/R_B^2) \quad [34]$$

We also note that from Eqs. 23 to 29, Eqs. 21 and 22 become

$$S = \Omega^2 \quad [35]$$



$$\begin{aligned}
T &= -\frac{R_b^2}{R} \Omega^2 \left[ 3 - 2\theta_i'(1 - \epsilon n \sqrt{3} \varphi_0) - \frac{3\theta_i'^2}{2} \operatorname{sn}^2 \sqrt{3} \varphi_0 \right] & [|\theta_i'| < \sqrt{3}] \\
&= -\frac{R_b^2}{R} \Omega^2 \left[ 3 - 2\theta_i'(1 - dn \theta_i' \varphi_0) - \frac{3\theta_i'^2}{2} \operatorname{sn}^2 \sqrt{3} \varphi_0 \right] & [|\theta_i'| > \sqrt{3}]
\end{aligned} \quad [36]$$

Eq. 20 is thus seen to reduce to the equation of a simple harmonic oscillator with a periodic forcing function related to the librational motion.

We now introduce a new dimensionless variable

$$\rho(\varphi_0) = \frac{Rr_1}{R_b^2} + 3 - 2\theta_i' \quad [37]$$

Eq. 20 may then be written

$$\rho'' + \rho = U(\varphi_0) \quad [38]$$

where the forcing function  $U(\varphi_0)$  is given by

$$\begin{aligned}
U(\varphi_0) &= -2\theta_i' \epsilon n \sqrt{3} \varphi_0 + \frac{3\theta_i'^2}{2} \operatorname{sn}^2 \sqrt{3} \varphi_0 & [|\theta_i'| < \sqrt{3}] \\
&= -2\theta_i' dn \theta_i' \varphi_0 + \frac{9}{2} \operatorname{sn}^2 \theta_i' \varphi_0 & [|\theta_i'| > \sqrt{3}]
\end{aligned} \quad [39]$$

The initial conditions on  $\rho(\varphi_0)$  are, from Eqs. 19 and 37

$$\rho(0) = 3 - 2\theta_i', \quad \rho'(0) = 0 \quad [40]$$

Following the method of variation of parameters, we assume the solution of Eq. 38 to be of the form

$$\rho(\varphi_0) = u(\varphi_0) \cos \varphi_0 + v(\varphi_0) \sin \varphi_0 \quad [41]$$

subject to the restriction

$$0 = u'(\varphi_0) \cos \varphi_0 + v'(\varphi_0) \sin \varphi_0 \quad [42]$$

An additional relation for  $u'(\varphi_0)$  and  $v'(\varphi_0)$  is obtained by substituting Eq. 41 into Eq. 38. Combining this relation with Eq. 42, we obtain

$$\begin{aligned}
u'(\varphi_0) &= -U(\varphi_0) \sin \varphi_0 \\
v'(\varphi_0) &= U(\varphi_0) \cos \varphi_0
\end{aligned} \quad [43]$$

It was not found possible to integrate Eq. 43 in closed form. However, using Fourier series expansions for the elliptic functions (20), we may write for  $U(\varphi_0)$

$$\begin{aligned}
U(\varphi_0) &= -\frac{4\pi\sqrt{3}}{K} \frac{|\theta_i'|}{\theta_i'} \left[ \sum_{m=0}^{\infty} \frac{q^{m+1/2}}{1+q^{2m+1}} \cos \omega_m \varphi_0 - \frac{3}{8\theta_i'} \sum_{m=0}^{\infty} \frac{q^{m+1/2}}{1+q^{2m+1}} \{3 + \theta_i'^2 - \omega_m^2\} \sin \omega_m \varphi_0 \right] & [|\theta_i'| < \sqrt{3}] \\
&= -\frac{4\pi\theta_i'}{K} \left[ \frac{1}{4} + \sum_{n=0}^{\infty} \frac{q^{n+1}}{1+q^{2n+2}} \cos \omega_n \varphi_0 - \frac{\sqrt{3}}{8} \sum_{n=0}^{\infty} \frac{q^{p+1/2}}{1+q^{2p+1}} \{3 + \theta_i'^2 - \omega_p^2\} \sin \omega_p \varphi_0 \right] & [|\theta_i'| > \sqrt{3}]
\end{aligned} \quad [44]$$

where

$$\begin{aligned}
\omega_m &= (m + 1/2) \pi \sqrt{3}/K \\
\omega_n &= (n + 1) \pi \theta_i'/K \\
\omega_p &= (p + 1/2) \pi \theta_i'/K
\end{aligned} \quad [45]$$

and  $q$  is Jacobi's nome

$$q(k) = e^{-\pi K(\sqrt{1-k^2})/K(k)} \quad [46]$$

It is seen from Eqs. 30, 44 and 45 that the fundamental frequency of the forcing function  $U(\varphi_0)$  is simply the librational frequency.

Substituting Eq. 44 into Eq. 43 and integrating term by term, we find series expressions for  $u(\varphi_0)$  and  $v(\varphi_0)$ . After combining these results with Eqs. 37 and 41, we finally obtain for  $r_1$

$$\frac{Rr_1}{R_b^2} = \{3 - 2\theta_i'\} \{\cos \varphi_0 - 1\} + \chi(\varphi_0) + \sigma(\varphi_0) \quad [47]$$

where  $\chi$  is a cosine series

$$\chi(\varphi_0) = \frac{4\pi\sqrt{3}}{K} \frac{|\theta_i'|}{\theta_i'} \sum_{m=0}^{\infty} \frac{q^{m+1/2}}{1+q^{2m+1}} \times \left[ \frac{\cos \omega_m \varphi_0 - \cos \varphi_0}{\omega_m^2 - 1} \right] \quad [|\theta_i'| < \sqrt{3}]$$

$$\chi(\varphi_0) = \frac{4\pi\theta_i'}{K} \sum_{n=0}^{\infty} \frac{q^{n+1}}{1+q^{2n+1}} \left[ \frac{\cos \omega_n \varphi_0 - \cos \varphi_0}{\omega_n^2 - 1} \right] + \frac{4\pi\theta_i'}{K} (\cos \varphi_0 - 1) \quad [|\theta_i'| > \sqrt{3}] \quad [48]$$

and  $\sigma$  a sine series

$$\sigma(\varphi_0) = -\frac{3\pi\sqrt{3}}{2|\theta_i'|K} \sum_{m=0}^{\infty} \frac{q^{m+1/2}}{1-q^{2m+1}} \times \{3 + \theta_i'^2 - \omega_m^2\} \left[ \frac{\sin \omega_m \varphi_0 - \omega_m \sin \varphi_0}{\omega_m^2 - 1} \right] \quad [|\theta_i'| < \sqrt{3}]$$

$$= -\frac{\theta_i'\pi\sqrt{3}}{2K} \sum_{p=0}^{\infty} \frac{q^{p+1/2}}{1-q^{2p+1}} \times \{3 + \theta_i'^2 - \omega_p^2\} \left[ \frac{\sin \omega_p \varphi_0 - \omega_p \sin \varphi_0}{\omega_p^2 - 1} \right] \quad [|\theta_i'| > \sqrt{3}] \quad [49]$$

Although this solution is not in closed form, the series  $\chi$  and  $\sigma$  are usually quite rapidly convergent, so that only the first few terms need to be considered for computational purposes. For as shown in Fig. 3,  $q$  is usually quite small except for  $|\theta_i'|$  near  $\sqrt{3}$ . In the limiting case  $|\theta_i'| = \sqrt{3}$ ,  $\sigma$  does not converge. However, since this situation is highly unstable to perturbations in  $\theta_i'$  (see Fig. 2), little generality is lost by this restriction of our solution to  $|\theta_i'| \neq \sqrt{3}$ .

Time histories of  $r_1$  and  $\varphi_1'$  have been calculated from Eqs. 34 and 45 to 49 for two typical values of  $\theta_i'$ , one of which corresponds to a tumbling motion of the satellite. The results, shown in Fig. 4, reflect the facts that the equation governing the behavior of  $r_1$  (and hence, from Eq. 34, that of  $\varphi_1'$ ) is that of a simple harmonic oscillator with a periodic forcing function, and that the forcing function is composed of an infinite number of harmonics.

## Resonance

Now the frequencies of these harmonics are integral multiples of the librational frequency. From Eq. 30, depending on the value of  $\theta_i'$ , the frequency of the librations in cycles per orbit may vary from 0 to  $\sqrt{3}$  (for  $|\theta_i'| < \sqrt{3}$ ) or to  $\infty$  (for  $|\theta_i'| > \sqrt{3}$ ). It is then evident that there are an infinite number of values of  $\theta_i'$  for which one of these harmonics has a frequency equal to the "natural" frequency of  $r_1$ , which from Eq. 38, is one cycle per orbital period. In such cases, we must anticipate a resonance phenomenon. Specifically, if one of the  $\omega$ 's ( $\omega_N$ , say) in Eqs. 48 and/or 49 is unity, then the  $N$ th term of the series  $\chi$  and/or  $\sigma$  must be revised as follows

$$\frac{\cos \omega_N \varphi_0 - \cos \varphi_0}{\omega_N^2 - 1} \rightarrow -\frac{1}{2} \varphi_0 \sin \varphi_0$$

$$\frac{\sin \omega_N \varphi_0 - \omega_N \sin \varphi_0}{\omega_N^2 - 1} \rightarrow \frac{1}{2} \{ \varphi_0 \cos \varphi_0 - \sin \varphi_0 \} \quad [50]$$

The inclusion of these secular terms (terms proportional to  $\varphi_0$ ) in the results for  $r_1$  and  $\varphi_1'$  means that in those cases where such modifications of Eqs. 48 and/or 49 are necessary, the first-order perturbations in the orbital motion of the satellite due to its dumbbellness grow indefinitely with increasing time. But when  $r_1$  and  $\varphi_1'$  become significantly larger than  $r_0$  and  $\varphi_0'$ , one of the basic assumptions of the successive-approximation technique used herein is violated. Thus, the occurrence of resonance in  $r_1$  and  $\varphi_1'$  does not mean that the satellite will oscillate so wildly about its unperturbed orbit, that it will eventually be removed from the orbit by atmospheric drag. Rather, it is indicative of a breakdown in the approach employed in this analysis.

From the above discussion, for the nonlinear effects which undoubtedly accompany this "resonance" to be important,

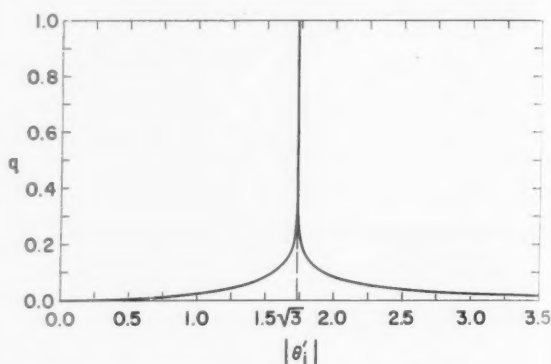


Fig. 3 Variation of Jacobi's nome with  $\theta_i'$

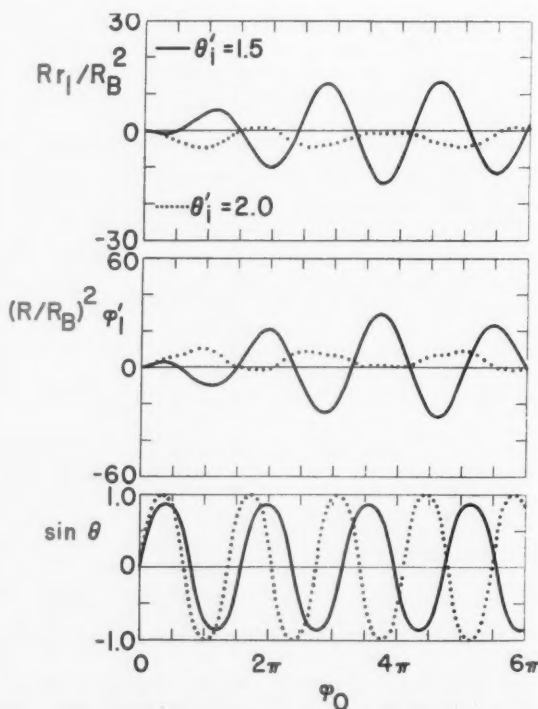


Fig. 4 Time histories of perturbations in planar motion of mass center of dumbbell satellite in nearly circular orbit; non-resonant librational frequency

it is necessary that the librational frequency be less than or equal to the orbital frequency. Thus, the critical values of  $|\theta'_i|$  all lie between 1.66675 and 1.78794. The most interesting cases are the end points of this range, when the period of the librations is  $2\pi/\Omega$ . The first-order perturbations induced in the orbital motion of the satellite are shown for two of these cases in Fig. 5.

## Conclusions

The purpose of this investigation was to study the coupling between the planar motions of and about the mass center of an asymmetric satellite. Although the analysis was specialized to the case of an idealized dumbbell, it can be generalized quite readily to cover satellites of more realistic shape. For as derived by Frick and Garber (2), the equations of the planar motion of such a satellite are identical in form with those used in the present analysis. If the motion is not planar, however, the situation is considerably more complex, regardless of the form of the satellite.

The fundamental assumption of the analysis was that the ratio of the length of the dumbbell to the radius of Earth was small enough that the solution could be expanded in powers of this parameter, all the coefficients of the series supposedly being of the same order of magnitude. The equations of motion were treated by successive approximations, with the zeroth-order equations describing the motion of a point mass at the mass center of the satellite. The first-order set of equations is essentially decoupled, i.e., they can be solved sequentially. Specifically, the motion of the satellite about its mass center is found to be independent of the perturbations induced in the motion of the mass center. The perturbations in the orbital radius can be found by solving a linear second-order differential equation which contains a periodic forcing term related to the librational motion. This result may then be used to find the perturbed angular velocity of the satellite algebraically.

That the librational motion of the satellite depends on only the unperturbed orbital motion justified the many previous analyses of satellite librations (2 through 9, 11 through 17) in which the induced perturbations in the orbit were not considered. More important for the purposes of this study, however, is the essential decoupling of the entire set of equations for the first-order perturbations induced by the dumbbellness of the satellite.

In the special case where the unperturbed orbit is circular, analytic solutions for the perturbed motion can be obtained. The librational motion is found in terms of elliptic functions, while the orbital radius and angular velocity are expressed in the form of Fourier series. Except for one degenerate case, which is highly unstable to perturbations in the initial conditions, these series may be truncated readily.

Ordinarily, the difference between the perturbed and unperturbed orbits is quite small. For certain frequencies of the librations, however, a resonance phenomenon occurs. That is, secular terms appear in the results for the perturbed orbital radius and angular velocity, so that it would appear that the satellite would oscillate with ever increasing amplitude about the unperturbed orbit. Actually, this is indicative of a breakdown in the assumptions of the analysis and of the importance of nonlinear effects for these cases. But when a linearized theory says "infinite," it is usually safe to read "large, but finite." Thus this result suggests that the interaction between the several degrees of freedom of a satellite can be quite important, and deserves considerably more careful consideration than has been given it in the past.

## Acknowledgment

The author is indebted to Donald Earl Ordway, Head, Aerophysics Section, for suggesting the problem; and to Richard Lesser of the Cornell University Computing Center, for programming and carrying out the necessary calculations.

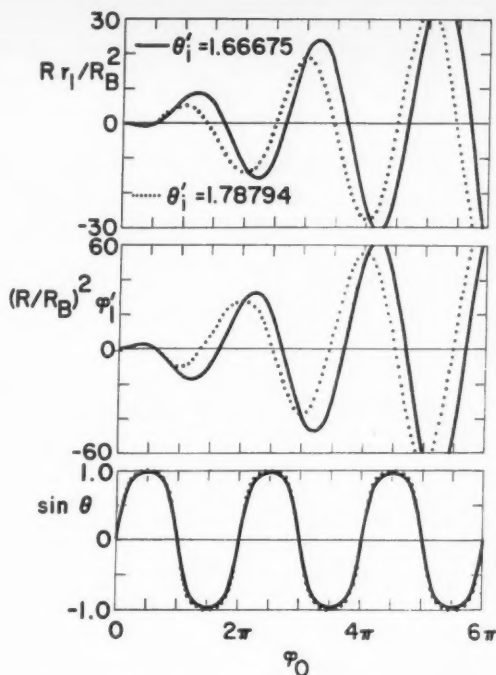


Fig. 5 Time histories of perturbations in planar motion of mass center of dumbbell satellite in nearly circular orbit; resonant librational frequency

## Nomenclature

$cn, dn, sn$	= Jacobian elliptic functions
$F, K$	= incomplete and complete elliptic integrals of first kind, respectively
$G$	= gravitational constant
$H_B$	= angular momentum of satellite about mass center of Earth
$i, j$	= unit vectors in directions of increasing $r_c$ and $\phi$ , respectively
$k$	= modulus of elliptic functions
$m$	= mass of satellite
$M$	= mass of Earth
$q$	= Jacobi's nome; see Eq. 46
$r_{a,b}$	= radius vectors from mass center of Earth to point masses of dumbbell
$r_c$	= radius vector from mass center of Earth to mass center of satellite
$r_n$	= coefficient of $\delta^{2n}$ in power-series expansion of $r_c$
$R$	= radius of unperturbed circular orbit
$R_B$	= radius of Earth
$S, T$	= see Eqs. 21 and 22
$u, v$	= see Eqs. 41
$U$	= forcing function in equation for $r_1$ ; see Eq. 39
$\delta$	= length of sat. llite
$\bar{\delta}$	= $\delta/R_B$
$\theta$	= angle between axis of dumbbell and $r_c$
$\rho$	= dimensionless parameter related to $r_1$ ; see Eq. 37
$\sigma$	= sine series; see Eq. 49
$\phi$	= angle describing sweep of $r_c$ in plane of motion
$\phi_n$	= coefficient of $\delta^{2n}$ in power-series expansion of $\phi$
$\chi$	= cosine series; see Eq. 48
$\omega_m, n, p$	= frequency of $m^{th}, n^{th}$ , or $p^{th}$ harmonic in forcing function $U$ ; cycles per orbit
$\Omega$	= angular velocity of satellite's mass center in unperturbed circular orbit
$( )$	= time derivative of $( )$
$( )'$	= derivative of $( )$ with respect to $\varphi_0$

## Subscripts

$i$  = at time  $t = 0$   
 $o$  = at  $\theta = 0$

## References

- 1 Ordway, D. E., "The Two-Dimensional Dumbbell Satellite," NAS-ARDC Special Study at Woods Hole, Mass., COM1-T25, Aug. 28, 1958, also "Coupled Planar Motion of a Dumbbell Satellite," IAS Aerospace Forum II, January 1961, and THERM, Inc., TAR-TN 611, June 1961.
- 2 Frick, R. H. and Garber, T. B., "General Equations of Motion of a Satellite in a Gravitational Gradient Field," Rand Corp. Res. Mem. RM-2527, Dec. 9, 1959.
- 3 Doolin, B. F., "Gravity Torque on an Orbiting Vehicle," NASA TN D-70, September 1959.
- 4 Beletskiy, V. V., "The Libration of a Satellite," *Izvestiya Akademii Nauk SSSR, Mekhanika*, no. 3, Academy of Sciences, USSR (Moscow), 1959 (translated as NASA TT F-10, May 1960).
- 5 Klemperer, W. B., "Satellite Librations of Large Amplitude," *ARS JOURNAL*, vol. 30, no. 1, January 1960, pp. 123-124.
- 6 King, J. P., Jr., "Motion of an Orbiting Vehicle About Its Center of Mass Due to the Gravity Gradient," presented at ARS Semi-Annual Meeting, Los Angeles, Calif., May 9-12, 1960 (ARS preprint 1222-60).
- 7 Stoker, T. A. J. and Vachino, R. F., "The Two-Dimensional Librations of a Dumbbell-Shaped Satellite in a Uniform Gravitational Field," Thesis, USAF Inst. of Tech., Wright-Patterson Air Force Base, Ohio.
- 8 Robinson, A. C., "On the Three-Dimensional Librations of a Dumbbell-Shaped Satellite Over an Oblate Earth," WCLJY Internal Memo 58-54, Wright-Patterson Air Force Base, Ohio, 1958.

- 9 Klemperer, W. B. and Baker, R. M. L., Jr., "Satellite Librations," *Astronautica Acta*, vol. 3, fasc. 1, pp. 16-27, and vol. 3, fasc. 3, 1957.
- 10 Roberson, Robert E., "Gravitational Torque on a Satellite Vehicle," *J. Franklin Inst.*, vol. 265, no. 1, January 1958, pp. 13-22.
- 11 Davis, W. R., "Determination of a Unique Attitude for an Earth Satellite," *Proc. Amer. Astronaut. Soc.*, 4th Annual Meeting, N. Y., January 1958, pp. 10-1 to 10-15. (AAS reprint 58-10).
- 12 Schindler, G. M., "On Satellite Librations," *ARS JOURNAL*, vol. 29, no. 5, May 1959, pp. 368-370.
- 13 Gillespie, W., Jr., Eide, D. G. and Churgin, A. B., "Some Notes on Attitude Control of Earth Satellite Vehicles," NASA TN D-40, December 1959.
- 14 Baker, R. M. L., Jr., "Librations on a Slightly Eccentric Orbit," *ARS JOURNAL*, vol. 30, no. 1, January 1960, pp. 124-126.
- 15 Baker, R. M. L., Jr., "Plane Librations of a Prolate Ellipsoidal Shell," *ARS JOURNAL*, vol. 30, no. 1, January 1960, pp. 126-128.
- 16 Nidey, R. A., "Gravitational Torque on a Satellite of Arbitrary Shape," *ARS JOURNAL*, vol. 30, no. 2, February 1960, pp. 203-204.
- 17 Doolin, B. F. and Triplett, W. C., "The Influence of Gravity on the Angular Motion of an Earth Satellite," *Proc. Amer. Astronaut. Soc.*, 6th Annual Meeting, N. Y., Jan. 18-21, 1960 (AAS preprint 60-34).
- 18 Synge, J. L. and Griffith, B. A., *Principles of Mechanics*, McGraw-Hill Book Co., Inc., N. Y., 1949, pp. 370-371.
- 19 Byrd, P. F. and Friedman, M. D., *Handbook of Elliptic Integrals for Engineers and Physicists*, Springer-Verlag, Berlin, 1954, p. 18.
- 20 Byrd, P. F. and Friedman, M. D., op. cit., pp. 303-306.
- 21 Rosner, H. R., "Motions of a Dumbbell Satellite," *Amer. Astronaut. Soc.*, Third Annual West Coast Meeting, Seattle, Wash., Aug. 8-11, 1960. (AAS preprint 60-70).
- 22 Schindler, G. M., "Satellite Librations in the Vicinity of Equilibrium Solutions," *Astronautica Acta*, vol. 5, fasc. 5, 1960, pp. 233-240.

# Controlled Rendezvous of Orbiting Space Stations

NORMAN S. POTTER<sup>1</sup>

Maxson Electronics Corp.  
 New York, N. Y.

The performance and optimization of satellite borne terminal acquisition and associated external gross guidance systems for effecting the rendezvous of orbiting space stations is investigated. Subject to very weak constraints, a broadly applicable analysis of the influence of the relative trajectories and the error in the information output of the vectoring and control environment is developed. The distribution of search effort, which reflects detection performance and data handling subsystem requirements, and the integration of the composite system, are discussed. The specification of the optimal search volume which maximizes the product of  $P_C$ , the probability of containment of the other orbiting body in the search volume, and  $P_D$ , the probability of terminal acquisition if it is so contained, is accomplished. As a special case of a general search theorem which is demonstrated, it is shown that if the relative angular positional error is Gaussian, with equal standard deviations in elevation and azimuth, and the terminal acquisition system interrogates the designated space volume at a uniform rate dictated by signal integration requirements, the composite acquisition probability is maximized by adjusting the search volume in such a manner that  $P_C = P_D$ . The substantial improvement in the acquisition probability resulting from the use of the search program that is so determined is quantitatively set forth. The optimal interrogation of the space volume designated to the terminal acquisition system when the search rate is data handling subsystem bandwidth limited is discussed, and a related theory developed and applied.

Presented at the ARS 15th Annual Meeting, Washington, D. C., Dec. 5-8, 1960.

<sup>1</sup> Manager, Systems Analysis.



THE RENDEZVOUS of space stations is dependent upon the ability of a vehicle-borne terminal control system to successfully detect and acquire in track other orbital bodies of interest at relative ranges that are commensurate with the characteristically high closure rates and other kinematic constraints of space operations. Its presence as a component of the composite guidance system is made necessary by the vectoring inadequacies of a distant ground-control environment, and its potential ability to accomplish its appointed task is critically dependent upon the effective integration of the two systems. Beyond providing a theoretic basis for the quantitative appraisal of terminal acquisition system performance, the analysis set forth herein seeks to introduce techniques which maximize the probability of effecting an acquisition without making undue demands for extensive commitment of a large bandwidth data handling subsystem, or extravagant energy consumption on the part of the sensory apparatus. In the main, the methods to be developed will be seen to be founded upon the full utilization of prior information, and the most economical allocation of the available search effort.

## Kinematic Preliminaries

### Fundamental Concepts

Elementary statistical arguments suffice to indicate the nature of the dependence of the acquisition probability upon the closure rate of the orbital vehicles. A more extensive discussion of important related considerations, such as the influence of data handling subsystem logic in discriminating against extraneous or spurious signals, is set forth in (1).<sup>2</sup> Let it be assumed for the present that the composite acquisition system, comprising a sensory apparatus and detector, periodically samples some portion of the overall surrounding space at a uniform rate. Then  $\psi_\lambda$ , the likelihood of acquisition on the  $\lambda$ th trial, may be written

$$\psi_\lambda \equiv \psi(R + \delta + (n - \lambda)vt) \quad [1]$$

in which  $R$  denotes the relative range at which the cumulative probability  $P$  of the occurrence is required,  $t$  is the search period, and  $v$  the relative range rate. The cumulative probability is of interest rather than that of success on a given interrogation since the most meaningful measure of operational performance is the probability of effecting the necessary acquisition by some critical minimal range by which some action must be accomplished, such as the initiation of the terminal control phase. The quantity  $\delta$  is a small range increment introduced to reflect the fact that, geometrically, the last scan preceding the attainment of the separation  $R$  may not occur at  $R$  but, with equiprobability, may lie anywhere within the half open interval  $[R, vt + R)$ . Accordingly, since  $P$  measures the likelihood of satisfying the detection criteria at least once during the sequence of  $n$  interrogations

$$P = 1 - \prod_{\lambda=1}^n (1 - \psi_\lambda)$$

$$\text{or} \quad \ln(1 - P) = \sum_{\lambda=1}^n \ln(1 - \psi_\lambda) \quad [2]$$

Denoting weighted means with respect to  $\delta$  by a superscript bar, it is shown in the above cited reference that  $P$  and  $\bar{P}$  may be used interchangeably with negligible error in a rapidly sampling system and, more specifically,  $\ln(1 - \bar{P}) \sim \ln(1 - P)$ . However

$$\ln(1 - P) = \frac{1}{vt} \sum_{\lambda=1}^n \int_0^{vt} \ln(1 - \psi[R + \delta + (n - \lambda)vt]) d\delta \quad [3]$$

<sup>2</sup> Numbers in parentheses indicate References at end of paper.

which, after the change of variables  $\rho = (R + (n - \lambda)vt) = \delta$ , assumes the form

$$\begin{aligned} \ln(1 - P) &= \frac{1}{vt} \sum_{\lambda=1}^n \int_{R+(n-\lambda)vt}^{R+(n-\lambda+1)vt} \ln(1 - \psi(\rho)) d\rho \\ &= \frac{1}{vt} \int_R^{R+nv} \ln(1 - \psi(\rho)) d\rho \quad [4] \end{aligned}$$

yielding, in conjunction with the above observations upon the degree of approximation that is involved

$$\begin{aligned} P &= 1 - \exp \left[ \frac{1}{vt} \int_R^{R+\Delta} \ln(1 - \psi(\rho)) d\rho \right] \\ &= 1 - \exp[-F(R, \Delta, t)/v] \quad [5] \end{aligned}$$

where  $\Delta = nv$  is the relative distance traversed during the search interval. Generally,  $\psi(\rho)$  is of exponential form and, particularly in the presence of the moderate signal amplitudes that will frequently obtain in operational practice, converges rapidly to zero with increasing  $\rho$ . It may be assumed that attempts to accomplish a terminal acquisition will be initiated at ranges that are effectively indefinitely great, for which  $\psi(\rho)$  is essentially null. Accordingly, if  $P_x$  denotes the cumulative probability of acquisition by separation  $x$  that obtains if search commences at the point at infinity,  $P = 1 - (1 - P_x)/(1 - P_{x+\Delta})$  and, from  $P_{x+\Delta} \sim 0$ , one must have  $P \sim P_x$ .

Momentarily setting aside the obvious consideration that the minimal admissible relative range  $R$  at acquisition is ordinarily a monotonically increasing function of  $v$ , a further refinement that will be investigated presently, from the above

$$P = 1 - (1 - P_0)^{v_0/v} \quad [6]$$

where  $P_0$  denotes some reference value of  $P$  obtained at closure rate  $v_0$ . Two cases of interest are the variation of  $P$  with the relative approach bearing angle, and the orbital altitude.

With respect to the first, assuming an essentially coplanar terminal situation so as to facilitate the expository discussion, it is clear that, as the bearing angle  $\beta$  increases from the anti-parallel trajectory situation, the absolute value of the closure rate declines rapidly, leading thereby to a substantial and progressive growth in  $P$  from  $P_0$  corresponding to  $\beta = 0$ . If the orbital velocity of the vehicles is  $v$ ,  $v = 2v \cos \beta$  for  $0 \leq \beta < \pi/2$ , so that

$$P = 1 - (1 - P_0)^{\sec \beta} \quad [7]$$

which is displayed in Fig. 1, as is the relative variation of  $v(\beta)$ . The contours confirm the dictates of superficial reasoning to the effect that a hypervelocity, forward hemisphere approach is a far less rational choice than is a relatively low closure rate approach from the after hemisphere. Whereas marginally effective performance at  $\beta = 0$ , indicated by the use of  $P_0 = 0.5$  for illustrative purposes, rapidly becomes essentially unity for even modest bearing angles, it follows, conversely, that an acquisition system which is not essentially perfect at large bearing angles will not have any operational utility whatsoever for  $\beta$  moderate to small.

To appraise the dependence of system performance on orbital altitudes circular orbits will be hypothesized so as to facilitate the illustrative analytic argument. Equating the centrifugal and gravitational forces

$$\begin{aligned} \frac{v_0}{v} &= \sqrt{\left(1 + \frac{h}{r}\right)} \\ P &= 1 - (1 - P_0)^{\sqrt{(1+\rho)}} \quad [8] \end{aligned}$$

where  $h$  and  $\rho$  denote respectively the altitude and its value in multiples of the Earth's radius  $r$ , and  $v_0$  is the orbital velocity in the vicinity of the Earth's surface. Both functions are displayed in Fig. 1. The magnification of the effect of the moderate monotonic decline of  $v(h)$  by the exponential form of  $P$  is clear. The enhancement of the performance of

an initially marginal system is substantial as the interesting case of the stationary orbit is approached. However, the indicated improvement is seen to be conservative when the

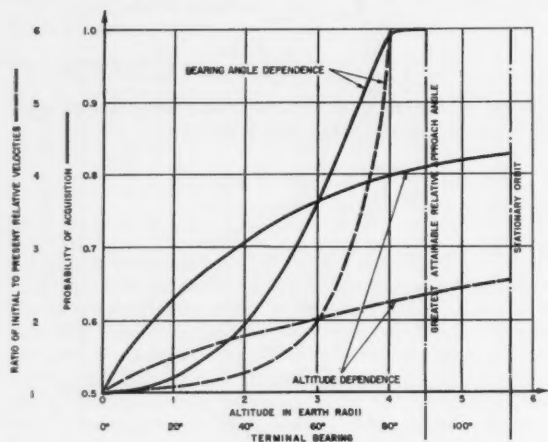


Fig. 1 Simplified dependence of acquisition probability on relative closure rate

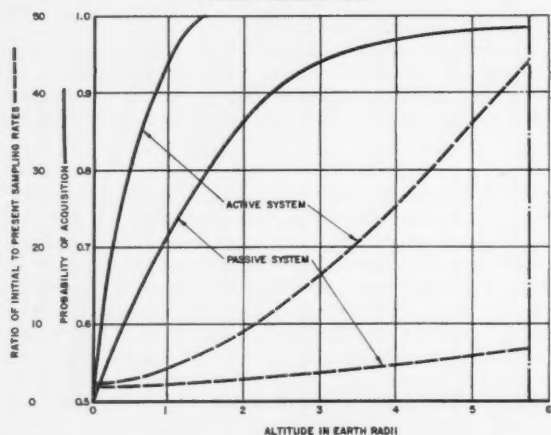


Fig. 2 Attainable information rate and acquisition probability as functions of orbital altitude

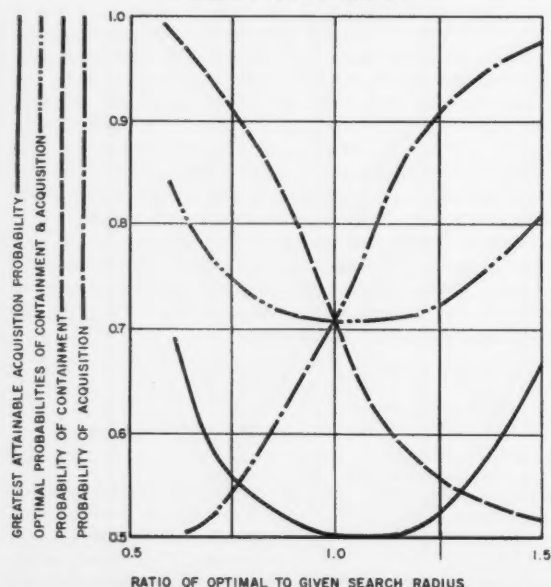


Fig. 3 Search optimization with moderate signal amplitudes

dependence of the required acquisition range upon the closure rate is introduced, as will now be done.

### System Requirements and Performance as Functions of the Orbital Altitude

For purposes of discussion, the very frequently applicable assumption that  $R = vT$ , where  $T$  is a constant determined by vehicle kinematic and data handling system time constants, will be made. Further, to facilitate acquisition, the sampling rate may be adjusted so as to yield some desired information rate into the data handling subsystem in the critical region. For example, all else fixed, by adjusting the signal integration time and therefore the sampling rate, the minimal mean time between successive positive interrogations, or the greatest attainable probability of achieving a confirmatory signal in a specified time interval, may be achieved. As shown in (1), with rapid amplitude fluctuation of the signal source, the first is yielded by arranging  $t$  in such a manner that  $\psi = e^{-1}$ , and the second by  $\psi = 0.5$ . Assuming an idealized integrator that operates upon signals that fluctuate substantially less rapidly than does the random noise input, the signal to noise amplitude ratio may be taken as proportional to  $\sqrt{t}$ , whence  $t \propto v^2$  where  $v$  is 2 or 4 according as the sensor is passive or active.

Lastly, noting that  $\psi \equiv \psi(\rho^*/ts)$  for any real system, where  $\rho$  is the instantaneous relative range and  $S$  is the mean signal power density

$$P = 1 - \exp \left[ \frac{1}{vt} \int_{v_t}^{\infty} \ln(1 - \psi(\rho^*/ts)) d\rho \right] \\ = 1 - \exp \left[ \frac{s^{1/v}}{vt^{1-1/v}} \int_{T/(LS)^{1/v}}^{\infty} \ln(1 - \psi(\rho^*)) d\rho \right] \quad [9]$$

Writing  $t = kv^2$ , where  $k$  is a constant that is a function of operational and system parameters, and using the same notation as before, one obtains

$$P = 1 - \exp \left[ \frac{s^{1/v}}{v^2 k^{1-1/v}} \int_{T/(Sk)^{1/v}}^{\infty} \ln(1 - \psi(\rho^*)) d\rho \right] \\ = 1 - \exp [-F(s, k, T)/v^2] \quad [10]$$

or

$$P = 1 - (1 - P_0)^{(P_0/v)^2} \quad [11]$$

which should be compared with Eq. 6. It is also apparent from Eq. 9 that, if  $t$  is fixed,  $P$  may be maintained constant over some angular sector by choosing dwell times over the individual space elements that are proportional to  $v(\beta)$ .

The dashed contours of Fig. 2 indicate the influence of a change in orbital altitude upon the sampling rate, as measured by the dwell time required across each interrogated space element, or the mean time between successive positive interrogations. The ratios displayed are those of initial low rendezvous altitude values to those which result when search is corrected for the decline of closure rate and therefore the required acquisition range with increasing orbital altitude. They demonstrate the improvement in information rate available to the acquisition system in the vicinity of critical vehicle separations in high altitude missions. The improvement in the acquisition performance of an initially marginal system,  $P_0 = 0.5$ , is shown by the solid contours. Clearly, an active system profits more by the operational change than does a passive one in both aspects.

### Search Field Optimization

#### Moderate Signal Amplitudes

To provide the basis of the further analysis, and to indicate directions of composite system performance improvement that do not conflict with the obvious weight, space,

and power consumption restrictions imposed by the space operational environment, the question of integration of the ground-control detection and track system and the satellite-borne terminal acquisition equipments will now be considered. Due to the inevitable observation errors a relative positional search sector, generally of reasonably large magnitude, must be designated which, with some desired probability, will contain the other vehicle. Plainly, the probability of containment is an increasing function of the sector size. Assuming the other vehicle to be so contained, it is an improvement that must be purchased at the price of a simultaneous reduction in acquisition probability.

The latter degradation follows from the obvious fact that, as the interrogated space volume increases, the mean energy flux density per unit period of time with which each portion of the space is illuminated if an active system is involved, or the radiation from the other orbital vehicle is received if passive operation is utilized, must then decline. Conversely, too small a sector increases the likelihood of effecting an acquisition if the other is indeed contained in it, but penalizes the probability of the latter occurrence. The optimal search sector, which is functionally dependent upon the performance of the satellite-borne high resolution equipment, as well as that of the ground-control environment, will now be investigated.

In the analysis conducted immediately below, the search volume will be assumed to be uniformly interrogated, although as the level of a priori information involved increases, the search may be optimally distributed so as to minimize the required power consumption or search duration needed to effect some given level of acquisition. This latter consideration will be investigated presently. Although in the following analysis it is represented as a physical cone of indefinite extent, the search volume is, in actuality, an  $n$ -dimensional space, only some of whose coordinates are geometric. Any definitive signal characteristic which is externally observable to both the ground-control environment and the satellite-borne sensory apparatus is worthy of consideration if the implementation of the related decision making operation that is then required is feasible. Certain of the more subtle issues involved relate to the interchange of information output and search time, an example of which is discussed below in effecting an optimal balance between spatial resolution and integrated signal amplitude.

Denoting the independent probabilities of containment and acquisition by  $P_c$  and  $P_D$ , respectively,  $P$ , the compound probability that both events will take place is then equal to  $P_c P_D$ . Let the search region, a cone of semi-apex angle  $\gamma$ , be uniformly swept, so that the search interval  $t$  is proportional to the solid angle, and the relative orbital positions of the two objects be known with statistically independent, Gaussian distributed errors of equal standard deviation  $\sigma$  in elevation and azimuth. Then  $P$  is maximized by adjusting  $\gamma$  in such a manner that  $P_c = P_D$ . As is well known, for moderate  $\gamma$  one must have

$$P_c \sim \frac{1}{2\pi\sigma^2} \left( 4 \int_0^{\pi/2} \left\{ \int_0^\gamma e^{-\rho^2/2\sigma^2} \rho d\rho d\theta P_c \right\} = 1 - e^{-\gamma^2/2\sigma^2} = 1 - e^{-a\theta} \right) \quad [12]$$

where  $a = 1/2\sigma^2$ ,  $\theta = \gamma^2$ ,  $e^{-\pi^2/2\sigma^2} \sim 0$ . The preceding is a statistical approximation since  $\gamma$  is bounded. Since, from Eq. 5,  $P_D = 1 - \exp(-F/vk\gamma^2) = 1 - \exp(-b/\theta)$ ,  $b = F/vk$

$$P \equiv P(\theta) = (1 - e^{-a/\theta})(1 - e^{-b/\theta}) \quad [13]$$

which is bounded, continuous, and vanishes at the origin and the point at infinity, so that it must have at least one maximum.

Differentiating the above with respect to  $\theta$ , one obtains

$$\begin{aligned} \frac{dP}{d\theta} &= \frac{1}{\theta} \left\{ a\theta e^{-a\theta} (1 - e^{-b/\theta}) - \frac{b}{\theta} e^{-b/\theta} (1 - e^{-a\theta}) \right\} \\ \text{or} \quad \frac{dP}{d\theta} &= -\frac{P}{\theta} \left\{ \left( \frac{1}{P_c} - 1 \right) \ln(1 - P_c) - \left( \frac{1}{P_D} - 1 \right) \ln(1 - P_D) \right\} \quad [14] \end{aligned}$$

which can vanish for positive definite, finite  $\theta$ , only if the bracketed expression does so.

The function  $y = (1/x - 1) \ln(1 - x)$  is monotonically increasing for  $0 < x < 1$ , and therefore single-valued over that interval, since

$$\frac{dy}{dx} = -\frac{1}{x^2} [x + \ln(1 - x)] = \sum_{\lambda=1}^{\infty} \frac{x^{\lambda-1}}{\lambda+1} > 0 \quad [15]$$

whence one must have  $P_c = P_D$ .

The above is a special case of a general search theorem to the effect that, if optima exist and the area density distribution of the observer-contact relative location  $f(\rho, \theta)$  is given, the probability of a successful acquisition  $P$  is maximized if the search field is bounded by an equi-density contour  $r \equiv r(\theta)$ . Since in this discussion the sampling period is assumed proportional to the area  $A$  of the search field, from the earlier analysis

$$P = P_c P_D = \int_0^{2\pi} \int_0^r f(\rho, \theta) \rho d\rho d\theta \times \left[ 1 - \exp \left( -K / \int_0^{2\pi} \int_0^r r^2 d\theta \right) \right] \quad [16]$$

Assuming the behavior of the functions involved to be appropriate, one may apply the conventional arguments of the variational calculus. Replacing  $r$  by  $r + \beta\eta$ , where  $\eta \equiv \eta(\theta)$  is an arbitrary function, and differentiating with respect to  $\beta$ , the required extremals are seen to be given by

$$\begin{aligned} 0 &= P_D \frac{\partial P_c}{\partial \beta} \Big|_{\beta=0} + P_c \frac{\partial P_D}{\partial \beta} \Big|_{\beta=0} = P_D \left( \int_0^{2\pi} \eta f(r, \theta) r d\theta \right) - \\ &P_c \left( K \exp \left( -K / \int_0^{2\pi} r^2 d\theta \right) \int_0^{2\pi} \eta r d\theta / \frac{1}{2} \left( \int_0^{2\pi} r^2 d\theta \right)^2 \right) \\ 0 &= \int_0^{2\pi} \eta r \left[ P_D f(r, \theta) - \frac{P_c}{A} (1 - P_D) \ln(1 - P_D)^{-1} \right] d\theta \quad [17] \end{aligned}$$

The observation that the bracketed factor in the integrand must vanish since  $\eta(\theta)$  is arbitrary leads to an equation of the form  $f(r, \theta) = C$ , and the desired result.

It is clear that if the problem were formulated as a variational one with the frequently imposed operational constraint  $P_c = C$ , a similar conclusion would result. Reference (3) discusses this, and programmed, nonuniform search of the search region. It is there shown that in representative situations optimal, uniformly distributed search leads to nearly equivalent system performance.

Returning to the special case discussed earlier, Fig. 3 displays the results of some representative computations. The composite system performance is assumed to be marginal, denoted by a compound acquisition probability  $P = 0.5$ , if other than optimal search regions are used. It is reasonable to inquire as to the magnitude of the improvement accruing to proper integration, in the above sense, of the external vectoring agency and the orbital vehicle. Denoting the optimal angular search radius by  $R$

$$P = (1 - e^{-aR^2})(1 - e^{-b/R^2}) \quad [18]$$

and  $P_D = P_C$  implies  $R^4 = b/a$ .

If a nonoptimal search radius  $r$  had been utilized

$$b/r^2 = (aR^4)/r^2 = ar^2(R/r)^4 \quad [19]$$

$$\text{whence } P = P_C[1 - e^{-b/R^2}] = P_C[1 - (1 - P_C)^{(R/r)^4}] \quad [20]$$

which relates the given containment probability to the resultant composite system performance and the ratio of the optimal to the given search radius. A related argument, or the observation that  $P_D = PP_C^{-1}$ , yields a corresponding expression involving  $P_D$  and, finally

$$\frac{R}{r} = \left\{ \frac{\ln(1 - P/P_C)}{\ln(1 - P_C)} \right\}^{1/4} = \left\{ \frac{\ln(1 - P_D)}{\ln(1 - P/P_D)} \right\}^{1/4} \quad [21]$$

These relationships are evaluated over a range of the ratio that may be expected to obtain in operational practice in which due consideration is not given to search optimization. The most frequent departure from optimal search volumes in conventional applications is toward values of  $R/r < 1$ . Containment probabilities which are excessive relative to the capabilities of the sensory apparatus result. The rapid decline of  $P_C$  with increasing  $R/r$  for  $P = 0.5$  and, conversely, the rapid increase in  $P_D$ , are apparent in Fig. 3.

Denoting the optimal selections of  $P_C$  and  $P_D$  by  $\tilde{P}_C$ ,  $\tilde{P}_D$  respectively

$$\begin{aligned} \tilde{P}_C &= 1 - e^{-\alpha R^2} = 1 - e^{-\alpha r^2(R/r)^2} = 1 - (1 - P_C)^{(R/r)^2} \\ \tilde{P}_D &= 1 - e^{-\beta/R^2} = 1 - e^{-(\beta/r^2)(r/R)^2} = 1 - (1 - P_D)^{(r/R)^2} \end{aligned} \quad [22]$$

the net effect of which is to reduce  $P_C$  and increase  $P_D$  where  $R/r < 1$  and, conversely, to reverse the sense of these revisions over the domain  $R/r > 1$ . The corrected values of both probabilities are displayed as one contour since, being optimally chosen,  $\tilde{P}_C = \tilde{P}_D$ . The greatest attainable composite probability of acquisition is  $\tilde{P} = \tilde{P}_C^2 = \tilde{P}_D^2$ , which is seen to rise rapidly for values of  $R/r$  reasonably different from unity. In the vicinity of  $R = r$ , the overall system is, in effect, already delivering the best performance possible, and nothing further can then be accomplished by these means.

### Large Signal Amplitudes

In the preceding discussion, the rate at which the search volume was interrogated was limited by signal integration time requirements. A brief discussion of acquisition performance in the presence of large signal amplitudes is of interest in view of the probable utilization of beacons and the possibility of deferring the initiation of search on a programmed or command basis until critical separations between the orbiting vehicles are reached, so as to minimize the energy consumption. Unfortunately, while the removal of sensory apparatus limitations from the discussion facilitates the problem, other restrictions are retained or simultaneously introduced. Among the most important of these are the consequences of data handling bandwidth limitations, since the entirety of the search region must be scanned within some greatest admissible time period  $T$  if the minimal separation acquisition region has been attained.

Accordingly, the question may be formulated as one in bandwidth reduction by inquiring as to the minimal time needed to interrogate a given number  $N$  of space resolution elements of width  $\delta$  or, in a related manner, investigating the problem of maximizing the number of space resolution elements that may be interrogated in the search interval  $T$ . Clearly, the latter optimizes system performance by yielding the greatest containment probability that is attainable since, as in the earlier discussion,  $P_C$  tends to be of the form  $1 - \exp(-kN)$ .

Since the task is fundamentally one of isolating the object sought for among the  $N$  elements, which may be grouped and rapidly interrogated as subsectors of the total search volume, the quantity to be minimized is

$$T = t \left( 1 + \sum_{i=1}^n n_i \right), \quad \theta = \delta \sum_{i=1}^n n_i, \quad \theta/\delta = N, n_n = 1 \quad [23]$$

The optimization process under consideration seeks to determine the best partition of the space into progressively smaller subgroups, the interrogation of each of which requires an essentially fixed time  $t$  which is dictated by data handling subsystem bandwidths. Then  $T$  represents the overall search time required with such system logic, and will be contrasted with that required for successive, sequential interrogation of each individual element  $tN$ .

Writing  $N = n_i \tilde{P}$ , where  $\tilde{P}$  denotes the remaining members of the product in Eq. 23,  $n_i = N/\tilde{P}n_i$  and

$$T = t(1 + S + (n_i + N/\tilde{P}n_i)) \quad [24]$$

if  $S$  represents all the terms in the sum, exclusive of  $n_i$  and  $n_i$ . Forming the partial derivatives with respect to the  $n_i$

$$\frac{\partial T}{\partial n_i} = t \left( 1 - \frac{N}{\tilde{P}n_i^2} \right) = t \left( 1 - \frac{n_j}{n_i} \right) \quad [25]$$

or  $n_j = n_i$  if the bracketed quantity is to vanish. Accordingly, each subgroup must contain the same number  $\nu$  of members as its predecessor, where  $N = \nu^n$ , and from Eq. 23

$$T = t(1 + \nu n) = t(1 + (\nu/\ln \nu) \ln N) \quad [26]$$

Differentiation of the above with respect to  $\nu$  shows that it is minimal for  $\nu = e$ , whence  $n = \ln N$ . In view of the degree

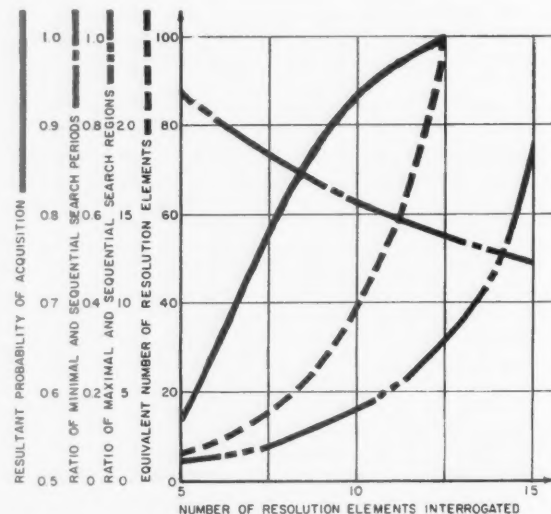


Fig. 4 Search optimization with large signal amplitudes

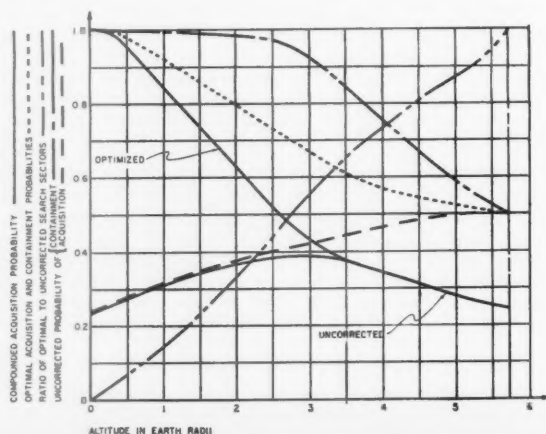


Fig. 5 Search optimization with variable orbital altitude



of approximation involved, setting aside the consideration that  $\nu$  and  $n$  are not, in point of fact, integral, the minimal value of  $T$ ,  $\bar{T}$ , may be taken as  $te \ln N$ . Fig. 4 displays the ratio  $\bar{T}/Nt = (e \ln N)/N$  for moderate values of  $N$  such as may obtain with reasonably close control of the terminal approach phase up to acquisition by the satellite-borne equipment. Plainly, the economies in data-handling subsystem commitment time yielded by the introduction of such techniques can become important as the accuracy of the external vectoring agency declines and the number of resolution elements that must be interrogated increases.

Rephrasing the problem, if the data-handling subsystem has sufficient flexibility to interrogate the search space by such means, rather than sequentially, one may enquire as to  $\bar{N}$ , the number of resolution elements that may be handled in a search period equal to that which would have obtained if such decision-making facilities had not been provided. From  $T = NT = et \ln \bar{N}$  one obtains  $\bar{N} = \exp(N/e)$  which, together with the ratio  $\bar{N}/n$ , is displayed in Fig. 4. The large increase in the equivalent number of elements  $\bar{N}$  with  $N$ , when interpreted directly as an improvement in the admissible search volume, indicates that substantial increases in  $P_c$  may be so effected.

To obtain quantitative insight into this consideration let it be assumed that sequential search is conducted and, due to restrictions upon the duration of the search period, the interrogated space volume is correspondingly restricted, leading thereby to some modest containment probability  $P_c$ . If search techniques that are optimal in the sense discussed above are then utilized, yielding a containment probability  $\bar{P}_c$

$$\bar{P}_c = 1 - (1 - P_c)\bar{N}/N = (1 - P_c)e^{N/e/N} \quad [27]$$

It will be recalled that  $\bar{P}_c$  corresponds to the acquisition probability since, by hypothesis,  $P_D = 1$ . The functional form indicates clearly that for even very modest  $N$ , if  $P_c$  assumes reasonable values,  $\bar{P}_c$  will be essentially unity. This observation is borne out by the appropriate contour of Fig. 4. In the computations,  $\bar{P}_c = 0.5$  to demonstrate the performance improvement that is possible with an otherwise marginal system.

#### System Integration with Variable Orbital Altitudes

Returning to the earlier analysis of the optimization of search in the presence of moderate signal amplitudes, the theory which has been developed will now be applied to the problem of optimizing the performance of a composite terminal acquisition system, whose external vectoring agency provides relative positional information which is characterized by range dependent statistical errors. It will be assumed that the vehicle-borne equipment is to be used over a large spectrum of orbital altitudes to obtain insight into the possibility of utilizing the same equipment in a variety of missions, and the resultant requirements for flexibility in the conduct of terminal acquisition search.

It is not unreasonable to assume, for purposes of the present discussion, that the ground control detection and tracking apparatus is consistently receiving signals of fairly large amplitude. The standard deviation of the presumably Gaussian transverse error is then proportional to the tracking range, or the altitude if the terminal elevation angle is largely invariant. It is emphasized, however, that these simplifying hypotheses are introduced largely to facilitate the exposition rather than to simulate a real operational environment with a high degree of precision. There are many significant physical phenomena connected with propagation through the Earth's magnetic field and the various bounding layers, and the track of hypervelocity objects that are significant in this regard.

Even setting the latter considerations aside, the influence of the relative geometry upon the error is generally more sub-

stantial than is implied by the hypothesized elementary range dependence, particularly if other than very strong signals are encountered. The information content derived on an individual interrogation declines with the signal amplitude as well as with broadening beam dimensions. If then discrete data tracking is used by the vectoring agency, more subtle and pronounced degradations are introduced. That is, the likelihood of effecting the correlation of data derived over some time interval is a declining function of the errors involved in the individual observations, and the number of detections which are actually made. Accordingly, the progressive degradation of the output of a smoothing program as signal amplitudes decline below high intensity levels is essentially exponential in form. Reference (2) discusses this consideration, as well as other topics that closely relate to the problem at hand. Indeed, the assumption of a standard deviation in transverse error that is proportional to the relative range is very nearly valid in that, once the signal amplitudes decline below the point at which that statistical model obtains, the further deterioration with opening range may be so rapid that, in effect, tracking essentially terminates.

If  $P_c$  and  $P_D$  are specified for a given altitude  $h$ , the ground-vectoring and vehicle-borne equipment must necessarily display highly divergent capabilities as  $h$  varies, unless compensation through control of the search program is provided. For the first, in conjunction with Eq. 12,  $\sigma \propto h$  implies that  $P_c$  is of the form  $1 - \exp(-k/h^2)$ . The velocity dependence of  $P_D$  has been investigated earlier, the results being embodied in Eqs. 6 and 11. In any event, with increasing altitude  $\sigma$  increases and  $P_c$  declines, whereas  $\bar{P}$  progressively declines, leading to an improvement in  $P_D$ , and conversely. Fig. 5 displays both functions for an initial assumption of marginal performance in each at the stationary orbital altitude. The computations of  $P_D$  utilized Eq. 6 and are therefore uncorrected for the increase in required acquisition range with orbital velocity. Accordingly, the indicated decline in  $P_D$  with the altitude is conservative. The relative increase in  $P_c$  is insufficient to continuously compensate for that deterioration and, after attaining a maximum, the compound acquisition probability product  $P_c P_D$  declines. It is readily seen that, in general, a best performance altitude exists in the above sense.

As has been indicated by the earlier analysis, the optimal integration of the two systems is dependent upon the appropriate adjustment of the magnitude of the search sectors so as to produce equality between the containment and acquisition probabilities. If then  $\theta$ ,  $\bar{\theta}$  denote respectively the interrogated space volume and its optima at some given altitude, from Eq. 18

$$\bar{P}_c = 1 - (1 - P_c)^{\bar{\theta}/\theta} \quad \bar{P}_D = 1 - (1 - P_D)^{\bar{\theta}/\theta} \quad [28]$$

where  $\bar{P}_c$  and  $\bar{P}_D$  represent the optima of the respective probabilities at  $h$ . From  $\bar{P}_c = \bar{P}_D$

$$\frac{\bar{\theta}}{\theta} = \sqrt{\frac{\{\ln(1 - P_D)\}}{\{\ln(1 - P_c)\}}}$$

$$\bar{P} = (\bar{P}_{c,D})^2 = \left[ 1 - (1 - P_{c,D}) \sqrt{\frac{\{\ln(1 - P_{D,c})\}}{\{\ln(1 - P_{c,D})\}}} \right]^2 \quad [29]$$

Both functions are displayed in Fig. 5 and show the substantial improvement yielded by the technique of controlling the search. The indicated variation in the desired space volume is seen to be large. The contour representing  $\bar{\theta}/\theta$  passes through the origin since, as reason suggests, "search-lighting" should be used in the absence of a relative positional error. The inferred improvement at very low altitudes is, of course, extravagant, due to the fact that the positional error does not in reality vanish at the origin, and the finiteness of the beam. The latter occupies an increasingly larger proportion of the shrinking search volume. The asymptotic approach of  $\bar{P}$  to  $P$  derives from the fact that the hypothe-

sized values of  $P_C$  and  $P_D$  at the stationary altitude were equal.

## Conclusions

1 The likelihood of effecting terminal acquisition between orbital vehicles is exponentially dependent upon their relative closure rate  $v$ , and is of the form  $1 - \exp(-k/v^2)$ , where  $v$  is two or four according as the vehicle-borne sensory apparatus is passive or active.

2 If the quality of the vectoring provided by the ground control environment is assumed to be essentially independent of the altitude of the orbital region, the performance of a given vehicle-borne terminal acquisition system improves markedly with increasing altitude.

3 The maintenance of a high order of performance on the part of the composite terminal acquisition system, comprised of an external vectoring agency and the vehicle-borne apparatus, is critically dependent upon the nature of the integration of the two subsystems, in particular the specification of an optimal search sector to be interrogated by the latter.

4 If an extremal exists, the optimum search field to be uniformly interrogated by the vehicle-borne acquisition system is defined by an equiprobability density of relative location contour. In particular, let the relative angular positional error of the orbital bodies, as specified by the external vectoring agency, be Gaussian, with equal standard deviations in elevation and azimuth. Then the composite terminal acquisition probability is maximized by adjusting the search volume designated to the vehicle in such a manner

that the probability of containing the other vehicle, and the probability of acquiring it if it is so contained, are equal.

5 If  $N$  space resolution elements are to be interrogated, and the vehicle-borne equipment scan rate is limited in data handling subsystem bandwidth rather than signal integration time, minimal-time search techniques greatly improve the probability of acquisition. If  $P$  had been the acquisition probability resulting from sequential interrogation of each individual element, and  $\bar{P}$  the optimized performance,  $\bar{P}$  is of the form

$$1 - (1 - P)^{(cN/\epsilon/N)}$$

## Acknowledgment

The author appreciatively recognizes the assistance provided by the Electronics Division of Maxson Electronics Corp., with which he is affiliated, in the use of its personnel and facilities for the preparation of the final paper.

## References

- 1 Potter, N. S., "Comparative Evaluation and Optimization of Airborne Target Detection Systems," *Proc., Second National Conf. on Military Electronics, Inst. of Radio Engrs., Washington, D. C., June 1958*.
- 2 Potter, N. S., "The Optimization of Astronautical Vehicle Detection Systems Through the Application of Search Theory," *Proc. Inst. Radio Engrs., vol. 48, no. 4, April 1960*.
- 3 Potter, N. S., "Guidance-Control System Integration in Satellite Rendezvous," *Proc., National Aerospace Electronics Conf., Inst. of Radio Engrs., Dayton, Ohio, May 1961*.

# Aerodynamic and Radiant Heat Input to Space Vehicles Which Re-Enter at Satellite and Escape Velocity

M. J. BRUNNER<sup>1</sup>

General Electric Co.  
Philadelphia, Pa.

An analysis of the aerodynamic and radiant heat input is presented for space vehicles re-entering at satellite and escape velocity. The magnitude of the heat flux and total heating for convection (laminar and turbulent flow) and radiation from the gas cap are given as a function of  $W/C_D A$ , re-entry angle, lift over drag ratio, and local pressure distribution. Consideration is given to re-entry at escape velocity with one skip at satellite velocity as a means for reducing the magnitude of the deceleration and heat flux.

A MAJOR consideration for a re-entrant space vehicle is the heating imposed during re-entry. The heating characteristics such as the magnitude of the heat flux, total heating, and heating time of particular interest applies specifically to the aerodynamic and radiant heat input to vehicles

which re-enter at satellite and escape velocity. The heat flux and total heating are given for both laminar and turbulent flow as a function of re-entry angle, lift over drag ratio, local pressure distribution and vehicle geometry. The radiant heat flux and total heating are also specified when applicable. Sufficient information will be presented to determine the heat input for any given vehicle re-entering at satellite or escape velocity.

At the outset, it should be noted that there is essentially

Presented at the ARS 15th Annual Meeting, Washington, D. C., Dec. 5-8, 1960.

<sup>1</sup> Specialist Advanced Studies Missile and Space Vehicle Dept.

little data available to verify the aerodynamic and radiant heat input at escape velocity. Numerous ground and flight test data, however, are available to verify the predictions at satellite velocity. The heating methods at satellite velocity will be extended to the escape velocity conditions. The reference enthalpy methods (1)<sup>2</sup> which have been successful in accounting for real gas and compressibility effects will be utilized for the aerodynamic heating evaluation. The radiant heating estimates will utilize extensions of the calculations of emissivity of high temperature air based on the various radiating species present in the air at a given temperature and density (2).

The trajectory was of particular importance in the study. In order to make the study in a reasonable length of time, with sufficient detail, and yet cover a wide range of vehicles, it was necessary to select a convenient method for specifying the motion of the vehicle. The re-entry conditions of particular interest concerned small re-entry angles and small lift over drag ( $L/D$ ) ratios. The vehicle motion selected was similar to that of Chapman (3), but extended to include a larger portion of the flight for total heating purposes. The selected method was chosen because the equations of motion could be reduced to one ordinary nonlinear differential equation by utilizing a mathematical transformation; a solution of this equation could apply to any vehicle for a given re-entry angle, re-entry velocity,  $L/D$  and planetary atmosphere.

Previous papers (3,4) have discussed satellite and escape velocity re-entry in a general way, but it is believed that this analysis will essentially present means for obtaining an evaluation of the heat input to a given re-entrant space vehicle for preliminary design purposes which may provide an insight into the heat protection system requirements.

### Trajectory Analysis

The motion of a hypersonic re-entry vehicle may be expressed as

$$\text{vertical} \quad \frac{dv}{dt} + \frac{u^2}{r} = g - \frac{L}{m} \cos \theta + \frac{D}{m} \sin \theta \quad [1]$$

$$\text{horizontal} \quad \frac{du}{dt} + \frac{uv}{r} = -\frac{D}{m} \left(1 + \frac{L}{D} \tan \theta\right) \cos \theta \quad [2]$$

Based on the assumptions of

$$\left| \frac{uv}{r} \right| \ll \left| \frac{du}{dt} \right| \quad \left| \frac{L}{D} \tan \theta \right| \ll 1$$

if the independent variable is chosen as  $\bar{u} = u/u_{\infty}$ , we assume an isothermal atmosphere ( $\rho_{\infty} = \rho_0 e^{-\beta y}$ ) and select a dimensionless independent variable as defined by Chapman (3) as

$$Z = \frac{\rho_0 \sqrt{r/\beta}}{2(m/C_D A)} \bar{u} e^{-\beta y} \quad [3]$$

Eqs. 1 and 2 can be reduced to the single equation

$$\bar{u} Z'' - \left( Z' - \frac{Z}{\bar{u}} \right) = \frac{1 - \bar{u}^2}{\bar{u} Z} \cos^4 \theta - \sqrt{\beta r} \frac{L}{D} \cos^3 \theta \quad [4]$$

A solution of this nonlinear second order differential equation for  $Z$  can be obtained by numerical methods for various initial conditions of  $\bar{u}$ ,  $\theta$  and  $(\sqrt{\beta r} L/D)$ . This method provides a convenient means of evaluating the heating. Once solutions are obtained, they will apply to a wide range of vehicles and planetary atmospheres. The uniqueness of the solution is brought about by the dependent variable  $Z$ . For any given planetary atmosphere a change in  $W/C_D A$  would simply require a change in altitude to satisfy the  $Z$  requirement at a given velocity  $\bar{u}$ . The re-entry angles

stated throughout the paper correspond to a velocity which is 0.9985 times the initial velocity.

It can be shown that the local path angle, time, and horizontal deceleration (3) are

$$\theta = \sin^{-1} \frac{Z' - Z/\bar{u}}{\sqrt{\beta r}} \quad [5]$$

$$t = \frac{1}{\sqrt{\beta g}} \int_{\bar{u}_2}^{\bar{u}_1} \frac{\cos \theta}{\bar{u} Z} d\bar{u} \quad [6]$$

$$-\frac{1}{g} \frac{du}{dt} = \sqrt{\beta r} \bar{u} Z / \cos \theta \quad [7]$$

### Aerodynamic Heating

Since the vehicles of interest in our discussion re-enter at satellite and escape velocity, they are exposed to very high temperature air, the properties of which deviate from an ideal gas. At velocities of about 3000 fps, the vibrational modes are excited; then dissociation starts for oxygen at about 7000 fps and for nitrogen at about 15,000 fps. The reference enthalpy method has been successful in predicting the heating for satellite re-entry where these chemical reactions are of major importance. At escape velocity the important reaction is the ionization of the oxygen and nitrogen atoms. Although there is little aerodynamic heating data at these conditions, it is believed that the reference enthalpy method will be useful in predicting the aerodynamic heating from an engineering standpoint. The convective heating used throughout this analysis was based on continuum flow. For all the re-entry conditions examined, the major and significant portion of the heating occurs in the continuum regime.

### Laminar

The stagnation point heat transfer rate was obtained from the Lees' analysis modified to account for real gas and compressibility effects using the reference enthalpy method (1) written in terms of  $\bar{u}$  and  $Z$  as follows

$$\dot{q}_s = K_1 \left( \frac{m}{C_D A} \right)^{0.5} R_N^{-0.5} \bar{u}^{2.72} Z^{0.5} \cos \theta^{-3.22}$$

$$K_1 = 1.89 \times$$

$$10^{-3} C_P^{0.14} T_B^{-0.36} \mu_B^{0.5} R^{-0.5} P_r^{-2/3} g^{0.75} r^{1.36} \beta^{0.25} f(m\gamma)$$

$$f(m\gamma) = \left( \frac{\gamma + 1}{\gamma} \right)^{0.5} \left( \frac{\gamma - 1}{\gamma + 1} \right)^{0.25} \left( \frac{\gamma + 3}{\gamma + 1} \right)^{0.25} \quad [8]$$

The time integrated stagnation heat flux is then

$$Q_s = \frac{K_1 (m/C_D A)^{0.5}}{R_N^{0.5} \sqrt{\beta g}} \int_{\bar{u}_1}^{\bar{u}_2} \frac{\bar{u}^{1.72} Z^{0.5}}{\cos \theta^{3.22}} d\bar{u} \quad [9]$$

In order to evaluate the laminar heat transfer at positions on the body other than at the stagnation point, the following relationship of Lees (5) applies

$$\frac{\dot{q}}{\dot{q}_s} = \frac{1/2(P/P_s)(u/u_{\infty})R\sqrt{R_N}}{\left[ \int_0^{\infty} (P/P_s)(u/u_{\infty})R^2 ds \right]^{1/2} \left[ (1/u_{\infty})(du/d\theta)_{\theta=0} \right]^{1/2}} \quad [10]$$

The effect of pressure ratio on laminar heating is shown in Fig. 1 for typical sphere cone shapes having a Newtonian pressure distribution over its surface. The maximum laminar heating occurs at a pressure ratio ( $p/p_s$ ) of one (stagnation point). The local body angle for a Newtonian pressure distribution is shown for convenience.

<sup>2</sup> Numbers in parentheses indicate References at end of paper.

### Turbulent

The turbulent heat transfer rate can be expressed conveniently considering real gas effects by a modified flat plate reference enthalpy method (1) written in terms of  $\bar{u}$  and  $Z$  as

$$\dot{q}_t = K_2(m/C_{DA})^{0.8} s^{-0.2} \bar{u}^{2.68} Z^{0.8} \cos \theta^{-3.48}$$

$$K_2 = 7.78 \times 10^{-4} p_r^{-2/3} C_p^{0.46} \mu_p^{0.2} g^{1.2} r^{1.34} \beta^{0.4} R^{-0.8} T_B^{-0.34} f(m\gamma p/p_s)$$

$$f(m\gamma p/p_s) = \left(\frac{\gamma+1}{\gamma}\right)^{0.8} \left(\frac{p}{p_s}\right)^{0.8} \left[1 - \left(\frac{p}{p_s}\right)^{(\gamma-1)/\gamma}\right]^{0.4} \times [1 + 1.272 (p/p_s)^{(\gamma-1)/\gamma}]^{-0.46}$$

[11]

The time-integrated turbulent heat transfer is then

$$Q_t = \frac{K_2(m/C_{DA})^{0.8}}{s^{0.2} \sqrt{\beta g}} \int_{\bar{u}_1}^{\bar{u}_2} \frac{\bar{u}^{1.68} Z^{-0.2}}{\cos \theta^{2.48}} d\bar{u} \quad [12]$$

The variation of turbulent heating with pressure ratio is shown in Fig. 1. The maximum turbulent heating occurs at a pressure ratio of about 0.60. Since this relation is a point function, once the pressure is known the heating can be readily obtained for a given velocity, altitude, and wetted length.

It should be noted that the aerodynamic heating (laminar and turbulent) will depend on the wall temperature. For convenience the above expressions for the heat transfer rates and total heating were based on zero wall temperature. When the wall temperature is greater than zero, correction (1) can be readily made to both the heat flux and total heat input.

### Radiation

The radiation from the gas cap surrounding the nose of a blunt vehicle re-entering at escape velocity may become a significant portion of the total heat input. The radiation heat input to a vehicle can be obtained from

$$\dot{q}_r = \alpha \epsilon_g \sigma T^4 \quad [13]$$

The emissivity  $\epsilon_g$  is the effective emissivity of the gas cap. It is the summation of the emissivity of all the significant radiant contributing species in high temperature air ( $\epsilon_g = \sum \epsilon_i$ ). Typical of the twenty-five species included were: (a)  $O_2$  and  $NO$   $\beta + \gamma$  of the broad band system; (b)  $N_2$  second

positive,  $N_2^+$  first negative,  $O_2$ ,  $O_2^+$  and  $N_2^+$  of the semisharp band system; and (c)  $O$ ,  $N$ ,  $A$ ,  $N_2$  and  $NO$  of the Kramers class of radiation. At escape velocity the radiation of the  $N$  species (electron capture forming the nitrogen atoms) is predominant.

The emissivity per unit length ( $\epsilon/l$ ) was obtained from the radiative species in high temperature air from one side of an optically thin plane gas cap of thickness  $l$  given by Kivel and Bailey (2). The effective emissivity  $\epsilon_g$  of the gas cap is then

$$\epsilon_g = (\epsilon/l)lk \quad [14]$$

The gas cap thickness  $l$  was determined from the Li-Geiger (6) relation

$$l = \frac{k'R_n(1 - \sqrt{k'(2 - k')})}{(1 - k')^2}$$

where

$$k' = \frac{\rho_\infty}{\rho_s} \quad [15]$$

which shows similar results as predicted by Hayes (7) and Serbin (8) at high stagnation density ratios represented by escape and satellite velocities. The Moeckel and Weston (9) properties of air were used throughout the analysis.

The radiant heat flux input to the stagnation point of a blunt nosed vehicle of one foot radius is shown in Fig. 2 as a function of altitude for various velocities ranging from 40,000 to 15,000 fps. As shown, the radiant heat flux becomes very large at escape velocity re-entry, especially at low altitude. For a given altitude and free stream velocity operation the gas cap thickness, and therefore the radiant heat flux input is proportional to the nose radius. This applies to relatively small changes in nose radius, since the effective emissivity per unit length actually decreases due to absorption (factor  $k$ ) as the gas cap increases. For a nose radius of one foot, this factor is about unity since the absorption is minor; but as the nose radius reaches 10 ft, this factor can become about 0.5. The absorption factor  $k$  not only is a function of gas cap thickness but temperature and density.

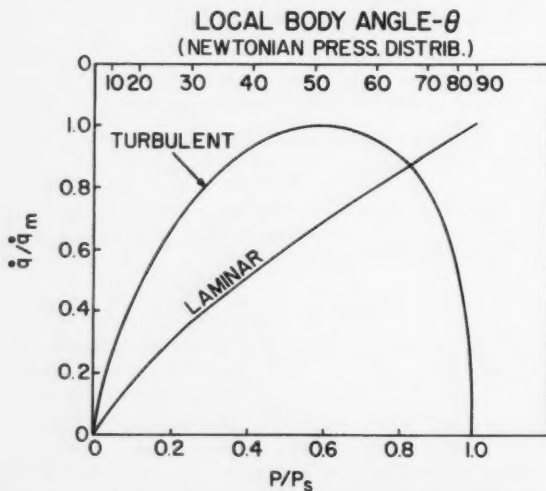


Fig. 1 Local to maximum heat flux ratio for turbulent and laminar flow vs. local pressure ratio

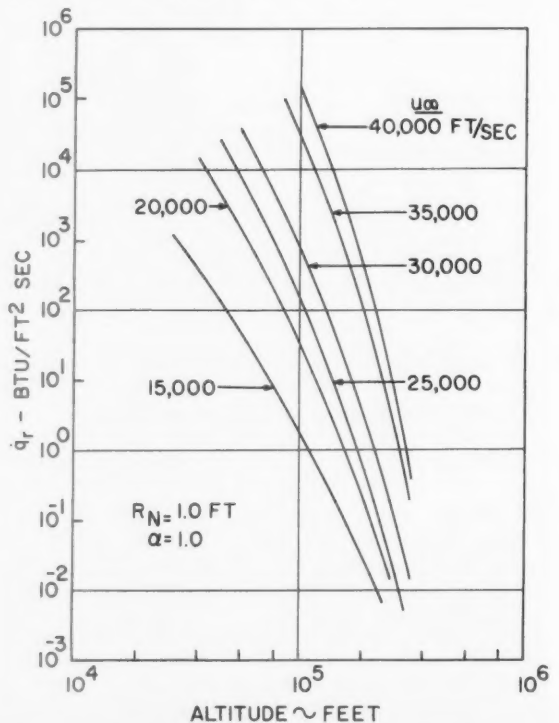


Fig. 2 Radiant heat flux from gas cap vs. altitude



In addition to the absorption, there are a number of other factors which will affect the radiation. The actual geometry will see radiation over the stagnation region at slightly lower temperatures than at the stagnation point; the emissivity  $\epsilon_p$  is limited to 1.0 as a maximum no matter how thick the gas cap becomes; and the radiation energy must be less than the stagnation energy. The above items will all tend to decrease the radiation from that given previously.

When nonequilibrium conditions occur, however, the resulting radiation will generally be higher than equilibrium radiation. Nonequilibrium conditions can occur when the relaxation time is large compared to the time required for a particle to traverse the gas cap. This condition will occur at high altitude but becomes less important as the size of the vehicle and the flight speeds increase. It has been shown (10) that nonequilibrium radiation can be as much as an order of magnitude higher than equilibrium conditions. Fortunately, nonequilibrium conditions exist generally at high altitude where the magnitude of the radiation is itself low. The overall effect of nonequilibrium radiation is in general of little concern for ICBM, Moon, Venus, or Mars probes, but it may be important for satellite applications. Although there are many possible sources of error and essentially no actual test results for radiation at escape velocity, the emissivity data used is the best available at present.

#### Effect of Ionization on the Aerodynamic Heating at Escape Velocity

Since the important reaction at escape velocity is the ionization of the oxygen atoms, it is of interest to evaluate the effect of this ionization on the aerodynamic heating. The stagnation temperatures at escape velocity will vary between about 15,000 and 8000 K at altitudes between 50,000 and 345,000 ft, the range considered in the study. Although these temperatures are very much higher than at satellite velocity, the gas is still far from being fully ionized. The degree of ionization varies from about 3 to 15% for these extreme conditions. The major influence of the ionization on the heating is its effect on the transport properties; namely, thermal conductivity, viscosity, and diffusion coefficient.

It is interesting to note that the transport properties for un-ionized and ionized gas compare as follows (11,12)

$$\text{un-ionized gases} \quad K_i \sim \mu_i \sim T^{1/2} \quad D_{ij} \sim T^{3/2} \quad [16]$$

$$\text{fully ionized gases} \quad K_i \sim \mu_i \sim T^{5/2} \quad D_{ij} \sim T^{7/2} \quad [17]$$

Since the application at escape velocity re-entry will be between these two extreme conditions, it is important to note that the degree of ionization encountered will have a relatively large influence on the thermal conductivity and a smaller influence on the viscosity and diffusion coefficient. The effect of the change in the power dependence of temperature for the transport properties will change the aerodynamic heating predictions somewhat. It has been shown (13) that the heat transfer rates at escape velocity due to ionization can be increased by about 10 to 20% over that for the extended un-ionized heating rates. This will have only a small influence on the overall heating rates and even less effect on the total heating for escape velocity re-entry. The degree of ionization at satellite velocity will be considerably less, and therefore its effect on the aerodynamic heating will be negligible. At re-entry velocities greater than escape velocity the effect of ionization will be more pronounced and may have a greater influence on the overall heating environment.

#### Re-Entry at Satellite Velocity

It is desired to consider the heat input to vehicles which re-enter at satellite velocity for a variety of re-entry angles and lift over drag ratios typical of the current interest in instrumented and manned flight. The radiation input for this type

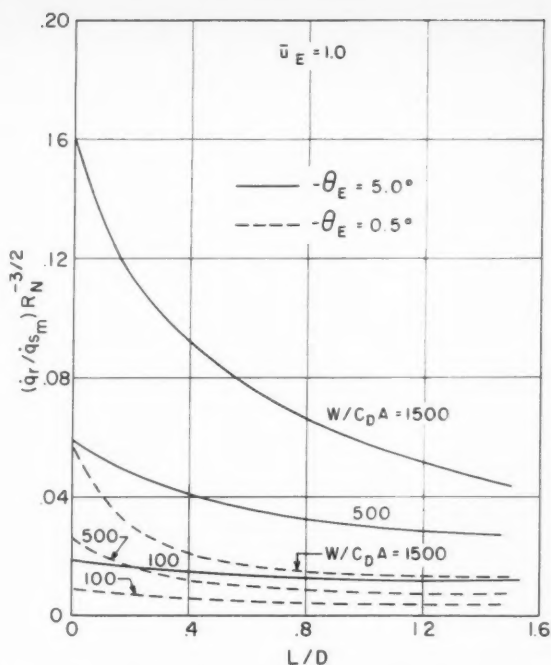


Fig. 3 Radiant to maximum stagnation heat flux ratio vs. lift over drag ratio for satellite re-entry

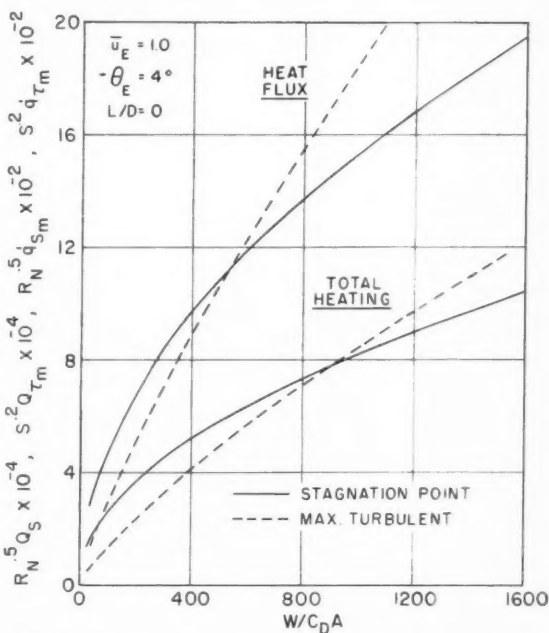


Fig. 4 Maximum heat flux (Btu/ft<sup>2</sup>-sec) and total heating (Btu/ft<sup>2</sup>) for laminar and turbulent flow vs.  $W/C_D A$  for satellite re-entry

of re-entry represents a small portion of the total heat input. The comparison of the radiation to the convective stagnation heating is shown in Fig. 3 as a function of lift over drag ratio for various typical values of  $W/C_D A$  and re-entry angles. The ratio  $\dot{q}_r/\dot{q}_s$  increases with increasing re-entry angle,

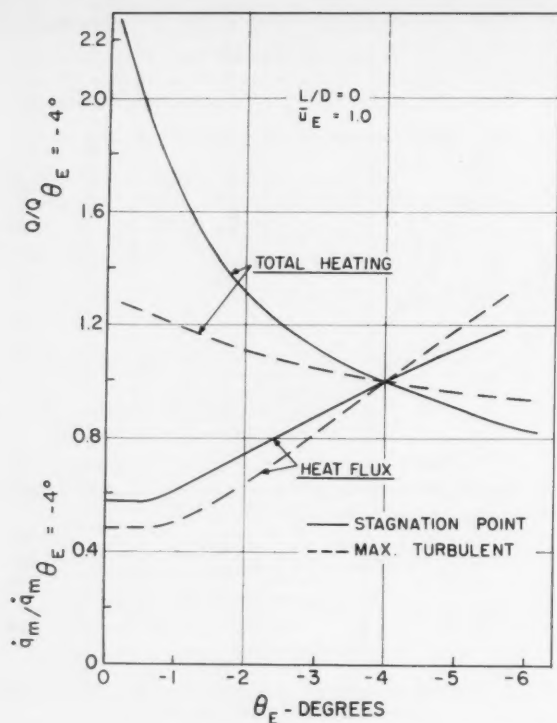


Fig. 5 Effect of re-entry angle on maximum heat flux and total heating for satellite re-entry

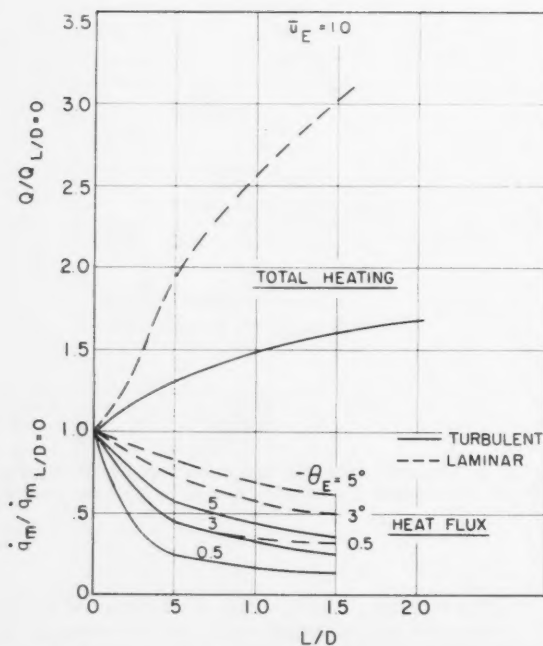


Fig. 6 Effect of lift over drag ratio on maximum heat flux and total heating for satellite re-entry

$W/C_D A$  and decreasing  $L/D$ . In general, it is in the order of 0.01 to 0.16 for vehicles with a one foot nose radius for re-entry up to  $-5$  deg from the horizontal. For this type of re-entry, the radiation represents only a minor portion of the total heat input.

The variation of the convective heat flux with re-entry conditions will be evaluated in dimensionless form for convenience. The magnitude of the heat flux and total heating will be referenced to that for re-entry at  $\theta_E = -4$  deg and  $L/D = 0$ . The base value for laminar and turbulent heat flux and total heating is shown in Fig. 4 as a function of  $W/C_D A$ . The laminar and turbulent heating varies as  $W/C_D A$  to the 0.5 and 0.8 power, respectively. For a referenced length of one foot and a  $W/C_D A$  of 500 lb/ft<sup>2</sup>, the maximum heat flux becomes about 1090 and 1070 Btu/ft<sup>2</sup>-sec and the maximum total heating becomes about 58,000 and 49,000 Btu/ft<sup>2</sup> for laminar and turbulent flow respectively. The stagnation and maximum turbulent ( $p/p_s = 0.6$ ) heat input are used as the basic reference quantities as the heating at other body positions of the vehicle can be readily obtained from these quantities as illustrated previously.

The variation of maximum heat flux and total heating for both laminar and turbulent flow is shown in Fig. 5 for a zero lift vehicle. The maximum heat flux decreases with decreasing re-entry angle but reaches a lower limit for angles of about  $-0.5$  deg. A similar but opposite trend exists for the total heating. The effect of  $L/D$  on the variation of heat flux and total heating is shown in Fig. 6. In all cases, lift decreases the maximum heat flux but increases the total heating;  $L/D$  was more effective in reducing the turbulent heating than for laminar heating. As the re-entry angle was decreased, the effect of  $L/D$  was more pronounced in the reduction of the maximum heating rate. The total heating was increased with  $L/D$ , and it was independent of the re-

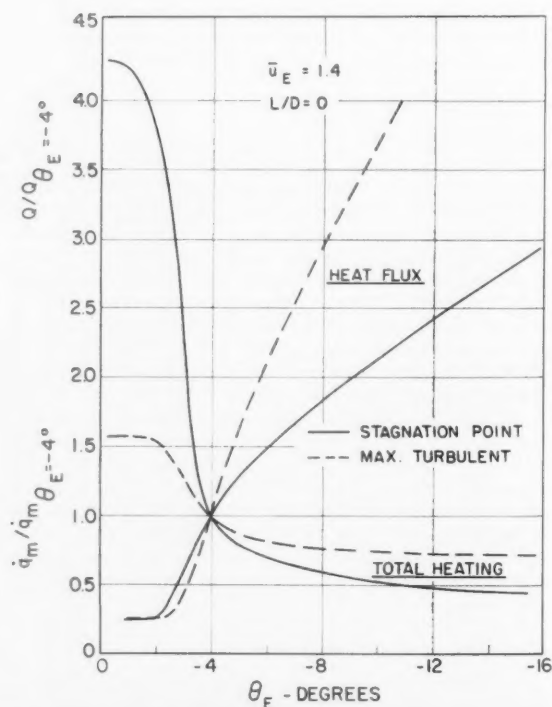


Fig. 7 Effect of re-entry angle on maximum heat flux and total heating for escape velocity re-entry

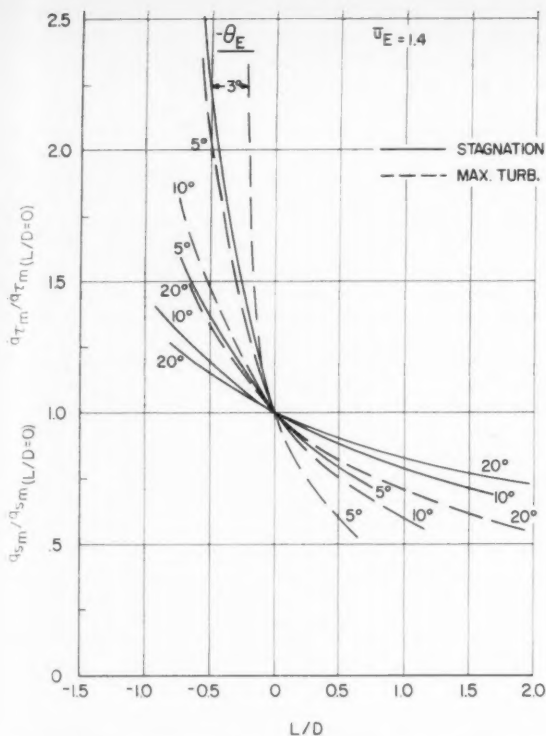


Fig. 8 Effect of lift over drag ratio on maximum heat flux for escape velocity re-entry

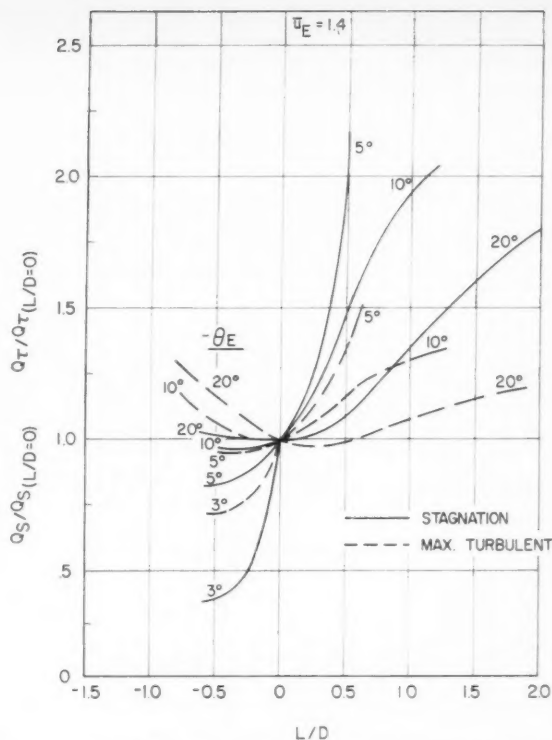


Fig. 9 Effect of lift over drag ratio on maximum total heating for escape velocity re-entry

entry angle up to a re-entry angle of  $-5$  deg. The laminar total heating increases more rapidly with  $L/D$  than the turbulent heating.

### Re-Entry at Escape Velocity

Re-entry at escape velocity represents the lower limit of velocity for vehicles returning from lunar or interplanetary flights. To obtain an understanding of the deceleration and heating for these flights, it is necessary to consider flights having a wide range of re-entry angles and lift over drag ratios. One important consideration for escape velocity re-entry is to re-enter at the minimum re-entry angle consistent with  $L/D$  to limit the deceleration and minimize the number of passes as desired. In general, as the deceleration decreases, so does the magnitude of the heat flux; but only at the expense of increased total heating.

The convective heat flux and total heat input for both laminar and turbulent flow are shown as a function of re-entry angle for zero lift vehicles in Fig. 7. As the re-entry angle decreases, the heat flux is reduced, while the total heating is increased. This trend holds until the re-entry angle is reduced down to about  $-1$  deg. A further reduction in angle will have little effect on heating. The influence of  $L/D$  on the heat flux and total heating is shown in Figs. 8 and 9 respectively for both laminar and turbulent flow. It should be noted that the results shown apply to flights having constant  $L/D$  throughout. A variation of  $L/D$  during flight may alter these results depending on the actual variation used. In general, as the  $L/D$  increases, the heat flux decreases. This trend is further increased by a decrease in re-entry angle. The total heating increases with increasing  $L/D$  except for the high re-entry angles. As the re-entry angle increases, the effect of  $L/D$  becomes less pronounced

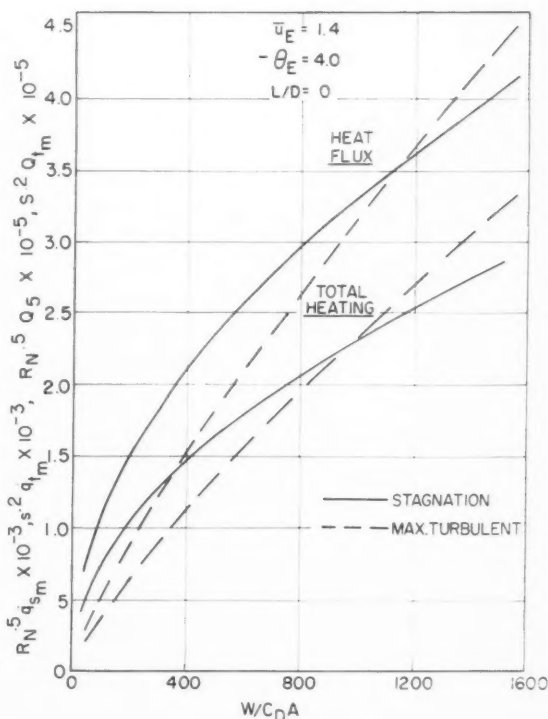


Fig. 10. Maximum heat flux and total heating for laminar and turbulent flow vs.  $W/C_D A$  for escape velocity re-entry

on the total heating. Up to  $-5$  deg the total heating increases rapidly with  $L/D$ , but at  $-20$  deg the total heating actually decreases as the lift is changed from negative to positive. Then, as  $L/D$  is increased above 0.3, the total heating increases. The above comparisons were all referenced to the heating at  $-4$  deg re-entry angle for convenience. The heat flux and total heat input at  $-4$  deg re-entry are shown in Fig. 10 as a function of  $W/C_{DA}$  for both laminar and turbulent flow. The heat flux and total heating for escape velocity re-entry are considerably higher than that for satellite re-entry. For a  $W/C_{DA}$  of 500 lb/ft<sup>2</sup> and a referenced length of one foot, the maximum heat flux becomes about 2350 and

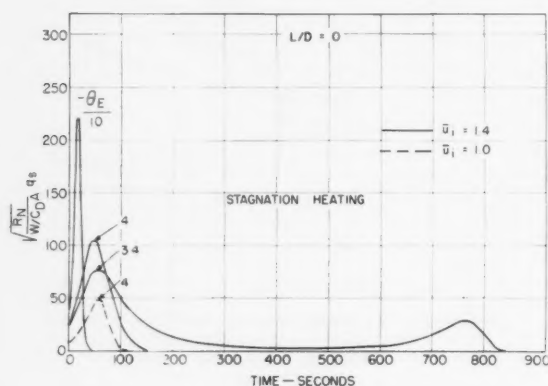


Fig. 11 Typical stagnation heat flux vs. re-entry time

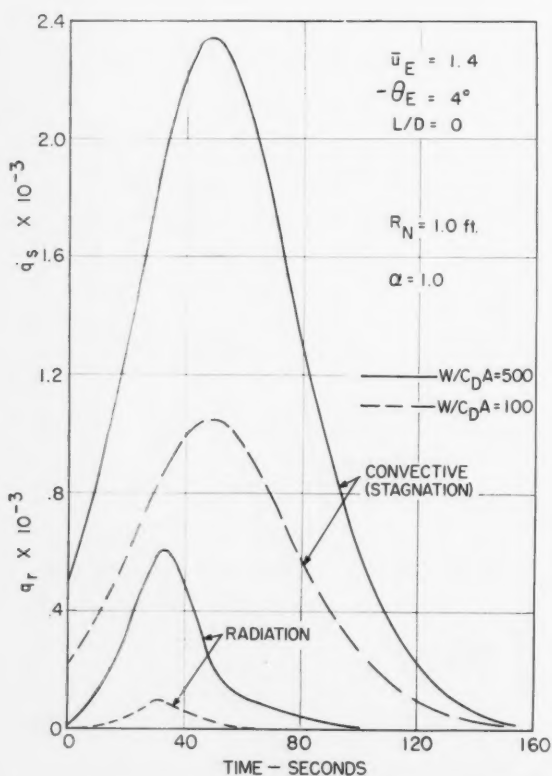


Fig. 12 Typical radiant and convective stagnation heat flux (Btu/ft<sup>2</sup>-sec) vs. time for escape velocity re-entry

1820 Btu/ft<sup>2</sup>/sec and the total heating becomes 164,000 and 134,000 Btu/ft<sup>2</sup> for laminar and turbulent flow, respectively. Typical stagnation heat flux curves are shown in Fig. 11 as a function of time for re-entry flights at  $-10$ ,  $-4$  and  $-3.4$  deg for zero lift vehicles. As the re-entry angle decreases, the maximum heat flux decreases, while the re-entry time increases. When the re-entry angle becomes small, a number of skips and passes may occur. This tendency increases as the lift increases. The heat flux for a  $-3.4$  deg re-entry shows a one skip flight. As the re-entry angle is reduced further, additional skips and/or passes will occur. The heat flux for a typical satellite re-entry is shown for reference. The heat flux is of course higher for an escape velocity flight. The turbulent heat flux curves are similar to the stagnation values, but displaced in time.

The radiant heat flux becomes a significant portion of the total heat input for escape velocity re-entry. The radiant and stagnation heat flux are shown for a typical flight of  $-4$  deg and  $L/D = 0$  in Fig. 12 for vehicles having a  $W/C_{DA}$  of 100 and 500. Although for this flight path the radiant heat flux is smaller than the convective, it is still a significant portion of the total heat input to the vehicle. Compared to a maximum stagnation heat flux of 2350 and 1050 Btu/ft<sup>2</sup> sec for a  $W/C_{DA}$  of 500 and 100 lb/ft<sup>2</sup>, respectively, for a one foot nose radius. As the radiant heat flux varies directly with  $R_n$  (neglecting absorption,  $k = 1.0$ ), while the stagnation heat flux varies as  $R_n^{-0.5}$ , it is readily seen that, even for this small re-entry angle flight for a vehicle with a large nose radius, the radiant heating will become a significant portion of the total heat input. It is therefore necessary to include the radiant heat input in any realistic evaluation of the total heat input to the re-entry vehicle.

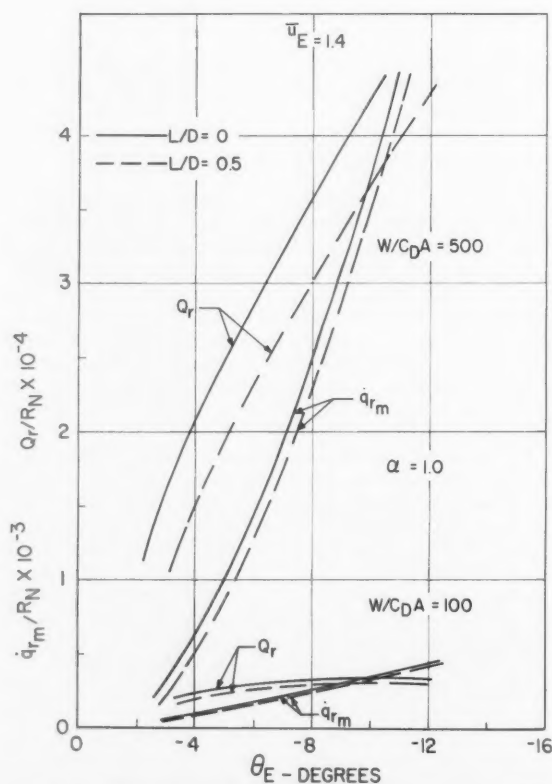


Fig. 13 Radiant heat flux and total heating vs. re-entry angle for escape velocity re-entry



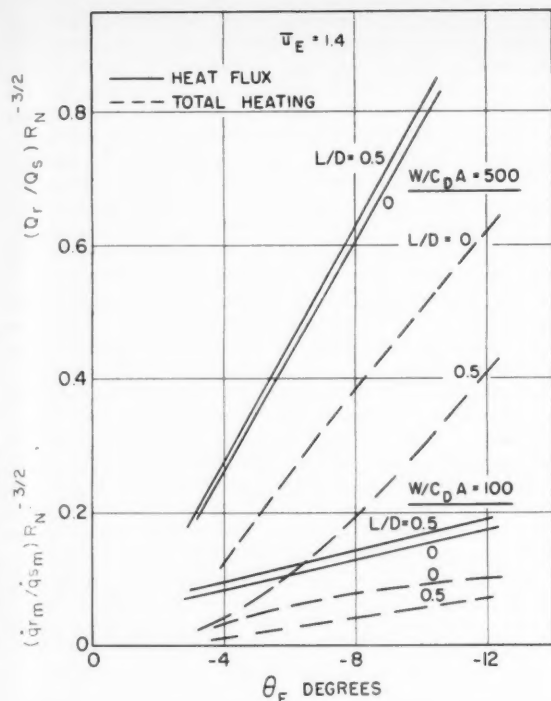


Fig. 14 Maximum radiant to maximum stagnation heat flux and total heating ratio vs. re-entry angle for escape velocity re-entry

Essentially, all the radiation exists between escape and satellite velocity, a compressed time scale compared to that for the convective heating. The magnitude of the maximum and total radiation input is shown in Fig. 13 as a function of re-entry angle,  $W/C_p A$ , and  $L/D$ . As  $L/D$  increases, the radiant heat flux and total heating decreases. Both the heat flux and total radiant heating increase with  $W/C_p A$ . A comparison of the radiant with the stagnation heating is shown in Fig. 14 as a function of re-entry angle. It should be noted that the maximum radiation and convective heat flux occurs at different points on the trajectory as indicated in Fig. 12. The radiation heat flux and total heating becomes a greater portion of the total heating as the re-entry angle is increased. The radiation heat flux increases from about 0.26 to 0.78 and the total radiant heating increases from about 0.12 to 0.50 of the stagnation heating when the re-entry angle increases from  $-4$  to  $-10$  deg at zero lift for a vehicle of one foot nose radius and  $W/C_p A$  of 500 lb/ft<sup>2</sup>. As the  $L/D$  increases, the radiant heat flux ratio increases, while the total radiation becomes a smaller portion of the total heating to the vehicle. It is noted that the radiant to stagnation convective heating is proportional to  $R_n^{3/2}$ . As the nose radius is increased, the ratio will increase very rapidly. This ratio actually increases as  $R_n^{3/2}$  only for relatively small changes in  $R_n$ . When the gas cap becomes relatively thick, the radiant to stagnation heating is proportional to  $k R_n^{3/2}$  due to absorption as described previously.

One of the major problems concerning escape velocity re-entry is to determine the optimum method of re-entry. In order to minimize the number of passes, deceleration, and heating during re-entry, the lift over drag ratio and re-entry angle must be closely regulated. The re-entry regime is shown in Fig. 15. It is apparent that  $L/D$  must be varied through the trajectory to minimize the heat input and the deceleration. It appears that a minimum number of passes

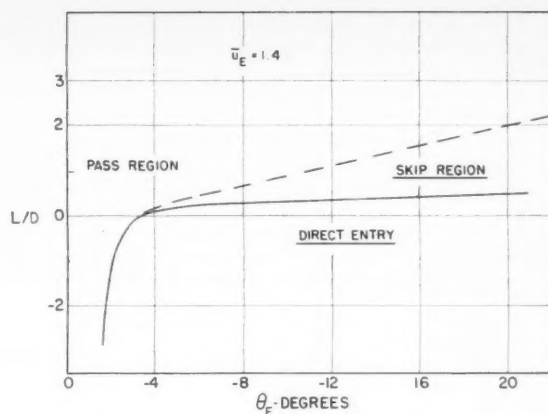


Fig. 15 Re-entry regime for escape velocity

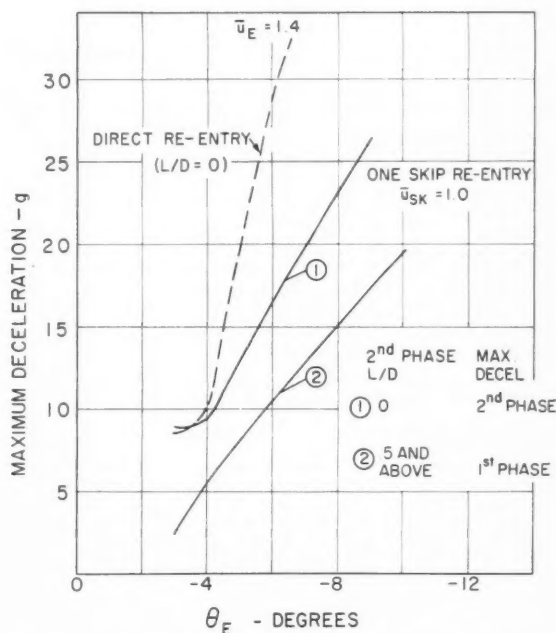


Fig. 16 Maximum deceleration vs. re-entry angle for direct entry and one skip flights ( $u_{sk} = 1.0$ )

are desirable to conserve time and improve accuracy. To obtain direct entry for re-entry angles of 0 to over  $-3$  deg, negative lift must be used. During the flight at  $u = 1.0$ , the  $L/D$  can be made positive to minimize the heating and deceleration. When the re-entry angle becomes greater than  $-4$  deg, negative lift is not actually required but, if used, it will greatly reduce the time of flight.

One method that appears attractive from a thermal and deceleration standpoint at escape velocity is to fly a trajectory with one skip at satellite velocity. The one skip type trajectory implies use of lift from escape velocity to satellite velocity. The magnitude of the  $L/D$  required is a function of the re-entry angle. For example, the  $L/D$  is about  $-0.2$  and  $+1.0$  for re-entry at  $-3$  and  $-10$  deg, respectively. A change of  $L/D$  at satellite velocity will permit normal re-entry from satellite velocity as described previously.

The maximum deceleration encountered with the one skip trajectory is shown in Fig. 16 as a function of re-entry angle. When the  $L/D$  is 0.5 or greater for the second portion of the flight (satellite velocity to impact), the maximum deceleration occurs in the first portion of the flight (escape to satellite velocity). When zero lift is used for the second portion, the maximum deceleration occurs in this second part of the flight. The deceleration for zero lift re-entry is given for reference purposes. This one skip flight allows re-entry at higher angles for the same maximum deceleration. A  $-6$  deg one skip flight will produce about the same maximum deceleration as a  $-4$  deg zero lift flight. Higher lift in the first portion

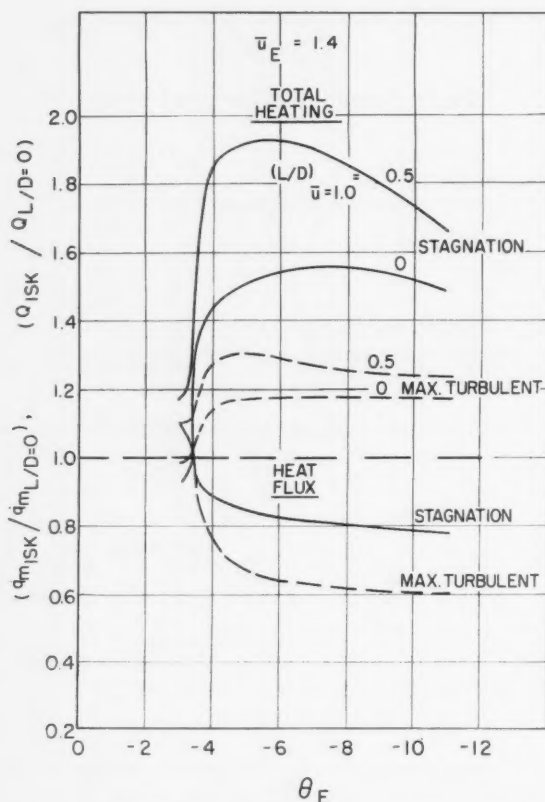


Fig. 17 Effect of one skip flight ( $\bar{u}_{SK} = 1.0$ ) on maximum heat flux and total heating for escape velocity re-entry

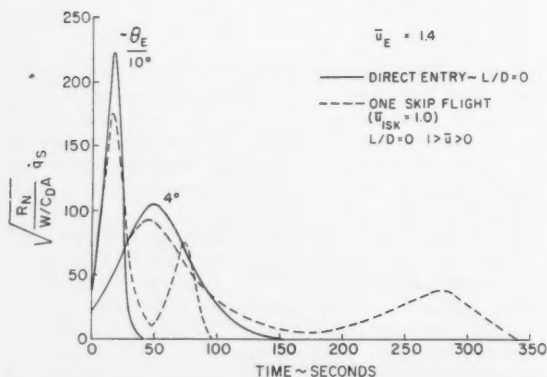


Fig. 18 Heat flux vs. time for escape velocity re-entry for direct entry and one skip flights ( $\bar{u}_{SK} = 1.0$ )

tion will reduce the deceleration even further, at the expense, however, of producing more skips which may occur at greater than satellite velocity.

The heat flux and total heating for the one skip flight is shown in Fig. 17 as a function of re-entry angle. The heat input is given in a dimensionless form ( $\dot{q}_{ISK}/\dot{q}_{L/D=0}$ ) and ( $Q_{ISK}/Q_{L/D=0}$ ), which denotes the ratio of the heat input for the complete one skip flight (from escape velocity to impact), compared to the normal zero lift direct re-entry flight. The maximum heat flux occurs in the first portion of the flight. The maximum stagnation heat flux is only 89 and 79% of the zero lift direct re-entry heat flux for  $-4$  and  $-10$  deg, respectively. The turbulent heating is reduced by a somewhat larger amount. The total heating for the one skip flight is increased and is a function of the  $L/D$  used for the second portion of the flight. As  $L/D$  increases, the total heating becomes larger. The total stagnation heating is about 1.44 and 1.51 times as great as the heating for direct zero lift re-entry at  $-4$  and  $-10$  deg, respectively. A much less total heating ratio occurs for the turbulent flow.

The heat flux for the one skip flight is shown in Fig. 18 as a function of time. The  $-4$  and  $-10$  deg one skip re-entry flights are shown with the direct entry flights for comparison purposes. In all cases the one skip flight has two heat flux pulses, while the direct re-entry flight has one. In general, the heat flux is lower and the time is longer than for a zero lift direct re-entry flight. The re-entry time of the one skip flight will depend on the  $L/D$  in the second portion of flight from satellite to impact. Zero lift was used in the second portion of the one skip flights shown in Fig. 18. There are many combinations of lift (4) which may be of further advantage to meet the specific requirements of a flight.

For unmanned flights where the deceleration is not a major consideration, it appears that direct entry with minimum re-entry time is desirable. Although the maximum heat flux may be materially increased by such flights, the total heating will be reduced and the heat protection system may actually be simplified.

## Conclusions

An analysis was made of the aerodynamic and radiant heat input to space vehicles which re-enter at satellite and escape velocity. The vehicle motion used throughout was similar to that of Chapman (3); the aerodynamic heating was described by the reference enthalpy method (1) for both laminar and turbulent flow; and the gas cap radiation was obtained from the significant radiating species in high temperature air (2). The important reaction at escape velocity is the ionization of oxygen and nitrogen atoms. At escape velocity the ionization will increase the heat transfer rates by about 10 to 20% over that for the extended nonionized heating rates (13). At satellite velocity the effect of ionization on the heating will be negligible. The maximum laminar and turbulent heating were specified for a wide range of  $W/CDA$ , re-entry angles, and lift over drag ratios. This analysis was made primarily to provide an understanding of satellite and escape velocity re-entry for preliminary design purposes.

Re-entry at satellite velocity is in general similar to re-entry at somewhat lower velocity, except the magnitudes of the deceleration and heating are higher. The radiant heat input is a small portion of the total heat input. At re-entry of  $-5$  deg and a  $W/CDA$  of 500 lb/ft<sup>2</sup>, the radiant heat flux amounts to less than 10% of the stagnation heat flux for a one foot nose radius and zero lift. In general, the aerodynamic heat flux decreases and the total heating increases with decreasing re-entry angle. A similar trend in heating occurs with increasing  $L/D$ . There is little change in heating between 0 and  $-0.5$  deg re-entry angle.

Re-entry at escape velocity presents a great many differences and complications compared to satellite re-entry. Skips and passes may readily occur depending on the re-

entry angle and  $L/D$ . The radiation from the gas cap becomes an appreciable portion of the total heat input. It can readily exceed the convective heating depending on the re-entry angle and nose radius. For a re-entry angle of  $-10$  deg, zero lift,  $W/C_D A$  of 500 lb/ft<sup>2</sup>, and one foot nose radius, the radiant heat flux is about 78% of the stagnation heat input. The aerodynamic heating varies with re-entry angle in a manner similar to that for satellite velocity, except the magnitude is different and there is little change in heating from 0 to  $-1$  deg re-entry angle. The effect of  $L/D$  on total heating becomes less pronounced as the re-entry angle is increased. At  $-20$  deg, the total heating at first decreases as  $L/D$  increases to 0.5; but then it increases with a further increase in  $L/D$ .

One method of re-entering at escape velocity is to utilize a one skip type trajectory ( $\bar{u}_{SK} = 1.0$ ) to minimize the deceleration and heating. A much wider re-entry corridor is available for this flight path. The maximum deceleration and maximum heat flux are materially reduced. This re-entry requires lift between escape and satellite velocity with normal re-entry from satellite to impact. For re-entry angles of  $-4$  deg and above there are, in general, two heat pulses compared to the one heat pulse for the direct zero lift type.

### Acknowledgment

The author would like to acknowledge the assistance of P. A. Yager with the calculations. This work was sponsored under Air Force contract AF 04(647)-269.

### Nomenclature

$A$	= area, ft <sup>2</sup>
$C_D$	= drag coefficient
$D$	= drag, lb
$D_{ij}$	= diffusion coefficient, ft <sup>2</sup> /sec
$g$	= acceleration of gravity, ft/sec <sup>2</sup>
$j$	= mechanical equivalent of heat ft-lb/Btu
$k$	= correction for nonoptically thin gas cap
$K$	= constant
$K_i$	= thermal conductivity, Btu/sec-ft deg R
$l$	= gas cap thickness, ft
$L$	= lift, lb
$m$	= mass, lb-sec <sup>2</sup> /ft
$p$	= pressure, lb/ft <sup>2</sup>
$\dot{q}$	= heat flux, Btu/ft <sup>2</sup> -sec
$Q$	= total heat, Btu/ft <sup>2</sup>
$r$	= radius from center of planet, ft
$R_n$	= nose radius, ft
$S$	= wetted length, ft
$T$	= temperature, deg R

$\bar{u}$	= $u/u_{sat}$
$u$	= horizontal velocity, fps
$v$	= vertical velocity, fps
$W$	= weight, lb
$t$	= time, sec
$y$	= altitude, ft
$Z$	= Eq. 3
$\alpha$	= absorptivity
$\beta$	= atmosphere constant, ft <sup>-1</sup>
$\epsilon$	= emissivity
$\theta_E$	= re-entry angle, deg
$\lambda$	= wavelength, ft
$\mu_i$	= viscosity, lb/sec ft
$\rho$	= density, lb/ft <sup>3</sup>
$\gamma$	= ratio of specific heats

### Subscripts

$B$	= base conditions
$g$	= gas cap
$L$	= laminar
$m$	= maximum
$s$	= stagnation
$t$	= turbulent
$1_{SK}$	= one skip trajectory
$SK$	= skip

### References

- 1 Brunner, M. J., "Analysis of the Aerodynamic Heating for a Re-Entrant Space Vehicle," *Trans. ASME, Series C*, vol. 81, no. 3, August 1959.
- 2 Kivel, B. and Bailey, K., "Tables of Radiation from High Temperature Air," AVCO Rep. 21, December 1957.
- 3 Chapman, D. R., "An Approximate Analytical Method for Studying Entry Into Planetary Atmospheres," NACA TN 4276, May 1958.
- 4 Lees, L., Hartwig, F. W. and Cohen, C. B., "The Use of Aerodynamic Lift During Entry Into the Earth's Atmosphere," ASME paper 59-AV-36.
- 5 Lees, L., "Laminar Heat Transfer Over Blunt Nosed Bodies at Hypersonic Flight Speeds," *JET PROPULSION*, April 1958, p. 259.
- 6 Li, Ting-Yi and Geiger, R. E., "Stagnation Point of a Blunt Body in Hypersonic Flow," *J. Aeronaut. Sci.*, vol. 24, no. 1, January 1957.
- 7 Hayes, W. D. and Probstein, R. F., *Hypersonic Flow Theory*, Academic Press, N. Y., 1959.
- 8 Serbin, H., "Supersonic Flow Around Blunt Bodies," *J. Aeronaut. Sci.*, Readers Forum, vol. 25, no. 1, Jan. 1958.
- 9 Moeckel, W. E. and Weston, K. C., "Composition and Thermodynamic Properties of Air in Chemical Equilibrium," NACA TN 4263, April 1958.
- 10 Camm, J. C., Kivel, B., Taylor, R. L. and Teare, D., "Absolute Intensity of Non-Equilibrium Radiation in Air and Stagnation Heating at High Altitudes," AVCO Research Laboratory Rep. 93, December 1959.
- 11 *Thermodynamics and Physics of Matter*, vol. 1, Princeton Series, Princeton Univ. Press, N. J.
- 12 Spitzer, L., *Physics of Fully Ionized Gases*, Interscience Publishers, N. Y., 1956.
- 13 Adams, Mac C., "A Look at the Heat Transfer Problem at Super-Satellite Speeds," (presented at the ARS 15th Annual Meeting, Washington D. C., Dec. 5-8, 1960. ARS preprint 1556-60).
- 14 Hansen, F. C., "Approximations For the Thermodynamic and Transport Properties of High Temperature Air," NASA TR 50-1959.

# A Simplified Model of Unstable Burning in Solid Propellants<sup>1</sup>

M. RICHARD DENISON<sup>2</sup>

Electro-Optical Systems, Inc.  
Pasadena, Calif.

ERIC BAUM<sup>3</sup>

Aeronutronic Division,  
Ford Motor Co.  
Newport Beach, Calif.

An analysis of the surface temperature, and hence mass flux, response of a solid propellant to a disturbance in gas pressure has been developed. Time lags in the gas phase are neglected while transient heat conduction in the solid is considered. The results are obtained by perturbing the conservation equations in both the gas phase and the solid phase. Stability conditions are obtained in terms of a few dimensionless parameters which depend upon the steady state conditions.

THE COUPLING of pressure disturbances with propellant combustion has been the subject of several recent investigations (1 through 5).<sup>4</sup> It is now generally accepted that this feature plays an important role in the mechanism of instability (6). The most elaborate of the recent analyses (2) obtains results in terms of eleven sets of parameters which can be varied independently. Many simplifications were required in order to obtain even this complex solution. The value of such an analysis is not in obtaining explicit mathematical relationships suitable for design calculations, but rather in obtaining an understanding of what physical conditions may be expected to have a large influence on the unstable burning phenomenon. Therefore, an analysis of comparable sophistication with results in a simpler form is desirable.

It was indicated by Hart and McClure (2) that a characteristic time for heat conduction in the solid is at least an order of magnitude greater than the characteristic times for the gas phase transport processes and the chemical reactions. This suggests that the gas may adjust very quickly to changes in conditions when compared to the response of the solid. In the case of periodic pressure disturbances, time lags in the solid phase may dominate, provided the period of the disturbance is large compared to the characteristic time for gas phase adjustment. Thus, there is an upper limit in the frequency of the pressure disturbance above which an analysis neglecting gas phase time lags does not apply. This limit, which would vary depending on the physical properties of the combustion gases, is on the order of  $10^4 - 10^5$  cps for many propellants.

The physical processes presumed to take place are as follows:

Consider first a step function increase in pressure. The response may be thought of as occurring in two phases. After the rapid application of the disturbance, the combustion zone moves quickly to a new position nearer the surface. Later it moves slowly as the surface temperature of the solid responds to the changed condition.

The mass flux leaving the surface is less than would normally occur at the new pressure because, during the first period, the surface temperature does not have time to adjust to its steady state value. When relative motion between the combustion zone and the surface becomes small, the mass

flux leaving the surface must equal that passing through the combustion zone. Therefore, the flame temperature must be reduced until the solid surface temperature adjusts to its new steady state value. In order to maintain a reduced flame temperature, heat must be lost from the gas phase. Hence, the solid effectively feels a sudden increase in heat flux at its boundary. The response of the solid forms the second phase of the process. As the solid gradually readjusts to the imposed heat flux conditions, new motions of the combustion zone and changes in heat flux occur. However, the velocity of the combustion zone, controlled by solid phase adjustments, is small compared to the gas velocity, so that at each instant a quasi-steady state exists. If the proper steady state heat flux to the solid surface and proper temperature distribution in the solid occur simultaneously, the new steady state will have been attained. If, however, when the proper heat flux and surface temperature occur the distribution of temperature inside the solid does not correspond to that of the new steady state, further adjustments in the solid temperatures are required. Such conditions may lead to unstable burning.

The response to a periodic pressure disturbance is somewhat different with respect to the gas phase. The characteristic time for the gas phase is again assumed to be considerably less than that of the solid. If, in addition, the period of the pressure fluctuation is large compared to the time constant for gas phase adjustment, no time lags in the gas phase need be considered. At very low frequencies, a succession of steady states occur in both the gaseous and the condensed phase. At these frequencies, even the solid can follow any changes in conditions and no resonance occurs. At moderately high frequencies although the gas phase can still respond instantly, time lags in the solid become important. Normally after transients have decayed, a steady oscillation in surface mass loss whose amplitude is small will be set up. However, if the forcing frequency is tuned to the natural frequency of the system, an oscillatory mass flux whose amplitude becomes large, or even tends to increase without bound, can occur. At still higher frequencies time lags in the gas phase may become important. Probably at these frequencies, the heat flux oscillations are too rapid to influence the solid temperature distribution. A study of the very high frequency response is beyond the scope of this analysis.

On the basis of the physical processes described, an analysis has been developed in which time lags in the gas phase are neglected while transient conduction in the solid phase takes place. The results are obtained by means of a perturbation of laminar flame conditions and transient heat conduction

Received Nov. 25, 1960.

<sup>1</sup> This work was carried out at Aeronutronic and was sponsored by the Naval Bureau of Weapons under Contract NOrd 17945.

<sup>2</sup> Principal Scientist, Fluid Physics Div.

<sup>3</sup> Research Engineer, Chemistry Dept.

<sup>4</sup> Numbers in parentheses indicate References at end of paper.



in the solid phase. No artificial time delays or empirical burning rate laws are introduced. Instead, the burning rate and heat flux laws are developed from the conservation equations. Of course, steady state burning itself is poorly understood so that the nonsteady analysis suffers from the same difficulties and various approximations must be made. The principal assumptions include homogeneous propellant, Lewis number of unity, single step combustion reaction of any order, no reactions in the solid state, vaporization according to an Arrhenius law and no erosive burning. It is hoped that the results will apply to more general systems with little modification. The model chosen has the advantage of simplicity. The stability conditions are obtained in terms of a few dimensionless parameters which depend upon the steady-state conditions only.

## Gas Phase Conservation Equations

It is assumed with regard to conservation of momentum that inertial and viscous terms are small and that the wavelength of any periodic disturbance is large compared to the distance from the combustion zone to the solid surface. Therefore, the momentum equation reduces to  $P = P(t)$ . With respect to species continuity, it is assumed that all diffusion coefficients are equal and that diffusion due to thermal gradients is small compared to that due to concentration gradients. In addition, a single chemical reaction of any order is assumed to occur in the combustion zone. The appropriate conservation equations for the gas phase are then as follows:

Overall continuity

$$\frac{\partial \rho}{\partial t} + \frac{\partial m}{\partial y} = 0 \quad [1]$$

Molecular species continuity

$$\rho \frac{\partial K_i}{\partial t} + m \frac{\partial K_i}{\partial y} - \frac{\partial}{\partial y} \rho D \frac{\partial K_i}{\partial y} = w_i(K_i, T; P) \quad [2]$$

where

$$w_i = M_i(v_i'' - v_i') \left[ k_f \Pi_j \left( \frac{\rho K_j}{M_j} \right)^{v_j'} - k_b \Pi_j \left( \frac{\rho K_j}{M_j} \right)^{v_j''} \right]$$

Atomic species continuity

$$\rho \frac{\partial \Gamma_m}{\partial t} + m \frac{\partial \Gamma_m}{\partial y} - \frac{\partial}{\partial y} \rho D \frac{\partial \Gamma_m}{\partial y} = 0 \quad [3]$$

where

$$\Gamma_m = \sum_i \frac{M_m}{M_i} \alpha_{mi} K_i$$

Energy

$$\rho \frac{\partial h}{\partial t} + m \frac{\partial h}{\partial y} - \frac{\partial}{\partial y} \frac{K}{C_p} \frac{\partial h}{\partial y} - \frac{\partial}{\partial y} \left[ \frac{K}{C_p} \{Le - 1\} \sum_i h_i \frac{\partial K_i}{\partial y} \right] = \frac{dp}{dt} \quad [4]$$

where

$$h = \sum_i K_i h_i \quad h_i = \int_0^T c_{pi} dT + h_i^\circ$$

A possible solution to the equation of atomic species conservation is  $\Gamma_m = \text{const}$ . This solution will later be found to satisfy the boundary conditions so Eq. 3 may be considered solved. In the remaining equations, all time derivatives are neglected due to the assumptions already discussed. The continuity equation then yields

$$m = m_w(t) \quad [5]$$

Define

$$\epsilon_i = K_i - \frac{\rho D}{m_w} \frac{dK_i}{dy} \quad [6]$$

The quantity  $\epsilon_i$  represents a fraction of the total mass flux associated with the  $i$ th species. The molecular species continuity equation becomes

$$m_w \frac{d\epsilon_i}{dy} = w_i \quad [7]$$

The conditions of constant atomic mass fractions and single reaction step serve to reduce the set of Eqs. 7 to a single equation in terms of a reference species arbitrarily chosen. Because  $\Gamma_m$  is constant

$$\sum_i \frac{M_m}{M_i} \alpha_{mi} K_i = \sum_i \frac{M_m}{M_i} \alpha_{mi} \epsilon_i = \Gamma_m \quad [8]$$

It is convenient to evaluate the constant at the outer edge of the flame zone where gradients are assumed to vanish.

Then

$$\sum_i \frac{M_m}{M_i} \alpha_{mi} (\epsilon_i - \epsilon_{if}) = 0 \quad [9]$$

$$\sum_i \frac{M_m}{M_i} \alpha_{mi} (K_i - K_{if}) = 0 \quad [10]$$

where  $\epsilon_{if} = K_{if}$  are the mass fractions at the outer edge of the flame zone. For a single reaction by conservation of atoms

$$\sum_i \alpha_{mi} (v_i' - v_i'') = 0 \quad [11]$$

Define

$$R_i = \frac{(v_i'' - v_i') M_i}{(v_r'' - v_r') M_r} \quad [12]$$

Then in terms of a reference species  $r$  by Eqs. 9 through 12

$$(\epsilon_i - \epsilon_{if}) = R_i (\epsilon_r - \epsilon_{rf}) \quad [13]$$

$$(K_i - K_{if}) = R_i (K_r - K_{rf}) \quad [14]$$

Since all the species can be determined in terms of a single reference species, only one of the set of Eqs. 7 must be considered.

In order to obtain an equation for the temperature distribution from the species continuity and energy equations, it is convenient to assume that the specific heats of all species are equal and constant. Although this assumption represents a rather crude approximation for some gas mixtures, the main features of the process should be retained. Under these conditions, it can be shown that

$$h = C_p T + (K_r - K_{rf}) Q_r + \sum_i K_i h_i^\circ \quad [15]$$

where

$$Q_r = \sum_i R_i h_i^\circ = \text{const}$$

Use of this relation in the energy equation and combination with the species conservation relation of Eq. 7 lead to

$$m_w \frac{d}{dy} \left( T - \frac{K}{C_p m_w} \frac{dT}{dy} \right) = - \frac{Q_r}{C_p} w_r \quad [16]$$

## Boundary Conditions

The mass flux issuing from the cold boundary depends upon a vaporization process. It is assumed that this process is far from equilibrium so that the back flux of molecules from

the gas can be neglected in comparison to the flux due to vaporization. The process is assumed to follow an Arrhenius law so that the mass flux relative to the burning surface is

$$m_w = I \exp(-E_w/RT_w) \quad [17]$$

The reactant species are assumed to be in perfect stoichiometric proportions so that complete combustion can occur. Furthermore, the flux of each reactant species is assumed to be always a fixed fraction of the total mass flux. Therefore,  $\epsilon_{jw}$  is known for the  $j$ th reactant at the surface. It is also reasonable to assume that there is no net mass flux for products of the combustion reaction which may have diffused to the surface. Therefore,  $\epsilon_{lw} = 0$  for the  $l$ th product of combustion.

At the hot boundary where  $T = T_f$  it is assumed that complete combustion occurs and all gradients vanish so that  $\epsilon_{jf} = K_{jf} = 0$  for the  $j$ th reactant. For product species from Eqs. 8 and 9

$$K_{lf} = \epsilon_{lf} = -\frac{R_l}{R_j} \epsilon_{jw} \quad [18]$$

Thus,  $\epsilon_i$  is known at both boundaries while  $K_i$  is known at the hot boundary. The value of  $K_i$  at the surface for cases in which diffusion is important cannot be determined until the solutions from the gas phase and solid phase are matched. In the special case of  $Le = 0$ , however,  $K_{iw} = \epsilon_{iw}$ .

Another boundary condition is supplied by a heat balance at the solid surface. The heat conducted into the solid is given by

$$\left(K \frac{\partial T}{\partial y}\right)_{sw} = \left(K \frac{\partial T}{\partial y}\right)_{ow} - \sum_i m_i w_i h_{i,w} + m_w h_{sw} \quad [19]$$

This can be put in an alternate form which will later prove convenient for matching solutions

$$\left(K \frac{\partial T}{\partial y}\right)_{sw} = \left(K \frac{\partial T}{\partial y}\right)_{ow} + m_w (C_s T_w - C_p T_w - L) \quad [20]$$

where

$$L = \sum_i \epsilon_i w_i h_i^0 - h_s^0$$

The quantity  $L$  represents the heat absorbed by vaporization and decomposition.

### Solution of Gas Phase Equations

The energy and species conservation equations can be integrated simultaneously to yield a relation for the temperature gradient at any point in the gas phase

$$\frac{K}{C_p m_w} \frac{dT}{dy} = -\left(T_f - T - \frac{Q_r}{C_p} \epsilon_r\right) \quad [21]$$

This relationship can then be used in the species continuity equation to eliminate  $dy$

$$\left(T_f - T - \frac{Q_r}{C_p} \epsilon_r\right) m_w^2 \frac{d\epsilon_r}{dT} = -\frac{K}{C_p} w_r(T, K_r; P) \quad [22]$$

In order to carry out integration in a simple manner, the variation of conductivity with temperature, the influence of the back reaction, and the variation of molecular weight are neglected. The rate of production of reactant  $r$  is therefore given by

$$w_r \cong -\nu_r' M_r k_f \left(\frac{PK_r}{R_0 T}\right)^n \prod (R_i)^{\nu_i'} \quad [23]$$

where

$$n = \sum \nu_i' \quad k_f = \beta \exp(-E_f/RT)$$

Since a single reaction step has been assumed,  $n$  should be an integer. However, some complicated reactions may be approximated by expressions of the above form when  $n$  is not an integer.

After introduction of dimensionless variables, Eq. 22 assumes the form

$$\left[\frac{Q_r}{C_p T_f} \epsilon_r - (1 - \theta)\right] \frac{d\epsilon_r}{d\theta} = -\Lambda \frac{K_r^n \exp[-\theta_a(1/\theta - 1)]}{\theta^n} \quad [24]$$

where

$$\theta = \frac{T}{T_f} \quad \theta_a = \frac{E_f}{RT_f} \quad \Lambda = \nu_r' M_r \beta e^{-\theta_a} \prod_j (R_j)^{\nu_j'} \frac{K}{C_p m_w^2}$$

In the special case of Lewis number equal to unity, the mass fraction can be expressed as a linear function of the temperature

$$Le = 1 \quad K_r = \frac{C_p T_f}{Q_r} (1 - \theta) \quad [25]$$

In order to solve Eq. 24 a numerical integration technique is required. It was suggested by von Kármán (7) that as a first step in the iteration processes, a linear relationship between mass fraction and temperature such as Eq. 25 should be substituted on the right hand side of Eq. 24 even though the relationship applies rigorously only to the case of  $Le = 1$ . Furthermore, von Kármán argues that for purposes of what he calls the zeroth order approximation, the second term in the brackets may be dropped in comparison to the first term. This corresponds to neglecting in the energy balance the change of heat content of the mixture in comparison to the heat transfer by conduction and the heat production by chemical reaction. With this assumption the variables are separated and Eq. 24 can be integrated. At the cooler boundary of the combustion zone where the ignition temperature is  $\theta_c$  the value of the mass flux fraction is  $\epsilon_{rc}$ .

For large  $\theta_a$  the integration can be carried out by means of asymptotic expansions. The result is

$$m_w \epsilon_{rc} \cong C_* P^{N/2} T_f^{(n/2+1)} \exp(-E_f/2RT_f) \quad [26]$$

where  $C_*$  is a constant. It is not essential to carry out further iterations to obtain better approximations to Eq. 26 since it is to be used only for an indication of the temperature and pressure dependence rather than for predicting burning rates. Although this approximate result applies strictly to the case of  $Le = 1$ , it should be a fair approximation for other values of Lewis number. Perhaps the influence of the order of reaction on the temperature dependence is not as accurate in other cases, but the temperature sensitivity should be dominated by the exponential term. In the region between the combustion zone and the solid surface, the rate of production is negligible so that from Eq. 7,  $\epsilon_{rc} = \epsilon_{rw}$ , which is known.

### Gas Phase Perturbation Relations

If a small pressure disturbance occurs, the temperature and mass flux will be disturbed from their steady state values. Let each physical quantity be the sum of a steady and perturbed component

$$m_w = \bar{m}_w + m_w' \quad P = \bar{P} + P' \quad T = \bar{T} + T' \quad (27)$$

After introduction of these expressions in the vaporization condition, Eq. 17, the burning rate law, Eq. 26, and the heat flux boundary condition, Eqs. 20 and 21, and retaining only first order terms in the perturbed quantities, the following expressions result

$$\frac{m_w'}{\bar{m}_w} = \frac{E_w}{RT_w} \frac{T_w'}{\bar{T}_w} \quad [28]$$

$$\frac{m_w'}{\bar{m}_w} = \frac{n}{2} \frac{P'}{\bar{P}} + \left( \frac{n+2}{2} + \frac{E_f}{2RT_f} \right) \frac{T_f'}{\bar{T}_f} \quad [29]$$

$$\frac{K_s}{\bar{m}_w C_s} \left( \frac{\partial T'/T_w}{\partial y} \right)_{sw} = \frac{m_w'}{\bar{m}_w} \left[ 1 + \frac{(\epsilon_{rw} Q_r - C_p T_f - L)}{C_s \bar{T}_w} \right] + \frac{T_w'}{\bar{T}_w} - \frac{C_p T_f'}{C_s \bar{T}_w} \quad [30]$$

If the temperature distribution in the solid were able to follow the heat transfer conditions imposed by pressure variations, then the flame temperature would not vary. Otherwise it can be seen from Eqs. 28 and 29 that if the mass flux at the combustion zone is to be able to follow changes in the mass flux issuing from the surface as determined by a lagging surface temperature, then the flame temperature must change. The set of Eqs. 28, 29, and 30 determine a heat flux boundary condition for transient conduction in the solid.

### Transient Heat Conduction in the Solid

If chemical reactions in the solid phase are neglected, the differential equation governing heat transfer in the solid phase is

$$\rho_s C_s \frac{\partial T}{\partial t} = -m_w C_s \frac{\partial T}{\partial y} + K_s \frac{\partial^2 T}{\partial y^2} \quad [31]$$

In the steady state the temperature distribution is given by

$$T - T_i = (T_w - T_i) \exp \left\{ \frac{\bar{m}_w C_s y}{K_s} \right\} \quad [32]$$

The heat flux is given by

$$K_s \left( \frac{\partial T}{\partial y} \right)_s = \bar{m}_w C_s (T_w - T_i) \exp \left\{ \frac{\bar{m}_w C_s y}{K_s} \right\} \quad [33]$$

These relations satisfy the boundary conditions

$$\begin{aligned} \text{at } y = 0, \quad T &= T_w \\ \text{at } y = -\infty, \quad T &= T_i \end{aligned} \quad [34]$$

By matching the heat flux at the surface given by Eq. 33 with that obtained from the gas phase boundary condition expressed by Eqs. 20 and 21, the following relationship is obtained for the steady state

$$(\epsilon_{rw} Q_r - C_p T_f - L) = -C_s T_i \quad [35]$$

For the perturbed equations it is convenient to introduce the following parameters

$$\Omega = \frac{\bar{m}_w^2 C_s}{\rho_s K_s} \quad A = \frac{E_w}{R \bar{T}_w} (1 - T_i/T_w)$$

$$y_* = - \frac{\bar{m}_w C_s}{K_s} y \quad [36]$$

The dimensionless distance is, therefore, measured inward from the surface. The perturbed differential equation is then given by

$$\frac{1}{\Omega} \frac{\partial T'/T_w}{\partial t} = \frac{\partial T'/T_w}{\partial y_*} - A \frac{T_w'}{\bar{T}_w} e^{-y_*} + \frac{\partial^2 T'/T_w}{\partial y_*^2} \quad [37]$$

The boundary condition at a large distance from the surface is given by

$$y_* \rightarrow \infty \quad T' \rightarrow 0 \quad [38]$$

At the surface, the heat flux boundary condition of Eq. 30 can be transformed by means of Eqs. 28, 29, 35, and 36 to yield

$$- \left( \frac{\partial T'/T_w}{\partial y_*} \right)_{sw} = q \frac{T_w'}{\bar{T}_w} + \alpha B \frac{P'}{\bar{P}} \quad [39]$$

where

$$\begin{aligned} q &= [1 + A(1 - \alpha)] & \alpha &= \frac{C_p T_f}{C_s (\bar{T}_w - T_i) \epsilon} \\ \epsilon &= \frac{n+2}{2} + \frac{E_f}{2RT_f} & B &= \frac{n}{2} \left( 1 - \frac{T_i}{\bar{T}_w} \right) \end{aligned}$$

By use of the Laplace transform the differential equation and boundary conditions become

$$\frac{P}{\Omega} v = \frac{dv}{dy_*} + \frac{d^2 v}{dy_*^2} - A v_w e^{-y_*} \quad [40]$$

at

$$y_* = \infty, \quad v = 0 \quad [41]$$

$$y_* = 0, \quad - \left( \frac{dv}{dy_*} \right)_w = q v_w + \alpha B F \quad [42]$$

where  $L(T'/T_w) = v$ ;  $L(P'/\bar{P}) = F$ .

The solution to Eq. 40 may be expressed as a linear sum of a solution to the homogeneous equation  $v_c$  and a particular solution  $v_p$ . Let

$$v_c = C e^{\lambda y_*} \quad [43]$$

The characteristic equation for  $\lambda$  is

$$\lambda^2 + \lambda - \frac{P}{\Omega} = 0 \quad [44]$$

The root which corresponds to a solution that satisfies the boundary condition at infinity is

$$\lambda = - \frac{1}{2} \left[ 1 + \sqrt{1 + \frac{4P}{\Omega}} \right] \quad [45]$$

The particular solution is

$$v_p = C_2 e^{-y_*} \quad [46]$$

The solution at  $y_* = 0$  will determine the surface temperature and hence the mass flux response. From the differential equation, Eq. 40, the following relation is obtained

$$\frac{P}{\Omega} C_2 = -A v_w \quad [47]$$

Use of the boundary condition given by Eq. 42 with the above relations leads to the Laplace transform of the solution

$$v = \frac{-\alpha B \lambda F}{\lambda^2 + q\lambda + A} \left\{ \left( 1 + \frac{A\Omega}{P} \right) e^{\lambda y_*} - \frac{A\Omega}{P} e^{-y_*} \right\} \quad [48]$$

The solution is given formally by the inverse Laplace transform

$$\frac{T'}{\bar{T}} = - \frac{\alpha B}{2\pi i} \int_{\gamma-i\infty}^{\gamma+i\infty} \frac{\lambda F e^{\lambda y_*}}{\lambda^2 + q\lambda + A} \left\{ \left( 1 + \frac{A\Omega}{P} \right) e^{\lambda y_*} - \frac{A\Omega}{P} e^{-y_*} \right\} dP \quad [49]$$

By making the change in variable

$$S = 1 + \frac{4P}{\Omega} \quad [50]$$

this can be written

$$\begin{aligned} \frac{T'}{T} &= \frac{\alpha B}{\pi i} \exp(-\ell\Omega/4) \int_{\gamma'-i\infty}^{\gamma'+i\infty} \frac{\Omega F(1+S^{1/2}) \exp(S\ell\Omega/4) \{ (S-1+4A) \exp[-1/2(1+S^{1/2})y_*] - 4Ae^{-y_*} \}}{4[S+2(1-q)S^{1/2}+4A-2q+1](S-1)} dS \\ &= \frac{\alpha B}{\pi i} \exp(-\ell\Omega/4) \int_{\gamma'-i\infty}^{\gamma'+i\infty} g(S) \exp(S\ell\Omega/4) dS \\ &= 2\alpha B \exp(-\ell\Omega/4) G\left(\frac{\ell\Omega}{4}\right) \end{aligned}$$

where

$$L\left\{G\left(\frac{\ell\Omega}{4}\right)\right\} = g(S)$$

Since (see Reference 8)

$$L^{-1}\{g(S)\} = \sqrt{\frac{4}{\pi\Omega\ell}} \int_0^\infty \exp(-\eta^2/\ell\Omega) L^{-1}_{(\eta)}\{ug(u)\} d\eta$$

where  $u = S^{1/2}$ , Eq. 51 can be written in the more convenient form

$$\frac{T'}{T} = 2\alpha B \exp(-\ell\Omega/4) \sqrt{\frac{4}{\pi\Omega\ell}} \int_0^\infty \exp(-\eta^2/\ell\Omega) L^{-1} \left\{ \frac{\Omega F u(1+u) [(u^2-1+4A) \exp(-1/2(1+u)y_*) - 4Ae^{-y_*}]}{4[u^2+2(1-q)u+4A-2q+1](u^2-1)} \right\} d\eta \quad [52]$$

Let

$$u^2 + 2(1-q)u + 4A - 2q + 1 = (u+u_1)(u+u_2)$$

where

$$u_1 = 1 - q - \sqrt{q^2 - 4A} \quad [53]$$

$$u_2 = 1 - q + \sqrt{q^2 - 4A} \quad [54]$$

Now consider the case in which pressure is a step function of time

$$F(P) = \frac{f}{P}$$

$$F(S) = \frac{4f}{\Omega(S-1)}$$

$$F(u) = \frac{4f}{\Omega(u^2-1)}$$

where  $f$  is the amplitude.

The inverse transform in Eq. 52 is

$$\begin{aligned} L^{-1} \left\{ \frac{fu[u^2-1+4A] \exp(-1/2(1+u)y_*) - 4Ae^{-y_*}}{(u+1)(u-1)^2(u+u_1)(u+u_2)} \right\} \\ = f[A_1 e^{-\eta} + A_2 e^{\eta} + A_3 \eta e^{\eta} + A_4 e^{-u_1 \eta} + A_5 e^{-u_2 \eta}] \quad \eta < \frac{y_*}{2} \end{aligned}$$

$$= f[(A_1 + B_1)e^{-\eta} + (A_2 + B_2)e^{\eta} + (A_3 + B_3)\eta e^{\eta} + (A_4 + B_4)e^{-u_1 \eta} + (A_5 + B_5)e^{-u_2 \eta}] \quad \eta > \frac{y_*}{2}$$

where:

$$A_1 = \frac{Ae^{-y_*}}{(u_1-1)(u_2-1)}$$

$$A_2 = \frac{-A(u_1 u_2 - u_1 - u_2 - 3)e^{-y_*}}{(1+u_1)^2(1+u_2)^2}$$

$$A_3 = \frac{-2Ae^{-y_*}}{(1+u_1)(1+u_2)}$$

$$A_4 = \frac{4A u_1 e^{-y_*}}{(1-u_1)(1+u_1)^2(u_2-u_1)}$$

$$A_5 = \frac{4A u_2 e^{-y_*}}{(1-u_2)(1+u_2)^2(u_1-u_2)}$$

$$B_1 = \frac{-A}{(u_1-1)(u_2-1)}$$

$$B_2 = \frac{e^{-y_*}}{(1+u_1)(1+u_2)} - A_2 - \frac{A y_* e^{-y_*}}{(1+u_1)(1+u_2)}$$

$$B_3 = \frac{2Ae^{-y_*}}{(1+u_1)(1+u_2)} = -A_3$$

$$B_4 = \frac{-u_1(u_1^2-1+4A) \exp[-(y_*/2)(1-u_1)]}{(1-u_1)(1+u_1)^2(u_2-u_1)}$$

$$B_5 = \frac{-u_2(u_2^2-1+4A) \exp[-(y_*/2)(1-u_2)]}{(1-u_2)(1+u_2)^2(u_1-u_2)}$$



Eq. 52 can now be written

$$\frac{T'}{T} = 2\alpha B f e^{-(t\Omega/4)} \sqrt{\frac{4}{\pi\Omega t}} \left\{ \int_0^\infty e^{-\eta^2/t\Omega} [A_1 e^{-\eta} + A_2 e^\eta + A_4 e^{-u_1\eta} + A_5 e^{-u_2\eta}] d\eta + \right. \\ \left. \int_{y_*/2}^\infty e^{-\eta^2/t\Omega} [B_1 e^{-\eta} + B_2 e^\eta + B_4 e^{-u_1\eta} + B_5 e^{-u_2\eta}] d\eta + \int_0^{y_*/2} A_3 \eta \exp \left[ \left( \frac{-\eta^2}{t\Omega} + \eta \right) \right] d\eta \right\}$$

which can be reduced to the form

$$\begin{aligned} \frac{T'}{T} = 2\alpha B f \left\{ A_1 \operatorname{erfc} \left( \sqrt{\frac{t\Omega}{4}} \right) + A_2 \operatorname{erfc} \left( -\sqrt{\frac{t\Omega}{4}} \right) + A_4 \exp \left[ (u_1^2 - 1) \frac{t\Omega}{4} \right] \operatorname{erfc} \left( u_1 \sqrt{\frac{t\Omega}{4}} \right) + \right. \\ A_5 \exp \left[ (u_2^2 - 1) \frac{t\Omega}{4} \right] \operatorname{erfc} \left( u_2 \sqrt{\frac{t\Omega}{4}} \right) + B_1 \operatorname{erfc} \left( \frac{y_*}{2\sqrt{t\Omega}} + \sqrt{\frac{t\Omega}{4}} \right) + B_2 \operatorname{erfc} \left( \frac{y_*}{2\sqrt{t\Omega}} - \sqrt{\frac{t\Omega}{4}} \right) \\ + B_4 \exp \left[ (u_1^2 - 1) \frac{t\Omega}{4} \right] \operatorname{erfc} \left( \frac{y_*}{2\sqrt{t\Omega}} + u_1 \sqrt{\frac{t\Omega}{4}} \right) \\ + B_5 \exp \left[ (u_2^2 - 1) \frac{t\Omega}{4} \right] \operatorname{erfc} \left( \frac{y_*}{2\sqrt{t\Omega}} + u_2 \sqrt{\frac{t\Omega}{4}} \right) \\ + A_3 \frac{t\Omega}{2} \left[ \operatorname{erfc} \left( -\sqrt{\frac{t\Omega}{4}} \right) - \operatorname{erfc} \left( \frac{y_*}{2\sqrt{t\Omega}} - \sqrt{\frac{t\Omega}{4}} \right) \right] \\ \left. + A_3 \sqrt{\frac{t\Omega}{\pi}} \left[ \exp \left( -\frac{t\Omega}{4} \right) - \exp \left\{ -\left( \frac{y_*}{2\sqrt{t\Omega}} - \sqrt{\frac{t\Omega}{4}} \right)^2 \right\} \right] \right\} \end{aligned} \quad [56]$$

Suppose, now, that the forcing function is sinusoidal, so that

$$\begin{aligned} F(t) &= f \sin \omega t \\ F(P) &= \frac{f\omega}{P^2 + \omega^2} \\ F(S) &= \frac{f\omega}{\frac{\Omega^2}{16} (s-1)^2 + \omega^2} \\ F(u) &= \frac{16f\omega}{\Omega^2(u+u_3)(u+u_4)(u+u_5)(u+u_6)} \end{aligned}$$

where

$$u_3 = \sqrt{1 + \frac{i4\omega}{\Omega}} \quad [57]$$

$$u_4 = \sqrt{1 - \frac{i4\omega}{\Omega}} \quad [58]$$

$$u_5 = -\sqrt{1 + \frac{i4\omega}{\Omega}} \quad [59]$$

$$u_6 = -\sqrt{1 - \frac{i4\omega}{\Omega}} \quad [60]$$

Proceeding in the same manner as in the case of a step pressure function, Eq. 51 reduces to

$$\frac{T'}{T} = \frac{8\alpha B f \omega}{\Omega} \exp \left( -\frac{t\Omega}{4} \right) \left\{ \sum_{n=1}^7 D_n \exp \left( u_n^2 \frac{t\Omega}{4} \right) \operatorname{erfc} \left( u_n \sqrt{\frac{t\Omega}{4}} \right) + \sum_{n=1}^7 E_n \exp \left( u_n^2 \frac{t\Omega}{4} \right) \operatorname{erfc} \left( \frac{y_*}{2\sqrt{t\Omega}} + u_n \sqrt{\frac{t\Omega}{4}} \right) \right\} \quad [61]$$

where

$$u_7 = -1 \\ D_n = \frac{4A u_n e^{-y_*}}{\prod_{m=1}^7 (u_m - u_n)} \quad (m \neq n) \quad [62]$$

$$E_n = \frac{-u_n(u_n^2 - 1 + 4A) \exp[-1/2(1 - u_n)y_*]}{\prod_{m=1}^7 (u_m - u_n)} \quad (m \neq n) \quad [63]$$

Since the purpose of this analysis is to examine the effect of pressure fluctuations on the burning rate of the propellant, one need only examine the solutions for temperature fluctuation at  $y_* = 0$ . The corresponding mass flux fluctuation can then be obtained from Eq. 28. At  $y_* = 0$ , the terms preceded by  $A_1, B_1, A_2, D_7$ , and  $E_7$  drop out.

It would be of interest, now, to obtain the steady state solution or, if the solution has no steady state and increases without limit, to determine under which conditions this occurs. This information can be obtained by examining the solution for large time. For large  $t$ , (9)

$$\exp\left(u_n^2 \frac{t\Omega}{4}\right) \operatorname{erfc}\left(u_n \sqrt{\frac{t\Omega}{4}}\right) \rightarrow \frac{1}{u_n \sqrt{\frac{t\Omega\pi}{4}}} \rightarrow 0 \quad \operatorname{Re}\{u_n\} > 0$$

$$\exp\left(u_n^2 \frac{t\Omega}{4}\right) \operatorname{erfc}\left(u_n \sqrt{\frac{t\Omega}{4}}\right) \rightarrow 2\exp\left(u_n^2 \frac{t\Omega}{4}\right) \quad \operatorname{Re}\{u_n\} < 0$$

so that, depending on the values of  $u_1$  and  $u_2$ , three forms of the solution are possible:  
For a step pressure function:

$$\text{I. } \frac{T_w'}{T_w} \rightarrow 4\alpha Bf(A_2 + B_2)y_* = 0$$

(steady state solution)

$$\text{for} \quad \operatorname{Re}\{u_1\} > 0 \quad \operatorname{Re}\{u_2\} > 0$$

or

$$\operatorname{Re}\{u_1\} < 0 \quad \operatorname{Re}\{u_2\} > 0 \quad \operatorname{Re}\{u_1^2 - 1\} < 0$$

or

$$\begin{aligned} \operatorname{Re}\{u_1\} < 0 \quad \operatorname{Re}\{u_2\} < 0 \\ \operatorname{Re}\{u_1^2 - 1\} < 0 \quad \operatorname{Re}\{u_2^2 - 1\} < 0 \end{aligned}$$

[64]

$$\text{II. } \frac{T_w'}{T_w} \rightarrow 4\alpha Bf \left\{ (A_2 + B_2)_{y_*=0} + (A_1 + B_1)_{y_*=0} \exp\left[(u_1^2 - 1) \frac{t\Omega}{4}\right] \right\}$$

(amplitude increasing without limit)

for  $u_1$  and  $u_2$  real with

$$u_1 < 0 \quad u_2 > 0 \quad u_1^2 - 1 > 0$$

[65]

$$\text{III. } \frac{T_w'}{T_w} \rightarrow 4\alpha Bf \left\{ (A_2 + B_2)_{y_*=0} + (A_1 + B_1)_{y_*=0} \exp\left[(u_1^2 - 1) \frac{t\Omega}{4}\right] + (A_3 + B_3)_{y_*=0} \exp\left[(u_2^2 - 1) \frac{t\Omega}{4}\right] \right\}$$

(amplitude increasing exponentially with time if  $(u_1^2 - 1)$  is real; increasing as an exponentially bounded sine if  $(u_1^2 - 1)$  is complex)

for

$$\begin{aligned} \operatorname{Re}\{u_1\} < 0 \quad \operatorname{Re}\{u_2\} < 0 \\ \operatorname{Re}\{u_1^2 - 1\} > 0 \quad \operatorname{Re}\{u_2^2 - 1\} > 0 \end{aligned}$$

[66]

For a sinusoidal pressure function:

$$\text{I. } \frac{T_w'}{T_w} \rightarrow \frac{16\alpha Bf\omega}{\Omega} \left\{ (D_5 + E_5)_{y_*=0} e^{i\omega t} + (D_6 + E_6)_{y_*=0} e^{-i\omega t} \right\}$$

(steady oscillatory solution)

[67]

$$\text{II. } \frac{T_w'}{T_w} \rightarrow \frac{16\alpha Bf\omega}{\Omega} \left\{ (D_5 + E_5)_{y_*=0} e^{i\omega t} + (D_6 + E_6)_{y_*=0} e^{-i\omega t} + (D_1 + E_1)_{y_*=0} \exp\left[(u_1^2 - 1) \frac{t\Omega}{4}\right] \right\}$$

(amplitude increasing without limit)

[68]

$$\text{III. } \frac{T_w'}{T_w} \rightarrow \frac{16\alpha B f \omega}{\Omega} \left\{ (D_1 + E_1)_{y_1=0} e^{i\omega t} + (D_1 + E_1)_{y_1=0} e^{-i\omega t} + \right.$$

$$\left. (D_2 + E_2)_{y_2=0} \exp \left[ (u_1^2 - 1) \frac{t\Omega}{4} \right] + (D_2 + E_2)_{y_2=0} \exp \left[ (u_2^2 - 1) \frac{t\Omega}{4} \right] \right\}$$

(amplitude increasing exponentially with time if  $(u_1^2 - 1)$  is real; increasing as an exponentially bounded sine if  $(u_1^2 - 1)$  is complex)

[69]

The conditions on  $u_1$  and  $u_2$  for the different types of solutions to occur are the same for the step and sine pressure functions.

### Stability Conditions in Terms of Steady State Parameters

For the step pressure function, the steady state solution, on substituting the definitions of  $A_1$  and  $B_2$ , becomes

$$\frac{T_w'}{T_w} = \frac{RT_w}{E_w} \frac{n}{2} f$$

This is to be expected, as one can readily see by inspecting Eqs. 28 and 29. For large time, one would expect the flame temperature to return to its initial value, in which  $(T_f'/T_f) = 0$ , whereupon, by eliminating  $m_w'/\bar{m}_w$  between the two equations, the above result follows. The conditions for which the unbounded increase in  $T_w$  is oscillatory or nonoscillatory can be found from the definitions of  $u_1$  and  $u_2$ . For  $q > 1$ ,  $q^2 - q - 2A > 0$ ,  $q^2 < 4A$  there is an unbounded oscillatory increase in  $T_w$ . The frequency of this oscillation is

$$\omega_u = \frac{\Omega}{2} (q - 1) \sqrt{4A - q^2} \quad [70]$$

For  $q > 1$ ,  $q^2 - q - 2A > 0$ ,  $q^2 > 4A$ , there is an unbounded nonoscillatory increase in  $T_w$ .

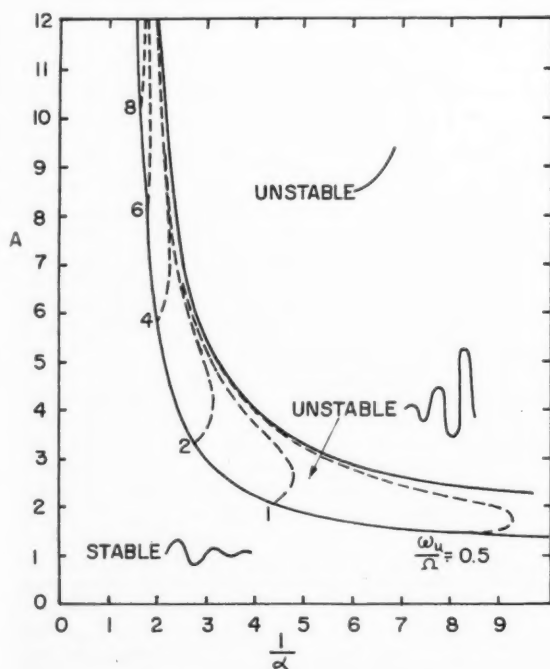


Fig. 1 Self-excited mode: stable and unstable regions; frequency of oscillatory instability

These instability criteria are the same for a step or for a sine pressure fluctuation or, for that matter, for any other functional form of pressure fluctuation. The portion of the solution that exhibits this unstable behavior can be called the self-excited mode, to distinguish it from transient, steady state, or steady oscillatory modes. As pointed out in the discussion below, this terminology should not be confused with that often used to describe the burning characteristics of rocket engines. The frequency of oscillation of the self-excited mode is shown in Fig. 1.

The steady oscillatory mode of surface temperature (and therefore, burning rate) fluctuation is given by Eq. 67. By substituting the definitions of  $D_1$ ,  $E_1$ ,  $D_2$  and  $E_2$  into this expression, it can be brought, after manipulation, into the form

$$\frac{T_w'}{T_w} = \frac{\alpha B f \frac{\omega}{\Omega} \sin \left[ \omega t - \tan^{-1}(b/a) - \frac{\pi}{2} \right]}{\sqrt{a^2 + b^2}} \quad [71]$$

where

$$a = A(1 + \lambda_r) - \frac{\omega}{\Omega} \lambda_i \quad b = \frac{\omega}{\Omega} (\lambda_r + q) + A \lambda_i$$

$$\lambda_i = -\frac{1}{2} \sqrt{\frac{-1 + \sqrt{1 + 16\omega^2/\Omega^2}}{2}} \quad [72]$$

$$\lambda_r = -\frac{1}{2} \left[ 1 + \sqrt{\frac{1 + \sqrt{1 + 16\omega^2/\Omega^2}}{2}} \right] \quad [73]$$

In the limit as  $\omega \rightarrow \infty$ ,  $\left| \frac{m_w'}{\bar{m}_w} \right| \rightarrow 0$

and as  $\omega \rightarrow 0$ ,  $\left| \frac{m_w'}{\bar{m}_w} \right| \rightarrow \frac{nf}{2}$

In general, the response amplitude will increase with increasing frequency of pressure fluctuation until it reaches a maximum and will then monotonically decrease toward zero with increasing frequency as illustrated in Fig. 2. The frequency at which the response is a maximum, or resonant frequency, can be found in an implicit form by maximizing Eq. 71 with respect to  $\omega$ .

The resonant frequencies obtained in this manner are plotted in Fig. 3, along with the burning rate fluctuation amplitude at this frequency. The curve on Fig. 3 along which the amplitude is infinite is also the boundary above which the self-excited mode amplitude increases with time (see Fig. 1). The resonant frequency on this line coincides with the frequency of the self-excited mode at the same point.

The effect of a change in steady state chamber pressure on the position of a propellant on Fig. 1 or Fig. 3 is not easily determined directly from these figures. One can clarify this effect by replotting the curve  $|m_w'/\bar{m}_w| = \infty$  from Fig. 3 using a new set of parameters which separate out the effect of  $T_w$ . Since  $T_w$  is the only one of the terms which changes with a change in pressure, this also serves to separate the effect of pressure. The new plot is shown in Fig. 4. Since an increase in  $P$  will increase  $T_w$ , the path followed on increas-

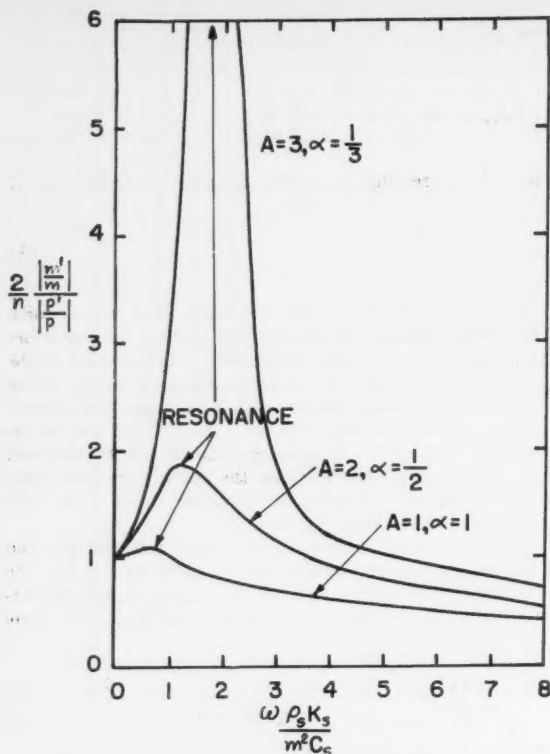


Fig. 2 Steady oscillatory mode: typical dependence of amplitude on frequency of pressure oscillation

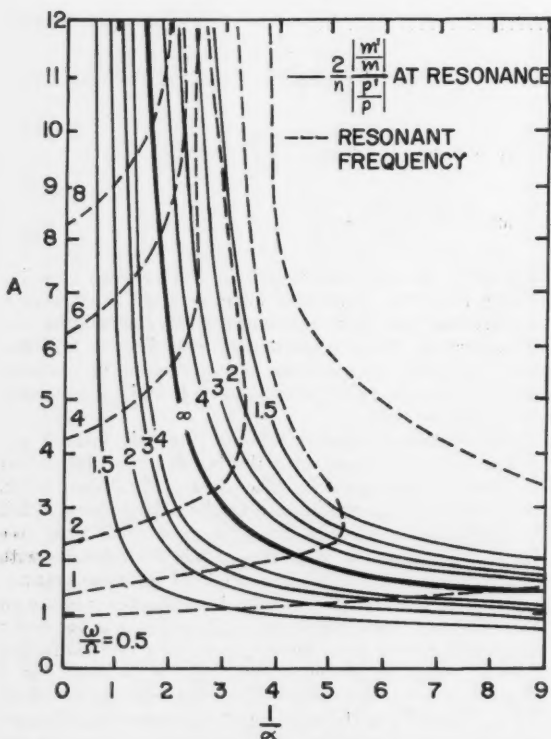


Fig. 3 Steady oscillatory mode: maximum (resonant) response amplitude and corresponding frequency

ing  $P$  is vertically upward. For any reasonable changes in pressure, the change in  $T_w/T_i$  can be expected to be quite small due to the exponential nature of Eq. 17. Depending on the initial position on Fig. 4, it can be seen that an increase in pressure can bring a propellant either toward or away from the curve  $|m_w'/\bar{m}_w| = \infty$ .

### Review of Approximations

Before proceeding with the discussion, the approximations which have been introduced in the process of making the problem mathematically tractable should be re-examined. The most important of these are:

1 The solutions of the time dependent mass and energy transport equations in the gas phase have been assumed to be closely approximated by the steady state solutions (these steady state solutions being functions of time due to the variation of the solid-gas interface boundary conditions with time). This requires that the relaxation time in the gas phase be much smaller than the characteristic time associated with the fluctuation of the property which is "driving" the system. The stable modes of burning rate fluctuation are driven by pressure fluctuations, so that the characteristic time is  $\tau_s = 1/\omega$ . The unstable modes are self-driven, with characteristic time

$$\tau_u = \frac{2}{\Omega(q-1)\sqrt{4A-q^2}} \equiv \frac{1}{\omega_u}$$

Orders of magnitude for the relaxation times in the solid and gas phases are given by (2)

$$\tau_{r \text{ solid}} \cong \frac{K_s \rho_s}{m_w^2 C_s}$$

$$\tau_{r \text{ gas}} \cong \frac{K_g \rho_g}{m_w^2 C_{pg}}$$

The limitations imposed on the solution are, therefore, that

$$\frac{K_g \rho_g}{C_{pg}} \ll \frac{K_s \rho_s}{C_s}$$

$$\omega \ll \frac{m_w^2 C_{pg}}{K_g \rho_g} \quad \text{for the stable modes}$$

$$\omega_u \ll \frac{m_w^2 C_{pg}}{K_g \rho_g} \quad \text{for the self-excited modes}$$

$K_s \rho_s / C_s$  is generally an order of magnitude greater than  $K_g \rho_g / C_{pg}$ , so the first limitation is not unduly restrictive. As for the second and third limitations,  $m_w^2 C_{pg} / K_g \rho_g$  ranges in value, for typical propellants and chamber pressures from 1000 to 50,000 sec<sup>-1</sup>. Much of the available data on oscillatory burning is, therefore, within the range of frequency for which this analysis is valid.

2 The assumption of a homogeneous propellant has been made. The nonhomogeneity of some propellants could, in itself, play an important role in the oscillatory burning phenomenon.

3 The gas phase reaction has been assumed to be described in terms of a simple  $n$ th order reaction. For most propellants, the gas phase reaction is more complex than this implies.

4 The process of vaporization of the solid has been idealized. The rate is assumed to be an Arrhenius type function of surface temperature. Together with the assumptions of a homogeneous solid with temperature independent transport properties, this implies that decomposition takes place only along the plane dividing the solid and gas phases.

5 The solution of the linearized equations is valid only for fluctuations of small amplitude. When large amplitudes are



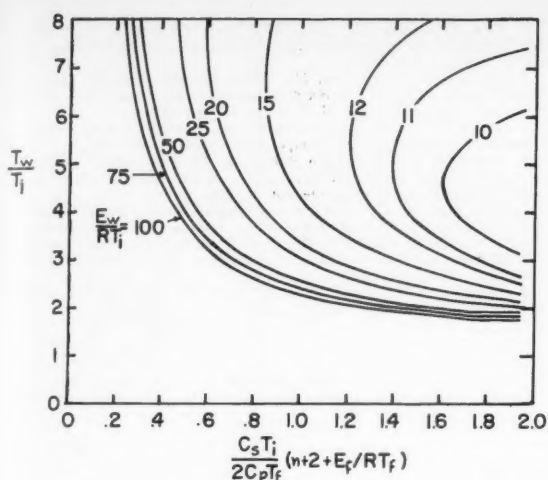


Fig. 4 Effect of wall temperature (pressure) on proximity to infinite resonant response amplitude for the steady oscillatory mode

predicted, the solution should be regarded only as an indication of the trend of the true solution.

It is apparent that this model differs in many respects from a real propellant, but it is hoped that those properties which influence the oscillatory burning phenomenon have been retained in the model. The fact that the model indeed exhibits such behavior is encouraging in this respect.

## Discussion

Many conditions have been established under which either the steady oscillatory mode or self-excited mode can lead to a large amplitude of the surface mass flux perturbation. However, it is difficult to interpret this analysis directly in terms of conditions under which a real solid propellant engine will exhibit large amplitude pressure oscillations, for two reasons. First, the entire analysis was based on small perturbations from the steady state so that only a tendency toward instability has been obtained. The original nonlinear equations must be solved to determine the behavior when large amplitudes occur. In addition, the results obtained give the response of propellant burning rate to a specified pressure perturbation, but give no information on the feedback process by which the pressure perturbation is, in turn, altered by the change in burning rate. Such information can be obtained through a more elaborate analysis, taking chamber geometry and dissipation into consideration, and including the effect of charge geometry on the boundary conditions at the propellant-gas interface. The results of the present investigation form a part of the foundation on which the more elaborate analysis can be constructed.

Because of the inherent difficulties involved in trying to extrapolate from the behavior of the model to the behavior of a rocket engine, some clarification of terminology is in order. It must be kept in mind that the results of this analysis give the response of the burning rate of a solid propellant to a prescribed pressure perturbation. The terminology used to describe the various modes of burning rate response (stable, unstable, resonance, resonant frequency, self-excited, steady oscillatory, etc.) apply in the customary manner to these results, but one should be careful not to confuse this nomenclature with that used to describe the burning characteristics

of rocket engines. One should therefore note that most instances of unstable burning in solid propellant motors involve pressure oscillations in the acoustic modes of the chamber, and would therefore be driven by the steady oscillatory mode of burning rate response. The unstable, self-excited modes of burning rate response could only be held responsible for the relatively rare instances of unstable burning in motors involving frequencies which are not acoustic modes of the chamber. The behavior to be expected due to the self-excited modes is somewhat obscured by the linearized mathematical treatment, wherein the analysis fails when amplitudes become large, but the analysis does give the conditions under which one might expect difficulty such as catastrophic pressure rise or chuffing; and in the case of periodic phenomena it gives the approximate frequency.

Finally it should be pointed out that the steady oscillatory response of burning rate to a sinusoidal pressure fluctuation was obtained in a relatively simple form. Combining Eqs. 28 and 71, one obtains

$$\frac{m_w'}{f \bar{m}_w} = \frac{n}{2} \frac{A \alpha \omega}{\Omega} \frac{\sin[\omega t - \tan^{-1}(b/a) - \pi/2]}{\sqrt{a^2 + b^2}}$$

where  $a$  and  $b$  are functions of  $A$ ,  $\alpha$  and  $\omega/\Omega$ . Other than  $\omega t$ , only four parameters are involved; the pressure exponent  $n/2$ , the dimensionless frequency  $\omega/\Omega$ , and the two dimensionless parameters  $A$  and  $\alpha$ .

## Nomenclature

- $A$  = dimensionless parameter (see Eq. 36)
- $B$  = dimensionless parameter (see Eq. 39)
- $C$  = specific heat of solid
- $C_p$  = specific heat of gas
- $D$  = diffusion coefficient
- $E_f$  = activation energy for combustion reaction
- $E_w$  = activation energy for vaporization and decomposition
- $f$  = amplitude of pressure disturbance
- $F$  = Laplace transform of pressure disturbance
- $h$  = enthalpy of mixture
- $h_i^\circ$  = heat of formation of  $i$ th species
- $k_b$  = backward rate coefficient
- $k_f$  = forward rate coefficient
- $K$  = thermal conductivity
- $K_i$  = mass fraction of  $i$ th species
- $L$  = heat of vaporization and decomposition (see Eq. 20)
- $Le$  = Lewis number
- $m$  = mass flux per unit area
- $M_i$  = molecular weight of  $i$ th species
- $n$  = order of reaction
- $P$  = pressure
- $P$  = Laplace transform variable
- $q$  = dimensionless parameter (see Eq. 39)
- $Q_r$  = heat of combustion (see Eq. 15)
- $R$  = gas constant
- $S$  = complex variable (see Eq. 50)
- $t$  = time
- $T$  = temperature
- $T_i$  = initial temperature of solid
- $u$  =  $S^{1/2}$
- $v$  = Laplace transform of disturbance in temperature
- $w_i$  = rate of production of  $i$ th species per unit volume
- $y$  = distance from propellant surface
- $y_*$  = dimensionless distance (see Eq. 36)
- $\alpha$  = dimensionless parameter (see Eq. 39)
- $\alpha_{mi}$  = number of atoms of atomic species  $m$  in the molecular species  $i$
- $\Gamma_m$  = atomic mass fraction
- $\epsilon_i$  = fraction of total mass flux associated with  $i$ th species
- $\lambda$  = eigenvalue (see Eq. 44)
- $\nu_i$  = stoichiometric coefficient of  $i$ th species
- $\rho$  = density
- $\omega$  = frequency of pressure oscillation
- $\omega_u$  = frequency of self-excited mode
- $\Omega$  = reciprocal of characteristic time of solid (see equation 36)

### Subscripts

- $f$  = conditions at outer edge of combustion zone  
 $g$  = property of gas  
 $r$  = property of reactant species  
 $S$  = property of solid  
 $W$  = conditions at propellant surface

### References

- 1 Green L., Jr., "Some Properties of a Simplified Model of Solid-Propellant Burning," *JET PROPULSION*, vol. 28, 1958, p. 386.
- 2 Hart, R. W. and McClure, F. T., "Combustion Instability: Acoustic Interaction with a Burning Propellant Surface," *J. Chem. Phys.*, vol. 30, 1959, p. 1503, or see Appl. Phys. Lab. Rep. TG-309, Johns-Hopkins Univ., Oct. 1958.
- 3 Bird, J. F., Haar, L., Hart, R. W. and McClure, F. T., "Effect of Solid Propellant Compressibility on Combustion Instability," *J. Chem. Phys.*, vol. 32, 1960, pp. 1423-1429.
- 4 Shinnar, R. and Dishon, M., "Heat Transfer Stability Analysis of Solid Propellant Motors," in *Solid Propellant Rocket Research* (M. Summerfield, ed.), Academic Press, N. Y., 1960, pp. 359-373.
- 5 Smith, A. G., "A Theory of Oscillatory Burning of Solid Propellants Assuming a Constant Surface Temperature," *ibid.*, pp. 375-391.
- 6 Cheng, S. I., "Resonance Burning in Solid-Propellant Rocket Engines," presented at Eighth Symposium on Combustion, Calif. Inst. of Tech., Pasadena, Calif., Aug. 29-Sept. 2, 1960.
- 7 Von Kármán, T., "The Present Status of the Theory of Laminar Flame Propagation," Sixth Symposium (International) on Combustion, The Combustion Inst., Aug. 19-24, 1956; Reinhold Publishing Corp., N. Y.
- 8 Erdelyi, A., *Tables of Integral Transforms*, Vol. 1, No. 33, McGraw-Hill, N. Y., 1954, p. 132.
- 9 Whittaker, E. T. and Watson, G. N., *A Course of Modern Analysis*, Macmillan, N. Y., 1946 p. 152.

# Experimental Investigation of Detonation in Unconfined Gaseous Hydrogen-Oxygen-Nitrogen Mixtures<sup>1</sup>

LEON H. CASSUTT<sup>2</sup>

Arthur D. Little, Inc.  
Cambridge, Mass.

An experimental program has been conducted to determine the detonability of unconfined hydrogen-oxygen-nitrogen mixtures during venting of a missile employing liquid hydrogen as a fuel or during an accidental spill from a storage or missile propellant tank. The mixtures investigated ranged from those formed by hydrogen combining with air to those in which there is no nitrogen dilution. During the tests, the gaseous mixtures were contained in 100-cu ft latex balloons; and upon initiation, measurements were made of the resulting peak overpressures. Initiation was accomplished by ignitors varying in strength from electric sparks to 100-gm explosive charges. The results of the experimental program have demonstrated that any mixture capable of sustaining a stable detonation wave when confined in a tube will detonate under unconfined conditions if the initiating impulse is sufficiently intense. For many hydrogen-oxygen compositions with no nitrogen dilution, initiation by a spark or flame source can produce full detonation. For hydrogen-air mixtures, detonation requires initiation by at least a 2-gm explosive charge.

**B**ECAUSE large missile systems will be needed for outer-space research, emphasis has recently been placed on increasing overall specific impulse through the use of liquid hydrogen as a fuel. Before storing and handling this liquid in

large quantities, however, the Air Research and Development Command asked Arthur D. Little, Inc., to study the characteristics of liquid hydrogen and to develop realistic safety criteria. Such criteria could bring about substantial savings in capital equipment costs of production, storage, and user facilities, and could point out safety devices which would prevent major losses.

After analyzing the probable causes of both known accidents at liquid hydrogen facilities and those which might oc-

Received Dec. 30, 1960.

<sup>1</sup> This work was sponsored by the United States Air Force Air Research and Development Command under Contract AF 18(600)-1687.

<sup>2</sup> Senior Chemical Engineer.

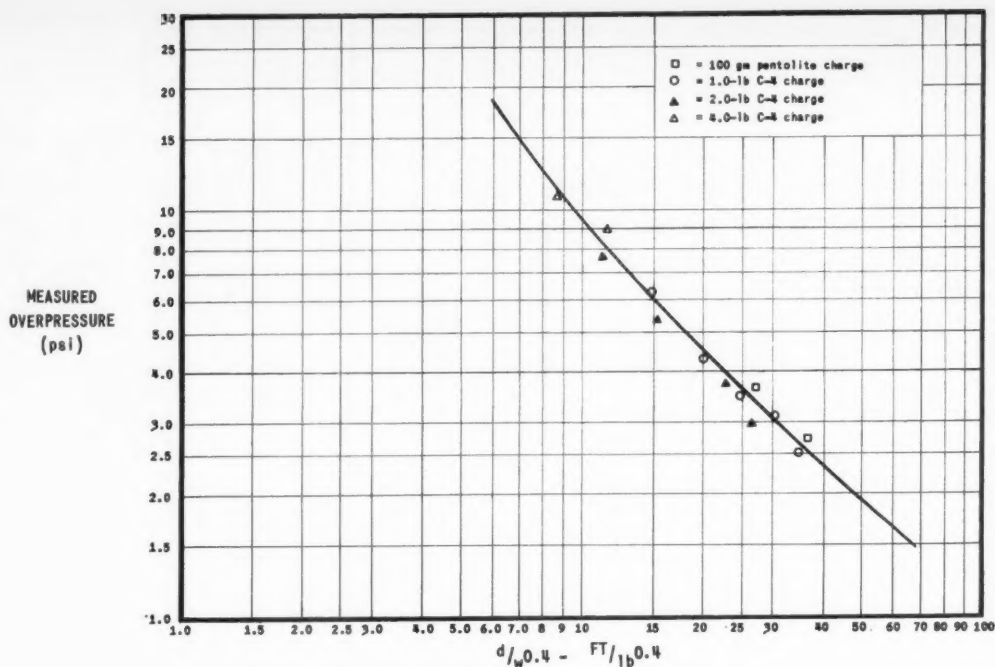


Fig. 1 Measured overpressures for small explosive charges

cur, ADL identified a number of possible hazardous situations. One of these concerned the detonability of unconfined hydrogen-oxygen mixtures. If these mixtures were detonable, venting of a missile utilizing the cryogenic fuel or an accidental spill from a storage or missile propellant tank could be disastrous. The composition of these mixtures could range from those with no nitrogen dilution (as in a missile where liquid oxygen is also being vented) to those where the only oxygen is that supplied by the surrounding atmosphere (as in a hydrogen-spill situation). It was important, therefore, to establish the conditions which might cause detonation.

### Previous Experimental Information

Considerable experimental data are available on the reaction of hydrogen-oxygen mixtures confined in tubes (1,2).<sup>3</sup> It has been shown that the detonable mixtures range from 15 to 90 mol % hydrogen and that the ignition energy requirements are among the lowest of any combustible fuel-oxygen mixture. The addition of nitrogen inhibits detonation to a certain extent, but the limits of detonability in air are still wide: 18-59 mol % hydrogen.

These data cannot be readily transferred from the two-dimensional to the three-dimensional case, however, because the mechanisms of plane detonation wave propagation and of spherical detonation wave propagation differ. Only in recent years had investigation revealed the existence of stable spherical detonation waves (3-8), and this work has been limited by the methodological difficulties involved; i.e., large volumes of gas are necessary for even a short path for the detonation wave in a spherical container. These studies indicated that in spherical detonation stronger initiation is generally required and detonation limits are reduced. Little of these data, however, pertain to the specific conditions necessary for spherical detonation of hydrogen-oxygen mixtures.

<sup>3</sup> Numbers in parentheses indicate References at end of paper.

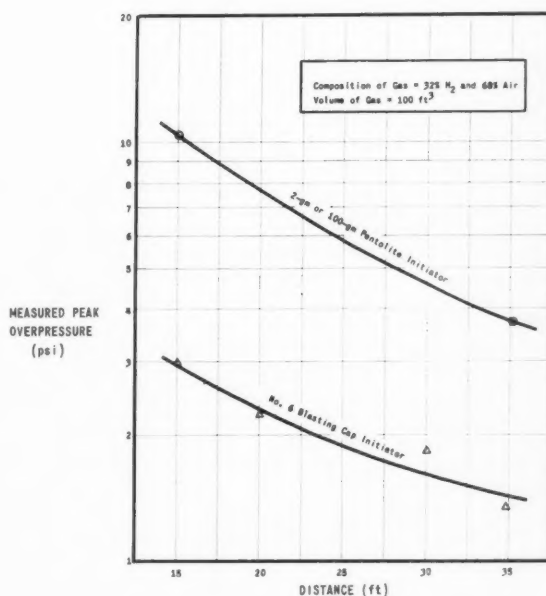


Fig. 2 Effect of initiator energy upon detonation yield of hydrogen-air mixtures

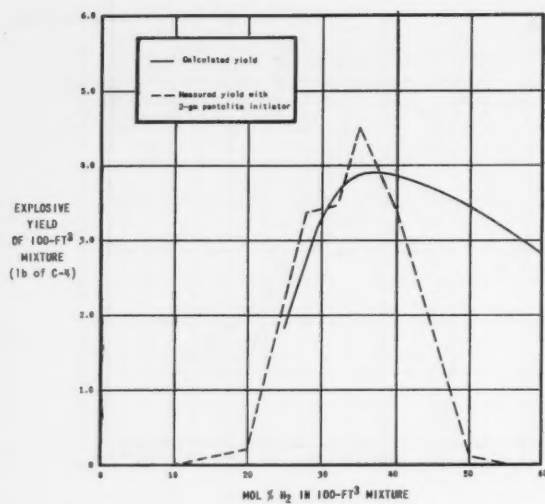


Fig. 3 Explosive yield of hydrogen-air mixtures in free space

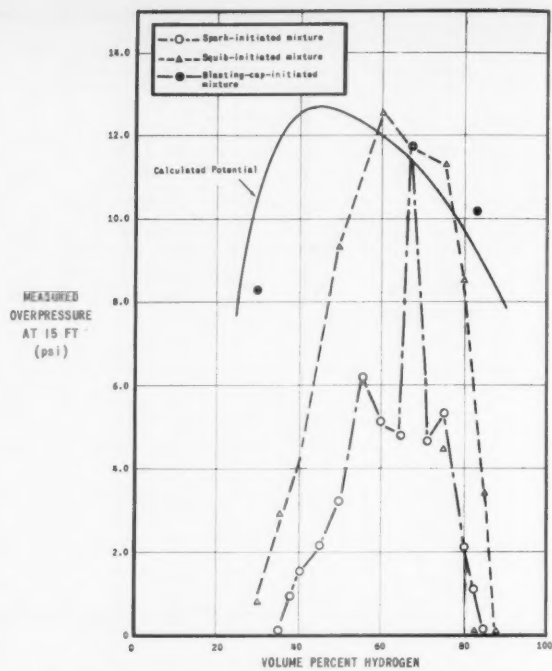


Fig. 4 Comparison of theoretical and experimental overpressures from reaction of hydrogen-oxygen mixtures

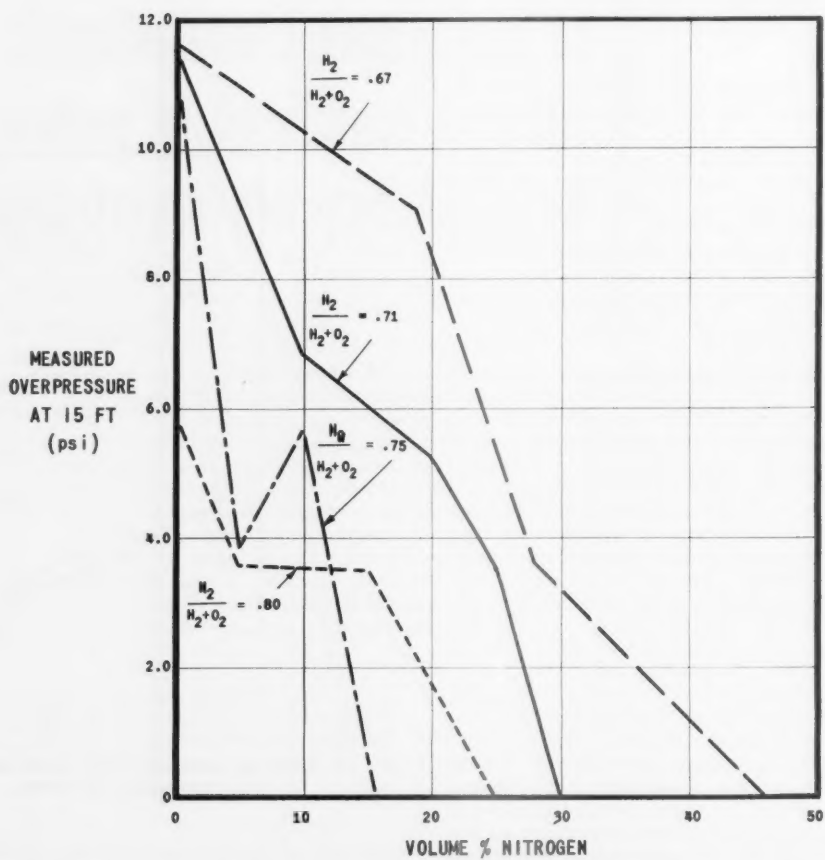


Fig. 5 Effect of nitrogen dilution on the detonability of fuel-rich hydrogen-oxygen gas mixtures, S-68 squib ignition



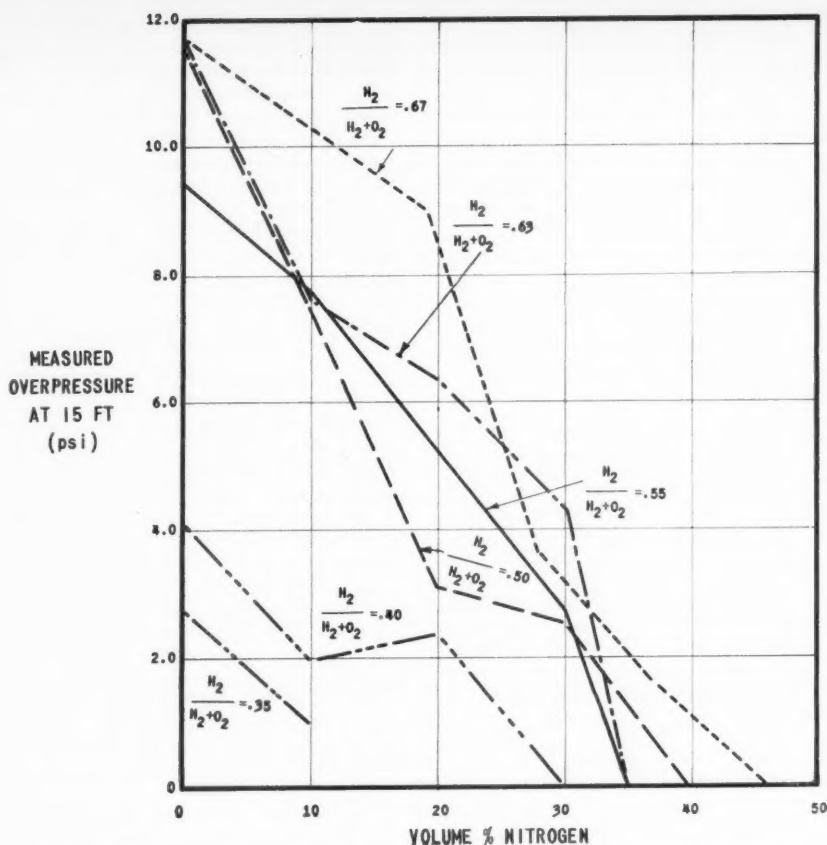


Fig. 6 Effect of nitrogen dilution on the detonability of fuel-lean hydrogen-oxygen gas mixtures' S-68 squib ignition

### Experimental Procedure

The experimental program undertaken sought to establish those mixtures which were detonable and the level of initiation energy they required. The experimental conditions were idealized in that uniform mixtures of the gases were tested rather than nonhomogeneous compositions, which would result from actual venting or spilling. The experimental setup consisted of a 6-ft diameter latex balloon (having a volume of 100 cu ft) filled with the mixture to be tested—the accuracy of gas metering being within 2.5%.

Since the filling pressure for the balloon was less than one inch of  $H_2O$ , essentially unconfined conditions were provided by the balloon. The initiating charge was located at the center of this sphere, and the magnitude of the peak overpressure was assumed to be the criterion for the existence of a detonation wave. The pressure was measured with five ceramic type blast gages spaced at 5-ft intervals and at a distance of 15–35 ft from the charge to be tested. The signal from each blast gage was fed through a cathode follower and isolation amplifier to an oscilloscope, where the scope trace was recorded with a Polaroid camera. The oscilloscope was activated by a trigger gage placed 10 ft from the charge.

The experimental setup was calibrated by the initiation of small C-4 and pentolite charges. The results of these tests are presented in Fig. 1, in which the distance from the explosive at which the overpressures were measured is divided by the explosive's weight raised to the 0.4 power. The 0.4-power function was employed because it best fit the rate of pressure fall off for the charges. Its value, however, would

be affected by both the size and shape of the charges and the degree of the shockwave's ground reflection.

### Tests With Hydrogen-Air Mixtures

Initial experiments with 100-cu ft balloons were conducted with hydrogen-air mixtures, since the first phase of the overall program was concerned with the storage and handling of liquid hydrogen alone.

The first test series was designed to establish minimum initiation energy requirements through the ignition of near-stoichiometric mixtures containing 32 mol % hydrogen and 68 mol % air (see Fig. 2).

The measured overpressures demonstrated the following:

- 1 The mixtures detonated completely when initiated by 2-gm or 100-gm pentolite charges. Based on the calibration data in Fig. 1, the explosive yield was equivalent to 3.5 lb of C-4 (i.e., 0.64 lb of C-4 per pound of gas mixture).

- 2 When No. 6 or No. 8 blasting caps were used as initiators (either cap is equivalent to about 0.5 gm of explosive), overpressures one third as high as those obtained with the pentolite charges were achieved. The explosive yield, therefore, was less than 0.2 lb of C-4, or a reduction of 95%.

- 3 Neither squib nor spark sources, when used as the initiator, gave significant overpressures, and there was no discernible evidence of a detonation. Combustion of the gases produced only slight charring of the wood dowel supporting the initiator.

Since the 2-gm pentolite charge had been established as the minimum amount of energy that was required for complete

detonation of the near stoichiometric hydrogen-air mixture, further tests incorporated this initiator so that the limits of detonability could be explored. The results of these additional tests are presented in Fig. 3. Because the energy supplied by the 2-gm charge was less than the minimum required for the borderline compositions, overpressures measured for these compositions varied significantly from one test to another. For this reason, only those data representing the maximum for the mixture were used to establish the limits. Fig. 3 compares these maximum yields for the various mixtures with their computed theoretical potential. It was assumed that the theoretical potential was equivalent to that of conventional explosives having the same heats of explosion. Full detonation is shown for mixtures containing less than 40 mol % hydrogen; only partial detonation occurs with the richer mixtures. The limits for significant yield (20–50 mol % hydrogen) were quite close to those reported for confined hydrogen-air mixtures: 18–59 mol % hydrogen. These results therefore substantiated conclusions based on the theoretical analysis (8), namely, that any mixture capable of sustaining a stable detonation wave when confined in a tube will detonate under unconfined conditions if the initiating impulse is sufficiently intense.

A few tests were made with hydrogen-air mixtures containing 35 mol % hydrogen in 400-cu ft balloons in an effort to determine whether a greater path length and larger gas volume would provide a transition from deflagration to detonation. In these limited tests, the blasting cap and 2-gm pentolite initiator produced yields that were directly related to the greater mass of gas involved; there was no evidence of a transition to full detonation with the blasting cap.

### Tests With Hydrogen-Oxygen Mixtures

The second phase of the experimental program was devoted to an evaluation of the detonability of unconfined hydrogen-oxygen mixtures without nitrogen dilution. Three initiating sources, representing several levels of ignition energy, were used: (a) spark source (of the order of 1–5 millijoule); (b) duPont 6-gr squib, which provided a strong flame source with some pressure amplification, (c) A No. 6 blasting cap (approximately 0.5 gm), which is a near minimum shockwave energy source.

The first series of tests, conducted with the stoichiometric ratio of hydrogen and oxygen, was designed to establish the minimum energy for full detonation. As shown in Fig. 4, all three initiating sources gave essentially the same overpressures. Based on the calibration curve (Fig. 1) their yield was equivalent to 1.30 lb of C-4 per pound of mixture, compared with the theoretical yield of 1.33 lb of C-4 per pound of mixture.

When it could be seen that the squibs and the spark source provided enough energy to completely detonate the stoichiometric mixtures, further tests were made with other ratios of hydrogen and oxygen. At this point, only one firing was made with each composition and initiator, since only the limits of detonability were being sought. The results of these tests are shown in Fig. 4.

Fig. 4 illustrates only the overpressures measured at 15 ft, but similar curves would result if data for other gage positions had been plotted. Points of zero overpressure in the experimental curve designate compositions for which no detectable shock wave was recorded. A small pressure rise (less than 0.2 psi at 15 ft) usually occurred; however, it resulted from the rapid combustion of the gases. Also presented in Fig. 4 is a curve which gives the estimated overpressures resulting from the complete detonation of these compositions as determined by theoretical computations. Although the specific values of measured overpressures can be considered only approximate—because of the limited testing with each composition—one can frame some general conclusions by comparing them with the theoretical values:

1 With the spark source as initiator, a decrease from full explosive yield occurred when the hydrogen content of the stoichiometric quantity was increased or decreased by only 4%. The approximate limit of detonability for 100-cu ft mixtures was 35–85 mol % hydrogen.

2 When squib initiation was used, a full explosive yield was obtained with mixtures containing 50–75 mol % hydrogen. The limit of detonability appeared to be 25–87.5 mol % hydrogen.

In tests made with No. 6 blasting caps as the initiator, a full explosive yield was achieved over a range of at least 30–82 mol % hydrogen.

### Effects of Nitrogen Dilution

In the foregoing tests, it was demonstrated that at least a 2-gm pentolite charge was required for complete detonation of an unconfined hydrogen-air mixture and that a spark or flame source was sufficient for a hydrogen-oxygen mixture. It is evident, therefore, that nitrogen dilution has a great deal to do with the detonability of these mixtures. For this reason, a number of tests were conducted to assess the extent of this dilution effect (see Figs. 5–9). As expected, the limiting nitrogen dilution occurred for the stoichiometric hydrogen-oxygen ratio  $H_2/H_2 + O_2 = 0.667$ . Increasing or decreasing the ratio of hydrogen from stoichiometric significantly reduced the percentage of nitrogen that could be added before essentially no detonation effects resulted. In the stoichiometric mixtures, the limiting dilution with squib initiation was approximately 46 mol % nitrogen; with spark initiation it was 35 mol %. In general, the allowable dilution for all ratios of hydrogen and oxygen was less with the spark source than with the squibs—a clear demonstration of the squib's greater initiation energy.

A comparison of the stoichiometric mixtures' measured detonation effects with their calculated potential shows that an immediate decrease from full yield occurred in spark-initiated mixtures when nitrogen was added (see Fig. 9). With squib ignition, this decrease was evident for dilutions greater than 20 mol %. When the blasting caps were used, however, complete detonation was obtained with nitrogen dilutions up to 46 mol %; and with the stoichiometric hydrogen-air mixture (55.6 mol % nitrogen), an overpressure of 2.9 psi was obtained at 15 psi—a yield equivalent to 5% of the calculated potential.

A unique effect was noted in tests with the spark-initiated mixtures: Except when compositions were near-stoichiometric and contained no nitrogen, the pressure wave fronts were less steep than those produced by other initiators. This effect became more pronounced when the nitrogen was increased; in fact, near the end points, it was impossible to measure overpressures at other than the first blast gage position. Two possible explanations are suggested for this phenomenon:

1 A deflagration wave is initially formed in the reacting gas. Moving outward, the wave builds up in intensity until, near the periphery of the balloon, a transition to detonation occurs. Enough of the deflagration wave precedes the detonation wave at the first gages so that a pressure front of reduced slope is recorded.

2 An intense deflagration wave is formed in the reacting gas, and no transition to detonation occurs. The wave then steepens, creating a shock front in the air as it moves away from the balloon.

The second explanation seems to be more reasonable than the first, because the formation of a detonation wave just at the periphery of the balloon would require a unique combination of mixture and initiation energy. Moreover, the phenomenon has been observed in all borderline mixtures ignited by a spark source; no other initiation has produced a similar effect. Steepening of the pressure front as it progresses away from the reaction zone probably occurs independently

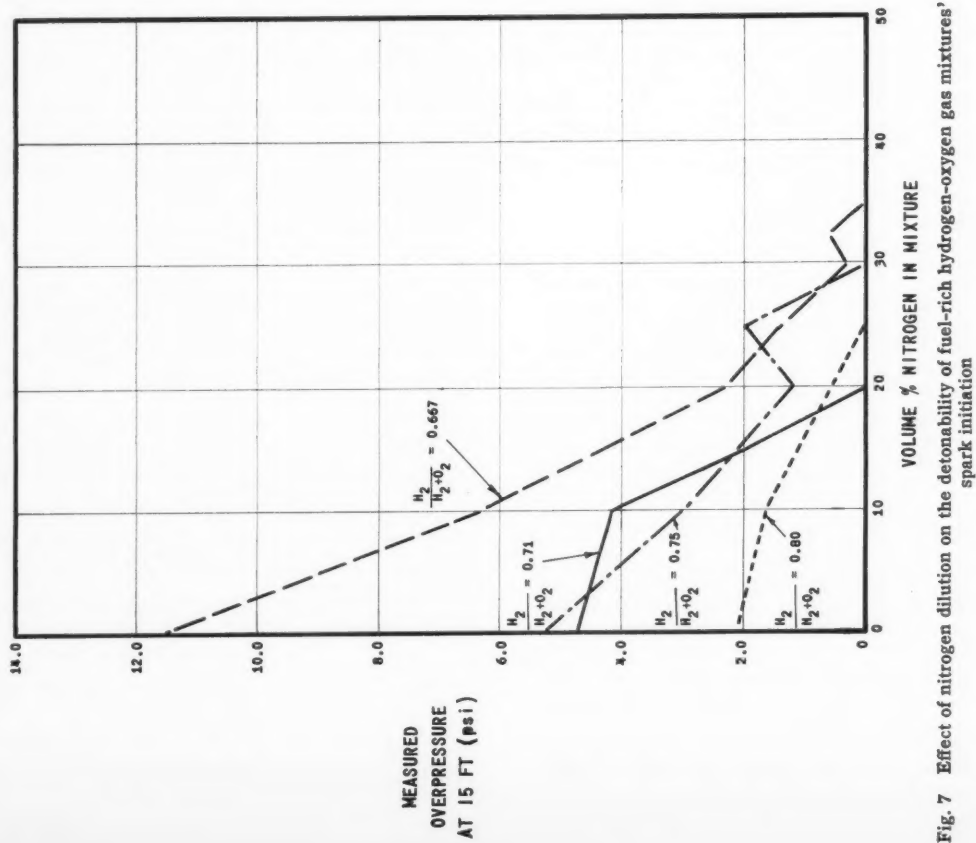


Fig. 7 Effect of nitrogen dilution on the detonability of fuel-rich hydrogen-oxygen gas mixtures, spark initiation

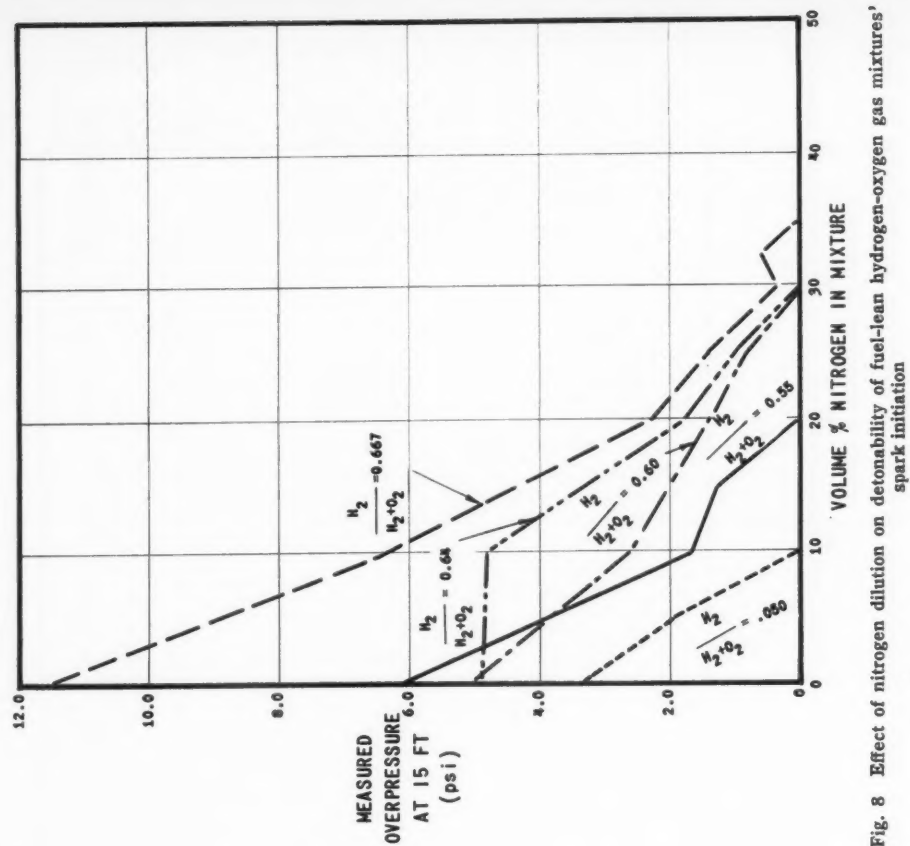


Fig. 8 Effect of nitrogen dilution on the detonability of fuel-lean hydrogen-oxygen gas mixtures, spark initiation

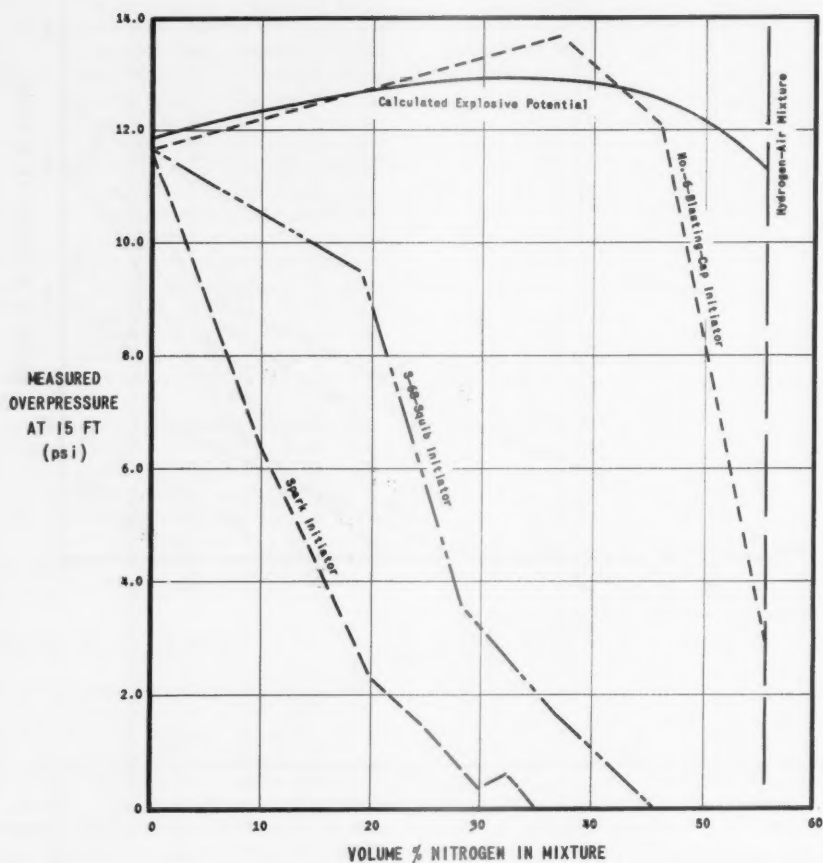


Fig. 9 Effect of nitrogen dilution on explosive potential of stoichiometric hydrogen-oxygen mixtures

of the sequence of events in the balloon; such an effect is normal in the degeneration of pressure waves. A better explanation of the shock fronts of low slope in the spark-initiated mixtures might be obtained if tests were made with larger volumes of gas (800 cu ft or more). If a stable detonation were being formed near the periphery of the 100-cu ft balloons, most of the gas in the larger volume would probably detonate fully. If the opposite sequence of events took place, it is unlikely that a significant increase in explosive effects would occur.

### Conclusions

On the basis of the experimental work carried out in this program, a number of conclusions can be drawn about the detonability of unconfined hydrogen-oxygen-nitrogen mixtures:

1 Any mixture capable of sustaining a stable shock wave will fully detonate under unconfined conditions if the initiating impulse is sufficiently intense.

2 An unconfined stoichiometric hydrogen-oxygen mixture will detonate completely if it is initiated by a spark or flame source.

3 Initiation by at least a 2-gm explosive charge is needed to fully detonate an unconfined hydrogen-air mixture.

4 The level of energy required for complete detonation rises as the percentage of hydrogen changes from stoichiometric and as nitrogen dilution increases.

### References

- 1 Lewis, B. and von Elbe, G., "Combustion, Flames, and Explosions of Gases," Academic Press, N. Y., 1951.
- 2 Ordin, P. M., "Hydrogen-Oxygen Explosions in Exhaust Ducting," NACA TN 3935, April 1958.
- 3 Zeldovich, Ya. B., "Distribution of Pressure and Velocity in the Products of a Detonating Explosion, and in Particular in the Case of a Spherical Propagation of the Detonation Waves," *J. Exper. Theor. Phys.*, (USSR), vol. 12, 1942, pp. 389-406.
- 4 Taylor, G., "The Dynamics of the Combustion Products Behind Plane and Spherical Detonation Fronts in Explosives," *Proc. Royal Soc. London*, vol. A-200, 1950, pp. 235-247.
- 5 Freiwald, H. and Ude, H., "Spherical Explosion Waves in Mixtures of Acetylene and Air," *Comptes Rendus*, vol. 236, 1953, pp. 1741-1743.
- 6 Manson, N. and Ferrie, F., "Contribution to the Study of Spherical Detonation Waves," Fourth Symposium (International) on Combustion, Baltimore, Williams and Wilkins Co., 1953, p. 486.
- 7 Jost, W., *Explosions und Verbrennungsvorgänge in Gasen*, Berlin, 1939, pp. 185-186.
- 8 Zeldovich, Ya. B., Kogarko, S. M. and Simonov, N. N., "An Experimental Investigation of Spherical Detonation of Gases," *Soviet Physics, Technical Physics*, vol. 81, 1957, pp. 1689-1713.



# Recent Hypersonic Studies of Wings and Bodies

MITCHEL H. BERTRAM<sup>1</sup>  
and  
ARTHUR HENDERSON Jr.<sup>2</sup>

Langley Research Center (NASA)  
Langley Field, Va.

Even though a great deal of theoretical and experimental information has been obtained in recent years on the flow over simple shapes in hypersonic flow, a great deal of confusion still exists on how to interpret and extrapolate the results obtained. This paper offers information recently obtained at Langley at Mach numbers ranging from 7 to 21 encompassing both work in air and helium on shapes ranging from rods to delta wings. The results indicate that in most cases methods for making useful estimates of pressure are in hand for the simple shapes. However, three-dimensional effects and the interaction between the components considerably complicates the flow fields over delta wings.

**T**HE FLOW phenomena encountered by vehicles in the re-entry Mach number range is complex. The extreme heating, loading, and stability problems which the designer must cope with are in many cases incompletely understood. The present paper is concerned with assessing the adequacy of currently available methods of predicting pressure and heat transfer distributions on the simple axisymmetric, two-dimensional, and delta wing configurations which will form components of re-entry vehicles.

The authors wish to acknowledge the aid of Lillian Boney of the Analytical Computing Branch of the Langley Research Center who supervised the numerical computations by the rotational characteristics method used in various parts of this paper.

Presented at the ARS Semi-Annual Meeting, Los Angeles, Calif., May 9-12, 1960.

<sup>1</sup> Acting Head, 11-Inch Hypersonic Tunnel Section.

<sup>2</sup> Head, Helium Tunnels Section. Member ARS.

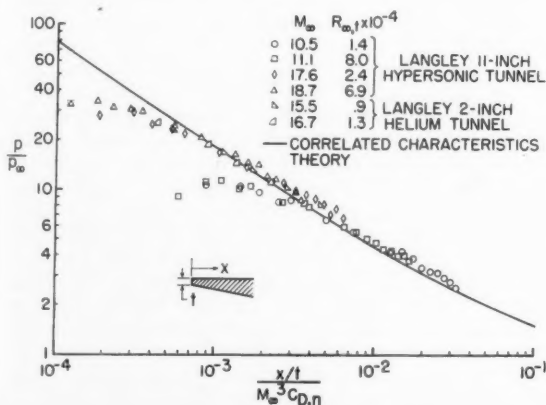


Fig. 1 Bluntness induced effects on flat plate in helium

## Results for Simple Shapes

### Blunt Flat Plate

Investigations on blunt flat plates have been conducted for some time now, but there still exists confusion on the applicability of blast wave theory, or what is believed to be its more accurate equivalent, characteristics theory correlated according to the parameters suggested by blast wave theory (1 and 2).<sup>3</sup> Much of the confusion may have been caused by the difficulty of interpreting results obtained in conical nozzles. These conical nozzles have been relied on for much of the very high Mach number results so far obtained. Lately, however, the interpretation of results from conical nozzles has been treated theoretically (2 through 4). Fig. 1 presents new surface pressure results obtained on a flat nosed flat plate in the contoured helium nozzles of the Langley

<sup>3</sup> Numbers in parentheses indicate References at end of paper.

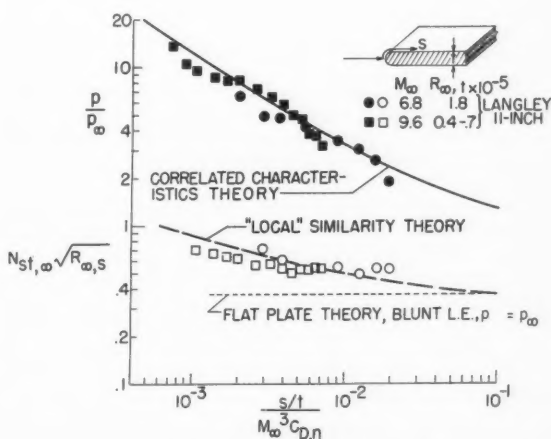


Fig. 2 Effect of bluntness induced pressures on heat transfer: slab wing,  $\alpha = 0$ ,  $\Lambda = 0$ , air

11-in. hypersonic tunnel and the conical nozzles of the Langley 2-in. helium tunnel over a nominal Mach range from 10 to 19. The abscissa utilizes the distance parameter suggested by two-dimensional blast wave theory (5 through 7).

The Mach 10 helium nozzle of the 11-in. tunnel had essentially no gradient in Mach number; however, the Mach 18 nozzle, even though contoured, had a slight positive gradient in Mach number which at most was 0.05 per inch resulting in  $M' \approx 0.005$  for the Mach 18.7 data and  $M' \approx 0.002$  for the Mach 17.6 data. No correction for the Mach number gradient has been applied to these data. For the data obtained in the conical nozzle of the 2-in. tunnel the Mach number gradient was about 1.15 per inch resulting in  $M' \approx 0.02$ . The buoyancy correction discussed in (2 and 4) was applied to these data. These data are compared to the curve for correlated characteristics theory (Reference 2, flat plate with a sonic-wedge nose in a helium medium) which for  $p/p_\infty > 1.2$  is accurately represented by

$$\frac{p}{p_\infty} = 0.169 \left( \frac{M_\infty^2 C_{D,n}}{x/t} \right)^{2/3} + 0.74 \quad [1]$$

The data are in general within about 10% of the theory except for the smallest values of the abscissa parameter at a given Mach number. These are values of  $x/t$  within about two diameters of the nose where the theory is not expected to apply.

Some pressure and heat transfer results obtained in air are shown in Fig. 2. Here the model is a slab with a hemicylinder nose tested at Mach 6.8 and 9.6. The Mach 6.8 data are that given in (8), and the Mach 9.6 results are pressure data from (9) and unpublished heat transfer results obtained by Feller and Blackstock. The model used to obtain the Mach 9.6 data is the same as that used for the Mach 6.8 data given in (8) except that there is additional instrumentation. Good agreement of the measured surface pressures with the theory is shown except near the nose as in Fig. 1 and near the trailing edge where there is evidence of pumping into the base region (theoretical surface pressure variation given by Eq. 1 with the coefficient 0.169 for helium replaced by the value 0.115 representative of air). The heat transfer data and theory are shown in the lower part of Fig. 2. The theory is hypersonic similarity theory (8) except that local values of the exponent  $n$  in the power law for the pressure were used. Since for any function the local value of the exponent in a power law fit to the function is given by  $n = WF'(W)/F(W)$  for Eq. 1 independent of the coefficient

$$n = \frac{2(p/p_\infty) - 0.74}{3(p/p_\infty)} \quad [2]$$

The prediction of the heat transfer coefficient in Fig. 2 appears to be adequate in accuracy.

#### Axisymmetric Induced Pressures

The blast wave analogy (2, 5 through 7 and 10) furnishes the designer with a rapid means of estimating blunt nose induced body pressures. However, its adequacy from the standpoint of accuracy has been seriously questioned. See, for instance, (11).

The blunted rod (axis aligned with the flow) is the three-dimensional analog of the blunted flat plate at zero angle of attack. As for the flat plate presented previously, Figs. 3 and 4 present the surface pressure ratio as a function of the distance parameter suggested by blast wave theory. Fig. 3 shows results in air and Fig. 4 in helium for rods with a hemisphere blunting. The experimental results in air (6, 12, and new data), because they were obtained at large values of the distance parameter

$$(s/d)/M_\infty^2 \sqrt{C_{D,n}}$$

corroborate an interesting detail of the pressure distribution predicted by the correlated characteristics theory (13). This

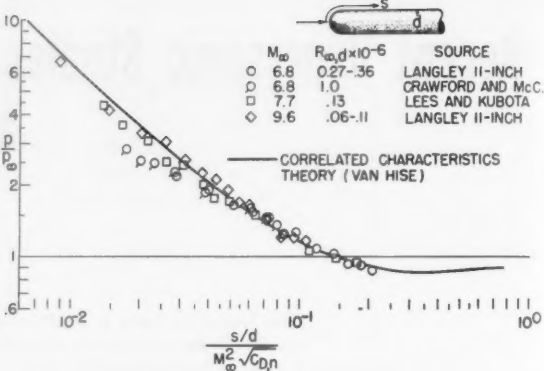


Fig. 3 Bluntness induced pressures on rod: air, hemisphere nose

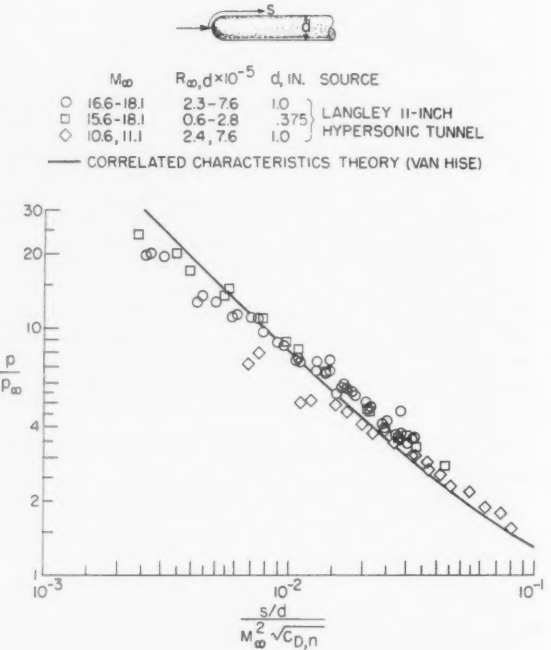


Fig. 4 Bluntness induced pressures on rod: helium, hemisphere nose

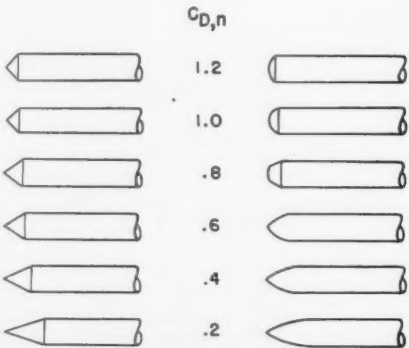


Fig. 5 Models used in investigation of nose shape independence concept

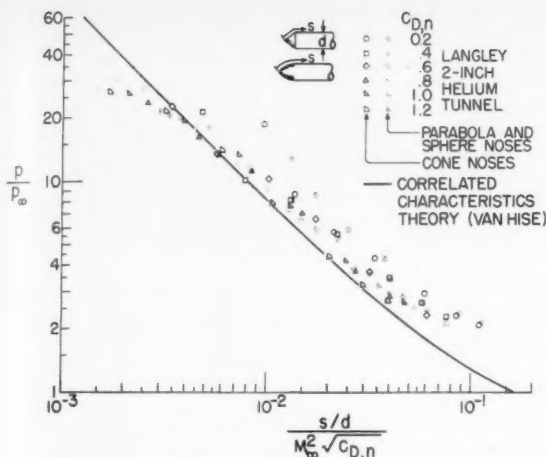


Fig. 6 Bluntness induced pressures on rod nose shape effect:  $M_\infty = 21$ ,  $R_\infty d = 8.5 \times 10^4$ , helium

detail is the portion of the pressure curve which drops below free stream static pressure. The characteristics theory was obtained for various curved and straight noses all with sharp tips for which the largest nose angle was a nearly sonic cone. As in the case of the flat plate, the pressures in the region of the junction do not correlate.

The helium data shown in Fig. 4 give results at lower values of the distance parameter than the air data but show much the same effects. The Mach 18 data were obtained from (14). The agreement with theory is generally good.

Inherent in the nose drag dependence is the implication that induced pressures are independent of nose shape. Thus, the models shown on Fig. 5 were designed to check experimentally the range of validity of the nose shape independence concept, and the extent to which induced pressures could be correlated by nose drag. Each of six pairs of models consists of two cylindrical rods with different nose shapes but the same nose drag. The nose drag coefficients vary from 0.2 to 1.2. Pressures were obtained at locations from 0.02 to 20 diam from the nose rod junction at  $M_\infty = 21$  in helium.

In our previous presentation for the blunted rod we had used surface distance from the stagnation point as our distance variable (Figs. 3 and 4). The surface pressure results given in Fig. 6 for the models shown in Fig. 5 also utilize surface distance in the blast wave parameter. One notes reasonable correlation and agreement with the theory for the rods with the highest drag noses. The lower drag noses deviate from correlation; this result seems reasonable based on the strong explosion (equivalent to high drag) concept embodied in the blast wave theory. The results may not be that simple, however, as shown in Fig. 7, where the plot is the same as that presented in Fig. 6 except that the distance used in the blast wave parameter has its origin at the junction of the nose and the rod. Note here that all of the different noses investigated show good correlation, certainly better than the correlation presented in Fig. 6, except in the region of the junction where, as discussed previously, the blast wave theory is not expected to apply anyway.

Recent unpublished results for the  $C_{D,n}$  0.2 and 1.2 noses at Mach 17 in helium, however, indicate that the surface distance parameter is to be preferred, since for a given nose drag coefficient there is good correlation of the pressures for the different Mach numbers. This is not the case in general when the junction distance method is used.

These results indicate that the blast wave theory furnishes

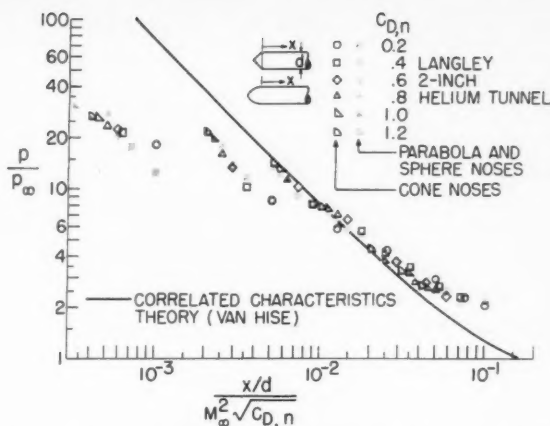


Fig. 7 Bluntness induced pressures on rod nose shape effect:  $M_\infty = 21$ ,  $R_\infty d = 8.5 \times 10^4$ , helium

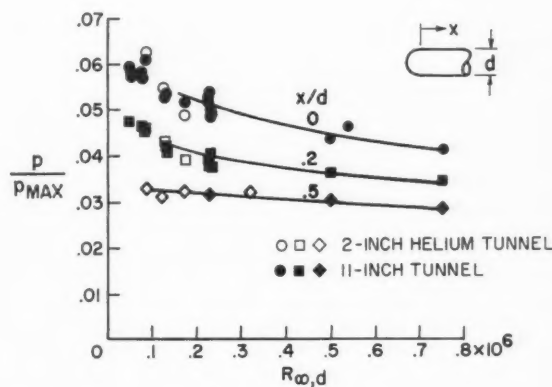


Fig. 8 Effect of Reynolds number on induced pressures on hemisphere cylinder:  $15.6 \leq M_\infty \leq 21$ ,  $\gamma = 5/3$

an excellent correlating parameter whose usefulness extends over a wide range of nose drags.

Up to this point no real consideration has been given to viscous effects. In the main an attempt has been made to keep the Reynolds numbers of the tests high enough so that the results could be considered inviscid. To determine the validity of this approach, results from a number of helium tests on hemisphere cylinders in the Langley 2-in. and 11-in. tunnels at Mach numbers in the range 15.6 to 21 have been collected (14 plus unpublished data). The surface pressure results for stations 0, 0.2, and 0.5 diam from the junction are shown in Fig. 8 as a function of the Reynolds number based on rod diameter. The pressure at the junction ( $x/d = 0$ ) is found to be a pronounced function of Reynolds number; however, the importance of Reynolds number is seen to decrease markedly at relatively small distances from the junction.

#### Delta Planform at Zero Angle of Attack

In this portion of the paper some results of studies on simple delta wings will be presented. Here we will consider the case of sharp flat delta wings and those with considerable amounts of leading edge bluntness, both from the standpoint of pressure and heat transfer.

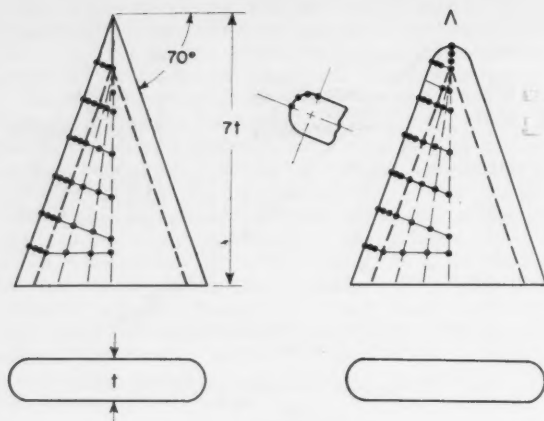


Fig. 9 Delta wing models

From practical considerations the delta wing in use would be blunted. Therefore, it is of interest to examine the pressures, flows, and heat transfer over a delta wing with a blunt nose and leading edge. Two of the wings which have been investigated are shown in Fig. 9. These wings are slabs with a cylinder with a sweep of 70 deg forming the leading edges. The model on the left had an apex formed by the intersection of the elements of the cylindrical leading edge on the centerline of the wing. On the model to the right the apex is a tangent sphere with the same diameter as the cylinder forming the leading edge. The actual diameter of the leading edge was  $\frac{3}{4}$  in.

Looking at the wing with the tangent sphere tip, one notices a similarity to the hemisphere-nosed rod if one opens the rod by splitting down the center. Clearly this modification to the rod changes the flow picture. One aspect of this change can be seen in Fig. 10 where a series of zero angle of attack planview schlieren are presented in air and in helium in the Langley 11-in. hypersonic tunnel. The bottom wing is 21

diam long and the top wing is 7 diam long and corresponds to a three times enlargement of that part of the bottom wing ahead of the dashed line. The Mach 6.9 and 9.6 air pictures are quite similar and the shock shape is not very different at Mach 11.1 and 18.4 in helium. The first part of the shock emanating from the nose is the same as that on a sphere; however, in the region where this nose shock would strike the leading edge there is an interaction between the bow shock and the leading edge detached shock characterized by the inflection which can be readily seen in the schlierens. The leading edge is thus seen to play a significant part in the flow over the wing.

The role of the leading edge or planform shape is also shown in surface flow studies of these wings obtained by Everhart in the Langley 11-in. hypersonic tunnel. In Fig. 11 are shown oil and carbon black surface flow studies of the blunt apex models at the same four Mach numbers as for the schlieren studies. In this case flow is from top to bottom on the figure. Again the top wings are 7 diam long and the bottom wings are 21 diam long. At Mach 6.9 and 11.1 in the upper pictures the broad horizontal stripes were brushed on and act as reservoirs for the streaming oil. The other wings were coated uniformly with oil. At the four Mach numbers shown the oil and lampblack streak patterns are roughly the same differing only in detail. Along the leading edge the flow picture is about what one expects from a swept cylinder. The Mach 6.9 flow picture is most readily discernible and roughly represents the pattern at all Mach numbers. As shown by this Mach 6.9 picture, if oil is not put into the central region of the slab portion of the wing, then no oil pattern is obtained because oil from the leading edge region cannot enter the central region. This central outflow is a consequence of the mass of air at high induced pressures which enters the wing over the apex region and is contained by the shock, the wing surface and the high pressure induced in the air coming from the leading edge region. That is, looking at the phenomena one way, the leading edge induced effects channel the energy from the nose "blast" down the center region of the slab. In this sort of picture dissipation must occur as this air moves further downstream and the proportion of the wing surface affected must become less. This can be seen if the 7-diam-long wing shown at the top is compared with the 21-diam wing at the bottom.

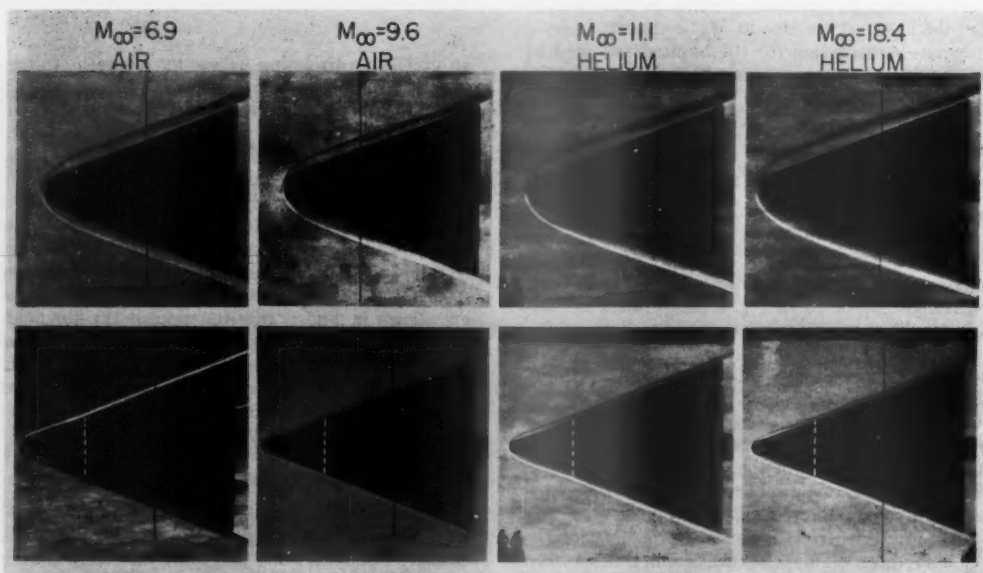


Fig. 10 Slab delta wings: schlieren studies at  $\alpha = 0$  deg



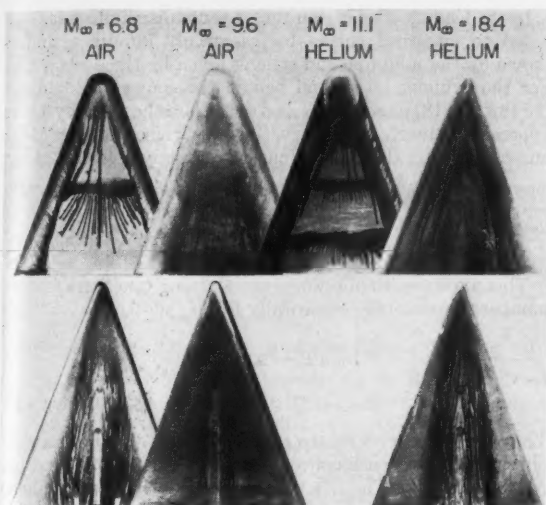


Fig. 11 Surface flow studies at  $\alpha = 0$  deg: blunt delta wing,  $\Lambda = 70$  deg

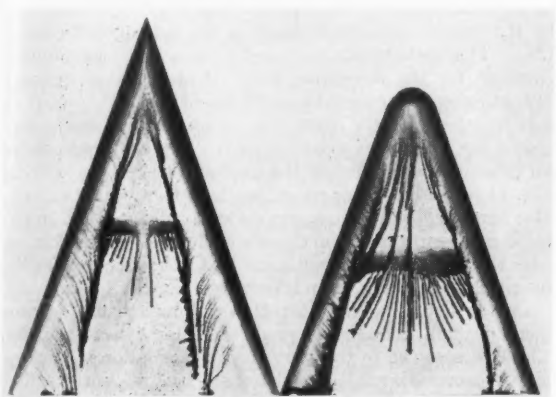


Fig. 12 Nose shape effect on blunt delta wing surface flow pattern,  $\alpha = 0$  deg: blunt wing,  $\Lambda = 70$  deg,  $M_\infty = 6.8$

On a wing as blunt as the 7-diam wing, changing the apex shape causes only a change in the degree of the effect on the surface flow pattern as illustrated in Fig. 12 where the flow patterns for the slab wing with the sharp apex and the wing with the tangent sphere nose are shown for comparison at a Mach number of 6.8. The region of central outflow is evident for both nose shapes; with less extent, however, in the case of the sharp nose wing.

At this point let us compare the pressures measured on the centerline of the blunt nose delta wing with those recorded from the hemisphere tipped rod which were presented earlier in this paper. Such a comparison for zero angle of attack is shown in Fig. 13 for Mach numbers ranging from 6.8 to 16.7. Consistently the pressures measured on the delta wing centerline are higher than those on the rod as a result of the channeling discussed previously. These pressures are essentially equal at the apex of the slab (junction of the sphere with the rod) and then depart rapidly from each other.

Thus far we have treated only the centerline of the blunt delta wing. It is of interest to determine effects over the entire wing. Figs. 14 and 15 present measured pressure distributions at zero angle of attack on the sharp nose and blunt nose slab delta wings at a Mach number near 10 in air and a Mach number of about 18 in helium. The pressures in terms of free stream static pressure are plotted against distance

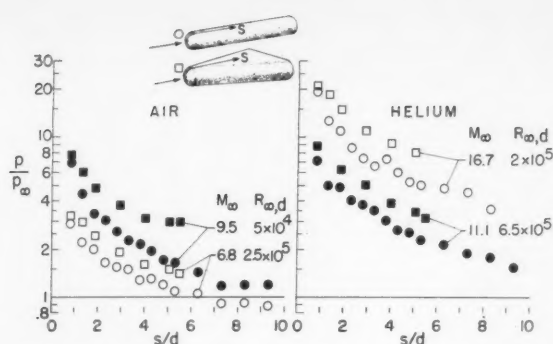


Fig. 13 Bluntness induced pressures on rod and delta wing,  $\alpha = 0$

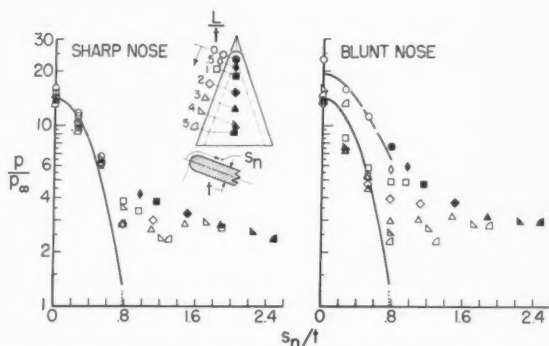


Fig. 14 Pressure distribution on blunt delta wing:  $\alpha = 0$ ,  $M_\infty = 9.5$ ,  $R_\infty, t = 4.5 \times 10^4$ , air

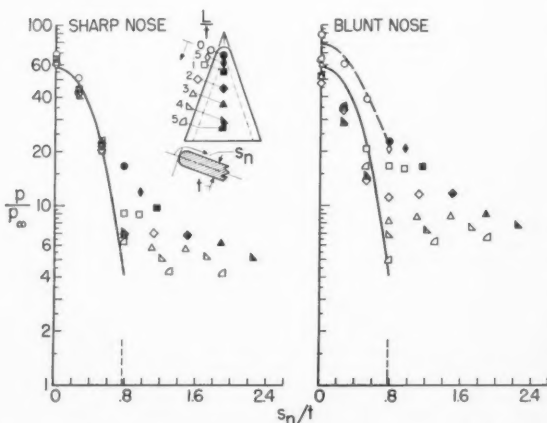


Fig. 15 Pressure distribution on blunt delta wing:  $\alpha = 0$ ,  $M_\infty = 18.4$ ,  $R_\infty, t = 5.1 \times 10^5$ , helium

normal to the leading edge nondimensionalized with respect to leading edge diameter. Qualitatively the results in air and helium are similar. On the slab the pressure is relatively constant at a given station (i.e., value of  $L/t$ ) on the wing. The center line is designated by the solid symbols. The decay in pressure along rays from the apex is evident and most clearly seen in the center line data. This is the effect that was presented in Fig. 13.

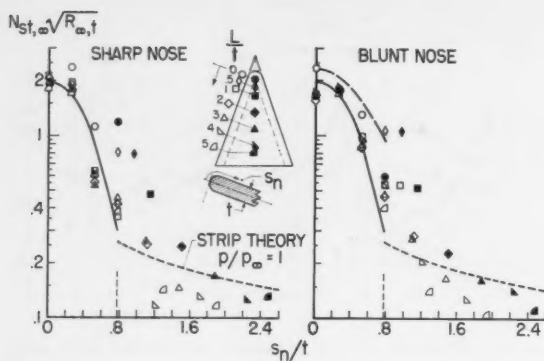


Fig. 16 Stanton number distribution on blunt delta wing:  $\alpha = 0$ ,  $M_\infty = 9.5$ ,  $R_\infty, t = 4.5 \times 10^4$ , air

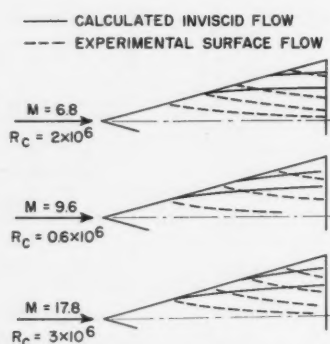


Fig. 17 Flow patterns at  $\alpha = 0$ : sharp leading edge delta wing;  $\Lambda = 75$  deg

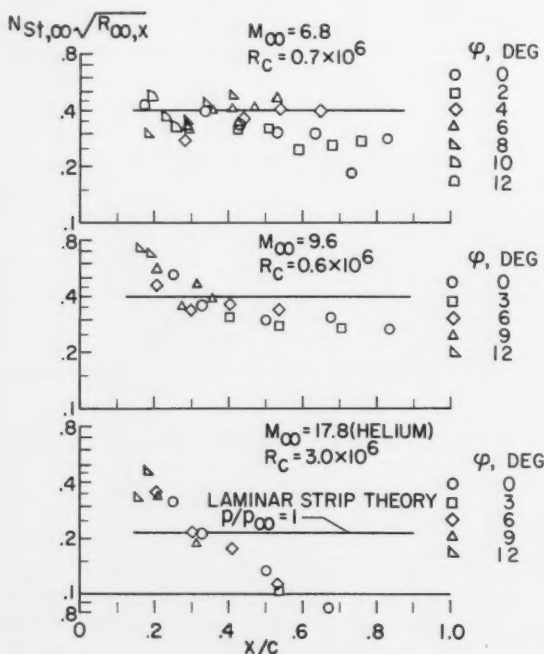


Fig. 18 Heat transfer distribution at  $\alpha = 0$ : sharp leading edge delta wing,  $\Lambda = 75$  deg

In the leading edge region the pressure distribution is compared to empirical curves for essentially infinite cylinders shown by the solid line and spheres given by the dashed line. For the cylinder in air and helium the sources of data are (15 through 18) plus unpublished data from the Langley 11-in. hypersonic tunnel. The curve for air which holds for Mach numbers greater than about four is accurately represented by

$$\frac{p}{p_{\max}} = \cos^2 \theta + 0.16 \sin^2 \theta - 0.00265 \theta^5$$

$$0 \leq \theta \leq 90 \text{ deg} \quad [3]$$

This pressure distribution is not a strong function of Mach number; for example, empirically for  $M_\infty \approx 3$

$$\frac{p}{p_{\max}} = \cos^2 \theta + 0.167 \sin^2 \theta - 0.00268 \theta^5$$

$$0 \leq \theta \leq 100 \text{ deg} \quad [4]$$

The empirical curves for the sphere pressure distribution were obtained from a consideration of (12, 18 through 22) and unpublished data. The  $L/t = 0$  station is a line on a sphere. Reasonable agreement of the data with these curves is noted with some interesting secondary effects.

The Stanton number distribution for these same wings is presented in Fig. 16. For reference purposes, Lees' theory for the heat transfer distribution around a cylinder and sphere by the integral method is shown in the leading edge region (23). This distribution was used with a modified Sibulkin equation for the stagnation point of an unswept cylinder (12) utilizing as the initial velocity gradient  $d(u/a_0)/d(s/t) = 2.19$  together with the cosine law for the effect of sweep suggested by Feller's experiments (24). The empirical curve for pressure distribution in the leading edge region shown in Fig. 14 was utilized in performing the integration. Reasonable agreement with the appropriate theories is noted in the leading edge region even though over most of the leading edge the known shock shape is not that to be expected for the infinite cylinder assumed in theory (see Fig. 10).

On the slab, however, strip theory (Monaghan's T-prime method) (25) gives a poor prediction of the heat transfer. The flow assumed in the strip theory calculation is more or less streamwise and, as we have seen in the surface flow streaks of Figs. 11 and 12, the surface flow directions are far from streamwise over a large portion of the wing. If the effects of surface pressure level and gradient are included in the theory (as, say, according to (8)), the agreement with experiment is not improved if streamwise flow is still assumed.

Thus far we have considered the delta wing with large amounts of blunting. The question arises of the flow on the seemingly simpler delta wing with a sharp leading edge. This wing, however, has its own peculiarities. On a sharp delta wing at hypersonic speeds near zero angle of attack, the rapid growth of the boundary layer at the leading edge has interesting consequences. As shown in Fig. 17 the boundary layer induced pressures cause the low energy air in the boundary layer near the surface to flow in toward the center of the wing and to pile up along the center line. The dashed lines representing this surface flow were traced from photographs of oil and lampblack streaks. The solid lines are the calculated stream lines external to the boundary layer based on the calculated boundary layer induced pressure gradient. Note that these stream lines in opposition to the flow lines near the surface are inclined away from the center line of the wing. The angle between the two sets of flow lines increases with increasing Mach number.

The effect of this induced inflow on the heat transfer is shown in Fig. 18 for the same three Mach numbers as for the flow lines of Fig. 17. Here heat transfer results obtained by Dunavant in air and Baradell and Blackstock in helium in the Langley 11-in. hypersonic tunnel in terms of the laminar correlation parameter based on tunnel test section static conditions are shown plotted against per cent distance from

the leading edge in the free stream flow direction. At Mach 6.8 ordinary strip theory with the T-prime method for zero pressure gradient appears to be adequate, although there is a tendency for the data at points nearest the center line to drop below this theory. At Mach 9.6 and 18 the heat transfer is increased above this theory for the points nearest the leading edge by the boundary layer induced pressures. However, there is a drop in the value of the heat transfer parameter with distance from the leading edge, and at the farthest distances from the leading edge there is a large discrepancy between the data and the strip theory. The deviation between strip theory and data increases with increasing Mach number.

#### Angle of Attack Effects for the Delta Planform

Up to now we have been considering the delta wing only at zero angle of attack. Actually the angle of attack case is probably of prime interest for practical purposes. To start, let us examine the top view schlieren photographs of blunt slab delta wing. This is the wing which we extensively investigated at zero angle of attack in the preceding section of this paper. The schlierens shown in Fig. 19 at Mach 6.9 present the same wings as in Fig. 10 at angles of attack of 10 deg, 20 deg, and 30 deg. Again the top wing in each set essentially represents a three times enlargement of the region ahead of the dashed line on the lower figure. If the extent of the nose influence is judged by the inflection in the leading edge shock, the blunt nose affects less of the wing length as the angle of attack increases. Since the spherical nose has a shock of fixed shape, that is, independent of angle of attack in the range shown here, this change in shock shape is mainly due to changes in the shock around the cylindrical leading edge with angle of attack. Far enough away from the nose at 0 and 10 deg angle of attack the shock is parallel to the leading edge. However, at 20 deg and, to a more noticeable extent, at 30 deg angle of attack the mainstream flow senses the local wing span, and the leading edge shock shape becomes conical in nature.

The question arises as to what this means in terms of the pressures on the wing. Thus, let us examine the center line pressure distribution on this blunt nosed delta wing. In Fig. 20 are shown experimental data for this wing at 0, 10, and 20 deg angle of attack and Mach 6.85 and 9.6 where the pressure parameter is  $p/p_{\text{MAX}}$ . The length parameter is distance along the surface on the center line of the wing in terms of leading edge diameters. The origin of the surface distance is always taken at the geometric stagnation point of the spherical nose. On the spherical nose there is a Mach number freeze; that is,  $p/p_{\text{MAX}}$  is a function only of position on the sphere and not of a free stream Mach number, and for clarity only the Mach 6.85 data are shown. On the slab portion of the high pressure side of the wing one notices that the pressure gradient induced by the blunt nose, which is so pronounced at zero angle of attack, becomes less severe with increasing angle of attack and virtually disappears at 20 deg angle of attack and greater. At zero angle of attack the induced pressures on the slab are essentially those presented in Fig. 13.

Next, we examine the shock in side view. In Fig. 21 the shock angle determined from schlieren photographs of the flat wings with leading edge sweeps from 60 to 75 deg as a function of angle of attack is shown. Included in this figure, but not identified, are wings with sharp and blunt noses and leading edges. Only measurements for essentially straight shocks are shown, so that data at angles of attack less than about 20 deg for the blunted wings and within about  $1\frac{1}{2}$  diam of the nose are excluded from this figure. The location of the body surface and two-dimensional oblique shock theory are included on this figure for reference. Note that while for shock angles greater than about 19 deg the delta wing shock angles deviate considerably from the two-dimensional theory, the incremental effect of Mach number seems to be

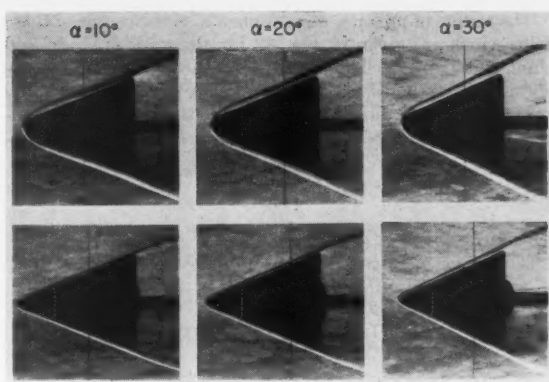


Fig. 19 Slab delta wings: schlieren studies at  $M = 6.9$

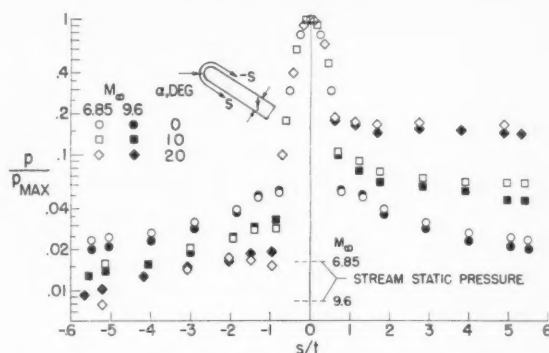


Fig. 20 Centerline distribution of pressure on blunt delta wing,  $\Lambda = 70$  deg

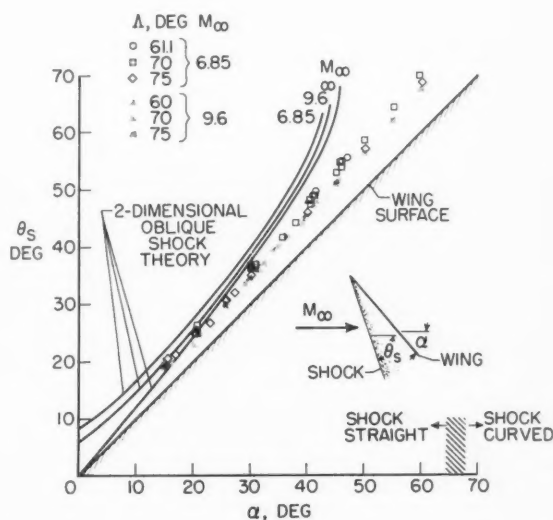


Fig. 21 Effect of Mach number on shock angle for flat delta wings

given with good accuracy by the theory, and it is expected that with further increases in Mach number there will be an almost negligible change in shock angle. Also noteworthy is the insensitivity of the shock angle to changes in sweep angle and the small shock standoff angle from the body surface.

The results of pressure measurements on the center of these delta wings are given in Fig. 22 for the various sharp and blunt delta wings. The pressures on the wing center line are normalized with respect to free stream static pressure and are presented as a function of angle of attack for Mach numbers of 6.85 and 9.6. In this data two sweep angles are in-

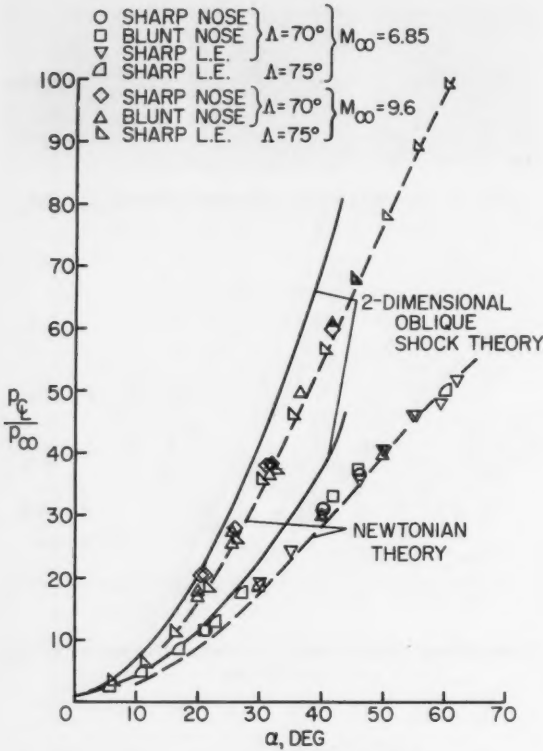


Fig. 22 Pressures on center line of flat delta wing

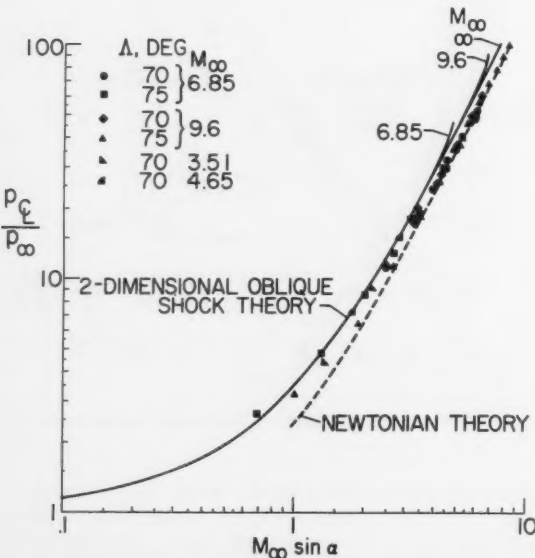


Fig. 23 Correlation of pressures on center line of flat delta wing

cluded (70 and 75 deg) and the data are coded so that you may differentiate between the blunt and sharp leading edge wings. There actually appears to be no significant difference between the pressures measured on the sharp and blunt leading edge wings for the two sweep angles shown as indicated by the shock angles presented in Fig. 21. This must be qualified for the blunt wings shown to exclude angles of attack below 20 deg and distances less than about 1.5 diam from the nose. At the higher angles of attack the measured pressures are well below the prediction of two-dimensional oblique shock theory, as would be expected from the measured shock angles. However, the pressures agree fairly well with the Newtonian theory.

We, of course, would like to be able to predict the pressures at Mach numbers other than those shown here. Thus, the data are next examined to show how these results may be correlated even though as yet there are no adequate theories for predicting the pressures on delta wings with detached shocks. Fig. 23 shows the good correlation which results from using the hypersonic similarity parameter  $M_\infty \sin \alpha$  suggested by both hypersonic oblique shock theory and Newtonian theory to correlate the wall to free stream static pressure ratios obtained on the center line of various flat delta wings. The results from exact two-dimensional oblique shock theory and Newtonian theory are included in this figure for reference. Only data where essentially no longitudinal pressure gradient exists on the center line have been included. To the data shown in Fig. 22 have been added some unpublished results obtained by Burbank in the Langley Unitary Plan Wind Tunnel at Mach numbers of 3.51 and 4.65 at angles of attack up to 45 deg. For these flat wings the sweep angles at which pressure data are available are only 70 and 75 deg; however, data for delta wings with sweep angles to at least as low as 60 should correlate with the results shown here based on the shock angle measurements presented in Fig. 21. With this correlation we may predict the center line pressures on a delta wing at Mach numbers considerably different from those of the tests.

Thus far the center line of the wing has been considered; let us look at the flow over the wing in a more general way. Again we examine surface oil flow results. Fig. 24 presents tracings obtained by Dunavant of surface flow streaks formed by flowing lubricating oil impregnated with carbon black on the sharp leading edge wing with 75 deg sweep at a Mach number of 9.6. The patterns are shown in 15 deg increments from 0 to 60 deg. The zero angle of attack pattern is essentially a repetition of the pattern previously presented in Fig. 17. There is a definite surface flow in toward the center of the wing caused by the pressure gradient induced by the thick boundary layer. However, as indicated in Fig. 17, because of this very gradient, the stream lines external to the boundary layer must be out away from the center of the wing. With increasing angle of attack, as shock loss effects start to predominate, the flow at the surface also turns out from

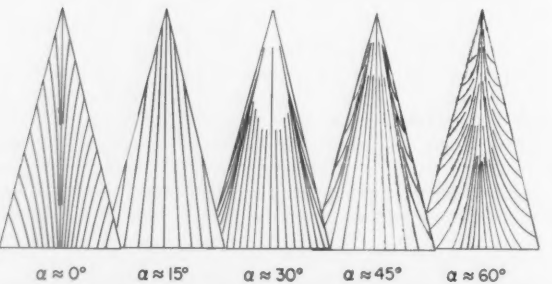


Fig. 24 Lower surface flow patterns on flat delta wings:  $M_\infty = 9.6$ ,  $\Lambda = 75$  deg



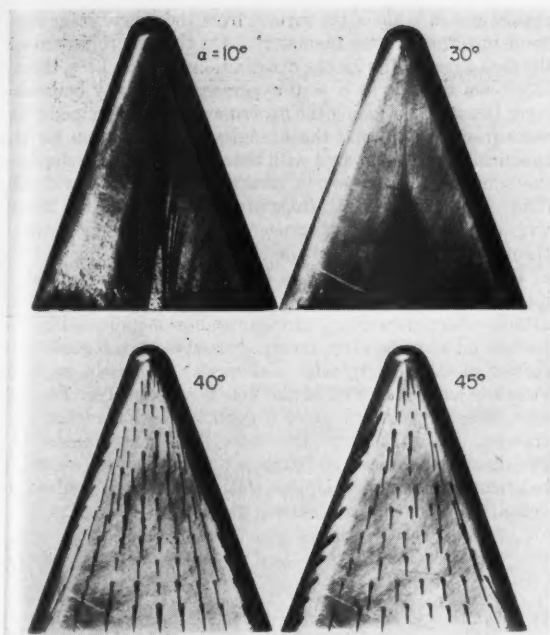


Fig. 25 Surface flow studies at angle of attack: blunt delta wing,  $\Lambda = 70$ ,  $M_\infty = 6.8$  deg

the center as shown at the three higher angles of attack. At 15 deg angle of attack the flow is away from the wing centerline, but it still comes in across the leading edge. At 30 deg angle of attack the flow has turned out to such an extent that in the sense of airflow direction the geometric leading edge has become a trailing edge. An interesting feature of the flow at 30 deg angle of attack is the appearance of a parting line at about 12 deg out from the center line of the wing. At 45 deg angle of attack the flow is very close to radial in the central region of the wing, and above this angle of attack the parting line is not a feature of the surface flow lines. At 60 deg angle of attack the flow lines, which for the most part were more or less straight at 15 and 30 deg angle of attack, appear to be hyperbolic in nature. It may be seen from the figure that the patterns are conical at angles of attack of 30 deg and greater.

The patterns exhibited by the blunt delta wing with 70 deg sweep are given in Fig. 25. These patterns, with modifications due to the presence of the large leading edge bluntness, are roughly similar to those presented for the sharp leading edge wing in Fig. 24.

Of course the problem arises of calculating these patterns. At 60 deg angle of attack the spanwise distribution in pressure was close to that obtained from measurements on a circular disk at 90 deg to a hypersonic flow (26). This pressure variation over a disk was then used to calculate the first order external stream lines assuming conicity from the apex and cross flow to the body ignoring the shock inclination to the body. The results of this calculation compared to the surface stream line pattern from Fig. 24 are shown in Fig. 26 for this angle of attack of 60 deg. There is a considerable discrepancy between the two patterns. However, this may be due to secondary flows in the boundary layer.

A case in which the external stream lines would closely match the surface stream lines would be a more or less radial flow. Dunavant and Bertram at Langley have developed a method based on three-dimensional cross flow to treat the delta wing at 90 deg angle of attack. A computation by this

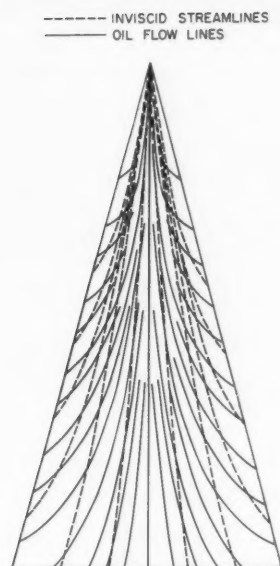


Fig. 26 Lower surface flow pattern at  $\alpha = 60$ : flat delta wing,  $M_\infty = 9.6$ ,  $\Lambda = 75$  deg

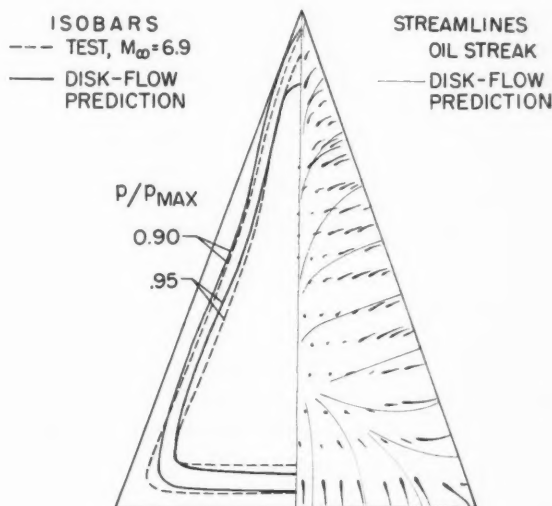


Fig. 27 Surface flow pattern at  $\alpha = 90$  deg

method for an essentially sharp delta wing with 70 deg of sweep is shown in Fig. 27 compared to surface oil streak and pressure measurements by Fetterman in the Langley 11-in. hypersonic tunnel. In this case a modification to the flow over a disk allows a good prediction of the surface stream lines and pressures on the wing.

The method of construction is shown in Fig. 28. Lines of constant velocity based on the empirical velocity distribution on the inscribed sharp edge disk, e. g. (26), are drawn parallel to the leading edge. Where these constant velocity lines intersect, vector addition is used to obtain the resultant velocity direction and magnitude. With this method pure radial flow is obtained in the shaded regions as no interaction

can occur. From these resultant velocities the first order streamlines and pressure distribution may be readily obtained. The construction is expected to be most accurate for not too slender winglike planforms.

To what extent is the heat transfer altered in the region of a blunt nose? Besides the question of nose effects there is also the problem of effects of the various flow patterns shown earlier. In Fig. 29 is presented the variation in heat transfer coefficient along the center line of the 70 deg swept wing with cylindrical leading edges and a spherical nose at Mach 9.6. This is the same shape wing for which the pressures were presented in Fig. 20 and the surface flow patterns in Fig. 25. The measured Stanton number has been referenced to the Stanton number

$$(N_{st,\infty} \sqrt{R_{\infty,d}})_{s=0} = 8.40$$

calculated for the stagnation point of the sphere (modified Sibulkin theory) (12), with an empirically determined initial velocity gradient  $d(u/a_0)/d(s/t) = 2.315$  and is plotted

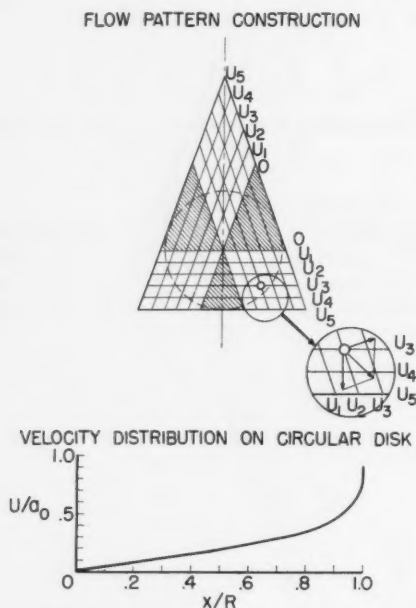


Fig. 28 Velocity distribution calculation at  $\alpha = 90$  deg.

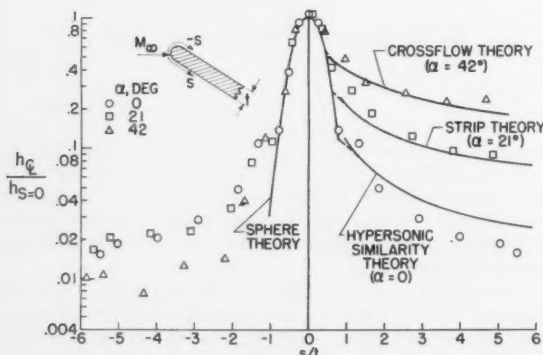


Fig. 29 Centerline distribution of heat transfer on blunt delta wing;  $\Lambda = 70$  deg, cylindrical leading edge, spherical nose,  $M_{\infty} = 9.6$

against distance along the surface from the sphere stagnation point in terms of nose diameters. On the sphere nose itself the data agree well with the distribution given by Lees, theory (23). On the slab at  $\alpha = 0$  hypersonic similarity boundary layer theory (8) utilizing the experimentally determined pressures from Fig. 20 and the Mangler transformation for the spherical nose is compared with the data. Near the shoulder the similarity theory shows reasonable agreement with the data; however, the data drops increasingly below the theory with increasing surface distance. This discrepancy between theory and experiment on the slab is not surprising in view of the surface flows shown in Fig. 11 which were not taken into account in applying the theory. At 20 deg angle of attack, where more nearly streamwise flow is indicated by the surface oil streaks, strip theory does give an adequate prediction of the heat transfer coefficient. When the angle of attack is as high as 42 and the flow is as shown in Fig. 25, then cross flow theory gives a good prediction of the heat transfer. In calculating the cross flow heat transfer the two-dimensional modified Sibulkin theory was used assuming independence of the spanwise stations with the center line velocity gradient at each station given by

$$\left[ \frac{d(u/a_0)}{d(s/b)} \right]_{\xi} = 0.745 + 1.57 \frac{t}{b} \quad [5]$$

In this case  $s$  is the spanwise surface distance from the wing center line at the local span  $b$ , and  $t$  corresponds to the edge diameter which in this case was taken as the wing thickness. The equation arrived at from disk data was taken to apply two-dimensionally.<sup>4</sup>

### Concluding Remarks

Our results show that for simple two- and three-dimensional shapes, blast wave theory in conjunction with characteristics theory is a powerful tool that can provide useful results in fluid mechanics work. The pressure distributions (and in previous work the heat transfer also) on simple shapes such as a blunted rod have been found to be predictable by these theories. As predicted by blast wave theory the nose drag itself is found to be the main influence on the induced pressures with the nose shape having little or no influence. Qualitatively, the phenomena experienced on a more complicated shape such as a delta wing at low angles of attack are explicable in terms of the contribution to the flow field of the individual components of which the wing is composed. As the angle of attack is increased the flow over the delta wing can change markedly and the approaches used at the lower angles of attack can be invalid.

### Nomenclature

- $a_0$  = stagnation point speed of sound
- $b$  = local wing span
- $c$  = root chord of delta wing
- $C_{D,n}$  = nose drag coefficient
- $d$  = maximum body diameter
- $h_{\xi}$  = heat transfer coefficient along center line of delta wing
- $h_{s=0}$  = stagnation point heat transfer coefficient
- $L$  = length of cylindrical leading edge
- $M_{\infty}$  = free stream Mach number
- $M' = \frac{dM_{\infty}}{d(x/t)}$
- $n$  = exponent for power law pressure variation
- $N_{st,\infty}$  = Stanton number based on tunnel test section static conditions
- $p_{\xi}$  = delta wing center line static pressure
- $p_{\infty}$  = free stream static pressure

<sup>4</sup> With more results available since these computations were done, a more S-shaped curve with the same end points given by Eq. 5 is believed to represent the data better. However, this more accurate velocity gradient will not significantly alter the cross flow calculations in Fig. 29.

$p_{\max}$	= stagnation pressure after a normal shock
$p$	= wall pressure
$R$	= radius of circular disk
$R_c$	= Reynolds number based on free stream conditions and root chord of delta wing
$R_{x,x}$	= Reynolds number based on tunnel test section static conditions and distance from leading edge parallel to body center line
$R_{x,s}$	= Reynolds number based on free stream conditions and $s$
$R_{x,d}$	= Reynolds number based on free stream conditions and $d$
$R_{x,t}$	= Reynolds number based on free stream conditions and $t$
$s$	= streamwise surface distance measured from geometric stagnation point
$s_R$	= distance along surface normal to leading edge of swept wing
$t$	= plate thickness
$U$	= velocity
$x$	= streamwise surface distance measured from model nose cylinder juncture or streamwise distance from leading edge of sharp delta wing
$\alpha$	= angle of attack
$\gamma$	= ratio of specific heats
$\theta$	= radial angle measured from stagnation point
$\theta_s$	= shock angle
$\varphi$	= ray angle on delta wing measured from center line
$\Lambda$	= sweep angle

## References

- Bertram, M. H. and Baradell, D. L., "A Note on the Sonic-Wedge Leading-Edge Approximation in Hypersonic Flow," *J. Aero. Sci.*, vol. 24, no. 8, August 1957, pp. 627, 628.
- Baradell, D. L. and Bertram, M. H., "The Blunt Plate in Hypersonic Flow," NASA TN D-408, 1960.
- Henderson, A. Jr. and Baradell, D. L., "Recent Work at Langley Research Center in the Development of Hypersonic Helium Tunnels," *Proc. Nat. Symposium on Hypervelocity Techniques*, Denver, Colo., *Inst. Aero. Sci.*, Oct. 20-21, 1960, pp. 131-141.
- Henderson, A. Jr., "Investigation of the Flow Over Simple Bodies at Mach Numbers of the Order of 20," NASA TN D-449, August 1960.
- Cheng, H. K. and Pallone, A. J., "Inviscid Leading-Edge Effect in Hypersonic Flow," *J. Aero. Sci.*, vol. 23, no. 7, July 1956, pp. 700-702.
- Lees, L. and Kubota, T., "Inviscid Hypersonic Flow Over Blunt-Nosed Slender Bodies," *J. Aero. Sci.*, vol. 24, no. 3, March 1957, pp. 195-202.
- Chernyi, G. G., "Hypersonic Flow Past an Airfoil with a Slightly Blunted Leading Edge," *Koklady, AN USSR*, vol. 114, 200.4, 1957, pp. 721-724, Morris D. Friedman, Inc., C-112.
- Bertram, M. H. and Feller, W. V., "A Simple Method for Determining Heat Transfer, Skin Friction, and Boundary-Layer Thickness for Hypersonic Laminar Boundary-Layer Flows in a Pressure Gradient," NASA 5-24-59L, June 1959.
- Bertram, M. H. and Blackstock, T. A., "Some Simple Solutions to the Problem of Predicting Boundary-Layer Self-Induced Pressures," NASA TN D-798, April 1961.
- Lin, S. C., "Cylindrical Shock Waves Produced by Instantaneous Energy Release," *J. Appl. Phys.*, vol. 25, no. 1, January 1954, pp. 54-57.
- Bogdonoff, S. M. and Vas, I. E., "A Study of Hypersonic Wings and Controls," IAS Paper 59-112; presented at the IAS National Summer Meeting, Los Angeles, Calif., June 16-19, 1959.
- Crawford, D. H. and McCauley, W. D., "Investigation of the Laminar Aerodynamic Heat-Transfer Characteristics of a Hemisphere-Cylinder in the Langley 11-Inch Hypersonic Tunnel at a Mach Number of 6.8," NACA Rep. 1323, 1957. (Supersedes NACA TN 3706, 1956.)
- Van Hise, Vernon, "Analytic Study of Induced Pressures on Long Bodies of Revolution with Varying Nose Bluntness at Hypersonic Speeds," NASA TR R-78, 1961.
- Mueller, J. N., Close, W. H. and Henderson, Arthur Jr., "An Investigation of Induced Pressure Phenomena on Axially Symmetric, Flow-Aligned, Cylindrical Models Equipped with Different Nose Shapes at Free Stream Mach Numbers from 15.6 to 21 in Helium Flow," NASA TN D-373, 1960.
- Penland, Jim A., "Aerodynamic Characteristics of a Circular Cylinder at Mach Number 6.86 and Angles of Attack Up to 90°," NASA TN 3861, January 1957.
- Beckwith, I. E. and Gallagher, J. J., "Experimental Investigation of the Effect of Boundary Layer Transitions on the Average Heat Transfer to a Yawed Cylinder in Supersonic Flow," NACA RM L56E09, July 1956.
- Beckwith, I. E. and Gallagher, J. J., "Local Heat Transfer and Recovery Temperatures on a Yawed Cylinder at a Mach Number of 4.15 and High Reynolds Numbers," NASA Memo 2-27-59L, April 1959.
- Vas, I. E., Bogdonoff, S. M. and Hammit, A. G., "An Experimental Investigation of the Flow Over Simple Two-Dimensional Axisymmetric Bodies at Hypersonic Speeds," Princeton Univ. Rep. 382, June 1957.
- Oliver, Robert E., "An Experimental Investigation of Flow Over Simple Blunt Bodies at Nominal Mach Number of 5.8," GARCIT Hypersonic Wind Tunnel Memo no. 26, June 1955.
- Machell, R. M. and O'Bryant, W. T., "An Experimental Investigation of the Flow Over Blunt-Nosed Cones at a Mach Number of 5.8," GARCIT Hypersonic Research Project Memo no. 32, June 1956.
- Beckwith, I. E., "Heat Transfer and Recovery Temperatures on a Sphere with Laminar, Transitional, and Turbulent Boundary Layers at Mach Numbers of 2.00 and 4.15," NACA TN 4125, Dec. 1957.
- Kendall, J. M. Jr., "Experiments on Supersonic Blunt-Body Flows," Jet Propulsion Lab. Progress Rep. No. 20-372, Calif. Inst. Tech., Feb. 1959.
- Lees, Lester, "Laminar Heat Transfer Over Blunt-Nosed Bodies at Hypersonic Flight Speeds," *JET PROPULSION*, vol. 26, no. 4, April 1956, pp. 259-269.
- Feller, William V., "Investigation of Equilibrium Temperature and Average Laminar Heat-Transfer Coefficients for the Front Half of Swept Circular Cylinders at a Mach Number of 6.9," NACA RM L55F08a, Aug. 1955.
- Monaghan, R. J., "An Approximate Solution of the Compressible Laminar Boundary Layer on a Flat Plate," R and M no. 2760, British A.R.C., 1953.
- Copper, Morton and Mayo, E. E., "Measurements of Local Heat Transfer and Pressure on Six 2-Inch-Diameter Blunt Bodies at a Mach Number of 4.95 and at Reynolds Numbers Per Foot Up to  $81 \times 10^6$ ," NASA Memo 1-3-59L, March 1959.

# Approximate Solution of Isentropic Swirling Flow Through a Nozzle<sup>1</sup>

ARTUR MAGER<sup>2</sup>

National Engineering Science Co.  
Pasadena, Calif.

This paper presents an approximate solution of swirling, potential flow through a nozzle. In this solution the radial velocity component is identically equal to zero, and hence the boundary conditions may not be satisfied exactly. The relation between the postulated velocity potential and the nozzle wall shape must thus be determined by use of the integrated continuity equation. In this process it is shown that at each axial position there exists a "minimum" radius at which the density becomes zero and the flow ceases to exist. The determination of the shape of this void region all along the nozzle is an essential feature of the solution. The results indicate that the void region near the nozzle axis causes a pronounced restriction of the flow area at the nozzle throat. Because of this, the mass flow is very appreciably affected by the swirl and, in this idealized case, for strong enough swirl it can be entirely stopped. Furthermore, the results also indicate that the swirl tends to produce rather large thrust losses when the nozzle exit to throat area ratio is near unity. For large values of this quantity, however, such as occur in practical rocket nozzles, these losses tend to decrease, so that the specific impulse in such cases is only slightly reduced by the swirl.

FOR EFFICIENT utilization of the propellant, the rocket nozzle should, in general, expand the flow of gases to the ambient pressure prevailing outside the nozzle. In the course of its flight, however, the ambient pressure outside the rocket changes very drastically, and as a result of this change the thrust produced by the nozzle must necessarily decrease from its design value. On the other hand, since the mass flow through the rocket is dependent only on the chamber conditions and the throat area, its value remains unaffected by the changing ambient pressure. Consequently, the specific impulse, which, after all, is a measure of the rocket's efficiency, must necessarily decrease.

From the above discussion, it is quite obvious that the decrease of the specific impulse could be prevented if the mass flow were regulated in proportion to the decreasing thrust. But the regulation of mass flow requires that either the chamber pressure be decreased or the throat cross sectional area be reduced. The regulation of the mass flow by the decrease of the chamber pressure is impractical, because a high chamber pressure is desirable for efficient burning of the propellant. If such pressure is not maintained, the attendant decrease of combustion efficiency will soon force an additional decrease of thrust and prevent the desired invariance of specific impulse.

Similarly, to accomplish the appropriate variation of the throat area of an axially symmetric exit nozzle, requires usually a very complex and heavy mechanism whose design is further handicapped by the severe heating problems existing in that region. For these reasons the mechanical variation of the rocket nozzle throat area is presently considered to be impractical, and therefore is not used. As a result of these difficulties, which prevent the regulation of mass flow, the rocket efficiency cannot be maintained at, or near, its design value all along its trajectory.

However, the nozzle geometry may also be varied artificially by other than purely mechanical means. Imagine, for example, that upstream of the throat the flow is imparted a slow swirling motion. The conservation of the angular momentum requires then (similarly to a whirling ice skater who brings his arms down) that in the passage through the narrow throat this swirling become very intense. One can thus see that as the flow nears the throat it is forced to proceed along a helical path with a continuously decreasing pitch. Its axial movement is thus impaired so that the addition of the swirl can be thought of as effectively constricting the throat's cross sectional area and thus, in fact, regulating the mass flow. Observe here that, for this type of control to be feasible, one must insure that its corresponding effect on the thrust does not lead to any additional losses which could impair the rocket's performance. One may expect this to occur downstream and far from the throat where, due to the conservation of the angular momentum, the swirl magnitude will again decrease. The swirling flow appears thus quite interesting from the standpoint of efficient rocket mass flow control, and hence there is a need to investigate its nature in detail.

The introduction of swirl into the flow ahead of the nozzle throat is currently considered also in connection with a number of devices which may prove important in other rocket engine applications. For example, in certain types of nuclear rockets the swirl of the spinning propellant has been proposed in order to retain the heavy uranium atoms inside the rocket chamber. Also, the swirling action is thought to affect the stability and efficiency of combustion and cause a redistribution of the total temperature, which may, in certain cases, lead to the reduction of heat transfer problems. Furthermore, swirling flow is also used in some plasma rockets where this type of flow not only protects the walls of the chamber, but also is necessary for arc stabilization. Since in all these devices the nozzle must necessarily operate with swirling flow, the understanding of such a flow is desirable if their design is to be carried out on any kind of a rational basis.

Presented at the ARS 15th Annual Meeting. Washington, D. C., Dec. 5-8, 1960.

<sup>1</sup> The major portion of this work was carried out during the author's association with ASTRO-The Marquardt Corp.

<sup>2</sup> Director of Sciences.



As a first step toward this end, the present paper gives the results of an analytical investigation which led to an approximate solution of swirling, potential flow through a nozzle. The major portion of this work was carried out at ASTRO (a division of The Marquardt Corp.) and the author takes this opportunity to express his thanks to the director, R. E. Fisher, for the permission to publish this work. In addition, the author would also like to express his appreciation to John Drake, who not only originally suggested this problem, but also, in the course of the investigation, made a number of valuable comments and suggestions.

To the best knowledge of the author, at present, there are only two experimental studies of swirling flow in nozzles (1, 2).<sup>3</sup> Unfortunately, these studies are not directly applicable to the subject of the present investigation and their data do not permit a quantitative comparison with the present results. For this reason a detailed experimental confirmation of swirling potential flow in nozzles is still lacking. Of course, once such a confirmation is attempted, the viscous effects, which are omitted from potential flow, will have to be considered. In swirling flow these effects will be important not only near the solid walls, but also at the axis of rotation. For this reason, one may expect the applicability of this type of solution to be somewhat more restricted than, say, in flows which have no swirl. On the other hand, to study the effects which, by definition, are excluded from potential flow, one needs the present solution so that it can serve as a boundary condition for the regions in which such effects are important.

It should also be noted that the actual physical mechanism by which the swirl is imparted to the flow ahead of the nozzle is similarly not considered in the present investigation. This process may, in some cases, produce a definite total pressure loss, which eventually must show itself as a decreased nozzle efficiency. In other words, because of the neglect of the viscous losses and the losses connected with the creation of the swirl, one should consider this to be an investigation of the upper bound of what may be achieved under the most ideal conditions. In this sense, then, the present results thus become a goal which one may strive for in an actual application.

## Analysis of the Flow Field

Consider a cylindrical, polar coordinate system  $r, \theta, x$  with the corresponding velocity components  $v, w, u$  respectively as illustrated in Fig. 1. In this system assume a potential  $\Phi$  which is not a function of  $r$

$$\Phi = [R(x)W(x)]\theta + \int U(x) dx \quad [1]$$

so that the velocity components are given by

$$v = 0, \quad w = \frac{1}{r} \Phi_\theta = \frac{WR}{r}, \quad u = (RW)_x \theta + U \quad [2]$$

Observe now that if the flow is to be axially symmetric one must have  $(RW)_x = 0$  or

$$RW = \text{const} \equiv K_1 \quad [3]$$

so that the total velocity  $V$  is given by

$$V^2 = v^2 + w^2 + u^2 = \left(\frac{K_1}{r}\right)^2 + U^2 \quad [4]$$

This flow, being derived from a potential function  $\Phi$ , must necessarily be irrotational; consequently the appropriate connection between the pressure  $p$  and the velocity  $V$  is furnished by the Bernoulli equation in the whole flow field and not just on the individual stream lines. For a given set of

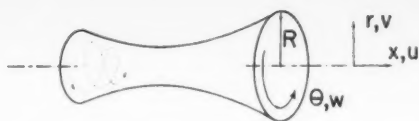


Fig. 1 Coordinates and velocity components

total conditions this connection is thus known regardless of the stream line distribution.

The postulated potential function must, however, satisfy the continuity equation, subject to the appropriate boundary conditions. Here, unfortunately, since the velocity  $v = 0$ , the boundary conditions may not be satisfied exactly; consequently the continuity equation is written in a once integrated form which bypasses this difficulty

$$\text{mass flow} = \int_A \rho u dA = \text{const} \equiv K_2 \quad [5]$$

This failure to satisfy the boundary conditions exactly and the subsequently required use of the integrated continuity equation is then the chief nature of the approximation here employed. For the flow to be valid we thus require that  $\Phi$ , or more specifically  $U(x)$ , satisfy Eq. 5, subject to a certain prescribed area variation  $A(x)$  and a certain specified value  $K_1$ .

In irrotational (and thus isentropic) flow, the density required for the solution of Eq. 5 is given by

$$\rho = \rho_t \left[ 1 - \frac{\gamma - 1}{2} \left( \frac{V}{a_t} \right)^2 \right]^{1/(\gamma - 1)} = \rho_t \left\{ 1 - \frac{\gamma - 1}{2a_t^2} \left[ \left( \frac{K_1}{r} \right)^2 + U^2 \right] \right\}^{1/(\gamma - 1)} \quad [6]$$

so that there exists therefore a limiting minimum value of  $r = r_0(x)$  at which the density is exactly zero and below which the flow cannot exist

$$r_0^2 \equiv \frac{\frac{\gamma - 1}{2} K_1^2}{a_t^2 - \frac{\gamma - 1}{2} U^2} \quad [7]$$

Upon substitution of this limiting value into Eq. 6 it is possible to write the density variation as

$$\rho = \rho_t \left\{ \left[ 1 - \frac{\gamma - 1}{2} \left( \frac{U}{a_t} \right)^2 \right] \left[ 1 - \left( \frac{r_0}{r} \right)^2 \right] \right\}^{1/(\gamma - 1)} \quad [6a]$$

so that Eq. 5 becomes

$$2\pi \rho_t U \left[ 1 - \frac{\gamma - 1}{2} \left( \frac{U}{a_t} \right)^2 \right]^{(1/\gamma - 1)} \times \int_{r_0}^R \left[ 1 - \left( \frac{r_0}{r} \right)^2 \right]^{(1/\gamma - 1)} r dr = K_2 \quad [5a]$$

since the integration need be carried only in the region where the flow takes place.

It is convenient now to define the following nondimensional quantities

$$\xi \equiv \frac{r}{R} \quad [8]$$

$$M^2 \equiv \frac{U^2}{a_t^2 - \frac{\gamma - 1}{2} U^2} \quad [9]$$

$$m \equiv \frac{K_2}{\rho_t a_t A^*} \quad [10]$$

<sup>3</sup> Numbers in parentheses indicate References at end of paper.

CREATIVE ELECTRONICS BY RCA

# NORAD ON THE ALERT

## Inputs from BMEWS Provide Instantaneous Missile Data Direct to NORAD Headquarters

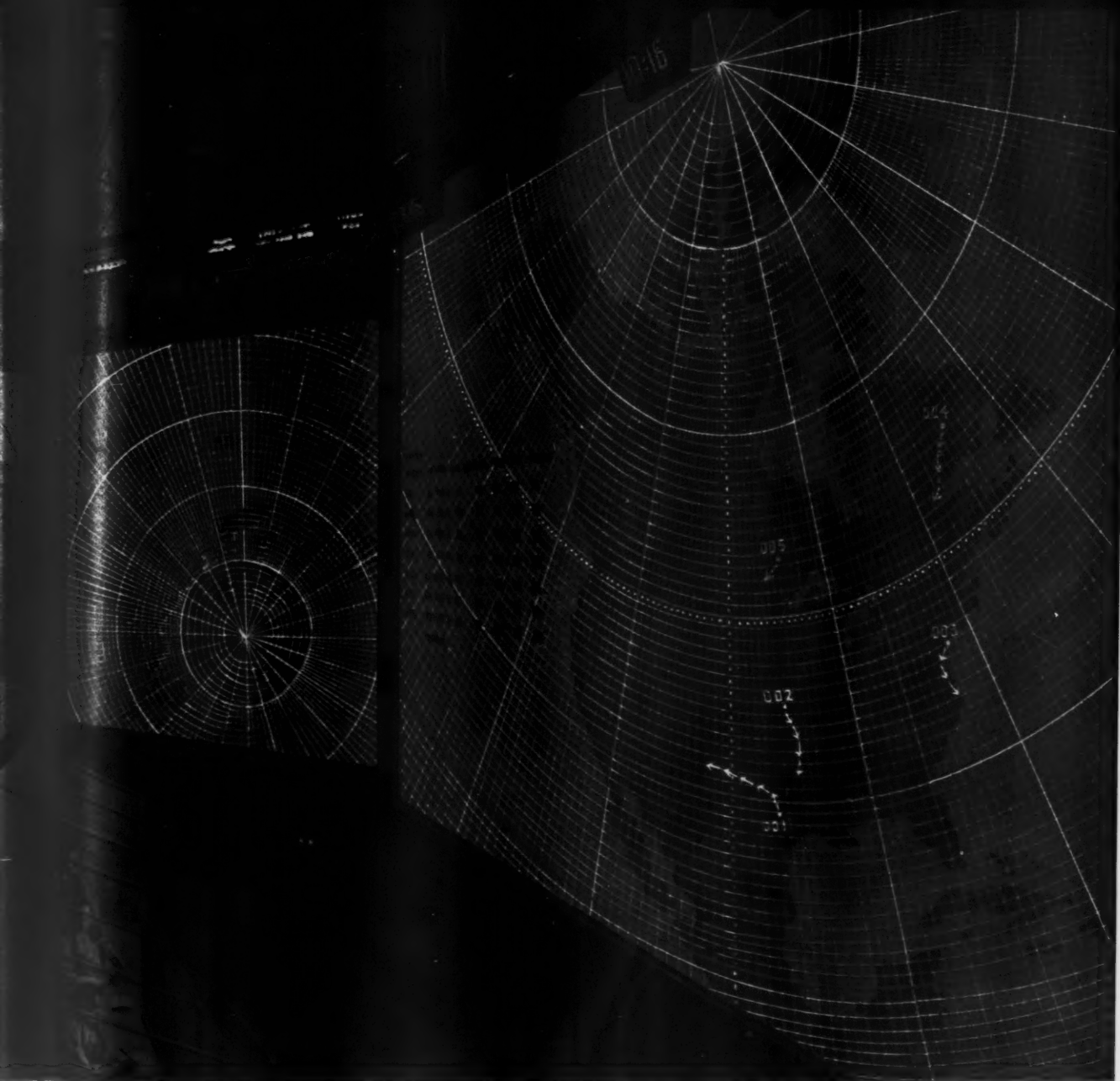
From our vast outer defense perimeter, over thousands of miles, to the nerve center of the North American Air Defense Command at Colorado Springs, the most advanced concept of data handling and checkout is being utilized in the BMEWS system. The stakes are high, for the purpose is defense of the North American Continent.

At BMEWS installations operated by USAF Air Defense Command, computers read out missile tracking data from giant radars. This information is simultaneously relayed to NORAD's Combat Operations Center.

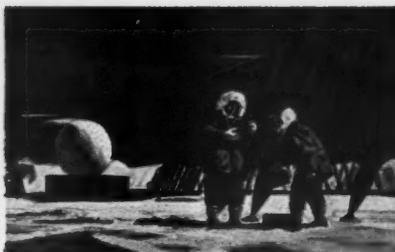
The Radio Corporation of America is prime systems contrac-

tor for BMEWS. At the COC, RCA's Display Information Processor computing equipment automatically evaluates missile sightings, launch sites and target areas. By means of data processing and projection equipment installed by RCA and a team of other electronics manufacturers, the findings are displayed on huge, two-story high map-screens in coded color symbols, providing the NORAD battle staff with an electronic panorama of the North American and Eurasian land masses.

The handling of BMEWS inputs at NORAD is an example of how RCA data processing capabilities are assuring the high degree of reliability so vital to continental defense.



At NORAD Headquarters, RCA computing equipment, the Display Information Processor (control console shown here) receives sightings data from BMEWS and processes it for automatic readout.



RCA is prime system contractor for the sprawling BMEWS three-site radar network whose probing electronic fingers reach deep into space to provide early warning of missile attacks.



RCA's Automatic Checkout & Monitoring equipment continuously tests and checks performance of portions of the system and alerts an operator when a monitored signal exceeds certain limits.

Out of the defense needs of today a new generation of RCA electronic data processing equipments has been born. For tomorrow's needs RCA offers one of the nation's foremost capabilities in research, design, development and production of data processing equipment for space and missile projects. For information on these and other new RCA scientific developments, write Dept. 434, Defense Electronic Products, Radio Corporation of America, Camden, N. J.



The Most Trusted Name  
in Electronics

RADIO CORPORATION OF AMERICA

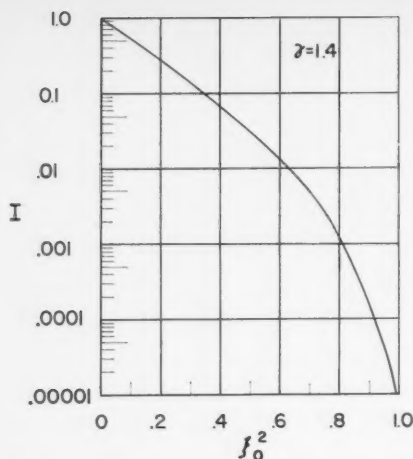


Fig. 2 Function  $I(\xi_0^2)$

$$\alpha(x) \equiv \left( \frac{K_1}{Ra_i} \right) \sqrt{\frac{\gamma-1}{2}} = \left( \frac{W}{a_i} \right) \left( \frac{a_i}{W_{max}} \right) = \frac{W}{W_{max}} \quad [11]$$

Observe here that though the definition of  $M$  does not involve the swirling component, nevertheless its value is not identical to what would exist if the flow had no swirl. Observe also that for a specified  $K_1$  and  $R(x)$ ,  $\alpha(x)$  is known and that it must reach its maximum value at the nozzle throat. The specification of this throat value of  $\alpha = \alpha^*$  (assuming, of course, that  $R^*a_i$  are known) is thus completely equivalent to the specification of  $K_1$ .

Using the above definitions, Eqs. 5a and 7 may be written after some manipulation as

$$f_1(\xi_0, M) \equiv \frac{MI}{\left(1 + \frac{\gamma-1}{2} M^2\right)^{\frac{\gamma+1}{2(\gamma-1)}}} = \left( \frac{A^*}{A} \right)^m \quad [5b]$$

$$f_2(\xi_0, M) \equiv \frac{\xi_0^2}{1 + \frac{\gamma-1}{2} M^2} = \alpha^2 \quad [7a]$$

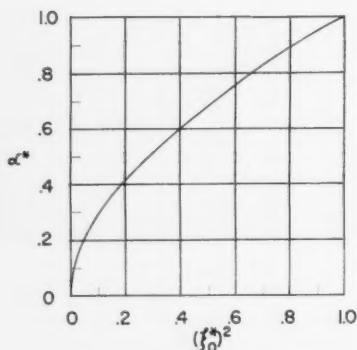


Fig. 3a Relation between the minimum radius and swirl magnitude at the throat

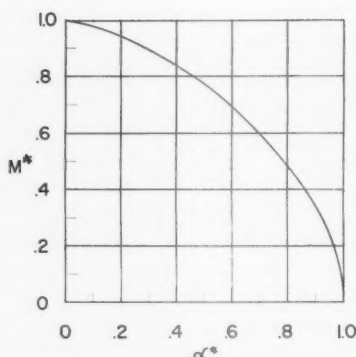


Fig. 3b Relation between the swirl magnitude and the Mach number of the related flow at the throat

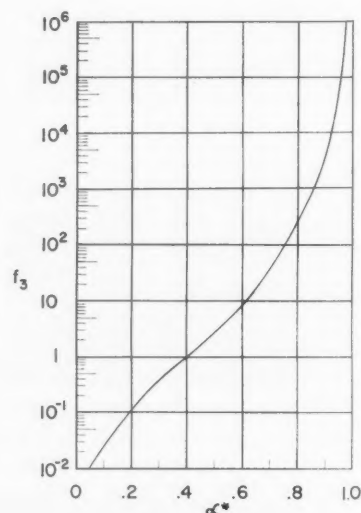


Fig. 3c Function  $f_3$

where

$$I(\xi_0, \gamma) \equiv \frac{2}{R^2} \int_{r_0}^R \left[ 1 - \left( \frac{r_0}{r} \right)^2 \right]^{1/(\gamma-1)} r dr = 2 \int_{\xi_0}^1 \left[ 1 - \left( \frac{\xi_0}{\xi} \right)^2 \right]^{1/(\gamma-1)} \xi d\xi \quad [12]$$

In general, the integration of Eq. 12 can be performed analytically only for certain special values of  $\gamma$  given by

$$\gamma = \frac{n+1}{n-1} \quad \text{with } n \text{ an integer} \quad [13]$$

For  $n = 6$  (e.g.,  $\gamma = 1.4$ ) this gives

$$I(\xi_0, 1.4) = \sqrt{1 - \xi_0^2} \left[ 1 + \frac{2}{3} \xi_0^2 (7 - \xi_0^2) \right] - \frac{5\xi_0^2}{2} \ln \left| \frac{1 + \sqrt{1 - \xi_0^2}}{1 - \sqrt{1 - \xi_0^2}} \right| \quad [14]$$

so that for  $\xi_0 \rightarrow 0$ ,  $I \rightarrow 1.0$ ; while for  $\xi_0 \rightarrow 1.0$ ,  $I \rightarrow 0$ . A plot of function  $I$  is shown in Fig. 2.

By concentrating our attention on the right hand sides of Eqs. 5b and 7a it becomes obvious that the functions  $f_1$  and  $f_2$  must have respectively a minimum and a maximum at the throat. But at the throat (with  $\alpha$  having its specified value  $\alpha^*$ ), Eq. 7a indicates that  $\xi_0^*$  is a function of  $M^*$  only, so that one must have there

$$\left( \frac{df_1}{dM} \right)^* = \left( \frac{\partial f_1}{\partial M} + \frac{\partial f_1}{\partial \xi_0} \frac{d\xi_0}{dM} \right)^* = 0 \quad [15]$$

and

$$\left( \frac{df_2}{dM} \right)^* = \left( \frac{\partial f_2}{\partial M} + \frac{\partial f_2}{\partial \xi_0} \frac{d\xi_0}{dM} \right)^* = 0 \quad [16]$$

which shows, upon elimination of  $(d\xi_0/dM)^*$  that the Jacobian of  $f_1^*$  and  $f_2^*$  vanishes

$$\left( \frac{\partial f_1}{\partial M} \frac{\partial f_2}{\partial \xi_0} \right)^* = \left( \frac{\partial f_1}{\partial \xi_0} \frac{\partial f_2}{\partial M} \right)^* \quad [17]$$

and thus  $f_1^*$  is functionally dependent on  $f_2^*$  or  $m = m(\alpha^*)$ .



In other words, as one might have expected, for all values of  $M^*$  and  $\xi_0^*$ , the mass flow  $K_2$  is always determined by the total conditions  $\rho_0 a_0$ , the throat area  $A^*$ , and the throat swirl magnitude  $\alpha^*$  only.

The appropriate values of  $M^*$  and  $\xi_0^*$  may also be determined from Eq. 17. Specifically, by substituting the appropriate values of the derivatives one obtains

$$\frac{(M^*)^2 - 1}{(\gamma - 1)(M^*)^2} = 1 - \frac{[1 - (\xi_0^*)^2]^{1/(\gamma - 1)}}{I^*} \quad [18]$$

and then by substituting the value of  $M^*$  as given by Eq. 7a

$$(M^*)^2 = \frac{2}{\gamma - 1} \left[ \left( \frac{\xi_0^*}{\alpha^*} \right)^2 - 1 \right] \quad [19]$$

One may write after some additional manipulation

$$\alpha^* = \xi_0^* \left\{ 1 - \frac{1}{\frac{3 - \gamma}{\gamma - 1} + \frac{2[1 - (\xi_0^*)^2]^{1/(\gamma - 1)}}{I^*}} \right\} \quad [20]$$

Eq. 20 determines thus, for each  $\alpha^*$ , the appropriate value of  $\xi_0^*$ . Its plot for  $\gamma = 1.4$  is shown in Fig. 3a. Once the  $\xi_0^*$  is thus found, Eq. 19 may be used to determine the corresponding value of  $M^*$ . It is interesting to note that for small values of  $\xi_0^*$  (and thus also small values of  $\alpha^*$ ) one gets

$$\xi_0^* = \alpha^* \sqrt{\frac{\gamma + 1}{2}} \quad [20a]$$

which upon substitution into Eq. 19 leads to  $M^* \rightarrow 1$ . In other words, for very small throat swirl magnitude, the related flow and the flow without swirl tend to become the same. In general, however, this is not true and the appropriate variation of  $M^*$  for each  $\alpha^*$  is shown in Fig. 3b. Observe also, that since the maximum possible value of  $\xi_0^*$  is unity, and since

$$\lim_{\xi_0^* \rightarrow 1} I = \frac{2}{7} (1 - \xi_0^{*2})^{7/2} \quad [14a]$$

therefore Eq. 20 shows that

$$\lim_{\xi_0^* \rightarrow 1} \alpha^* = \xi_0^* \left[ 1 - \frac{1}{14} (1 - \xi_0^{*2}) \right] = 1 \quad [20b]$$

or in other words, for the throat to be completely void of flow,  $\alpha^*$  must have its maximum possible value and  $M^*$  (see Eq. 19) approaches zero like

$$\lim_{\xi_0^* \rightarrow 1} M^* = \sqrt{\frac{5}{7} (1 - \xi_0^{*2})} \quad [20c]$$

Once the  $M^*$  and  $\xi_0^*$  are known, the appropriate non-dimensional mass flow is found from Eq. 5b

$$m = \frac{M^* I^*}{\left[ 1 + \frac{\gamma - 1}{2} (M^*)^2 \right]^{\frac{\gamma + 1}{2(\gamma - 1)}}} \quad [5c]$$

It is thus immediately apparent, from the above relation, that for  $\alpha^* \rightarrow 0$ ,  $m$  tends to its one-dimensional value, while for  $\alpha^* \rightarrow 1$ ,  $m$  tends to zero.

In this way all the pertinent quantities necessary for the determination of the flow in the nozzle are thus established. To proceed with the computations at any other position different from the throat one has

$$\alpha = \frac{R^*}{R} \alpha^* \quad [11a]$$

which permits one to eliminate the area between Eqs. 7a and

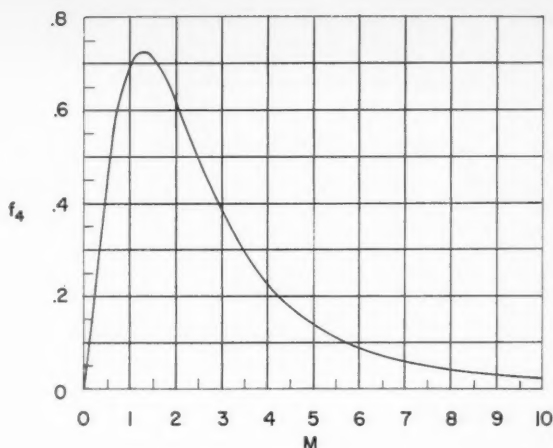


Fig. 4 Function  $f_4$

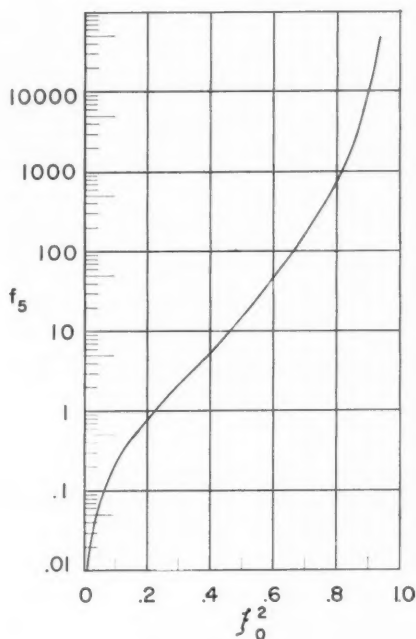


Fig. 5 Function  $f_5$

5b. This is conveniently done by defining

$$s(\alpha^*) \equiv \frac{(\alpha^*)^2}{m} \quad [21]$$

$$f_4(M) \equiv \frac{M}{\left( 1 + \frac{\gamma - 1}{2} M^2 \right)^{\frac{3 - \gamma}{2(\gamma - 1)}}} \quad [22]$$

$$f_5(\xi_0) \equiv \frac{\xi_0^2}{I} \quad [23]$$

which then, for any given  $\alpha^*$ , result in a relation between  $M$

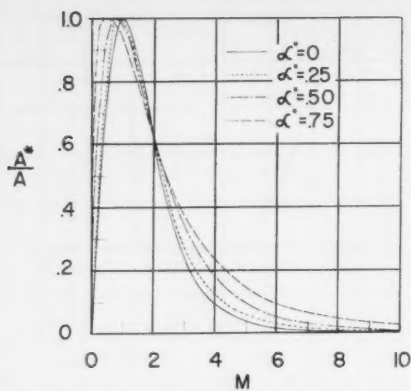


Fig. 6 Relation between the nozzle cross sectional area and the Mach number of the related flow for various swirl magnitudes

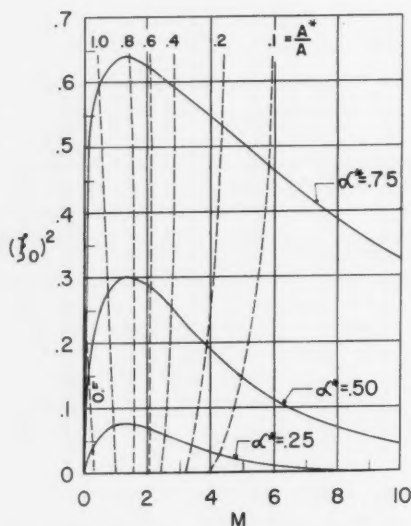


Fig. 7 Relation between the minimum radius and the Mach number of the related flow for various swirl magnitudes and nozzle cross sectional areas

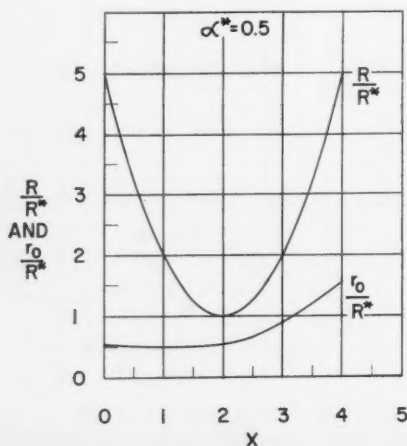


Fig. 8 Flow boundaries for swirl of magnitude  $\alpha^* = 0.5$

and  $\xi_0$  valid everywhere in the nozzle

$$f_3 f_4 = f_5 \quad [24]$$

The functions  $f_3$ ,  $f_4$ , and  $f_5$  are illustrated in Figs. 3c, 4 and 5, respectively. By choosing a value of  $M$ , the corresponding  $f_4$ ,  $f_5$ , and  $\xi_0$  are found in this order. Observe that for any given  $M$  (and thus  $f_4$ ) a decrease of  $\alpha^*$  will reduce  $f_5$  and thus  $\xi_0$  until eventually, at  $\alpha^* = 0$ ,  $\xi_0$  will be identically zero everywhere in the nozzle. The relation between the area and Mach number (see Eq. 25) becomes then one-dimensional, and the related flow is thus one-dimensional everywhere in the nozzle and not just at the throat. Furthermore, for  $\alpha^* \rightarrow 1$ ,  $f_5 \rightarrow \infty$  (because  $m \rightarrow 0$ ), and since  $f_4$  is finite,  $f_3$  must become infinite and  $\xi_0$  must be unity everywhere in the nozzle.

Knowing the relation (appropriate for a given value of  $\alpha^*$ ) between  $M$  and its corresponding  $\xi_0$ , permits one, by use of Eq. 7a or 5b, to determine also the relation between  $M$  and its area ratio  $A^*/A$  (which, of course, is valid only for the particular value of  $\alpha^*$ )

$$\frac{A^*}{A} = \frac{1}{m} \left( \frac{MI}{1 + \frac{\gamma-1}{2} M^2} \right)^{\frac{\gamma+1}{2(\gamma-1)}} = \frac{(\xi_0/\alpha^*)^2}{1 + \frac{\gamma-1}{2} M^2} \quad [25]$$

The computed variations of  $A^*/A$  ( $M$ ) for  $\alpha^* = 0$ , 0.25, 0.50, and 0.75 are shown in Fig. 6. As may be seen from this figure all of the curves are quite similar in shape and differ but little from the one-dimensional (e.g.,  $\alpha^* = 0$ ) relation. These differences become somewhat more obvious when examining Fig. 7, which in a sense is a convenient summary of the present results. Shown in this figure are curves of  $\xi_0$  ( $M$ ), for various values of  $\alpha^*$ , with the lines of constant  $A^*/A$  also plotted across. From these lines it is immediately apparent that when located far downstream of the throat (e.g., for large values of  $M$ ), the Mach number of the related flow tends to be somewhat larger than the Mach number of the one-dimensional flow at same  $A^*/A$ . Similarly, when located far upstream of the throat (e.g., for small values of  $M$ ) the Mach number of the related flow tends to be somewhat smaller than the Mach number of the one-dimensional flow at same  $A^*/A$ . In addition, it may also be seen in that figure, that for each  $\alpha^*$ , the  $\xi_0(M)$  tends to a maximum slightly downstream of the throat. Since this suggests that the swirl tends to produce its greatest blockage near the throat, one may expect a pronounced effect on the mass flow even for relatively low values of  $\alpha^*$ . One must be careful, however, when interpreting the Fig. 7, to note that maximum values of  $\xi_0$  do not necessarily imply the maximum values of  $r_0$ . This is clearly shown in Fig. 8 where the actual flow boundary for  $\alpha^* = 0.5$  and  $R/R^* = 1 + (x-2)^2$  is plotted. As may be seen from this figure, downstream of the throat  $r_0/R^*$  continuously increases.

It is interesting to note here that the photographs of (1) show a core void of water which has a shape very similar to that given by the  $r_0/R^*$  curve of Fig. 8. This occurs, in spite of the constant density, because, at small radii, the rising circumferential velocity causes a drop in pressure which is probably sufficient to produce cavitation. Similarly (2), which is concerned with the use of swirling for thrust reversal purposes, gives evidence that the exit flow from the nozzle is sharply spread, just as one may expect from the computations illustrated in Fig. 8. These references, then, give some, although admittedly meager, qualitative confirmation of the present analytical results.

One should also remember here that the real flow near the axis of rotation is subject to viscous effects, and thus the potential flow solution is invalid there. In fact, because of these viscous effects, near the axis the circumferential velocity is likely to have a distribution representative of the "solid body rotation," e.g., be proportional to the radius. One may

expect thus that the density will not monotonically decrease to zero and, consequently, this region will not be completely void of flow. Still, because of the sharp change in the character of the circumferential velocity, this viscous region should be easily recognizable and may again be considered as a sort of "core." It is important to note here also that because of the viscous nature of this "core" the effect of the ambient pressure outside the nozzle can propagate through it past the throat and into the nozzle and that the axial flow there may well be reversed.

### Effect on Mass Flow and Specific Impulse

Once the values of  $M$  and  $\xi_0$  for any given area ratio and, of course, specified swirl strength (e.g.,  $\alpha^*$ ) are known, all other quantities may easily be found. Of great interest, therefore from the engineering standpoint, is the comparison of such swirling flow with the ideal, one-dimensional flow. In particular, one would like to know how the swirl affects the mass flow and the specific impulse. While such comparisons may be carried out in different ways, we shall consider here two nozzles of the same geometry whose flow occurs at the same total conditions. Denoting the one-dimensional values by subscript 1, one then has from Eq. 5c for the ratio of mass flows

$$\frac{m}{m_1} = \frac{m(\alpha^*)}{m(\alpha^* = 0)} = \left( \frac{\gamma + 1}{2} \right)^{\frac{\gamma+1}{2(\gamma-1)}} \left[ 1 + \frac{\gamma-1}{2} (M^*)^2 \right]^{\frac{\gamma+1}{2(\gamma-1)}} \quad [26]$$

and this relation is shown in Fig. 9. As may be seen from this figure, even relatively weak swirl causes a pronounced reduction of mass flow and, in fact, for  $\alpha^* > 0.8$  all mass flow is essentially blocked.

To carry out a similar comparison of specific impulse, one needs to determine first the variation of the nozzle thrust. But this may not be computed until the ambient pressure is specified. Since in the swirling nozzle there are regions void of flow, in order to bypass any possible difficulties related to a conceivable existence of "back flow," it has been assumed that the ambient pressure is always zero. With this assumption the thrust of the swirling nozzle may be written non-dimensionally as

$$\frac{\text{thrust}}{p_t A} \equiv T = \frac{1}{p_t A} \int_A (p + \rho u^2) dA \quad [27]$$

It takes little manipulation to show that

$$\frac{p + \rho u^2}{p_t} = \frac{1 + \gamma M^2}{\left( 1 + \frac{\gamma-1}{2} M^2 \right)^{\gamma/(\gamma-1)}} \times \left[ 1 - \left( \frac{\xi_0}{\xi} \right)^2 \right]^{1/(\gamma-1)} \left[ 1 - \frac{(\xi_0/\xi)^2}{1 + \gamma M^2} \right] \quad [28]$$

which, when substituted into Eq. 26 and integrated, gives eventually

$$T = \frac{1}{\left( 1 + \frac{\gamma-1}{2} M^2 \right)^{\gamma/(\gamma-1)}} [\gamma(1 + M^2)I - (\gamma-1)(1 - \xi_0^2)^{\gamma/(\gamma-1)}] \quad [27a]$$

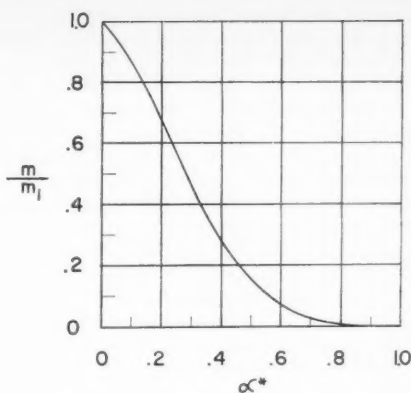


Fig. 9 Effect of swirl on mass flow

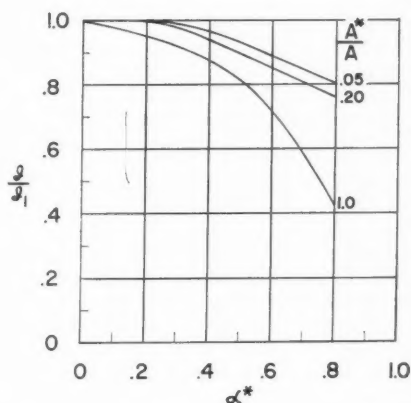


Fig. 10 Effect of swirl on the specific impulse

so that

$$\frac{T}{T_1} = \frac{T(\alpha^*)}{T(\alpha^* = 0)} = \left( \frac{1 + \frac{\gamma-1}{2} M_1^2}{1 + \frac{\gamma-1}{2} M^2} \right)^{\gamma/(\gamma-1)} \times \frac{[\gamma(1 + M^2)I - (\gamma-1)(1 - \xi_0^2)^{\gamma/(\gamma-1)}]}{1 + \gamma M_1^2} \quad [29]$$

and the specific impulse ratio may now be computed from

$$\frac{J}{J_1} = \frac{T}{T_1} \frac{m_1}{m} \quad [30]$$

It is very clear from Eq. 29 that for a specified swirl strength  $\alpha^*$ , the greater the value of  $\xi_0^2$ , the smaller the ratio of the thrust. Consequently one may expect from the variation of  $\xi_0^2$ , as shown in Fig. 7, that the thrust of the swirling flow will be smaller than that for the one-dimensional flow when the nozzle exit area is not much larger than the throat area. Furthermore, since the mass flow ratio is dependent only on the magnitude of  $\alpha^*$  and does not vary along the nozzle, this loss of thrust will reflect itself also in the decrease of the specific impulse.

The physical mechanism responsible for this inefficiency follows, of course, from the conservation of the angular momentum. According to this principle, near the throat the swirling flow must become relatively stronger because of the decrease of the perpendicular distance from the axis of rotation. Consequently, the flow there has a greater tendency to move in a circumferential direction at the expense of the axial motion, and thus the thrust must suffer. Far away from the throat, however, where the swirling flow grows relatively weak again, no such losses occur.

This variation of thrust losses with the  $A^*/A$  ratio has rather important consequences which are particularly apparent for small but finite values of  $\alpha^*$ . As may be seen from Fig. 7, one then obtains at sufficiently large values of  $M$  a vanishingly small value of  $\xi_0^2$ . Consequently Eq. 29 may be approximated under these conditions by

$$\frac{T}{T_1} \bigg|_{\substack{\alpha^* \rightarrow 0 \\ M \rightarrow \infty}} = \left( \frac{M_1}{M} \right)^{2/(\gamma-1)} \quad [29a]$$

On the other hand, the ratio of the Mach numbers may be obtained from Eq. 25 in terms of the mass flow ratio as

$$\frac{M}{M_1} \left( \frac{1 + \frac{\gamma-1}{2} M_1^2}{1 + \frac{\gamma-1}{2} M^2} \right)^{(\gamma+1)/[2(\gamma-1)]} = \frac{m}{m_1} \frac{1}{I} \quad [31]$$

which for small  $\alpha^*$  and large  $M$  may be approximated by

$$\left( \frac{M_1}{M} \right) \bigg|_{\substack{\alpha^* \rightarrow 0 \\ M \rightarrow \infty}} = \frac{m}{m_1} \quad [31a]$$

Consequently, as is apparent from Eqs. 29a and 31a, the decrease of the thrust, in that case, is equal exactly to the decrease of the mass flow, so that the specific impulse is completely unaffected by the swirl. This may be seen in Fig. 10, where the computed variation of the specific impulse ratio is plotted for various nozzle expansion ratios as a function of swirl strength. As may be seen from this figure, even for reasonably large values of  $A^*/A$  and  $\alpha^*$  the specific impulse is only slightly affected by the swirl. For example, at  $\alpha^* = 0.5$  and  $A^*/A = 0.2$ , the specific impulse is decreased by 10% from its one-dimensional value. Since for the same condi-

tions (see Fig. 9) the mass flow is restricted to only 15% of its one-dimensional value, it is obvious that the use of the swirl is very promising from the standpoint of the mass flow control.

## Nomenclature

$A$	= nozzle cross sectional area = $\pi R^2$
$a$	= speed of sound
$f_i$	= functions of $\xi_0$ , $M$ , and $\alpha^*$ ( $i = 1, 2, 3, 4, 5$ )
$I$	= non-dimensional specific impulse
$I$	= function of $\xi_0$ (Eq. 12)
$K_i$	= constants ( $i = 1, 2$ )
$M$	= Mach number of related flow (Eq. 9)
$m$	= non-dimensional mass flow (Eq. 10)
$n$	= integer
$p$	= pressure
$R$	= nozzle wall radius
$r, \theta, x$	= cylindrical polar coordinates
$T$	= non-dimensional thrust (Eq. 27)
$U$	= function of $x$ only = axial velocity
$u, v, w$	= velocity components in $x, r, \theta$ directions, respectively
$V$	= total velocity
$W$	= circumferential velocity at the wall
$\alpha$	= local, non-dimensional swirl strength (Eq. 11)
$\gamma$	= ratio of specific heats
$\xi$	= non-dimensional radius ratio
$\rho$	= density
$\Phi$	= velocity potential

## Subscripts

0	= boundary of region void of flow
1	= one-dimensional value at same $A^*/A$ and same total conditions
$t$	= total conditions

Coordinate subscripts denote partial differentiation  
Star above values signifies conditions at the throat

## References

- 1 Binnie, A. M., Hookings, G. A. and Kamel, M. Y. M., "The Flow of Swirling Water Through a Convergent Divergent Nozzle," *J. Fluid Mech.*, vol. 3, no. 3, Dec. 1957, pp. 261-274.
- 2 Iserland, K., "Untersuchungen über die Umlenkung eines freien Luftstrahls mit Hilfe von Drall," Mitteilungen aus dem Institut für Aerodynamik ETH Zürich, Verlag Leemann Zürich Nr. 25, 1958.



# Technical Notes

## Investigation of Rocket Flow Problems by Means of Short Duration Flow Devices

R. C. WEATHERSTON<sup>1</sup> and A. HERTZBERG<sup>2</sup>

Cornell Aeronautical Laboratory, Inc., Buffalo, New York

THE RAPID development of the rocket engine over a period of the last two decades has been paced by the operation of experimental or prototype models on static test stands. Such testing gives insight to both component and composite design integrity that cannot be obtained in any other way. It appears, however, that short (millisecond) duration flow devices which exploit established shock tube techniques could be expediently and economically employed for certain rocket tests pursuant to a final configuration. In special cases, such devices afford the only practical means of rocket flow simulation. An example of this is the investigation of exhaust interference effects and resultant base heating of clustered rockets at extremely high altitudes. This note discusses short duration flow devices and the techniques employed to investigate the problems associated with nonequilibrium nozzle flow, heat transfer, and rocket base heating.

The ability of the shock tube to generate controlled flows of high temperature air has led to its development as a tool for research of hypersonic flow phenomena (1,2).<sup>3</sup> Since these flows are of millisecond duration, the development of fast response instrumentation was effectively stimulated. Force, pressure and heat transfer can be now accurately measured during a test lasting only a few milliseconds (3). These developments permit the shock tube and other short duration flow devices to be used in fields of application where the virtue of short test time may be enjoyed. The almost instantaneous establishment of a hot steady flow for periods of a few milliseconds also permits the use of simple models and apparatus that do not have to be compromised by considerations of cooling. Distinction among physical effects can in some cases be resolved more accurately than in continuous, hot flow experiments.

Several types of short duration flow devices can be employed to study the problems of interest here. These devices exploit either shock waves or expansion waves to establish rapidly and to sustain a desired steady flow. These devices are characterized by long tubes, rupture diaphragms or quick opening valves to start the flow process, and they incorporate shock tube type instrumentation. There are, however, operational differences that render one device more suitable than another for a particular application. For example, in some

basic studies it is advantageous to use a variety of well defined test gases. A modified tailored interface shock tunnel (4) as illustrated in Fig. 1 is useful for this application. The phenomenon of nozzle starting has been investigated (5), and it is shown that the transient time required to establish steady flow in the nozzle is short compared to the duration of steady flow from the shock tube. For a test where a rocket exhaust is to be duplicated and the test gas is the product of a combustion process, other short duration flow devices may be gainfully employed. In one such device, the fuel and oxidizer are mixed in a closed tube. The mixture is ignited, and shortly after combustion is completed a diaphragm is ruptured and the flow starts. The flow will be steady during the time it takes an expansion wave to traverse the tube, reflect from the closed end and return to the diaphragm. Fig. 2 is a sketch of such a device. In a similar device (Fig. 3), the mixture may be released from the tube before combustion and then burned, as used, at constant pressure in a chamber immediately downstream from the diaphragm station. These combustion type devices do not depend upon aerodynamic heating of the gas, as does the shock tube, and they afford considerably more test time per length of tube. This is particularly true of the latter device (Fig. 3) where the waves propagate relatively slowly through the cold gas.

### Nonequilibrium Flow Kinetics in Nozzles

Considerable attention recently has been focused on the problem of nonequilibrium losses in rocket nozzles (6). For example, in the case of an arc heated rocket employing hydrogen as a propulsive gas, nonequilibrium imposes a serious limitation on the maximum efficiency that can be obtained. Studies of these phenomena, which involve subtle and complex chemistry, are particularly well suited for the modified shock tunnel technique. The flexibility of the shock tunnel

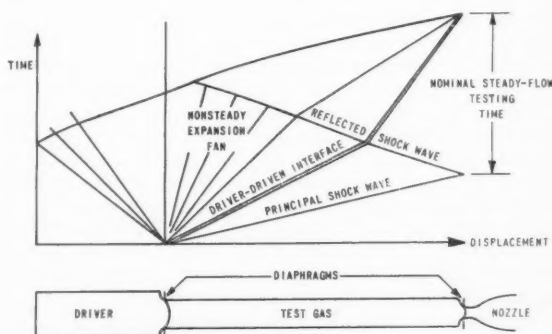


Fig. 1 Illustration of the tailored-interface shock tunnel for the study of rocket nozzle flow problems

Received March 25, 1961.

<sup>1</sup> Principal Research Engineer.

<sup>2</sup> Head, Aerodynamic Research Dept.

<sup>3</sup> Numbers in parentheses indicate References at end of paper.

EDITOR'S NOTE: The Technical Notes and Technical Comments sections of ARS JOURNAL are open to short manuscripts describing new developments or offering comments on papers previously published. Such manuscripts are usually published without editorial review within a few months of the date of receipt. Requirements as to style are the same as for regular contributions (see masthead page).

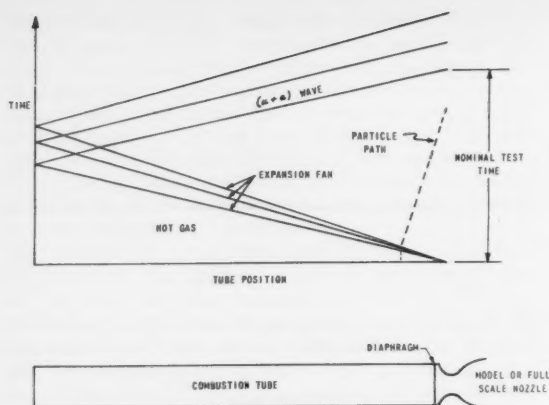


Fig. 2 Schematic illustration of pre-combustion short duration flow device

approach is illustrated in nozzle kinetic studies, since a wide range of operating pressures and temperatures can be achieved and the composition of the test gas is known with extreme precision. The development of a steady flow test device to study this wider range of test conditions would be relatively difficult, and the distinction of nonequilibrium effects from other losses might be difficult to appraise.

At the present time the Cornell Aeronautical Laboratory, Inc., is actively engaged in a program using the shock tunnel technique to study various facets of the nonequilibrium problem.<sup>4</sup> Experiments for these studies are being carried out in an instrumented nozzle that is attached to the end of a tailored interface shock tunnel (Fig. 1). The subsonic portion of the nozzle constitutes the reflection surface in the shock tube proper. The nozzle is equipped with high frequency SLM pressure transducers and observation windows through which spectroscopic observations are made. From the knowledge obtained from such instrumentation and the gas stagnation condition at the nozzle inlet, which can be well defined from measurements within the shock tube, the state of the gas or degree of dissociation can be determined. It is hoped that by gaining a better insight into the fundamental nature of these phenomena improved operational techniques can be devised whereby the nonequilibrium losses in rocket nozzles can be minimized.

#### Heat Transfer to Nozzle Walls

The simplicity and versatility of testing nozzles with short duration flows may well be appreciated by those who are familiar with continuous flow testing of rocket nozzles. Heat transfer rates in high performance rocket nozzles may be as high as several thousand Btu per square foot per second. In continuous nozzle flow tests, the nozzle walls must be very thin and vigorously cooled from the back side. These conditions militate against steady flow heat transfer instrumentation. To alleviate such difficulties transient heat transfer measurements of a few seconds duration are resorted to by C. H. Liebert et al. (7). The full advantages of transient heat transfer techniques are realized with flows of millisecond duration and shock tube type instrumentation. Intimately connected with the application of the shock tube to nozzle heat transfer studies is the thin film resistance thermometer. By measuring the rate of surface temperature rise with this gage, heat transfer rates can be determined with a degree of accuracy comparable to that attained from the most pain-

staking instrumentation in steady flow experiments. Furthermore, by shielding the gage with a thin layer of quartz or other transparent material that completely blocks the convection heat transfer during the short test time or by using gages of different emissivities, radiative and convective heat transfer can be separately evaluated. Since these two modes of heat transfer do not follow the same scaling laws, their distinction is helpful to the analyst who is involved with a situation wherein both mechanisms of heat transfer are significant.

#### Base Heating

The problems of base heating and engine compartment cooling of rocket and rocket clusters have received considerable attention during the last few years (8) and are currently being investigated at CAL (9).<sup>5</sup> These problems can be roughly divided into two classes. The first class is associated with low altitude booster configurations and includes mutual jet interaction effects and aerodynamic and chemical interaction effects of the fuel rich rocket jets with the external air flow. If flow patterns are established in accordance with transient aerodynamic scaling parameters which predict stability in the time allowed for three or four acoustic passages across the largest dimension of the base model (10), then short duration techniques will reveal credible information. Localized external burning effects would probably not invalidate test results. If, however, there are long range burning propagation effects or pulsating flash backs, then short duration testing would be of limited use. The general altitude-velocity range of interest for the first class of problems is approximately from ground zero to 40,000 ft at 1500 fps depending upon configuration. To study this class of problems both the short duration flow device and a model of the base of a rocket cluster would be placed inside of a conventional subsonic-transonic wind tunnel. Since the test durations are short, it may be worthwhile to fabricate a low pressure, short duration flow device to simulate the external flow around the missile.

<sup>5</sup> This work is being supported by Marshall Space Flight Center (NASA) under Contract No. NAS 8-823.

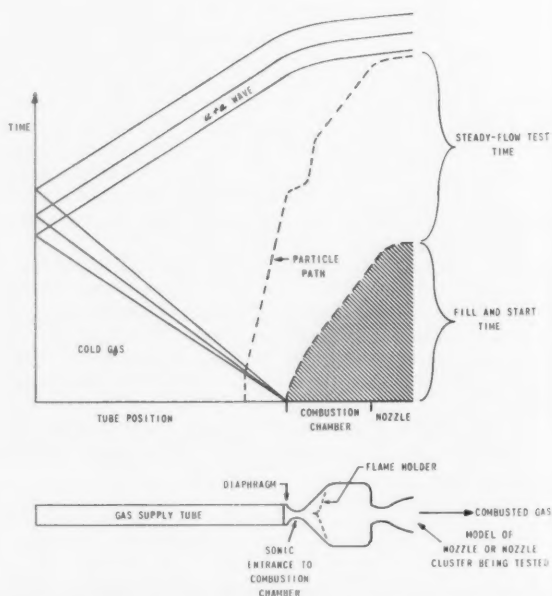


Fig. 3 Schematic illustration of post-combustion short duration flow device

<sup>4</sup> This work is being supported by Goddard Space Flight Center (NASA) under Contract No. NAS 5-670 and by the Air Force through the Office of Scientific Research under Contract No. AF 49(638)-792.

The second class of problems deals with high altitude base heating effects. In this class, the atmospheric density is low and it does not affect the more predominant jet cluster interaction phenomena. This class of problems is clearly suited to short duration testing. The attainment of a low pressure environment for short duration testing could easily be attained by evacuating a chamber into which the model will discharge. It may well be appreciated that if a low external pressure environment were to be sustained in the presence of prolonged jet flow, a truly prodigious pumping capacity would be required. The dimensions of the low pressure chamber need only be large enough so that, during a few-millisecond test, the disturbances emanating from the nozzle exhaust and reflecting from the chamber walls would not appreciably influence the static pressure level near the jets. It is hoped that the establishment of reliable scaling laws would circumvent the need for large scale testing; however, if the need existed, even full scale models could be tested with short duration flow devices. The separation of convection and radiative heat transfer terms, as could be accomplished by this testing means, would greatly assist in establishing such scaling laws.

It is hoped that this note will stimulate the application of short duration test devices to the study of rocketry problems discussed here. The simplicity and economy of such testing is apparent. In certain areas, short duration testing may provide the only feasible means of obtaining information of interest. However, the authors do not mean to imply that short duration testing may be applied to all rocket flow simulation studies; discretion must be used. In all it appears that short

duration test devices may be gainfully employed to augment established testing techniques in several areas of interest.

## References

- 1 Hertzberg, A. and Wittliff, C. E., "Studying Hypersonic Flight in the Shock Tunnel," I.A.S. paper 60-67, IAS Summer Meeting, Los Angeles, Calif., June 28-July 1, 1960.
- 2 Kaegi, E. M., Warren, W. R., Harris, C. J. and Geiger, R. E., "The Capabilities of the Shock Tunnel in the Study of the Aerodynamics of Atmospheric Entry," ARS paper 1554-60, ARS 15th Annual Meeting, Washington, D. C., Dec. 5-8, 1960.
- 3 Wittliff, C. E. and Rudinger, G., "Summary of Instrumentation Development and Aerodynamic Research in a Hypersonic Shock Tunnel," Cornell Aeronaut. Lab. Rep., no. AD-917-A-2, August 1958.
- 4 Hertzberg, A., Smith, W. E., Glick, H. S. and Squire, W., "Modification of the Shock Tube for the Generation of Hypersonic Flow," Cornell Aeronaut. Lab. Rep., no. AD-789-A-2, AEDC-TN-55-15, AD 63559, March 1955.
- 5 Glick, H. S., Hertzberg, A. and Smith, W. E., "Flow Phenomena in Starting a Hypersonic Shock Tunnel," Cornell Aeronaut. Lab. Rep., no. AD-789-A-3, AEDC-TN-55-16, AD 63558, March 1955.
- 6 Hall, J. G., Eschenroeder, A. Q. and Klein, J. J., "Chemical Non-equilibrium Effects on Hydrogen Rocket Impulse at Low Pressures," Cornell Aeronaut. Lab. Rep., no. AD-1118-A-8, November 1959.
- 7 Liebert, C. H., Hatch, J. E. and Grant, R. W., "Application of Various Techniques for Determining Local Heat Transfer Coefficients in a Rocket Engine from Transient Experimental Data," NASA TN D-277, April 1960.
- 8 Goethert, B. H. and Barnes, L. T., "Some Studies of the Flow Pattern at the Base of Missiles with Rocket Exhaust Jets," AEDC-TR-57-12, revised June 1960.
- 9 Bird, K. D., Reece, J. W. and Smith, W. E., "The Application of Short-Duration Techniques to the Experimental Study of Base Heating," presented at the Second Symposium of Rocket Testing in Simulated Space and High-Altitude Environments, Arnold Engng. Dev. Center, Tullahoma, Tenn., June 28-29, 1961.
- 10 Rudinger, G., "The Reflection of Pressure Waves of Finite Amplitude from an Open End of a Duct," *J. Fluid Mech.*, vol. 3, Pt. 1, p. 48, October 1957.

## Transport Properties of Dissociated Air

W. L. BADE<sup>1</sup>

Avco RAD, Wilmington, Mass.

E. A. MASON<sup>2</sup> and K. S. YUN<sup>3</sup>

Institute for Molecular Physics, University of Maryland,  
College Park, Md.

**C**ALCULATIONS of the transport properties of high temperature air have been carried out previously by Stupochenko et al. (1),<sup>4</sup> Greifinger (2), Green (3), Hansen (4), Scala and Bauknight (5), and Bauer and Zlotnick (6). It is of interest to examine the agreement, or lack thereof, between the results of these various calculations. Fig. 1 shows curves of viscosity vs. temperature for equilibrium air at the density ratio  $\rho/\rho_0 = 0.1$ , based upon (1 through 6). It is apparent that the different calculations do not agree at all well, the lowest and highest values shown differing by more than a factor of two at 8000 K.

The species properties which are significant for determining the transport coefficients of a gas mixture are the molecular weights and the pair interaction potentials between the various types of gas particle present. An examination of the assumptions and approximations used in the investigations cited (1 through 6) reveals that the principal source of discrepancies is the use of markedly different atomic interaction potentials by the various authors.

Subsequently to the performance of the above investiga-

tions, knowledge of the interaction potentials between the various species of partially dissociated air has increased remarkably. As a result of work carried out by Vanderslice, Mason et al. (7 through 10), the interactions N-N, N-O and O-O, as well as the relevant atom-molecule and molecule-molecule interactions, are now known quantitatively. The availability of this body of new information makes possible a significant improvement in the accuracy of transport property calculations for high temperature air. The present note reports approximate values for the viscosity of equilibrium air, based upon a portion of this new information. The purpose of this work is to evaluate the accuracy of previous calculations (1 through 6) in the light of present knowledge concerning the interaction potentials in partially dissociated air. More extensive and accurate calculations of the transport properties of air and its component species are in progress at our respective laboratories, and will be reported in the near future.

The present calculations are carried out by approximating air as a mixture of nitrogen atoms and molecules, with a composition determined from that of equilibrium air by considering O<sub>2</sub> and NO as identical with N<sub>2</sub>, and O as identical with N. Use of this convenient "atom-molecule" approximation avoids the prodigious amount of computation required in a five- or six-component calculation. Since the interactions of oxygen and nitrogen are not very different and since, after all, air is composed principally of nitrogen, the errors produced by use of this approximation are no larger than those occasioned by uncertainties in present knowledge of the interaction potentials.

The viscosity of pure molecular nitrogen has already been calculated by Amdur and Mason (11) from the best available interaction data; their results are used without modification in the present investigation. The viscosity of pure atomic nitrogen is calculated from the interaction potentials given by Vanderslice, Mason and Lippincott (7) for the four electronic quantum states of the N-N system. In the first

Received May 25, 1961.

<sup>1</sup> Principal Scientist, Arc Sciences Section, Physics Research Dept. Member ARS.

<sup>2</sup> Professor of Molecular Physics.

<sup>3</sup> Research Associate in Molecular Physics.

<sup>4</sup> Numbers in parentheses indicate References at end of paper.

Table 1 Interaction potentials for the N-N system

State	Statistical weight	Form of potential given (7)	Form of potential used	Parameter values
${}^7\Sigma_u^+$	7/16	exponential repulsion	exponential repulsion, Eq. 2	$A = 5.09 \times 10^{-10}$ erg $r^* = 0.363$ Å
${}^5\Sigma_g^+$	5/16	Morse function	rigid sphere, Eq. 3	$r_s = 1.43$ Å
${}^3\Sigma_u^+$	3/16	exponential attraction	power law attraction, Eq. 4	$B = 1.12 \times 10^{-10}$ erg Å <sup>n</sup> $n = 6.61$
${}^1\Sigma_g^+$	1/16	exponential attraction	power law attraction, Eq. 4	$B = 3.16 \times 10^{-10}$ erg Å <sup>n</sup> $n = 6.98$

Chapman-Enskog approximation, the viscosity of a one-component gas is given by (12)

$$\mu = 0.625 kT/\Omega^{(2,2)} \quad [1]$$

In accordance with the results of Mason, Vanderslice and Yos (13), the collision integral  $\Omega^{(2,2)}$  for pure atomic nitrogen is computed as the weighted average of the collision integrals for the individual potentials corresponding to the four possible collision states, the weighting factors being the statistical weights given in Table 1.

Vanderslice, Mason and Lippincott (7) give the potential for the  ${}^7\Sigma_u^+$  state of N-N as a repulsive exponential function.

$$\phi(r) = A e^{-r/r^*} \quad [2]$$

with the values of  $A, r^*$  given in Table 1. The collision integral for this potential is computed using results recently published by Monchick (14). The potential for the  ${}^5\Sigma_g^+$  state is given (7) as a Morse function, and those for the  ${}^3\Sigma_u^+$  and  ${}^1\Sigma_g^+$  states as attractive exponentials (in the relevant region of separations). Tabulations of collision integrals are not available for those last two types of potential, and these functions are approximated in the present calculations by a rigid sphere potential

$$\phi(r) = \begin{cases} 0 & \text{for } r > r_s \\ \infty & \text{for } r < r_s \end{cases} \quad [3]$$

and two attractive power law potentials

$$\phi(r) = -B r^{-n} \quad [4]$$

with parameter values given in Table 1. The collision integrals for the rigid sphere potential (Eq. 3) are known analytically (12). Values of  $\Omega^{(2,2)}$  for the attractive power law function, Eq. 4, can be calculated using the results of Kihara, Taylor and Hirschfelder (15).

The viscosity of the binary mixture of nitrogen atoms and molecules representing equilibrium air is calculated from the viscosities for pure N<sub>2</sub> and N using Wilke's (16) approximate formula

$$\mu = \mu_1[1 + G_{12}x_2/x_1]^{-1} + \mu_2[1 + G_{21}x_1/x_2]^{-1} \quad [5]$$

$$G_{ij} = \frac{1}{2\sqrt{2}} \left( 1 + \frac{M_i}{M_j} \right)^{-1/2} \left[ 1 + \left( \frac{\mu_i}{\mu_j} \right)^{1/2} \left( \frac{M_j}{M_i} \right)^{1/4} \right]^2 \quad [6]$$

Table 2 Viscosity of equilibrium air

T (°K)	$\mu$ (millipoise)				
	0.1 atm	1 atm	10 atm	100 atm	1000 atm
3000	0.87	0.86	0.85	0.85	0.85
4000	1.13	1.12	1.09	1.08	1.07
5000	1.37	1.36	1.34	1.32	1.29
6000	1.67	1.61	1.58	1.54	1.51
7000	1.97	1.91	1.82	1.78	1.74
8000	2.20	2.17	2.11	2.03	1.97

with mole fractions  $x_i$  determined from the tables of Logan and Treanor (17) by lumping N<sub>2</sub>, O<sub>2</sub> and NO together as "species 1" and N, O as "species 2." The results are given in Table 2.

The error resulting from use of the approximate formulas 5, 6 in place of the accurate Chapman-Enskog formulas is probably at most a few per cent (11,16). The "atom-molecule" binary approximation tends to overestimate the viscosity of air by roughly 5%. The largest error in the calculation arises from use of the relatively crude rigid sphere potential for the state  ${}^5\Sigma_g^+$  of the N-N system, and may amount to as much as 10%. The overall error in the calculated values of viscosity is thus estimated to be 10 or 15%, the values in Table 2 probably being too high.

The results are also plotted in Fig. 1 for comparison with those of the previous calculations. The high temperature viscosity values calculated by Greifinger (2), Green (3), Hansen (4), and Scala and Baulknight (5) lie substantially below those obtained here. These four calculations are all marred to a greater or lesser extent by lack of knowledge of the atom-atom interactions or by uncritical use of interaction potentials derived from low temperature gas property measurements. Amdur and Ross (18) have emphasized that use of potentials based upon low temperature data can lead to serious errors in calculations of high temperature properties. The viscosity values calculated by Bauer and Zlotnick (6) are higher than those computed in the present note, but the

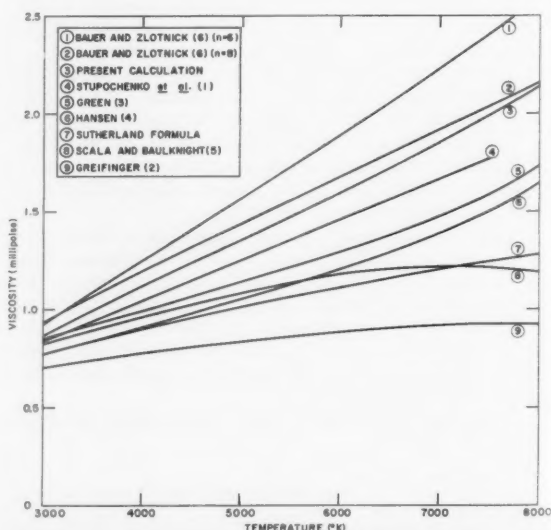


Fig. 1 Viscosity of equilibrium air at  $\rho/\rho_0 = 0.1$



discrepancy is within the estimated error of the former. Although the viscosity results of Stupochenko et al. (1) are slightly lower than those of the present note, the difference is of the same order as the estimated error in the present calculations.

#### Nomenclature

- $A$  = parameter in repulsive exponential potential, Eq. 2  
 $B$  = parameter in attractive power law potential, Eq. 4  
 $G_{ij}$  = see Eq. 6  
 $k$  = Boltzmann constant  
 $M_i$  = molecular weight of  $i$ th species  
 $n$  = parameter in attractive power law potential, Eq. 4  
 $r$  = interatomic distance  
 $r^*$  = parameter in repulsive exponential potential, Eq. 2  
 $r_s$  = parameter in rigid sphere potential, Eq. 3  
 $T$  = absolute temperature  
 $x_i$  = mole fraction of  $i$ th species  
 $\mu$  = viscosity  
 $\mu_i$  = viscosity of  $i$ th pure species  
 $\phi$  = atomic interaction potential  
 $\rho$  = air density  
 $\rho_0$  = standard air density,  $1.234 \times 10^{-3}$  gm/cm<sup>3</sup>  
 $\Omega^{(2,2)}$  = collision integral for determining viscosity

#### References

- 1 Stupochenko, E. V., Dotsenko, B. V., Stokhanov, I. P. and Samuilov, E. V., "Method of Calculation of the Transport Coefficients of Air at High Temperatures," *ARS JOURNAL*, vol. 30, no. 4, 1960, pp. 394-402.
- 2 Greifinger, P. S., "Transport Coefficients of Dissociating and Slightly Ionizing Air," Rand Corp., Santa Monica, Calif., RM-1794, April 1957.

- 3 Green, M. S., "The Transport Properties of Air at Elevated Temperatures," National Bureau of Standards, Tech. Progress Rep. 5237, Oct. 1956; revised Aug. 1957.
- 4 Hansen, C. F., "Approximations for the Thermodynamic and Transport Properties of High Temperature Air," NACA TN 4150, March 1958.
- 5 Scala, S. M. and Baulknight, C. W., "Transport and Thermodynamic Properties in a Hypersonic Laminar Boundary Layer. Part 1. Properties of the Pure Species," *ARS JOURNAL*, vol. 29, no. 1, 1959, pp. 39-45.
- 6 Bauer, E. and Zlotnick, M., "Transport Coefficients of Air to 8000 K," *ARS JOURNAL*, vol. 29, no. 10, 1959, pp. 721-728.
- 7 Vanderslice, J. T., Mason, E. A. and Lippincott, E. R., "Interactions between Ground State Nitrogen Atoms and Molecules. The N-N, N-N<sub>2</sub>, and N<sub>2</sub>-N<sub>2</sub> Interactions," *J. Chem. Phys.*, vol. 30, no. 1, 1959, pp. 129-136.
- 8 Vanderslice, J. T., Mason, E. A. and Maisch, W. G., "Interactions between Oxygen and Nitrogen: O-N, O-N<sub>2</sub> and O<sub>2</sub>-N<sub>2</sub>," *J. Chem. Phys.*, vol. 31, no. 3, 1959, pp. 738-746.
- 9 Vanderslice, J. T., Mason, E. A. and Maisch, W. G., "Interactions between Ground State Oxygen Atoms and Molecules: O-O and O<sub>2</sub>-O<sub>2</sub>," *J. Chem. Phys.*, vol. 32, no. 2, 1960, pp. 515-524.
- 10 Vanderslice, J. T., Mason, E. A., Maisch, W. G. and Lippincott, E. R., "Potential Curves for N<sub>2</sub>, NO and O<sub>2</sub>," *J. Chem. Phys.*, vol. 33, no. 2, 1960, pp. 614-615.
- 11 Amdur, I. and Mason, E. A., "Properties of Gases at Very High Temperatures," *Phys. of Fluids*, vol. 1, no. 5, 1958, pp. 370-383.
- 12 Hirschfelder, J. O., Curtiss, C. F. and Bird, R. B., *Molecular Theory of Gases and Liquids*, John Wiley and Sons, N. Y., 1954, pp. 526-527.
- 13 Mason, E. A., Vanderslice, J. T. and Yos, J. M., "Transport Properties of High-Temperature Multicomponent Gas Mixtures," *Phys. of Fluids*, vol. 2, no. 6, 1959, pp. 688-694.
- 14 Monchick, L., "Collision Integrals for the Exponential Repulsive Potential," *Phys. of Fluids*, vol. 2, no. 6, 1959, pp. 695-700.
- 15 Kihara, T., Taylor, M. H. and Hirschfelder, J. O., "Transport Properties of Gases Assuming Inverse Power Intermolecular Potentials," *Phys. of Fluids*, vol. 3, no. 5, 1960, pp. 715-720.
- 16 Wilke, C. R., "A Viscosity Equation for Gas Mixtures," *J. Chem. Phys.*, vol. 18, no. 4, 1950, pp. 517-519.
- 17 Logan, J. G., Jr. and Treanor, C. E., "Tables of Thermodynamic Properties of Air from 3000°K to 10,000°K at Intervals of 100°K," Cornell Aeronaut. Lab., Buffalo, N. Y., Rep. BE-1007-A-3, Jan. 1957.
- 18 Amdur, I. and Ross, J., "On the Calculation of Properties of Gases at Elevated Temperatures," *Combustion and Flame*, vol. 2, no. 4, 1958, pp. 412-420.

## Lunar Landing Sites Selection

CARL TROSS<sup>1</sup>

Aeronutronic, Div. of Ford Motor Co., Newport Beach, Calif.

IN DESIGNING lunar trajectories it is desirable to minimize fuel requirements and impact variations caused by injection parameter uncertainties. This can be accomplished by choosing a design trajectory which intersects the desired lunar landing site so that all en route propulsion requirements correct only for errors incurred in vehicle injection and in decelerating the payload. In order to minimize variations caused by sensitivity or injection parameter uncertainties we must examine trajectory dynamics. All trajectories are essentially parallel to each other as they approach the moon. A given variation in injection parameters causes trajectory displacements which are about the same for all vehicles having comparable energy. We immediately see, then, that these trajectory variances cause impact displacements which are approximately proportional to the secant of the angle of incidence at the point of contact. This function is minimized if we choose an impact whose angle of incidence is normal to the lunar surface. As a result of studying empirical normal lunar trajectories it appears that they all impact the moon near the lunar equator, so that high energy vehicles strike near the prime meridian and low energy vehicles near the east limb, Fig. 1.

In an attempt to verify this occurrence analytically, A. Liu<sup>2</sup> studied this problem from two-body theory and indeed

Received Mar. 27, 1961.

<sup>1</sup> Project Manager, Space Technology Operations. Member ARS.

<sup>2</sup> Liu, A., "Normal Lunar Impact Analysis," *J. Astronaut. Sci.*, vol. 8, no. 2, Summer 1960.

verified the empirical results. In his paper Liu points out that for rectilinear orbits normal impact occurs on the equator and that the semi-latus rectum of the orbit not only affected the impact latitude, but to a slight extent served to modify impact longitude, see Fig. 2. From this analysis it can be seen that normal lunar impacts occur only in a 10 deg band along the lunar equator in the eastern hemisphere. It follows that to minimize sensitivities the impact site must correspond to the normal impact area. Since for many missions such impact sites are too restrictive, we are forced to relax the impact area dimensions. This area can be extended by allowing impact incidence up to 60 deg, which increases the impact area to extend approximately from 30 W to 90 E deg longitude and from 40 N to 40 deg S latitude, and thereby increases the maximum sensitivities by only about 15%. If the desired impact point does not fall within these limits and it is desired to maintain comparable sensitivities, then some sort of en route trajectory modification is required.

With regard to the matter of normal lunar impact sites, let us consider the normal lunar ascent problem for a one impulse return voyage to Earth. Here we find that the ascent site is situated in the Western hemisphere symmetrically placed with respect to the normal landing site.<sup>2</sup> We can see, therefore, that if we choose a normal impact site, then a normal ascent will not return the vehicle to Earth but will send the vehicle into an orbit whose energy is greater than the moon's. Therefore it becomes immediately apparent that if a return voyage is planned, then the true normal impact site is not necessarily the most desirable for the ascent in the return voyage.

Thus we conclude that normal trajectories will serve such early lunar voyages as Ranger and Surveyor. For later missions which require a return voyage, landing site requirements should probably be re-examined in order to locate one site suitable for both landing and take off, and simultaneously minimizing trajectory sensitivity.

For some missions it may be desirable to situate the payload in an area where more temperate climatic conditions prevail. For such payloads the lunar polar regions should be investigated. Here six months of daylight and six months of night prevail, whereas the equatorial day is only about two weeks long and the night is of about the same duration. The longer duration of daylight means that polar temperatures

are quite constant over a six month period. Furthermore, the sun's rays strike the moon's pole at a very small angle, which implies that the polar day experiences moderate temperature, possibly as much as 50C lower than the maximum equatorial temperature. It is conceivable that lunar experiments may be performed for which it is desired to utilize this more moderate relatively constant climate.



Fig. 1 Normal impact points

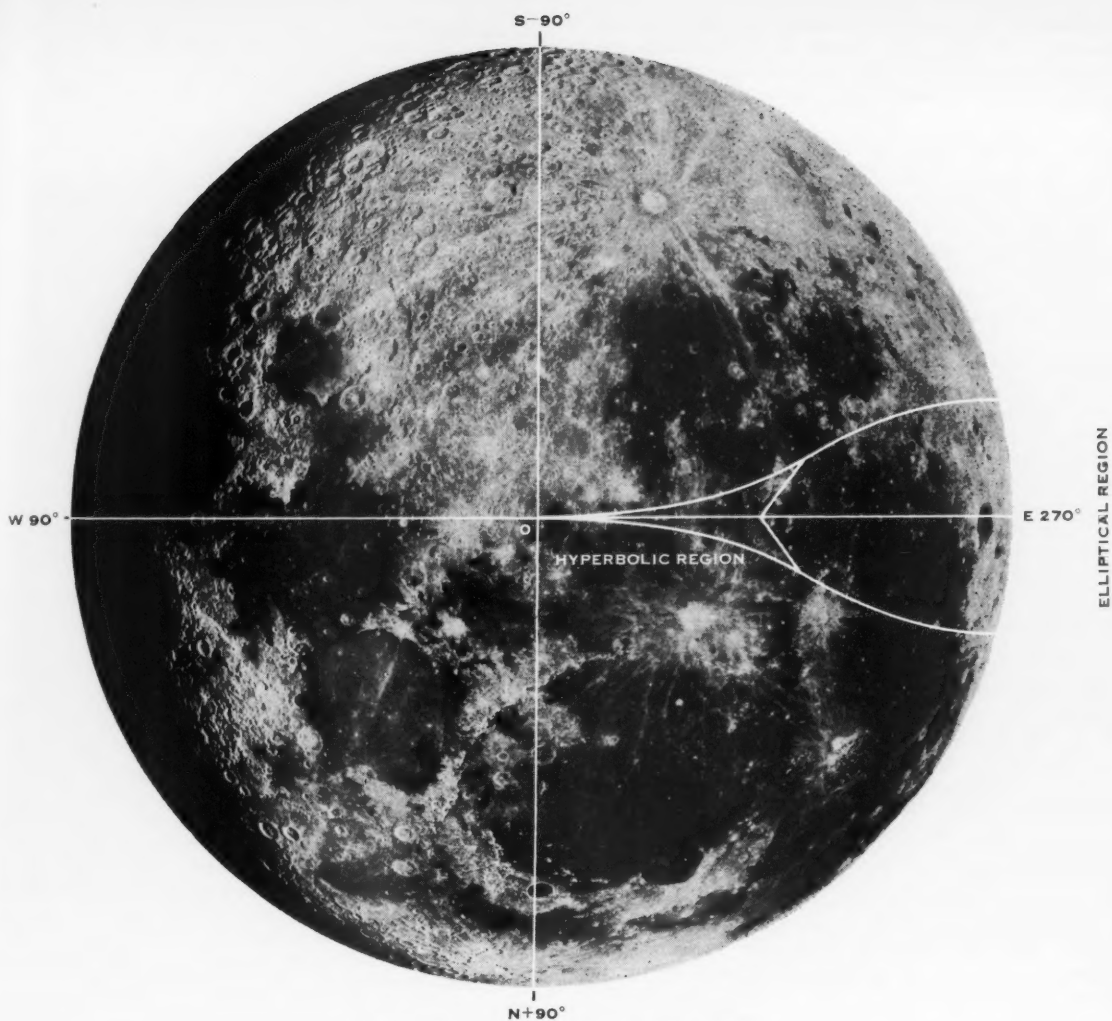


Fig. 2 Normal lunar impact for direct orbits

## Rudimentary Launch Guidance Methods for Deep Space Missions<sup>1</sup>

CARL G. PFEIFFER<sup>2</sup>

California Institute of Technology,  
Jet Propulsion Laboratory  
Pasadena, Calif.

Presented at the ARS Semi-Annual Meeting, May 10, 1960, Los Angeles, Calif.

<sup>1</sup> This paper presents results of one phase of research carried out under Contract No. NASw-6, sponsored by the NASA.

<sup>2</sup> Group Leader, Powered-Flight Analysis Group.

This paper discusses the analytic design of launch to injection guidance systems for a deep space mission where injection is considered to be the point where the last stage rocket propulsion ceases and free fall to the target begins. A commonly used technique for defining guidance equations is briefly outlined, and it is pointed out that a rather complex guidance computer will be called for if no simplifications in the equations are to be made. This is undesirable for an on-board guidance system, and may not be warranted if the inherent errors in the electro-mechanical devices making up the system are significantly large. Rudimentary launch guidance methods are then discussed, i.e., systems which do not mechanize some of the less significant terms in the guidance equations and/or do not attempt to compensate for path variation of gravity

during flight. The results of a computer study of two rudimentary guidance systems for lunar missions are presented, demonstrating that these systems might give adequate accuracy for some deep space missions.

#### Guidance System Design

THE USUAL steps in the design of deep space launch to injection guidance systems are:

- 1 Establish the performance parameters of the vehicle.
- 2 Determine a standard trajectory which has the desired characteristics. See (1, 4).<sup>3</sup>
- 3 Mechanize a set of guidance equations that will cause the mission to be accomplished in the presence of perturbations.

Guidance can be accomplished with radio commands from the ground or by an on-board computer employing inertial and/or celestial sensing devices. Only self-contained, inertial guidance systems will be considered in this paper.

Any guidance system is affected by two fundamental classes of errors:

1 Approximation errors, that arise from not mechanizing a sufficient number of terms in the guidance equations, and/or from not compensating for nonstandard gravitational acceleration during the flight.

2 Component errors, that arise from inaccuracies in the electro-mechanical devices that comprise the system.

A complete guidance system is, by definition, not subject to the first type of errors, while a rudimentary guidance system is affected by both types. It may be appropriate to accept a rudimentary system if the latter type errors are large enough to be the major source of concern, or if extreme accuracy is not required for the mission. The gain from this approach would be in reducing the weight, cost, complexity and/or unreliability of the guidance system. The loss in accuracy due to the former type errors will be discussed.

#### Guidance Equations

Perturbation methods are often employed to define guidance equations. At the standard impact time on a perturbed trajectory the vehicle possesses some miss vector in three-dimensional space. Each component of the miss vector can be expressed in terms of coordinate deviations at injection, i.e., let  $\mathbf{M}(\Delta q_i)$  = the miss vector at the standard impact time

$$\mathbf{M}(\Delta q_i) = \langle M_1(\Delta q_i), M_2(\Delta q_i), M_3(\Delta q_i) \rangle$$

where the  $\Delta q_i$  ( $i = 1, 2, \dots, 6$ ) are the variations in the injection coordinates, and  $\Delta q_7$  is the variation in injection time. For the purpose of this discussion the  $q_i$  for  $i = 1$  to  $i = 6$  may be thought of as position and speed coordinates in an inertially fixed Cartesian coordinate system.

The three functions of seven variables

$$M_j(\Delta q_i), j = 1, 2, 3; i = 1, 2, \dots, 6, 7$$

can be obtained by computing a large number of perturbed trajectories and finding the partial derivatives of  $M_j$  with respect to  $q_i$  from finite differences. The equations for  $M_j$  are then represented as Taylor series expansions in terms of the variables  $\Delta q_i$ . See (3) for a more complete discussion. There are, theoretically, an infinite number of terms in each expansion, so the analyst must decide how many terms are significant. Once the three miss equations have been obtained, it is possible to null them simultaneously at injection by the three modes of pre-injection guidance, that is, pitch steering, yaw steering and shut-off command.

The  $\Delta q_i$  defined above are in terms of the true coordinate differences, while an in-flight inertial sensor can only measure accelerations due to contact forces (thrust, drag and lift). The true and measured coordinate differences, compared at the same time, would not be the same because the vehicle

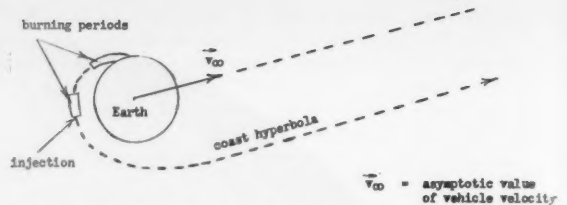


Fig. 1 Post-injection trajectory for interplanetary missions

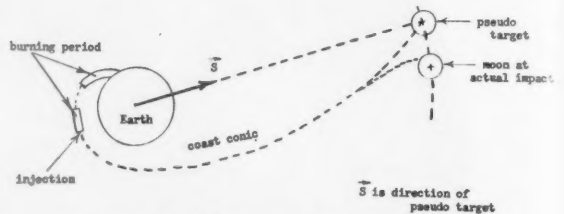


Fig. 2 Post-injection trajectory for lunar missions

experiences different gravitational acceleration on a perturbed flight. This effect is the path variation of gravity. Thus, corrections to the accelerometer readings must be made that account for gravitational acceleration. The gravity compensation can be derived from measured quantities, but a digital computer is necessary in order to do it.

It can be seen from the foregoing discussion that a rather complex guidance computer is called for in order to mechanize a complete guidance system. It is thus apropos to consider what would be lost by using a more rudimentary system. It must be remembered that no matter how exact the guidance equations are theoretically, the system can be no more accurate than the electromechanical devices that comprise it. The present state of component development may therefore obviate the need for complex guidance computations.

#### Elimination of Higher Order Terms

The analyst must decide how many terms in the guidance equations are required in order to keep the approximation errors small compared to the component errors. This decision depends very strongly upon practical considerations which are unique to each mission, but deletion of all but the linear terms can almost always be tolerated. The justification for this comes from an analysis of the post-injection trajectory.

The near Earth post-injection trajectory can be approximated very accurately by a two-body orbit (1, 4). The task of the injection guidance system is to cause the vehicle to attain an orbit that satisfies certain criteria which can be described in terms of energy, angular momentum, position of perigee and orientation of plane of motion (4). Just what the relationship between these elements must be in order to satisfy the guidance equations can be determined from an analysis of the standard trajectory. The near-Earth coast trajectory for interplanetary missions is always a hyperbola (4) since the vehicle must escape Earth. The guidance task for this case is to hold the direction of the escape asymptote fixed in space, and to keep the magnitude of the escape speed (equal to the square root of the vis viva) at its standard value (see Fig. 1).

The use of two-body approximations for lunar missions is not so straightforward. A commonly used technique is to define a pseudo, or offset, lunar target. This is accomplished by recomputing a standard trajectory with the mass of the moon set equal to zero, and letting the pseudo target be the coordinates of the vehicle when it reaches the moon's distance.

<sup>3</sup> Numbers in parentheses indicate References at end of paper.



The motivation for this method can be understood by imagining an observer on the moon, and considering the vehicle path he would observe near impact. It should be clear that a vehicle heading toward the center of the moon will have a velocity relative to the moon which is fixed in direction, independent of whether or not the moon has mass. Thus, aiming at a massless but offset moon is sufficient for guidance purposes, and the two-body approximation can be used. It should be noted that the vehicle's path in inertial space will be affected by the moon's mass, causing the vehicle to impact at a different time and speed and at a different point in space. This effect is illustrated in a somewhat exaggerated fashion in Fig. 2.

Having demonstrated that a two-body approximation is reasonable for injection guidance analysis, and having observed that such an orbit is determined by its orbital elements, it only remains to justify that the first order variation of these elements dominate the higher order terms. The expansion of orbital elements in terms of injection coordinate deviations is calculated in (5) and will not be reproduced here. It is shown that the higher order terms are not significant for coordinate deviations of the size to be expected in guided flight.<sup>4</sup> It therefore seems reasonable to assume that the linear terms in the guidance equations are sufficient.

#### Path Variation of Gravity

The integral of gravitational acceleration that the vehicle experiences up to injection may be nonstandard because of variations in injection time and variation in the flight path up to injection. The first effect may be compensated by a time term in the guidance equations, but the second type of variation is more difficult to handle. It may be compensated

by computing gravitational acceleration from the measured quantities, or it can simply be ignored. To understand the effect of neglecting path variation of gravity, consider the velocity component given by

$$\dot{X}_p = \dot{X}_{p0} + \int \ddot{X}_{pm} - \int \frac{\mu X_p}{r^3}$$

where  $\ddot{X}_{pm}$  is the thrust acceleration in the  $X_p$  direction,  $\mu$  is the gravitational constant, and  $r$  is distance from the center of Earth.  $\mu X_p/r^3$  is the gravitational acceleration in the  $X_p$  direction. Then

$$\delta \dot{X}_p = \delta \dot{X}_{p0} + \delta \left[ \int \ddot{X}_{pm} dt \right] + \int \left( \frac{\mu X_p}{r^3} \right) \left[ 3 \frac{\delta r}{r} - \frac{\delta X_p}{X_p} \right] dt$$

The  $\delta \dot{X}_{p0}$  can be assumed known, and accelerometers can measure  $\int \ddot{X}_{pm} dt$ . The path variation of gravity, which the accelerometers cannot sense, is given by the last term of the equation.

A similar analysis can be made for the other components of velocity error and for the position error, but the complete path variation effect for a given perturbation is very difficult to obtain analytically. It can be evaluated from perturbed trajectory runs on a high speed computing machine, and this will be discussed in the next section. It will be seen that path variation of gravity is quite significant.

#### Results of a Computer Study

A computer study of two rudimentary guidance systems for lunar missions was made by C. E. Kohlhasse and A. E. Dickin-

Table 1 Results of computer study of rudimentary guidance systems<sup>a</sup>

Perturbation <sup>b</sup>	Trajectory flight time, hr	Guidance System One					Guidance System Two				
		$\Delta x$ , km	$\Delta y$ , km	$\Delta v$ , m/sec	$\Delta \gamma$ , rad	Miss, km	$\Delta x$ , km	$\Delta y$ , km	$\Delta v$ , m/sec	$\Delta \gamma$ , rad	Miss, km
Flow rate error in third stage of +1.7%	36	+6.47	3.14	-3.12	+0.0006	79.4	+6.48	3.39	-0.48	+0.0011	608
	63	+6.32	0.83	-1.30	+0.001	523	+6.33	0.83	-0.53	+0.001	391
Flow rate error of +2% in second stage	36	+6.04	1.05	-4.06	+0.0005	510	+6.90	5.91	-3.16	+0.0014	679
	63	-0.44	9.70	-8.51	+0.0008	1062	-0.86	7.87	-8.63	+0.0004	1833
Flow rate error of +2% in first stage	36	-5.27	17.68	-14.84	+0.0018	1398	-11.97	23.79	-12.58	+0.0029	3228
	63	-8.85	2.79	-3.92	-0.0007	1368	-71.14	56.58	-49.75	-0.0001	7763
Specific impulse variation of +1.3% in third stage	36	+3.42	1.64	-1.63	+0.0003	42.7	+3.36	1.76	-0.28	+0.0005	312
Flow rate error of 2% in second and third stage	36	+17.16	6.39	-9.43	+0.0016	617	+14.48	9.89	-3.72	+0.0026	1453
	63	...	...	...	...	...	...	...	...	...	...
Thrust misalignment of 0.5 deg in second and third stage	36	+2.73	2.78	-2.91	+0.0005	157	-6.76	11.48	-18.29	+0.0049	2627
	63	-26.87	33.53	-27.20	+0.0043	6058	-28.68	24.32	-28.26	+0.0025	8333
Flow rate error of +2% in first stage, +0.87% in second stage, and +0.70% in third stage; thrust misalignment of 0.5 deg last two stages	36	-0.71	20.60	-19.14	+0.0025	1436	-14.54	38.10	-39.44	+0.0084	5120
	63	-2.70	2.48	-4.15	-0.0002	1617	-75.40	54.50	-65.23	+0.0008	18,710

<sup>a</sup> See the section Results of a Computer Study for definition of Guidance Systems One and Two.

<sup>b</sup> The injection coordinate errors listed are in terms of:  $x$  = downrange distance over the sea-level sphere;  $y$  = altitude;  $v$  = speed; and  $\gamma$  = angle of the velocity vector above the local horizontal.

son at the Jet Propulsion Laboratory. System One mechanized all the linear terms in the guidance equations but made no compensation for path variation of gravity. The equations were obtained by the method outlined in the section Guidance Equations. System Two used a body-fixed accelerometer integrator to shut off each stage at the standard value of measured speed with attitude control by autopilot. Two basic lunar trajectories were studied: one a direct ascent from launch with a 36-hr flight time, the second having a coast (parking orbit) of about 600 sec between second and third stage, and a 63-hr flight time. A three-stage vehicle was assumed, with approximately 10,000 fps of velocity added by each stage. The study was conducted by assuming flow rate errors,  $I_{sp}$  variations, and thrust offset in one or more of the stages, and then computing these perturbed trajectories to determine miss at the moon. Table 1 lists the results.

The miss distance was obtained by taking the trajectory only to injection and then computing the magnitude of the miss vector from the linear error equations. Therefore, the error at the target does not show the effect of neglecting higher order terms, and the target error for System One is strictly due to path variation of gravity.

No component errors were assumed for the study, since it is only the approximation errors which distinguish a rudimentary guidance system from a complete one. Thrust offsets were included, however, because a system with an inertially fixed platform (such as in System One) can detect and compensate for this error, while an autopilot system cannot.

## Experimental Performance of a Pulsed Gas Entry Coaxial Plasma Accelerator<sup>1</sup>

P. GLOERSEN,<sup>2</sup> B. GOROWITZ<sup>3</sup> and W. PALM<sup>4</sup>

General Electric Co., Philadelphia, Pa.

The performance of a pulsed gas entry coaxial type plasma accelerator has been evaluated by several experimental techniques. Impulse, kinetic energy, specific impulse, mass flow and propellant species were investigated for single pulse operation of the accelerator fired into an oversize test chamber pumped down to a pressure of  $10^{-6}$  mm of Hg. Kerr cell photography of the luminous plasma exhaust indicate a high ratio of unidirectional kinetic energy to thermal energy in the plasma exhaust, as demonstrated by the small amount of lateral spreading of the plasma in the oversize test chamber. Calorimeter measurements indicate that at least 25% of the energy originally stored in the capacitor (4500j) appears as unidirectional kinetic energy in the plasma exhaust, 1125 j. Rotating mirror camera records show that initial portions of the plasma emanate at a specific impulse as high as 25,000 sec, and that subsequent portions emanate at a specific impulse of 6000 sec.

**T**HE EARLY stages of development of a pulsed gas entry plasma accelerator for potential application in space vehicle propulsion and attitude control have been concerned primarily with the examination of various geometries con-

<sup>1</sup> This work was performed under the auspices of the U. S. Air Force, Ballistic Missile Div., Contract 04 (647)-269.

<sup>2</sup> Project Leader, Experimental Plasma Physics, Space Sciences Lab.

<sup>3</sup> Physicist, Plasma Experiments, Space Sciences Lab.

<sup>4</sup> Specialist, Experimental Plasma Physics, Space Sciences Lab.

It will be noted that the autopilot-velocimeter system gives rather good results when compared to System One. This can be understood by referring to the conic elements (4). Controlling the direction of the thrust vector and integral of thrust acceleration holds the variation in energy and angular momentum to an acceptably small value, and these parameters are most important for determining the post-injection trajectory.

The results of the study have to be interpreted from the standpoint of mission requirements and magnitude of component errors that can be expected. The miss distances shown in Table 1 might be quite acceptable if the electro-mechanical devices comprising the system have inherent inaccuracies that give significantly large errors at the target. When the statistical average of all error sources has been computed, it may be that a complete guidance system cannot be justified. Thus, rudimentary guidance systems deserve serious consideration for missions in the immediate future.

## References

- 1 Clarke, V. C., Jr., "Design of Lunar and Interplanetary Ascent Trajectories," TR-32-30, Jet Propulsion Lab., Pasadena, Calif., July 1960.
- 2 Moeckel, W. E., "Departure Trajectories for Interplanetary Vehicles," TN D-80, NASA, Washington, D. C., November 1959.
- 3 Pfeiffer, C. G., "Guidance for Space Missions," EP-656, Jet Propulsion Lab., Pasadena, Calif., June 1959.
- 4 Ehricke, K. A., *Space Flight*, Vol. 1, D. Van Nostrand Co., N. Y., January 1960.
- 5 Pfeiffer, C. G., "Rudimentary Launch Guidance Methods for Deep Space Missions," TR 34-43, Jet Propulsion Lab., Pasadena, Calif., April 1960.

sidered most capable of producing the desired interactions between the self-excited magnetic fields and the plasmas generated by the accelerator discharges. In this paper, we shall discuss the construction and operation of two coaxial types of accelerator, and shall report the results of some preliminary evaluations of their performance.

## Construction and Operation

The coaxial geometries currently under investigation in our laboratory are shown in Fig. 1. Of the two devices pictured, the cylindrically coaxial accelerator is similar in some respects to that used by Marshall (1).<sup>5</sup> The conical geometry was

<sup>5</sup> Numbers in parentheses indicate References at end of paper.

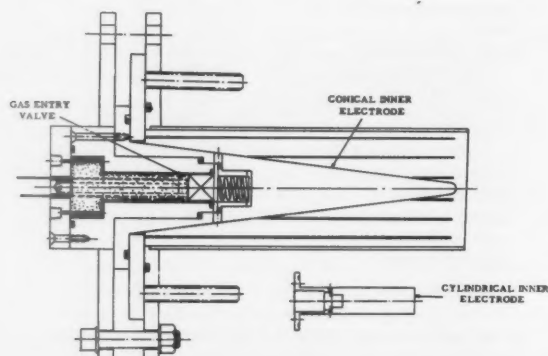


Fig. 1 Pulsed gas entry coaxial accelerator

chosen to determine what advantages, if any, would arise from producing a magnetic field in which the instantaneous intensity is higher at the breech than at the muzzle end of the accelerator. It is appropriate to mention in advance that no significant differences were observed in the operation of

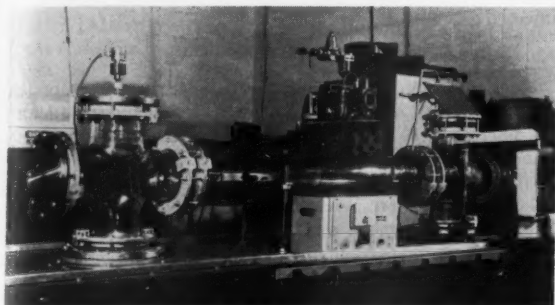


Fig. 2 Single shot, coaxial plasma accelerator test facility

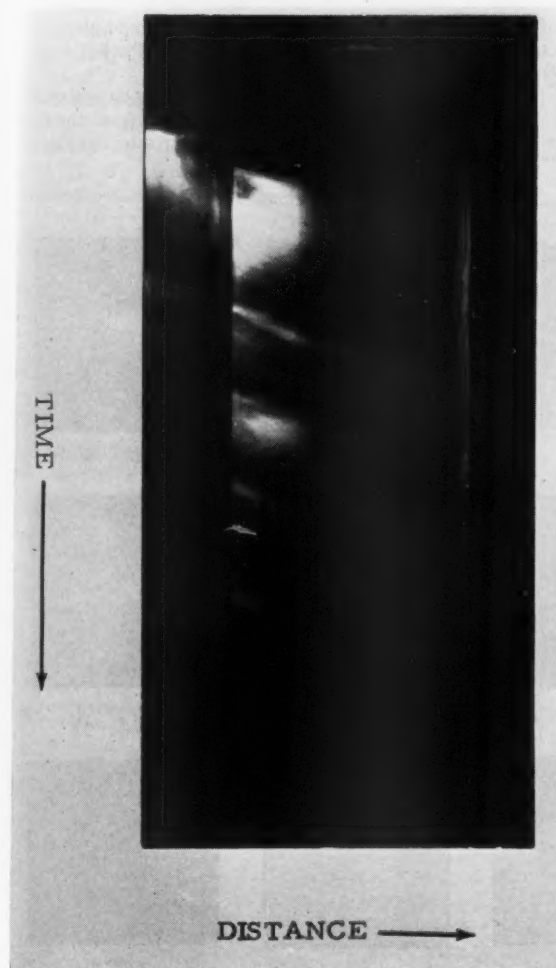


Fig. 3 Streak camera record of plasma luminosity; 10 kv-90 $\mu$ f; propellant-nitrogen

these two geometries indicated by the experiments to be reported here.

Prior to firing the accelerator, the bank of six, 15  $\mu$ f capacitors was charged to voltages ranging from 10-14 kv. In the absence of an external switch, these potentials appeared also at the terminals of the accelerator. However, since the accelerator was evacuated to pressures between  $10^{-6}$  and  $10^{-6}$  mm of Hg, there occurred no breakdown between its electrodes until the gas density was increased to an appropriate value. Thus in order to fire the accelerator, the desired amount of gas (usually argon) was admitted by a quick acting gas entry valve (2) and allowed to flow into the discharge section. When the gas density became sufficiently high in the region between the coaxial electrodes, the discharge broke down.

A test chamber with an ID of 6 in. and a length of 7 ft was constructed in order to observe the operation of these devices as they are fired into a vacuum. The experimental apparatus is shown in Fig. 2.

#### Measurements

##### Rotating mirror camera

A rotating mirror camera with a writing speed of about 3 mm/microsec was used to obtain time records of the plasma luminosity produced by the acceleration process both inside and outside the gun. The field of view of the camera included one of the slots in the side of the accelerator and a portion of the test section extending 35 cm beyond the muzzle end. A slit was used to confine the observations of the exhaust to a small region near the middle of the test section. As a result, it was possible to observe any plasma motion inside the accelerator as well as the motion of the plasma after it left the accelerator. A typical record is shown in Fig. 3. The muzzle of the gun is defined on this record by the sharp boundary of bright light about one-fifth of the way across from the left-hand side of the record. The breech is to the left of the boundary; the test section is on the right. It can be seen that for the first microsecond or two after breakdown, the luminosity is confined to a region between the breech and the gas outlet holes inside the accelerator. It is possible that this represents the time taken to ionize the injected gas. After this ionization period, the plasma travels inside the gun toward the muzzle with a well-defined leading edge velocity. Upon leaving the muzzle, it continues across the entire test section under observation with about this same velocity (10.3 cm/microsec for 10 kv, 25 cm/microsec for 14 kv). This luminosity reaches the muzzle at about the time that the accelerator current has reached its maximum value. The leading edge of the luminosity reaches the end of the test section under observation (about 45 cm from the muzzle) by the end of the first half cycle. Ideally, the accelerator should have been this long in order to take advantage of all of the energy stored in the capacitor. Such will be the case in subsequent models. It can be seen that except in the immediate region of the muzzle, the plasma is relatively non-luminous. The bright plasma at the muzzle may be due to species eroded off the glass insulator at the breech of the gun, as well as the glass sleeve around the slotted outer conductor. Evidence for this was marked erosion on both of these pieces that became apparent after a number of runs. (See also the spectral data presented.)

Additional weaker emanations appear to be expelled from the muzzle as a result of subsequent half-cycles of discharge. The velocities measured here are about one-half that of the plasma ejected during the first half-cycle.

It should be noted that luminosity inside the gun gives no strong evidence in support of a current sheath model (3) of operation of the accelerator. While there is a well-defined leading edge to the moving plasma, the more or less uniform luminosity between the gun breech and the leading edge could equally well indicate an approximately uniform radial discharge current in this region.

**Table 1 Performance of pulsed gas entry coaxial accelerator**

Capacitor energy	$E = \frac{1}{2}CV^2$	4500 j
Impulse	$I = mv$	3950 dyne-sec
Velocity	$v$	10.3 cm/microsec
Propellant mass injected	$m$	53 $\mu$ gm nitrogen
Plasma kinetic energy	$Q = \frac{1}{2}mv^2$	1125 j
Maximum efficiency	$\frac{1}{2}vI/E$	45%
Minimum efficiency	$Q/E$	25%
Propellant mass calculated	$m = \frac{1}{2}I^2/Q$	650 $\mu$ gm
Propellant mass calculated	$m = I/v$	385 $\mu$ gm
Velocity calculated	$v = 2Q/I$	5.7 cm/microsec

#### Calorimeter—pendulum measurements

For the impulse and energy transfer determination, a combination calorimeter and pendulum was hung in the upright 6-in. test section located adjacent to the muzzle end of the accelerator. The data from these measurements for one set of operating conditions are collected in Table 1, along with the velocity from the rotating mirror camera record, and the measured amount of gas injected by the quick acting valve. Since mass and velocity are well over-determined by these measurements, some interesting comparisons become possible. First of all, the discrepancy in the efficiencies, velocities and masses determined in the various ways indicated in Table 1 is not surprising, when it is noted that the calorimeter measurements tend to give a pessimistic answer due to inefficient conversion of the directed kinetic energy to heat and subsequent collection in the calorimeter. The

rotating mirror record, on the other hand, gives only the leading edge velocity, which may be higher than the velocities of any portion of the plasma following behind, and hence may give an optimistic estimate of the velocities. It should be noted, also, that ballistic pendulum action was assumed, since the other extreme (kinetic energy conserving pendulum) would require that no heat be collected by the calorimeter. The erosion of the glass cover sleeve for the outer slotted conductor may account for the fact that both calculated masses are many times larger than the measured mass of the injected gas.

#### Kerr cell camera

As a first step in studying the detailed properties of the plasma exhaust, a Kerr cell shutter with an exposure time of 0.2 microsec was used in conjunction with a variable delay line and a camera in order to obtain information on the appearance of the luminous plasma at various times after accelerator breakdown. A series of such records is shown in Fig. 4. It should be mentioned that the accelerator was fired into an oversize chamber in order also to measure the lateral spreading of the plasma, and hence determine the temperature of the plasma. The distribution of the current upon the arrival of the plasma at the muzzle and after its exit is not clearly known. The third frame of Fig. 4 might be suggestive of the extended current sheath model suggested by Lovberg (3) with a central flare and an apparently spherical outer return sheath, blown out by the magnetic pressure. However, if the current remains inside the accelerator, the outer luminous gases seen in the third frame could also have bounced back off a downstream obstruction in the test chamber.

If the outer luminosity of the third frame can be neglected, it can be deduced that the plasma emanating from the gun has a small amount of thermal energy relative to the kinetic

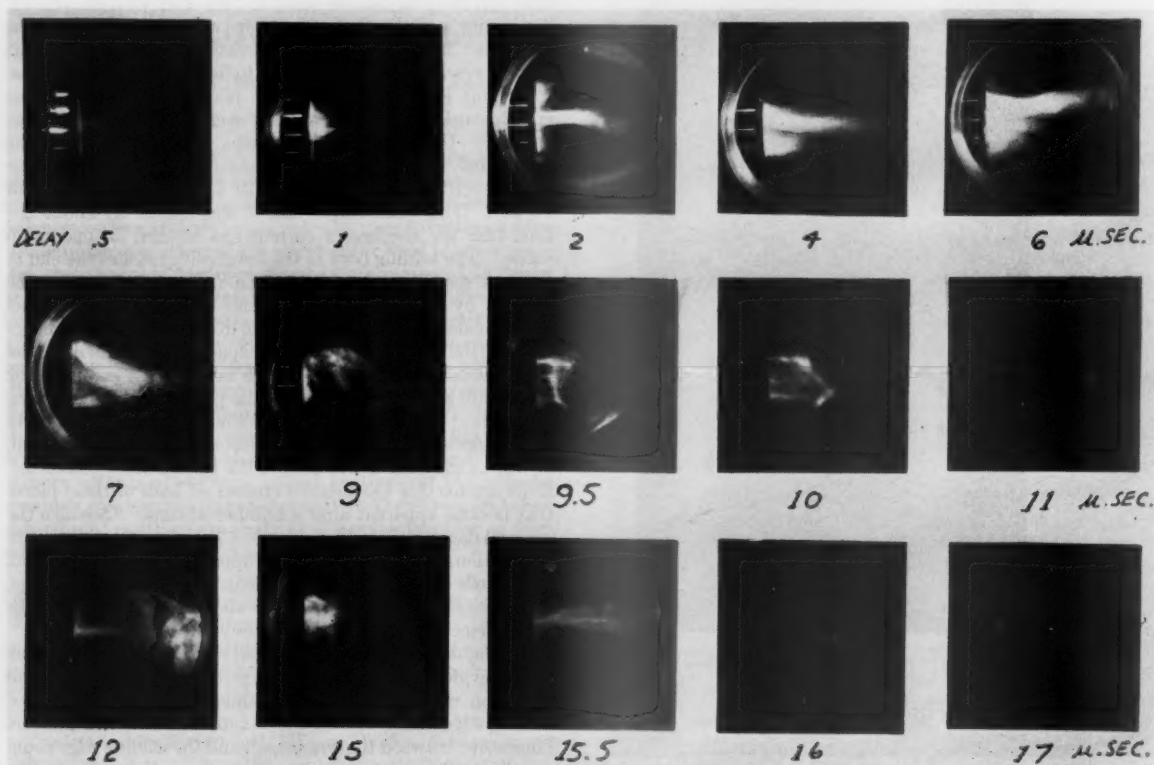


**Fig. 4 Kerr cell study of plasma produced by coaxial accelerator firing into a vacuum**



energy, in all three half-cycles of current shown here, as evidenced by the lack of spreading of the exhaust after it leaves the muzzle. This lack of spreading is shown also in Fig. 5 which is a time exposure of the exhaust luminosity.

#### Features of the Plasma Impact at the End Plate

During the course of the experiments, it was noticed that each time the accelerator was fired, a bright flash appeared at the other end of the test chamber, located about 7 ft from the accelerator. After a number of runs, it was noticed that an etch pattern of about 3 in. in diameter was formed on the brass end plate. Since the muzzle of the accelerator also had a diameter of 3 in., this observation suggests that perhaps there is little lateral spreading of the plasma in flight. Time of flight records taken with the Kerr cell camera indicate an average velocity of about 5.3 cm/microsec over the entire length of the test chamber, representing a considerable deceleration of the plasma over this testing length.

#### Spectral measurements

A high resolution Bausch and Lomb Ebert type grating spectrograph was used to analyze the luminosity in the exhaust from the accelerator. The wavelength range covered was from 3000 Å to 7000 Å. Under no conditions were spectral lines, e. g., A I, A II, due to the injected gas observed in emission. Furthermore, only a few Cu II lines with low intensity appeared in the exhaust, considerably reducing the possibility that electrode materials are a major constituent of the plasma. All of the strong lines were due to species traceable to the Pyrex insulator and sleeve of the accelerator: O I, II, III; Si I, III, IV; B I, II, III; Ca II; and K II. This is typical of results obtained earlier with a pulsed gas entry T-tube accelerator (4). Efforts at obtaining injected gas spectra by including impurities of low excitation potential substances such as  $\text{Fe}(\text{CO})_5$  in the injected gas were to no avail. In the case of the T-tube, injected gas spectra were obtained when the self-triggering mode of operation was replaced by an external switch fired at various times after the injection of the gas. The injected gas spectra gradually disappeared as the delay time to firing was reduced to zero, indicating that the tendency to form shock waves in the injected gas, with accompanying shock heating, became less as the delay time was decreased.

The spectral data should not be interpreted to mean that all of the exhaust consists of eroded Pyrex plus some electrode material. It may very well be that the injected gas also is present in the exhaust, though nonluminous. This can be determined by absorption spectroscopy techniques, which are being initiated at this writing.

#### General Comments

It should be emphasized that while only one specific impulse and thrust are discussed here, other experiments have indicated that these values can be either decreased or increased independently over considerable ranges.

In addition to these techniques discussed, we are undertaking detailed diagnostics of the gun exhausts by electrical, pressure and further spectral measurements. Secondly, we have assembled a large vacuum testing tank capable of being pumped at over 75,000 l/sec over a pressure range from  $3 \times 10^{-6}$  to  $10^{-4}$  mm of Hg. Used with a 100 kw capacitor charging power supply this permits observation of repetitively pulsed plasma accelerators under conditions closely simulating those of outer space. The new facility is shown in Fig. 6.



Fig. 5 Time exposure of plasma fired into vacuum chamber

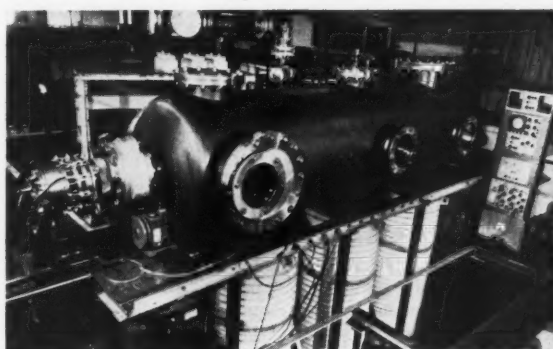


Fig. 6 Test facility—plasma acceleration studies

#### References

- 1 Marshall, J., "Performance of a Hydromagnetic Plasma Gun," *Physics of Fluids*, vol. 3, 1960, p. 134.
- 2 Gorowitz, B., Mises, K., and Gloersen, P., "A Magnetically Driven, Fast-Acting Valve for Gas Injection into High Vacua," *Rev. Sci. Instr.*, vol. 31, 1960, pp. 146-148.
- 3 Lovberg, R., "The Magnetic Acceleration of Plasma," paper G-3 read at the Nov. 2-5, 1960 meeting of the Division of Plasma Physics (APS) at Gatlinburg, Tenn.
- 4 Gloersen, P., Gorowitz, B., Bethke, G. and Palm, W., "Plasma Propulsion-Performance of a T-Tube Plasma Accelerator Fired into a Vacuum," General Electric Co. TIS Rep. no. R60SD454, October 1960.

# Segmenting of Radiators for Meteoroid Protection

ROBERT E. ENGLISH<sup>1</sup> and DONALD C. GUENTERT<sup>2</sup>

NASA Lewis Research Center, Cleveland, Ohio

**A**BILITY to tolerate bombardment by meteoroids in space is a critical problem in the design of waste-heat radiators for power supplies. Three basic philosophies in design are readily apparent: (a) One meteoroid puncture ends the vehicle's useful life. (b) If the vulnerable surface is segmented, only the punctured segments need be sacrificed. (c) A system for repair could largely eliminate failures from puncture by meteoroids. Some aspects of this problem are discussed in (1).<sup>3</sup> The specific purpose of the analysis herein is to explore the manner in which segmenting (philosophy b) might be exploited in order to obtain minimum initial weight for specified probability for successful completion of the mission. If the radiator is composed of comparatively heavy, invulnerable segments, useful radiator area available at the end of the flight would be about the same as at the beginning and only a small amount of extra area need be provided in order to compensate for punctures. On the other hand, use of lightweight segments results in high probability of puncture for each segment; in this case, considerable extra area must initially be provided so that sufficient area will still be available at the end of the flight. The manner in which these opposing points of view might be compromised in order to achieve minimum radiator weight is susceptible to a simple analysis based on probability.

If for each of  $N$  identical segments the probability of not being punctured is  $p$ , then the probability  $S$  of having  $N_s$  or more segments not punctured during the vehicle's useful life as given by the cumulative binomial distribution function is

$$S = \sum_{n=N_s}^N \frac{N!}{n!(N-n)!} (1-p)^n p^{N-n} \quad [1]$$

For each segment, the probability  $p$  of no puncture is given by the following term from the Poisson distribution (2)

$$p = e^{-hat{a}t} \quad [2]$$

where  $h$  is average puncture rate per unit area,  $a$  is vulnerable area of each segment, and  $t$  is required useful life of the radiator. The average rate of puncturing  $h$  depends on, among other things, wall thickness, wall material, and form of construction. The value of  $h$  may thus be considered to be somewhat under control of the designer of the space vehicle. For this analysis, the vulnerable surface will be considered as one layer of a single material. Presumably, a thick wall would yield a low value for  $h$ , and a thin wall a high value.

The rate of puncturing  $h$  is herein estimated from two criteria, one related to depth of penetration and the other to rate of flux of meteoroids. References (3 through 5), for example, conclude that, for a given particle velocity, the depth of penetration in a semi-infinite, solid target is directly proportional to the cube root of the mass of the impinging particle. This conclusion is herein extrapolated as follows: The thickness of wall  $\tau$  that a meteoroid will barely penetrate is proportional to the cube root of meteoroid mass. The increase in number-frequency of meteoroids with decreasing meteoroid size within the range of interest is taken by Watson (6) and Whipple (7) as  $10^{0.4}$  for each unit change in visual magnitude; this is equivalent to taking the rate of flux of meteoroids of a given or greater mass  $m$  to be inversely proportional to the mass. Any intrinsic variation in meteoroid velocity with

Received May 11, 1961.

<sup>1</sup> Chief, Power Conversion Systems Branch.

<sup>2</sup> Research Engineer.

<sup>3</sup> Numbers in parentheses indicate References at end of paper.

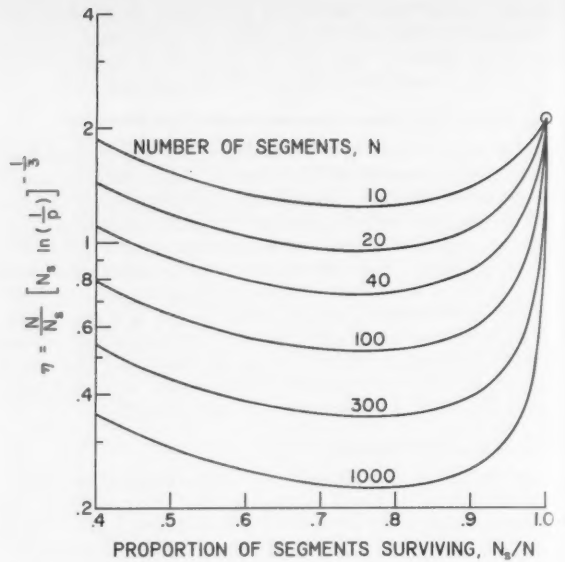


Fig. 1 Weight of vulnerable surface for survival probability  $S$  of 0.9

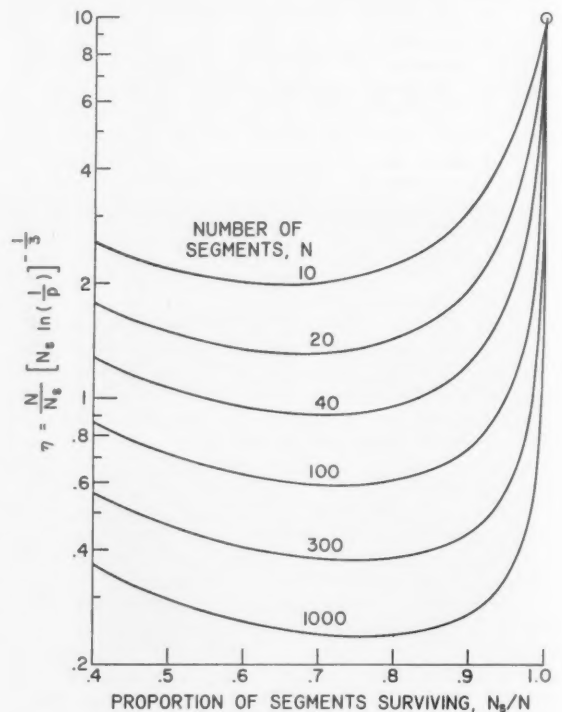


Fig. 2 Weight of vulnerable surface for survival probability  $S$  of 0.999

meteoroid mass is herein neglected. Combination of these criteria yields

$$h \sim m^{-1} \sim \tau^{-3} \quad [3]$$

The problem treated herein is not only that of providing a required unpunctured area at the end of a flight, but also of

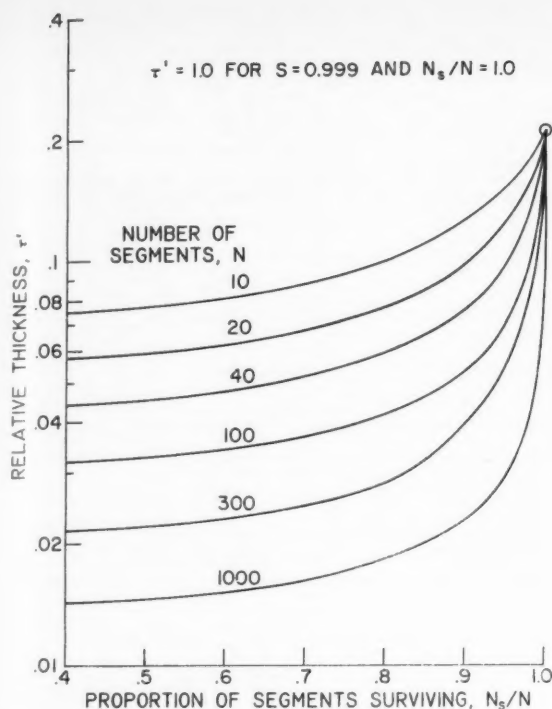


Fig. 3 Relative thickness of vulnerable surface for survival probability  $S$  of 0.9

doing this for a minimum initial weight of vulnerable surface material; that is, for

$$\frac{W}{N_s a} = \rho \tau \frac{N}{N_s} \quad [4]$$

where  $W$  is initial weight,  $\rho$  is surface material density, and  $N_s a$  is required final area;  $W/N_s a$  must be minimized. Eq. 4 considers weight of only the vulnerable surface and neglects any effects associated with manifolding, finning, or structure. Eqs. 2 through 4 can be combined to give

$$\frac{W}{N_s a} \sim \eta (N_s a t)^{1/3} \text{ where } \eta \equiv \frac{N}{N_s} \left[ N_s \ln(1/p) \right]^{-1/3} \quad [5]$$

For analysis of a given vehicle and mission,  $N_s a t$  is considered to be constant. Segmenting influences weight per unit required area  $W/N_s a$  by affecting the term  $\eta$ . Variation in  $\eta$  with number of segments  $N$  and number of surviving segments  $N_s$  is shown in Figs. 1 and 2 for two survival probabilities  $S$ . The circled points to which all the curves converge represent the case of an unsegmented radiator ( $N = N_s = 1$ ). The term  $\eta$  and thus weight per unit required area continually decrease with increasing number of segments. The value of  $N_s/N$  for minimum  $\eta$  increases with number of segments  $N$ . For very large numbers of segments

$$p \approx N_s/N$$

and selection of  $N_s/N$  to minimize weight per unit area in Eq. 5, then yields

$$(N_s/N)_{\min} = e^{-1/4} = 0.78$$

where the subscript min denotes minimum weight.

In general,  $\eta$  in Figs. 1 and 2 attains a minimum value in the region of  $N_s/N$  near a value of three-fourths.

Variation of the relative wall thickness  $\tau'$  of the radiator surface with number of segments  $N$  and number of surviving segments  $N_s$  is presented in Figs. 3 and 4 for two survival probabilities. In these plots, the wall thickness corresponding to the case of an unsegmented radiator ( $N = N_s = 1$ ) with survival probability of 0.999 was taken as unity.

The term  $N_s a t$  in Eq. 5 is independent of the degree of segmenting and indicates that, for constant  $\eta$ , weight per unit required area increases with required area  $N_s a$  and mission time  $t$ . Large radiators for missions of long duration will thus have heavy vulnerable surfaces, whether the surface is segmented ( $N > 1$ ) or unsegmented ( $N = N_s = 1$ ).

Segmenting offers the greatest potential gain for those missions requiring high survival probability  $S$ ; for  $S$  of 0.999, use of 100 segments rather than 1 reduces  $\eta$  and thus vulnerable surface weight in Fig. 2 by a factor of 16. Alternatively, for 100 segments, survival probability  $S$  can be increased from 0.9 to 0.999 with 14% increase in vulnerable surface weight, whereas a 370% increase is required for an unsegmented radiator.

Segmenting for meteoroid protection, while apparently reducing the severity of one problem, introduces another and different type of problem affecting reliability. A system employing segmenting and requiring mechanisms for leak detection and damage isolation is certainly more complex than a system without these features. Also, additional weight is required for the repair mechanisms, and any additional

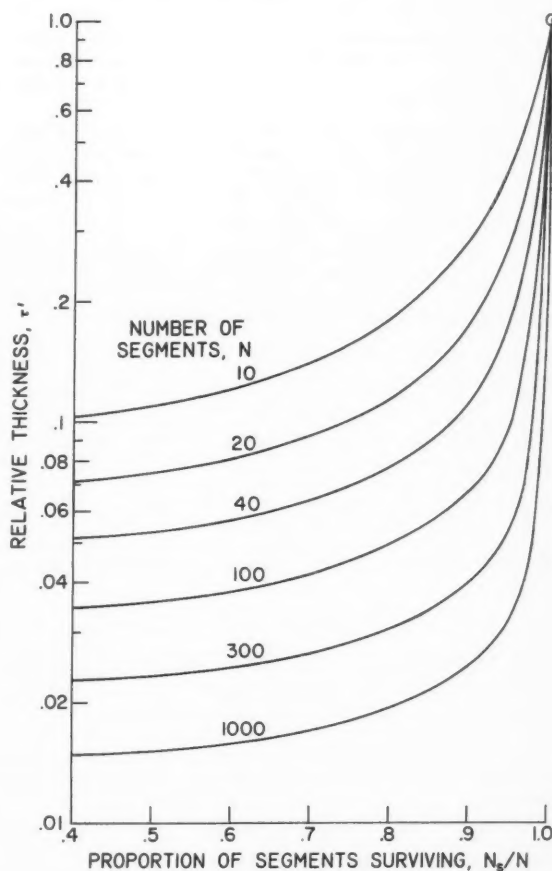


Fig. 4 Relative thickness of vulnerable surface for survival probability  $S$  of 0.999

manifolding. The extent to which segmenting will be advantageous will largely depend on the degree of success in solving these latter problems.

## References

- 1 Rosenblum, L. and English, R. E., "Nuclear-Electric Systems in Space," in Seminar on Advanced Energy Sources and Conversion Techniques, vol. I, ASTIA no. AD 209 301, Nov. 3-7, pp. 243-253.
- 2 Mood, A. M., *Introduction to the Theory of Statistics*, McGraw-Hill, N. Y., 1950, pp. 54-61.
- 3 Clay, W. G. and Partridge, W. W., "Wax Modelling Studies of High-Speed Impact," AFOSR-TN-56-257, ASTIA no. AD 88 977, June 1956.
- 4 Bjork, R. L., "Effects of a Meteoroid Impact on Steel and Aluminum in Space," RAND Corp. Rep. P-1662, Dec. 16, 1958.
- 5 Summers, J. L. and Charters, A. C., "High-Speed Impact of Metal Projectiles in Targets of Various Material," *Proc., Third Symposium On Hypervelocity Impact*, vol. 1, Armour Research Foundation of Ill. Inst. of Tech. Chicago, February, 1959, pp. 101-110.
- 6 Watson, F. G., *Between the Planets*, Harvard Univ. Press, Cambridge, Mass., 1956, p. 92.
- 7 Whipple, F. L., "The Meteoritic Risk to Space Vehicles," 8th Internat. Astronaut. Congress, Springer-Verlag, Vienna, 1958, pp. 418-428.

## Some Remarks on Solar Sail

A. POZZI<sup>1</sup> and L. de SOCIO<sup>2</sup>

Institute of Aeronautics, University of Naples, Italy

LATELY many experts in spatial sciences are interested in the problem of solar wind applied to astronautical propulsion. Therefore it is necessary at this time to study the equations governing the motion of a solar pressure ship.

Interesting solutions have been given by Tsu (1)<sup>3</sup> and London (2). The former obtained approximate solutions neglecting  $\ddot{u}$  with respect to  $v^2/r$ ; these solutions seem to be very simple and accurate for low values of  $\alpha$ . [For meaning of symbols, refer to (1, 2).] However with this method, correlated boundary conditions are lost as a consequence of neglecting the derivative. Thus, only one particular flight condition can be investigated, i.e., Tsu's results can be used only by starting with a uniquely determined initial velocity vector.

The latter solution (2) is an exact one; London indeed integrates the motion equations in closed form but still only for a particular case, and the general integral is not given. Furthermore, London's results are less suitable than Tsu's because the solutions are in implicit form.

Both cases are related to particular initial conditions; thus the possibility of discussing the influence of initial velocity on the ship performance is lost. A purpose of this note is to show very simply how such an investigation can be performed.

### Motion Equations and Solutions

Motion equations can be written

$$C_1 \left( \frac{r_0}{r} \right)^2 = \dot{u} - \frac{v^2}{r} \quad [1]$$

$$C_2 \left( \frac{r_0}{r} \right)^2 = \dot{v} + \frac{uv}{r} \quad [2]$$

where the  $C_i$ 's, when the sail setting is constant, are constants given by

$$C_1 = -a_0 + \alpha \cos^3 \theta \quad C_2 = -\alpha \sin \theta \cos^2 \theta$$

The general integral of this system contains two arbitrary constants, e.g., the components  $u_0$  and  $v_0$  of the initial velocity.

Tsu's method neglects  $\ddot{u}$  in Eq. 1 obtaining  $v$ , which derived, and with the aid of Eq. 2, gives  $u$ .

In the present method, rather than assuming an approximate expression for  $\ddot{u}$  (namely, zero) we shall approximate  $v^2/r$ .

We assume the following approximate expression for the

ratio  $v/v_0$ , where  $v_0$  is the  $v$  at  $r = r_0$

$$\frac{v}{v_0} = \left( \frac{v}{v_0} \right)_L = \left( \frac{r_0}{r} \right)^{1/2}$$

where the subscript  $L$  indicates London's values.

In this way the value of  $\ddot{u}$  is always exact at  $r = r_0$ . The integration of the first motion equation leads to the following expression for  $u$

$$u = r_0^{1/2} \left[ 2 \left( C_1 + \frac{v_0^2}{r_0} \right) \left( 1 - \frac{r_0}{r} \right) + \frac{u_0^2}{r} \right]^{1/2} \quad [3]$$

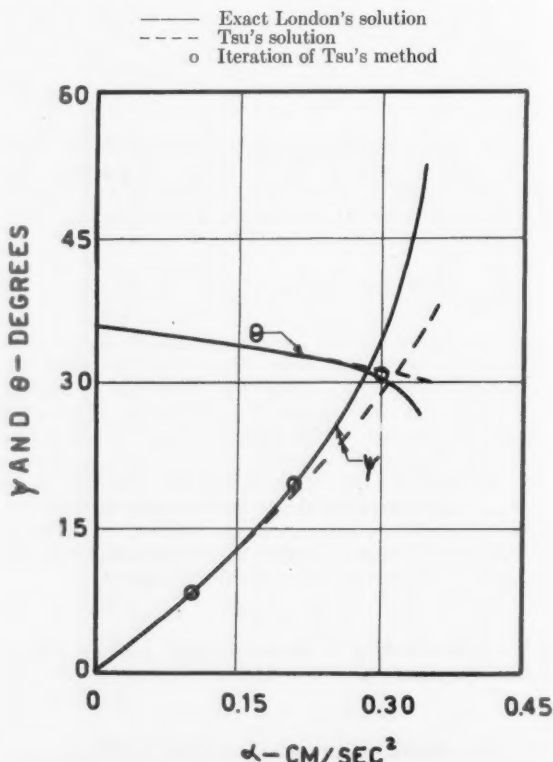


Fig. 1  $\psi$  angle and sail setting

Received March 9, 1961.

<sup>1</sup> Assistant Professor of Aerodynamics.

<sup>2</sup> Assistant Professor of Applied Aerodynamics.

<sup>3</sup> Numbers in parentheses indicate References at end of paper.



The second equation of motion gives the expression for  $v$

$$v = r_0^{1/2} \frac{r_0}{r} \left\{ \frac{v_0}{r_0^{1/2}} + \frac{C_2}{u_\infty} \left[ \ln \frac{\frac{u_0}{r_0^{1/2}} - \frac{u_\infty}{r_0^{1/2}}}{\frac{u_0}{r_0^{1/2}} + \frac{u_\infty}{r_0^{1/2}}} - \frac{\left[ 2 \left( C_1 - \frac{v_0^2}{r_0} \right) \left( \frac{r}{r_0} - 1 \right) + \frac{u_0^2}{r_0} \right]^{1/2} - \frac{u_\infty}{r_0^{1/2}} \left( \frac{r}{r_0} \right)^{1/2}}{\left[ 2 \left( C_1 + \frac{v_0^2}{r_0} \right) \left( \frac{r}{r_0} - 1 \right) + \frac{u_0^2}{r_0} \right]^{1/2} + \frac{u_\infty}{r_0^{1/2}} \left( \frac{r}{r_0} \right)^{1/2}} \right] \right\} \quad [4]$$

where  $u_\infty$  is the value of  $u$  at  $r = 0$ , i.e.,  $r_0^{1/2} \left[ 2 \left( C_1 + \frac{v_0^2}{r_0} \right) + \frac{u_0^2}{r_0} \right]^{1/2}$ . We note that this solution coincides with London's exact solution if we assume his values for  $u_0$  and  $v_0$ .

Eqs. 3 and 4 solve our problem. Indeed we have two arbitrary constants  $u_0$  and  $v_0$  and hence the solution is general.

If  $u_0$  and  $v_0$  are not very different by London's values we expect that the results are still accurate; in all cases the method could be iterated to have better approximations. To have an idea of the convergence of the iteration procedure,

we have applied it to improve Tsu's solution obtaining the following expression for a second approximation

$$u_2 = u_1 / \left[ 1 - 2 \left( \frac{C_2}{C_1} \right)^2 \right]^{1/2}$$

$$v_2 = v_1 \left[ 1 - 2 \left( \frac{C_2}{C_1} \right)^2 \right]^{1/2}$$

$$\psi_2 = \psi_1 / \left[ 1 - 2 \left( \frac{C_2}{C_1} \right)^2 \right]$$

where subscript 1 indicates Tsu's values. Tsu's approximation, our second approximation and London's solution are shown in Fig. 1.

The influence of initial velocity and the value of  $\theta$  which minimizes the travel time can be investigated by using Eqs. 3 and 4.

These problems will be treated in a forthcoming paper.

## References

- 1 Tsu, T. C., "Interplanetary Travel by Solar Sail," *ARS JOURNAL*, vol. 29, no. 6, June 1959, p. 422.
- 2 London, H. S., "Some Exact Solutions of the Equation of Motion of a Solar Sail With Constant Sail-Setting," *ARS JOURNAL*, vol. 30, no. 2, February 1960, p. 198.

## Book Notes

**Electrostatic Propulsion**, D. B. Langmuir, E. Stuhlinger, and J. M. Sellen Jr., Academic Press, N. Y., London, 1961, 579 pp.

**Sections:** 1. Ion Generation; 2. Ion Acceleration and Impact Effects; 3. Neutralization; 4. Techniques and Testing.

This volume is a compilation of 29 Technical Papers selected mainly from a Symposium of the AMERICAN ROCKET SOCIETY, held at the U. S. Naval Postgraduate School, Monterey, Calif., Nov. 3 and 4, 1960. The purpose of this specialists' conference was to promote an exchange of ideas in the field of electrostatic propulsion, with most emphasis on problems where current scientific opinions differ.

**Physical Chemistry in Aerodynamics and Space Flight**, A. L. Myerson and A. C. Harrison, Pergamon Press, London, N. Y., Paris, 1961, 288 pp.

**Sections:** 1. Surface and Solid Phase Reactions; 2. Gas Phase Reactions and Kinetics; 3. Experimental Methods and Simulation; 4. Thermodynamic and Transport Properties of Gases.

This book brings to light new and direct applications of physical chemistry to aerodynamics and space flight. A knowledge of physical chemical phenomena at very high temperatures over a wide range of physical conditions is shown to be

necessary to progress in space flight. The book is based on a conference arranged by the Space Sciences Laboratory of General Electric's Missile and Space Vehicle Department and the Air Force Office of Scientific Research, held Sept. 1-3, 1959, at the University of Pennsylvania.

**Elementary Fluid Mechanics**, 4th ed., J. K. Vennard, John Wiley & Sons, Inc., N. Y., London, 1961, 570 pp. \$7.95.

**Chapters:** 1. Fundamentals; 2. Fluid Statics; 3. Kinematics of Fluid Motion; 4. Flow of an Incompressible Ideal Fluid; 5. Flow of a Compressible Ideal Fluid; 6. The Impulse-Momentum Principle; 7. Flow of a Real Fluid; 8. Similitude and Dimensional Analysis; 9. Fluid Flow in Pipes; 10. Liquid Flow in Open Channels; 11. Fluid Measurements; 12. Elementary Hydrodynamics; 13. Fluid Flow about Immersed Objects; **Appendix:** Symbols and Dimensions of Quantities, Physical Properties of Water, Wave Velocities, The ICAO Standard Atmosphere, Basic Operations with Partial Derivatives, Properties of Areas and Volumes, Cavitation, The Expansion Factor, Dimensional Analysis of Certain Problems, Mathematical Details of Turbulent Pipe Flow.

This is a textbook designed for beginners studying fluid mechanics. The emphasis here is on physical concepts rather than on mathematical devices, since the author feels that some oversimplification is justified in introducing the subject to beginners. This fourth edition attempts to include new and broader concepts which have been evolved in the field. There are more than 100 problems provided to which the student can apply principles learned from the text. References are given to guide the

reader in seeking broader treatments of the topics discussed in this volume.

**Text-Book on Spherical Astronomy**, W. M. Smart, Cambridge University Press, N. Y. 1960, 430 pp. \$3.95.

**Chapters:** 1. Spherical Trigonometry; 2. The Celestial Sphere; 3. Refraction; 4. The Meridional Circle; 5. Planetary Motions; 6. Time; 7. Planetary Phenomena and Heliographic Co-Ordinates; 8. Aberration; 9. Parallax; 10. Precession and Nutation; 11. The Proper Motions of the Stars; 12. Astronomical Photography; 13. Determination of Position at Sea; 14. Binary Star Orbits; 15. Occultations and Eclipses; **Appendix.** The Method of Dependences, Stellar Magnitudes, the Coelostat, Astronomical Constants, Dimensions of the Sun, Moon and Planets, Elements of the Planetary Orbits for the Epoch 1931 January 0, G.M. NOON, Elements and dimensions of the Satellites, Secular Parallax.

The text of this book is based on lectures given at the University of Cambridge and on a parallel course given in Practical Astronomy at the Observatory. Information as given in older textbooks on Spherical Astronomy is linked to that which has been currently developed. In addition to traditional type instruction, there are discussions on such subjects as heliographic co-ordinates, proper motions, determination of position at sea, the use of photography in precise astronomical measurements and the orbits of binary stars. At the end of each chapter, a collection of exercises is provided, compiled with permission from examinations given at London University, Cambridge Colleges, and several are from Ball's *Spherical Astronomy*.

The books listed here are those recently received by the ARS from various publishers who wish to announce their current offerings in the field of astronautics. The order of listing does not necessarily indicate the editors' opinion of their relative importance or competence.

**Frame Analysis**, A. S. Hall, and R. W. Woodhead, John Wiley & Sons, Inc., N. Y., London, 247 pp. \$8.50.

*Contents:* 1. Definitions; 2. Basic Concepts; 3. Method of Influence Coefficients; 4. Evaluation of Flexibility; 5. Flexibility Transformations; 6. Axis Transformations; 7. Flexibility Analysis of a Single Member; 8. Transformations for a Single Member; 9. Method of Slope Deflection; 10. Stiffness Analysis of a Single Member; 11. Stiffness of a Frame; 12. Relaxation Methods; 13. Coefficient of Restraint; *Appendix:* Some Notes on Matrix Algebra.

The subject of this book is a mathematical analysis of structural frames. Principles of Flexibility Analysis and Stiffness Analysis are discussed and unified. The author shows how all other techniques are variants of these two principal and reciprocal methods of analysis. Matrix algebra is gradually introduced, and then used more extensively through the latter part of the text. This is a book suitable mainly for senior students and structural engineers.

**Elements of Nuclear Engineering**, G. Murphy, John Wiley & Sons, Inc., N. Y., London, 213 pp. \$7.50.

*Contents:* 1. The Engineer and Nuclear Energy; 2. Nuclei and Nuclear Reactions; 3. Radiation; 4. Introductory Reactor Theory; 5. Engineering Considerations of Nuclear Power; 6. Radiation Detection; 7. Shielding and Radiation Effects; 8. Industrial Uses of Radioisotopes; *Appendix.*

The subject matter presented here deals with nuclear transformations and their applications in industry and engineering. The field of nuclear engineering its general scope and potentialities, are outlined. The book is not a full course in nuclear physics, but is intended for the undergraduate student as an introductory course in nuclear engineering.

**Telescopes**, G. P. Kuiper, and B. M. Middlehurst, The University of Chicago Press, Illinois, 1960, 255 pp. \$8.50.

*Contents:* 1. The 200 Inch Hale Telescope; 2. The Lick Observatory 120 Inch Telescope; 3. Design of Reflecting Telescopes; 4. Schmidt Cameras; 5. Telescope Driving Mechanisms; 6. The Transit Circle; 7. The Photographic Zenith Tube and The Dual-Rate Moon-Position Camera; 8. The Impersonal Astrolabe; 9. Astronomical Seeing; 10. Astronomical Seeing and Observatory Site Selection; 11. Radio Telescopes; 12. Radio-Astronomy Radiometers and Their Calibration; *Appendix.*

This is the first of nine volumes in a series called *Stars and Stellar Systems* which was planned by senior astronomers from the U. S. and abroad in 1955. This first volume describes research tools used through the progress of astronomy. Types of astronomical telescopes, driving mechanisms, atmospheric conditions affecting performance, and the selection of observation sites are discussed. A list of current major optical telescopes, radio telescopes and interferometers along with useful data concerning them is included.

The level of material is appropriate for graduate students, as well as for professional astronomers and scientists in other fields requiring astronomical information.

**Airborne Radar**, D. J. Povejsil, R. S. Raven and, R. Waterman, D. Van Nostrand Co., Inc., N. J., Toronto, N. Y., London, 1961, 823 pp.

*Contents:* 1. Elements of the Airborne Radar Systems Design Problem; 2. The Development of Weapons System Requirements; 3. The Calculation of Radar Detection Probability and Angular Resolution; 4. Reflection and Transmission of Radio Waves; 5. Techniques for Signal and Noise Analysis; 6. Generic Types of Radar Systems and Techniques; 7. The Radar Receiver; 8. Regulatory Circuits; 9. Automatic Tracking Circuits; 10. Antennas and RF Components; 11. The Generation of Microwave Power; 12. Display System Design Problems; 13. Mechanical Design and Packaging; 14. Airborne Navigation and Ground Surveillance Radar Systems.

This book is one of a series titled *Principles of Guided Missile Design*, edited by Grayson Merrill, U.S.N. (Ret.), which systematically assembles current unclassified material on guided missile technology. This volume relates basic radar technology to overall weapons system design. The way in which mathematical models may be developed to solve radar design problems is emphasized. Various types of radar systems such as monopulse systems, pulse doppler systems and passive detection systems are discussed. The book is primarily designed for weapon system engineers, military personnel and graduate students in the field.

**The Physical Principles of Astronautics**, A. I. Berman, John Wiley & Sons, Inc., N. Y., London, 350 pp.

*Contents:* I. Principles of Astronomy: 1. The Earth and the Moon. 2. Physics of the Solar System. II. Foundation of Mechanics: 3. The Laws of Dynamics. 4. Potential and Kinetic Energy. III. Dynamics of Space Flight: 5. Orbital Theory; 6. Transfer Orbits and Space Navigation; 7. Orbital Perturbations; 8. Propulsion Dynamics; *Appendices.*

This book is an introduction to the field of astronautics, appropriate for a technical audience rather than for laymen. It can be used as the text in a one-semester course for undergraduate or beginning graduate students, as a secondary text in astronomy and mechanics courses, or as a guide for those studying astronautics on their own. A reader with a background in introductory physics and calculus is adequately equipped to understand the material. Many illustrative examples are worked out within the text, and unsolved problems are given the student after each chapter. Vector notation is employed, and a short introduction to vectors is included in the appendix for those unfamiliar with its usage.

**Legal Problems of Space Exploration**, Legislative Reference Service, Library of Congress, Washington, D. C., 1961, 1392 pp.

*Contents:* I. Selected articles, arranged

chronologically; II. The Law of Outer Space; Report to the National Aeronautics and Space Administration. Project reporters for the American Bar Foundation: Leon Lipson and Nicholas deB. Katzenbach; III. International Negotiations Regarding the Use of Outer Space, 1957-1960. Prepared in the Historical Office, Bureau of Public Affairs, Department of State; IV. Communist viewpoints: Guides to the study of Communist views on the legal problems of space exploration and a bibliography, by Robert D. Crane; V. *Appendixes:* VI. Selected References on the Legal Problems of Space Exploration, compiled by Kenneth Anderson Finch.

This is a Senate document, printed with illustrations, based on the symposium "Legal Problems of Space Exploration" held March 22, 1961 under Lyndon Johnson as chairman. The document was prepared for the use of the Committee on Aeronautical and Space Sciences, United States Senate, by the Legislative Reference Service; Library of Congress. It should be of use to many in the scientific and legal professions.

**Proceedings of the Air Force-Navy-Industry Propulsion Systems Lubricants Conference**, Air Research and Development Command, Southwest Research Institute, Texas, 1961, 246 pp. \$7.50.

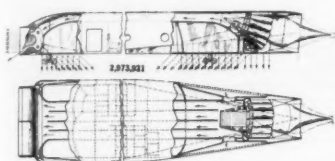
*Contents:* Introduction; Welcoming Address; Keynote Address; Trends in Commercial Air Transport; General Electric Views on Jet Engine-Lubrication; Aviation Lubricant Requirements; Gas Turbine Engine Picture; Gas Turbine Lubricants Picture — 1960; Base Fluid Studies on High-Temperature Lubricants; Bearing Lubrication with Additive Fuel; High-Temperature Gear Lubrication; Fundamentals of Rolling-Element Bearing Lubrication, Performance of High-Temperature Bearings Lubricated with Synthetic Lubricants, Radiation Effects on Aircraft Turbine Lubricants; Survey of Solid-Film Lubricants, Survey of Development in Rocket Propulsion; Trends in Flight Vehicle Power; Rocket Engine and Flight Vehicle Power Lubrication Requirements; Wear and Friction in Liquid Nitrogen and Hydrogen of the Materials Combinations Carbon-Stainless Steel and Carbon-Carbon; Lubrication with Propellants; A Test for Impact Sensitivity of Materials in Contact with Liquid Oxygen; Gear and Bearing Lubrication in Extreme Environments; Powdered and Gaseous Lubricants for Use in Ball Bearings at Temperatures from Room Temperature to 1200°F; Gas Lubrication of Bearings at Very High Temperatures, Liquid-Mercury Lubricated Hydrosphere Bearings; Registration List.

These are the Proceedings of the Air Force-Navy-Industry Propulsion Systems Lubricants Conference, an Air Research and Development Command presentation held in San Antonio, Texas, on Nov. 15, 16 and 17, 1960. The Conference was co-sponsored by the Wright Air Development Division and the Southwest Research Institute. Five sessions were held, at which a total of 22 technical papers were presented.

# New Patents

George F. McLaughlin, Contributor

**Wingless supersonic aircraft (2,973,921).** N. C. Price, Westwood, Calif.



Capable of vertical ascent or descent. Efficient performance at low, intermediate and high altitude at subsonic or supersonic speeds. Positive propulsion system air control.

**Asymmetrically variable supersonic inlet system (2,969,939).** M. A. Sulkin (ARS member), G. W. Campbell and L. C. Young, Gardena, Calif., assignors to North American Aviation, Inc. (ARS corporate member).

Wedge dividing fluid inlet conduit into a plurality of ducts. Each duct has a variable ramp which may be independently moved to deform the wedge.

**Rotating inlet for jet engines (2,970,431).** D. L. Harshmann, Forest Park, Ohio, assignor to Curtiss-Wright Corp.

Combined ramjet and turbojet. Air approaching a hollow member forming the forward extension at an angle rotates the member and alters inlet capture area.

**Fuel control for dual heat source power plant (2,970,436).** J. S. Sims Jr., Simsbury, Conn., assignor to United Aircraft Corp. (ARS corporate member).

Fuel flow continuously modified in response to temperature changes while heat exchanger is varying heat of power plant.

**High temperature pumping system (2,970,437).** R. J. Anderson, Wickliffe, Ohio, assignor to Thompson Ramo Wooldridge, Inc. (ARS corporate member).

Ram air or air from turbine is selectively admitted to heat exchanger to provide a suitable temperature for refrigeration components.

**Missile simulator (2,971,274).** W. E. Thornton, Los Angeles, Calif., assignor to Del Mar Engineering Laboratories.

System for displaying on a cathode ray tube viewing screen the path of a simulated missile fired from an aircraft in flight.

**Jet propulsion device for operation submerged in water (2,971,325).** C. A. Gongwer (ARS member), Azusa, Calif., assignor to Aerojet-General Corp. (ARS corporate member).

Steam injector pump discharges into reaction chamber. Water is drawn into frusto-conical nozzles from a duct by action of steam passing through nozzles.

**Temperature limiting system for gas turbine exhaust area control (2,971,326).** N. K. Peters, D. A. Reynick, South Bend, Ind., assignors to The Bendix Corp. (ARS corporate member).

Variable area exhaust nozzle actuated by means of a signal representing actual engine operating temperature and a signal representing a desired temperature.

**Discharge control of an overexpanding propulsion nozzle (2,971,327).** T. K. Moy and R. G. Glenn, Merriam, Ohio, assignors to Westinghouse Electric Corp. (ARS corporate member).

Pistons responsive to differential pressure between gaseous fluid in exhaust nozzle and atmospheric air move fluid into nozzle to prevent fluid over-expansion.

**Control system for air inlet bypass (2,971,328).** G. H. McLafferty (ARS member), Manchester, Conn., assignor to United Aircraft Corp. (ARS corporate member).

Means responsive to a difference in two signals for controlling amount of air bled from air inlet duct to conform to requirements of compressor.

**Air-inlet shock controller (2,971,330).** J. W. Clark (ARS member), Glastonbury, Conn., assignor to United Aircraft Corp. (ARS corporate member).

Signal generator in a downstream subsonic region of flow in a duct sends a signal upstream toward shock wave in supersonic fluid flow, varying parameter of flow.

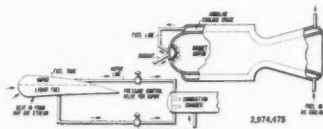
**Apparatus for guided missiles (2,971,437).** H. Surtees, Hayes, Middlesex, England.

Optical aiming device. Eyepiece mounted to aim at a target is connected to a servo system and an automatic program system.

**Ceramic-to-metal seals (2,972,808).** C. V. Litton, Grass Valley, Calif., assignor to Litton Engineering Laboratories.

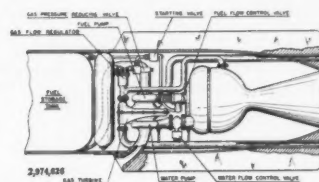
Method of producing a hermetic seal between a metallic sleeve and metallized surface of a ceramic cylinder, producing a continuous metal bond between them.

**Method of operating a rocket motor (2,974,475).** J. J. Kolfenbach and J. P. Longwell (ARS members), Westfield, N. J., assignors to Esso Research and Engineering Co. (ARS corporate member).



Fuel tanks in high speed flight cooled by absorbing frictional heat in a layer of hydrocarbon fuel in heat exchange relation with the aircraft surface.

**Apparatus for jet propulsion through water (2,974,626).** Dr. F. Zwicky (ARS member), Pasadena, Calif., assignor to Aerojet-General Corp. (ARS corporate member).



Conduits lead from propellant to a pump to an injector, and from nacelle water inlet to a pump to an injector. Turbine driven by reaction chamber gas.

**Light chopper (2,972,812).** T. H. Jackson Jr., Los Angeles, Calif., assignor to Northrop Corp. (ARS corporate member).

Optical star tracker for focusing image of an interesting star, a scanner disc chopping any deviation of the image, and means for indicating magnitude of deviation.

**Rocket motors (2,972,859).** F. J. Porcher, Edbraston, England, assignor to Imperial Chemical Industries, Ltd.

Two charges spaced apart in a casing. Gas flows to remote end of one charge to cushion static gas and equalize pressure. End surfaces of charges are ignited simultaneously.

**Explosive operated valve (2,972,998).** R. L. Detwiler, Silver Springs, Md., assignor to the U. S. Navy.

Frangible diaphragm in a casing chamber seals a pair of fluid passages. A cutter in chamber ruptures diaphragm when driven by an explosive charge.

**Attitude control system for space vehicles (2,973,162).** Dr. W. Haeussermann (ARS member), Huntsville, Ala.

Rotary mass on a space vehicle for turning vehicle about its axis. A mechanism expels materials in a direction such as to cause vehicle to assume desired attitude.

**Wing severing device (2,973,164).** R. E. Grill (ARS member), Long Beach, Calif., assignor to Northrop Corp. (ARS corporate member).

Explosive charge inside each wing, outboard of body. Simultaneous detonation of charges severs wings from body along predetermined lines.

**Turbine principle helicopter-type blade for aircraft (2,973,166).** B. Stahmer (ARS member), Omaha, Neb.

Two closely spaced vertical thrust units on each side of an aircraft arranged for downward thrust when rotating in opposite directions, driven from exhaust of horizontal jet engines above wing.

**Propellant (2,973,255).** J. R. Eiszher, Park Forest, Ill., assignor to Standard Oil Co. (Ind.).

A binder of a synthetic polymeric base material, an ammonium nitrate combustion catalyst, an oxime, and ammonium nitrate.

**EDITOR'S NOTE:** Patents listed above were selected from the Official Gazette of the U. S. Patent Office. Printed copies of patents may be obtained from the Commissioner of Patents, Washington 25, D. C., at a cost of 25 cents each; design patents, 10 cents.



# Technical Literature Digest

M. H. Smith, Associate Editor

The James Forrestal Research Center, Princeton University

## Propulsion and Power (Combustion Systems)

Effects of Injection Location on Combustion Instability in Premixed Gaseous Bipropellants Rocket Motors, by J. R. Osborn and L. R. Davis, *Purdue Univ., Jet Propulsion Center, Rep. 1-61-1*, Jan. 1961, 76 pp.

Riemann's Problem for a Laval Nozzle, II. Two-Dimensional Treatment, by Rudolf Schatz, *Munich, Technische Hochschule, Mathematical Institute, Tech. Note 2*, Dec. 1960, 26 pp. (AFOSR 415).

The Effect of Rapid Liquid-Phase Reactions on Injector Design and Combustion in Rocket Motors, by Gerard W. Elverum Jr. and Peter Staudhammer, *Calif. Inst. Tech. Jet Propulsion Lab. Prog. Rep. 30-4*, Aug. 1959, 42 pp.

Third Annual Conference on Aviation and Astronautics, Tel-Aviv and Haifa, Israel, Inst. Tech., Dept. of Aeron. Engng. (reprint from *Bull. Research Council of Israel*, vol. 9C, no. 1-2, Feb. 1961), 121 pp.

Preliminary Development of an Annular Jet Injector, by A. Kogan and M. Victor, pp. 79-106.

Spaceflight Technology, Commonwealth Spaceflight Symposium 1st, London, 1959, Kenneth W. Gatland, ed., Academic Press, N. Y. 1960, 365 pp.

Solid Propellant Rockets for High-Altitude and their Economics, by W. T. Fisher, pp. 91-106.

An Air-Breathing Engine to Work at Mach Numbers Greater than M-5.0, by W. F. Hilton, pp. 223-237.

Analysis of Partial Admission Axial Impulse Turbines, by Hans D. Linhardt and David H. Silvern, *ARS JOURNAL*, vol. 31, no. 3, March 1961, pp. 297-308.

Pressure Forces on Variable Conical Nozzles, by W. A. Woods, *Aircraft Engng.*, vol. 33, no. 386, April 1961, pp. 100-102.

Heat Release Rate, Temperature and Pressure in Solid Rocket Instability, by F. T. McClure, R. W. Hart and J. F. Bird, *ARS JOURNAL*, vol. 31, no. 3, March 1961, p. 367.

Advances Uncooled Nozzle for Solid Propellant Rocket, by Chuk-Ching Ma, *ARS JOURNAL*, vol. 31, no. 3, March 1961, pp. 368-369.

Hydraulic Analog Investigation of a Plug Nozzle, by R. H. Page and A. P. Meyer, *ARS JOURNAL*, vol. 31, no. 3, March 1961, pp. 447-448.

Effect of Scale Size on a Rocket Engine with Suddenly Frozen Nozzle Flow, by Ronald Watson, *ARS JOURNAL*, vol. 31, no. 3, March 1961, pp. 452-453.

Ballistic Missile and Space Technology v. II: Propulsion and Auxiliary Power Systems, (Symposium on Ballistic Missile and Space Technology, 5th, Los Angeles, Aug. 1960), Donald P. Le Galley, ed., Academic Press, N. Y., 1960, 441 pp.

Application of the Density Ratio Method for the Interpretation of Radiographic Film of Large Solid Propellant Rockets, by Richard J. Mascis, pp. 3-54.

Bleed Gas from a Solid Propellant Rocket Engine to Power an Auxiliary Power Supply, by C. W. Shoun, pp. 383-408.

A Discussion of Several Criteria for Determining the Propellant Bias for Optimum Performance of Liquid Propellant Stages, by A. H. MacPherson, pp. 87-109.

National Symposium on Space Electronics and Telemetry, San Francisco, Sept. 1959, Proc., Sponsored by the Professional Group of Space Electronics and Telemetry of the Inst. of Radio Engineers, Inst. of Radio Engineers, N. Y., 1959, 1 v.

A PCM Data Acquisition and Processing System for Solid Propellant Engine Testing, by J. P. Knight, No. 5.1, 9 pp.

Importance of Combustion Chamber Geometry in High Frequency Oscillations in Rocket Motors, by J. R. Osborn and J. M. Bonnell, *ARS JOURNAL*, vol. 31, no. 4, April 1961, pp. 482-486.

Ignition of Solid Propellant Rocket Motors by Injection of Hypergolic Fluids, by Carl C. Ciepluch, Harrison Allen Jr. and Edward A. Fletcher, *ARS JOURNAL*, vol. 31, no. 4, April 1961, pp. 514-518.

Stability Problem of the Flow with Combustion in Variable Area Duct, by Andrzej Kowalewicz, *ARS JOURNAL*, vol. 31, no. 4, April 1961, pp. 558-559.

A Comparison of Analytical and Experimental Local Heat Fluxes in Liquid-Propellant Rocket Thrust Chambers, by William E. Welsh Jr. and Arvel B. Witte, *Calif. Inst. Tech., Jet Propulsion Lab. Tech. Rep. 32-43*, Feb. 1961, 20 pp.

Evaluation of Several Ram-Jet Combustor Configurations Using Pentaborane Fuel, by John W. Sheldon and A. J. Cervinka, *NACA Res. Mem. E57A24*, April 1957, 43 pp. (Declassified by authority of NASA TPA no. 45, May 11, 1961.)

Flight Performance of a 2.8 KS 8100 Cajun Solid-Propellant Rocket Motor, by Dorothy B. Lee, *NACA Res. Mem. L56K01*, Jan. 19, 1957, 12 pp. (Declassified by authority of NASA TPA no. 45, May 11, 1961.)

Experimental Performance of Area Ratio 200, 25, and 8 nozzles on JP-4 Fuel and Liquid-Oxygen Rocket Engine, by J. Calvin Lovell, Nick E. Samanich and Donald O. Barnett, *NASA Tech. Mem. X-382*, Aug. 1960, 16 pp. (Declassified by authority of NASA TPA no. 45, May 11, 1961.)

Static Investigation of Paddle Vane Oscillating in Jet of 1,300-Pound-Thrust Rocket Motor, by Wade E. Lanford, *NASA Mem. 10-19-58L*, Nov. 1958, 18 pp. (Declassified by authority of NASA TPA no. 45, May 11, 1961.)

Rocket-Engine Throttling, by William A. Tomazic, *NACA Res. Mem. E55J20*, Dec. 1955, 2 pp. (Declassified by authority of NASA TPA no. 45, May 11, 1961.)

Effect of Flame-Holder Design on Altitude Performance of Louvered-Liner Afterburner, by Paul E. Renas and Emmert T. Jansen, *NACA Res. Mem. E53H15*, Oct. 1953, 41 pp. (Declassified by authority of NASA TPA no. 45, May 11, 1961.)

Rapid Method for Plug Nozzle Design, by H. Greer, *ARS JOURNAL*, vol. 31, no. 4, April 1961, pp. 560-561.

Experimental Study of Combustion Instability in Solid Rocket Propellants, by Leland A. Watermeier, *ARS JOURNAL*, vol. 31, no. 4, April 1961, pp. 564-565.

Solid Propellant Rocket Motors, by W. R. Maxwell and G. H. S. Young, *Royal Aeron. Soc., J.*, vol. 65, no. 604, April 1961, pp. 252-266.

## Propulsion and Power (Non-Combustion)

Application of Ferroelectricity to Energy Conversion Processes, by W. H. Clingman and R. G. Moore Jr., *J. Appl. Phys.*, vol. 32 no. 4, April 1961, pp. 675-681.

Thermodynamics of Thermally Regenerated Fuel Cells, by J. B. Friauf, *J. Appl. Phys.*, vol. 34, no. 4, April 1961, pp. 616-620.

Solar Collectors for Use in Thermionic Power Supply Systems in Space, by L. D. Wing and K. E. Cameron, *ARS JOURNAL*, vol. 31, no. 3, March 1961, pp. 327-333.

Voltage - Current Characteristics of Tungsten Electrodes in Cesium Vapor, by L. H. Stauffer, *ARS JOURNAL*, vol. 31, no. 3, March 1961, pp. 322-326.

Space Flight Technology, Commonwealth Space Flight Symposium 1st, London, 1959, Kenneth W. Gatland, ed., Academic Press, N. Y., 1960, 365 pp.

The Performance of Nuclear Thermal Fission Rockets, by O. H. Wyatt, pp. 139-153.

Institute of the Aeronautical Sciences, Proceedings of the Frontiers of Science and Engineering Symposium, Los Angeles, Sept. 1959, Cosponsored by the Inst. of the Aeronaut. Sci. and the Univ. of Calif., Inst. of the Aeronaut. Sci., N. Y., 132 pp.

Nuclear Power, by Edward Teller, pp. 129-132.

Elementary Magnetohydrodynamic Machines, by Amiya K. Sen, *Mass. Inst. Tech., Dept. of Elect. Engng.*, June 1958, 89 pp. (MS thesis, available only on microfilm.)

Irradiation Effects of 22 and 240 Mev

EDITOR'S NOTE: Contributions from Professors E. R. G. Eckert, E. M. Sparrow and W. E. Ibele of the Heat Transfer Laboratory, University of Minnesota, are gratefully acknowledged.



Protons on Several Transistors and Solar Cells, by W. C. Hulten, W. C. Hornaker and John L. Patterson, *NASA Tech. Note D-718* April 1961, 28 pp.

Thermionics and Thermoelectricity, by Edda Barber, *Calif. Inst. Tech., Jet Propulsion Lab. Literature Research* 294, Dec. 1960, 185 pp.

A Study of Laminar Compressible Viscous Pipe Flow Accelerated by an Axial Body Force, with Application to Magnetogas-dynamics, by E. Dale Martin, *NASA Tech. Note D-855*, April 1961, 69 pp.

Performance Evaluation of a Two Dimensional Ion Rocket Using Through-Feed and Porous Tungsten Ionizers, by David L. Lockwood and Ronald J. Cybulski, *NASA Tech. Note D-766*, April 1961, 53 pp.

Ballistic Missile and Space Technology v. II: Propulsion and Auxiliary Power Systems, Symposium on Ballistic Missile and Space Technology, Donald P. LeGalley, ed., Academic Press, N. Y., 1960, 441 pp.

Charged Metal Droplets for Propulsion, by V. E. Krohn and H. Shelton, pp. 129-136.

Isotopic Fueled Thermionic Generators, by Robert J. Harvey and G. N. Hatsopoulos, pp. 409-441.

A One-Megawatt Nuclear Electrical Power Plant for Space Applications, by D. P. Ross, E. Ray, E. G. Rapp and J. E. Taylor, pp. 373-382.

Nuclear Space Power—SNAP II, by F. D. Anderson, D. J. Cockeram, H. M. Dieckamp and J. R. Wetch, pp. 347-372.

Parametric Performance Studies of Electrical Thrust Generators for Space Applications, by A. V. LaRocca, pp. 243-298.

Electrostatic Lift for Space Vehicles, John C. Cook, pp. 203-241.

A Pulsed Plasma Accelerator Employing Electrodes, by S. Georgiev, R. Feinberg and G. S. Janes, pp. 183-201.

Electrostatic Analysis of Ion Jet Neutralization, by H. M. DeGroff, W. D. Halverson and R. A. Holmes, pp. 159-182.

A Versatile Ion Source for Propulsion, by Stanley Singer, pp. 137-157, 34 refs.

Thermoelectric Materials and Devices, Irving B. Cadoff and Edward Miller, eds., Reinhold Publishing Corp., N. Y., 1960, 344 pp.

Thermoelectric Phenomena, by Nicholas Fuschillo, pp. 1-17.

The Thermoelectric Circuit, by Irving B. Cadoff and Edward Miller, pp. 18-30.

Thermoelectric Figure of Merit, by Nicholas Fuschillo, pp. 31-46.

Thermionic Emission Thermoelectricity, by George N. Hatsopoulos and John A. Welsh, pp. 47-54.

Calculation of Efficiency of Thermoelectric Devices, by B. Sherman, R. R. Heikes and R. W. Ure Jr., pp. 199-226.

Design Calculations for Thermoelectric Generators, by Douglas L. Kerry, pp. 227-249.

Direct Conversion Applied to Nuclear Heat Sources, by Melvin Barnat, pp. 275-317.

Nuclear Electric Power for Space Missions, by Terry W. Koerner and John J. Paulson, *Aero/Space Engng.*, vol. 20, no. 5, May 1961, pp. 18-19, 44-49.

Fluidized Solids as a Nuclear Fuel for Rocket Propulsion, by L. P. Hatch, W. H. Regan and J. R. Powell, *ARS*



Original painting by Louis Kibak, 1961

Man's accelerating progress toward mastering his environment is experiencing a startling thrust as a result of experimentation in nuclear space propulsion and controlled thermonuclear reactions.

Qualified applicants are invited to send resumes to:  
Director of Personnel Division 61-61

**los alamos**  
scientific laboratory  
OF THE UNIVERSITY OF CALIFORNIA  
LOS ALAMOS, NEW MEXICO

All qualified applicants will receive consideration for employment without regard to race, creed, color, or national origin. U.S. citizenship required.

JOURNAL, vol. 31, no. 4, April 1961, pp. 547-548.

**Small MHD Power Generator Using Combustion Gases as an Energy Source**, by G. J. Mullaney and N. R. Dibelius, *ARS JOURNAL*, vol. 31, no. 4, April 1961, pp. 555-557.

**A Family of Radioisotope-Fueled Auxiliary Power Systems for Lunar Exploration**, by Robert J. Wilson, *Astronaut. Sci. Rev.*, vol. 3, no. 1, Jan-March 1961, pp. 19-26.

**Three-Phase Static Inverters Power Space-Vehicle Equipment. Deliver 500 Watts at Full Load**, by R. J. Kearns and J. J. Rolfe, *Electronics*, vol. 34, no. 18, May 5, 1961, pp. 70-73.

**End Effect Losses in dc Magnetohydrodynamic Generators**, by Roland A. Boucher and Dennis B. Ames, *J. Appl. Phys.*, vol. 32, no. 5, May 1961, pp. 755-759.

**Calculation of the Maximum Efficiency of the Thermionic Converter**, by John H. Ingold, *J. Appl. Phys.*, vol. 32, no. 5, May 1961, pp. 679-772.

**Oscillation and Saturation Current Measurements in Thermionic Conversion Cells**, by R. J. Zollweg and Milton Gottlieb, *J. Appl. Phys.*, vol. 32, no. 5, May 1961, pp. 890-894.

**A Simplified Analysis of the Dynamics of Plasma Guns**, by J. G. Linhart, *Nuclear Fusion*, vol. 1, no. 2, 1961, pp. 78-100.

**Duct Flow in Magnetohydrodynamics**, by C. C. Chang and Th. S. Lundgren, *Zeitschrift Angewandte Math. Phys.*, vol. 12, no. 2, March 25, 1961, pp. 100-114.

## Materials and Structures

**A New Approach to the Analysis of the Deflection of Thin Cantilevers**, by R. Frisch-Fay, *J. Appl. Mech. (ASME Trans., Series E)*, vol. 28, no. 1, March 1961, pp. 87-90.

**On the Bending of Circular Cylindrical Shells by Equal and Equally Spaced End Radial Shear Forces and Moments**, by Paul Seide, *J. Appl. Mech. (ASME Trans., Series E)*, vol. 28, no. 1, March 1961, pp. 117-126.

**On the Buckling of Circular Cylindrical Shells Under Pure Bending**, by Paul Seide and V. I. Weingarten, *J. Appl. Mech. (ASME Trans., Series E)*, vol. 28, no. 1, March 1961, pp. 112-116.

**Stress Distribution in a Rotating Spherical Shell of Arbitrary Thickness**, by M. A. Goldberg, V. L. Salerno and M. A. Sadowsky, *J. Appl. Mech. (ASME Trans., Series E)*, vol. 28, no. 1, March 1961, pp. 127-134.

**Viscoelastometer for Measurement of Flow and Elastic Recovery**, by Richard J. Overberg and Herbert Leaderman, *J. Res. National Bur. Standards (C. Engng. and Instrumentation)*, vol. 65, no. 1, Jan.-March 1961, pp. 9-22.

**Enthalpy and Specific Heat of Nine Corrosion-Resistant Alloys at High Temperatures**, by Thomas B. Douglas and Andrew C. Victor, *J. Res. National Bur. Standards (C. Engng. and Instrumentation)*, vol. 65, no. 1, Jan.-March 1961, pp. 65-70.

**Creep Collapse of Long Cylindrical Shells Under High Temperature and External Pressure**, by Thein Wah and R. Kirk Gregory, *J. Aerospace Sci.*, vol. 28, no. 2, March 1961, pp. 177-188.

**The Melting Points of Tantalum Carbide and of Tungsten**, by Charles F. Zalabak, *NASA Tech. Note D-761*, March 1961, 21 pp.

**Mechanism of the Oxidation of Nickel and Chromium Alloys**, by D. V. Ignatov and R. D. Shamgunova, *NASA Tech. Transl. F-59*, March 1961, 104 pp. (Transl. of Russian book, published in Moscow, 1960).

**Analysis of Effective Thermal Productivities of Honeycomb-Core and Corrugated-Core Sandwich Panels**, by Robert T. Swann and Claud M. Pittman, *NASA Tech. Note D-714*, April 1961, 62 pp.

**An Experimental Study on Multi-wall Structures for Space Vehicles**, by D. G. Younger and S. Lambert (Aeronautic Div., Ford Motor Co.), *Wright Air Dev. Div. Tech. Rep. 60-800*, Dec. 1960, 60 pp.

**Materials for Ramjet Engines and Components**, by C. W. Bosseler, *The Johns Hopkins Univ., Appl. Physics Lab. TG 370-14*, Dec. 1958, 59 pp.

**Broad-Band Ultraviolet Filters**, by Charles B. Childs, *NASA Tech. Note D-697*, April 1961, 8 pp.

**Buckling of Circular Conical Shells Under Axisymmetric External Pressure**, by Josef Singer, *Israel Inst. Tech., Dept. Aeron. Engng. Rep. 12*, (Tech. Note 1) Nov. 1960, 27 pp., 3 figs. (AFOSR TN 60-711)

**General Theory of Large Deflections of Thin Shells**, by E. H. Dill, *NASA Tech. Note D-862*, March 1961, 21 pp.

**Tensile Properties of Pyrolytic Graphite to 5000°F**, by W. V. Kotlensky and H. E. Martens, *Calif. Inst. Tech., Tech. Rep. 32-71*, March 1961, 18 pp.

**Factors in Evaluating Fatigue Life of Structural Parts**, by Walter Ilg, *NASA Tech. Note D-725*, April 1961, 10 pp.

**Tensile and Compressive Creep of 6Al-4V Titanium-Alloy Sheet and Methods for Estimating the Minimum Creep Rate**, by Howard L. Price and George J. Heimerl, *NASA Tech. Note D-805*, April 1961, 19 pp.

**Cermets**, J. R. Tinklepaugh and W. B. Crandall, eds., Reinhold Publishing Corp., N. Y., 1960, 239 pp. 544 refs.

**Physicochemical Aspects of Cermets**, by M. Humenik Jr. and T. J. Whalen, pp. 6-49.

**Preparation of Oxides**, by Thomas S. Shevlin, pp. 50-55.

**Slip Casting of Cermets**, by Berthold C. Weber, pp. 58-72.

**Infiltration Process**, by Claus Goetzl, pp. 73-81.

**Resistance Sintering of Cermets Under Pressure**, by Fritz V. Lenel, pp. 81-85.

**A Summary of Good Practice in the Pressing of Cemented Carbides**, by John V. West, pp. 86-96.

**Alumina-Metal Cermets**, by Thomas S. Shevlin, pp. 97-108.

**Chromium-Alumina Base Cermets**, by Claude L. Marshall, pp. 109-118.

**Metal-Modified Oxides**, by Berthold C. Weber and Murray A. Schwartz, pp. 119-121.

**Properties of Titanium Carbide-Metal Compositions**, by John Wambold, pp. 122-129.

**Titanium Carbide-Metal Infiltrated Cermets**, by Claus Goetzl, pp. 130-145.

**Titanium Carbide-Steel Cermets**, by Martin Epner and Eric Gregory, pp. 146-149.

**Chromium Carbide Applications**, by R. F. Pozzo and John V. West, pp. 150-153.

**Container Materials for Melting Reactive Metals**, by Berthold C. Weber and Murray A. Schwartz, pp. 154-157.

**Electronic Refractory Cermets**, by Leo

J. Cronin, pp. 158-167.

**Cermets in Friction Materials**, by Howard B. Huntress, pp. 168-169.

**Metal Reinforcement and Cladding of Cermets and Ceramics**, by J. R. Tinklepaugh, pp. 170-180.

**An Impact Test for Use with Cermets**, by E. J. Soxman, J. R. Tinklepaugh and M. T. Curran, pp. 181-190.

**Application of Cermets to Nuclear Devices**, by J. R. Johnson, pp. 191-196.

**Application of Cermets to Aircraft Power Plants**, by Andre J. Meyer Jr. and George C. Deutsch, pp. 196-207.

**The Inflated Satellite: Characteristics in Sunlight and Darkness**, by Herman Mark and Simon Ostrach, *Aero/Space Engng.*, vol. 20, no. 4, April 1961, pp. 10-11, 30, 32, 35-36.

**Applications of Materials to Solid-Rocket Nozzles**, by Edward W. Ungar, *ASTRONAUTICS*, vol. 6, no. 4, April 1961, pp. 24-26, 83-86.

**Composite Ceramic-Metal Systems**, by A. V. Levy, S. R. Locke and H. Leggett, *ASTRONAUTICS*, vol. 6, no. 4, April 1961, pp. 27-29, 58.

**Expandable Structures of Space**, by J. T. Harris, and F. J. Stimler, *ASTRONAUTICS*, vol. 6, no. 4, April 1961, pp. 30-31, 92-94.

**Reinforced Carbonaceous Materials**, by Brennan A. Forcht and Milton J. Rudick, *ASTRONAUTICS*, vol. 6, no. 4, April 1961, pp. 32-33, 88-89.

**New Shapes for Glass Fibers**, by Irving J. Gruntfest and Norris F. Dow, *ASTRONAUTICS*, vol. 6, no. 4, April 1961, pp. 34-35, 80-82.

**Tungsten-Base Composites**, by Samuel R. Maloof, *ASTRONAUTICS*, vol. 6, no. 4, April 1961, pp. 36-37, 56.

**Dynamic Stability of a Conducting, Cylindrical Shell in a Magnetic Field**, by J. G. Linhart, *J. App. Phys.*, vol. 32, no. 3, March 1961, pp. 500-506.

**Wissenschaftliche Gesellschaft für Luftfahrt e.v. (WGL), Jahrbuch, 1959**, Herausgegeben von Hermann Blenk, Braunschweig, Friedr. Vieweg & Sohn, 1960, 442 pp.

**Development and Structural Aspects of Large Solid Propellant Rocket Motor Cases**, by W. Boccins, pp. 331-343.

**New Developments in Aluminum Alloys**, by P. Brenner, pp. 343-357. (In German)

**High Temperature Materials Under Dynamic Stresses**, by A. J. Kennedy, pp. 365-369.

**New Developments in Heat Resistant Metallic Materials**, by von den Steinen, pp. 370-376. (In German)

**Steels for High Flight Speeds**, by R. Oppenheim, pp. 376-383. (In German)

**Present Status of Development of Heat Resistant Titanium Alloys**, by H. H. Weigand, pp. 383-388. (In German)

**Reaction Sintering Processes and Corresponding Sintered Materials for High Temperatures**, by E. Meyer-Hartwig, pp. 390-394. (In German)

## Fluid Dynamics, Heat Transfer and MHD

**Stagnation Point Flow of Magnetized Blunt Body in Hypersonic Flow**, by S. I. Pai and E. T. Kornowski, *Gen. Electric Co., Missile and Space Vehicle Dept., T.I.S. R61SD037*, March 1961, 13 pp.

**Base-Pressure Measurements with Wire-Supported Models at Supersonic Speeds**, by J. Don Gray, *Arnold Engng. Dev. Center, Tech. Note 61-23*, March 1961, 24 pp.

**Flow in the Base Region of Axisymmetric and Two-Dimensional Configurations**, by Milton A. Beheim, *NASA Tech. Rep. R-77*, 1961, 32 pp.

**Introductory Study of Airloads on Blunt Bodies Performing Lateral Oscillations**, by P. T. Hsu and Holt Ashley, *Mass. Inst. Tech., Fluid Dynamics Res. Lab. Rep. no. 59-9*, Nov. 1959, 86 pp.

**External-Drag Estimation for Slender Conical Ducted Bodies at High Mach Numbers and Zero Angle of Attack**, by E. Floyd Valentine, *NASA Tech. Note D-648*, March 1961, 29 pp.

**Charts for Determining Skin-Friction Coefficients on Smooth and on Rough Flat Plates at Mach Numbers up to 5.0 with and Without Heat Transfer**, by Darwin W. Clutter, *Douglas Aircraft Co., E. Segundo Div. Rep. ES 29074*, April 1959, 106 pp.

**Preliminary Experimental Investigation of the Flow About a Blunt Body with Flow-Separation Spikes at  $M_\infty = 7.9$** , by Victor Zakkay, *Brooklyn, Polytech. Inst., Dept. Aerospace Engng., PIBAL Rep. 631*, Feb. 1961, 15 pp., 8 figs. (AFOSR 219)

**Review of Results of an Early Rocket Engine Film-Cooling Investigation at the Jet Propulsion Laboratory**, by William E. Welsh Jr., *Calif. Inst. Tech., Jet Propulsion Lab. Tech. Rep. 32-58*, March 1961, 21 pp.

**Diffuser Performance in the Open-Jet Hypersonic Wind Tunnel**, by Jacques A. F. Hill, *Mass. Inst. Tech., Naval Supersonic Lab., Analysis and Research Group, AR Memo 243*, May 1958, 16 pp.

**On the Interaction Between Stream and Body in a Free-Molecule Flow, Part II: Momentum Exchanges**, by Silvio Nocilla, *Torino, Politecnico, Laboratori di Meccanica Applicata, Tech. Note 17*, Sept. 1960, 27 pp. (AFOSR TN 60-914: part 2)

## Instrumentation and Communications

**Wind Tunnel Study of the Influence of Orifice Geometry and Flow Rates on the Measured Pressure Error of a Static Pressure Probe at Mach 3**, by Glen W. Zumwalt, *Sandia Corp., Tech. Mem. 315-60* (71), Nov. 1960, 24 pp., 10 figs.

**Theoretical Characteristics of Several Fluid-Metering Instruments**, by M. D. Bennett, *Sandia Corp., Res. Rep. 4446*, April 1960, 52 pp.

**Theory of Stroboscopic Oscillography**, by V. A. Vol, *The Johns Hopkins Univ., Appl. Phys. Lab., TG 230-T162*, Nov. 1960, 13 pp. (Transl. from *Radiotekhnika*, vol. 13, no. 8, Aug. 1959, pp. 63-70.)

**High Temperature Thermometry Seminar, Oak Ridge National Laboratory, Oct. 1-2, 1959, Proceedings**, W. R. Grimes and D. R. Cuneo, eds., *Atomic Energy Commission TID-7586*, part I, Aug. 1960, 171 pp.

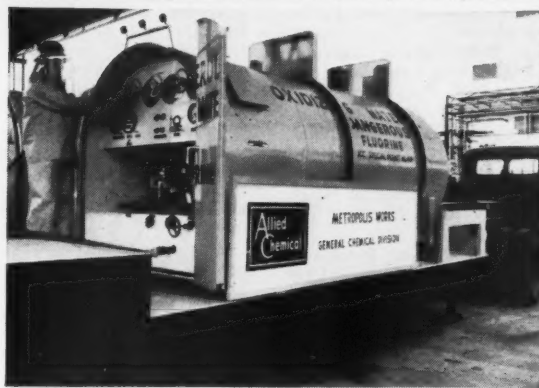
**Some Results of Base-Metal Thermocouple Research at Oak Ridge National Laboratory**, by J. F. Potts and D. L. McElroy, pp. 1-5.

**Effect of Environment on the Stability of Chromel/Alumel Thermocouples**, by Forbes S. Sibley, pp. 16-22.

**Uniqueness of Thermal EMF's Measured in Molybdenum, Rhenium, Tungsten, Iron and Copper**, by F. W. Kuether, pp. 23-30.

**Stability of Rhenium/Tungsten Thermocouples in Hydrogen Atmos-**

A General Chemical-designed tank trailer for the bulk shipment of liquid fluorine.



# 320-million lb.-miles of LIQUID FLUORINE from ALLIED CHEMICAL

Multiply the number of pounds of liquid fluorine that we've produced by the number of miles we've shipped it . . . and you come up with a total of 320-million pound-miles! This notable record is one more proof that liquid fluorine is no harder to handle than other advanced propellants.

Allied Chemical's General Chemical Division is a prime source for fluorine . . . your number one fluorine authority. We have supplied tonnage quantities to every major propulsion program using this ultimate oxidizer . . . and we can make bulk shipments to any part of the country.

Our experience in producing, storing and shipping large quantities of liquid fluorine has led to the development of handling and storage techniques that make this super-high-energy oxidizer completely practical to use. Let us share our experience and knowledge with you. If you'd like our fluorine technical bulletins, just mail the coupon below.

First in  
Fluorine  
Chemistry



**GENERAL CHEMICAL  
DIVISION**

40 Rector Street, New York 6, N.Y.

**GENERAL CHEMICAL DIVISION**

40 Rector Street, New York 6, N.Y.

ARS-81

Please send me bulletin(s) checked:

- ☐ Fluorine (Pd-TA-85413)  
☐ Liquid Fluorine Unloading Procedure (PD-TB-85411)

Name \_\_\_\_\_

Company \_\_\_\_\_

Address \_\_\_\_\_

City \_\_\_\_\_ Zone \_\_\_\_\_ State \_\_\_\_\_

Title \_\_\_\_\_



- phere, by J. C. Lachman and F. W. Kuether, pp. 31-36.
- High-Output Noble Metal Thermocouples and Matching Lead Wire, by R. B. Clark and W. C. Hagel, pp. 37-43.
- High-Temperature Thermocouples Based on Carbon and Its Modifications, by N. R. Thielke and R. L. Shepard, pp. 44-52.
- Distributed Seebeck Effect at High Temperatures, by R. J. Freeman, pp. 53-68.
- Monochromatic Radiation Pyrometry for Gas Temperature Measurement, by Richard H. Tourin, pp. 69-80.
- A Dichromatic Radiation Pyrometer, by Richard H. Tourin, pp. 81-95.
- Reliability Assurance in Sheathed Thermocouples for Nuclear Reactors, by George Johannesson, pp. 96-99.
- Thermocouples for Measurement of Temperatures of Gas-Cooled Surfaces, by W. E. Browning and H. L. Hemphill, pp. 100-109.
- Heat Transfer Measurements in an Electric-Arc Driven Wind Tunnel, by R. L. Ledford, pp. 110-119.
- Changes in EMF Characteristics of Chromel/Alumel and Platinum/Platinum-Rhodium, by M. J. Kelly, pp. 120-129.
- LITR Experiments Relating to Rhodium/Tungsten and Platinum/Platinum-Rhodium Thermocouples, by D. B. Tranger, pp. 130-139.
- A Summary of Experience with In-Pile Thermocouples, by J. C. Wilson, pp. 140-143.
- Error Analysis of Plate Type Fuel Element Temperature Measurements, by J. A. McCann, pp. 144-156.
- Temperature Instrumentation of Metallic Uranium Fuel Pins, by Dieter L. Hall, pp. 157-167.
- Progress on Development of a Reference Curve for the Iridium Versus 40% Rhodium Thermocouples, by G. F. Blackburn and F. R. Caldwell, pp. 168-171.
- Radiation from Openings Traversed by Progressive Waves, by Jacques Ernest, Paris, Université, Faculté des Sciences, (Thesis, D. Sci. Phys), Dec. 1960, 193 pp. (In French)
- The Goldstone Station Communications and Tracking System for Project Echo, by Robertson Stevens and Walter K. Victor, Calif. Inst. Tech., Jet Propulsion Lab., Tech. Rep. 32-59, Dec. 1960, 57 pp.
- American Vacuum Society, Transactions of the Sixth National Symposium on Vacuum Technology, Philadelphia, Oct. 1959 (includes Cumulative Index of 1954-1959 Symposia), C. Robert Meissner, ed., Pergamon Press, N. Y., Symposium Publications Div., 1960, 335 pp.
- New Method for Vacuum Measurements in the Molecular Range of Pressures, by N. A. Florescu, pp. 75-81.
- Advances in the Design of Vacuum Gauges Using Radioactive Materials, by J. R. Roehrig and G. F. Vanderschmidt, pp. 82-84.
- The Theory and Design of Subminiature Ionization Gauge Tubes, by R. L. Ramey, pp. 85-88.
- A Multi-point Vacuum Measuring System for Low Pressure Wind Tunnels, by P. L. Vitkus, pp. 89-93.
- Apparatus for Electron Optical Study of Low-Density Gas Flow, by S. R. Mielczarek, D. C. Schubert and L. Marton, pp. 206-209.
- Satellite Networks for Continuous Zonal Coverage, by R. David Luders, ARS JOURNAL, vol. 31, no. 2, Feb. 1961, pp. 179-184.
- Low Resolution Unchopped Radiometer for Satellites, by Rudolf A. Hanel, ARS JOURNAL, vol. 31, no. 2, Feb. 1961, pp. 246-250.
- Pressure Measurement in Liquids and Gases (Including Pressure Differences), by Walter Wuest, Archiv für Tech. Messen, no. 300, Jan. 1961, pp. 21-22. (In German)
- A Transistorized Automatic Single-Channel Scintillation Gamma-Spectrometer, by A. N. Pisarevskii, L. D. Soshin and Yu. E. Selyaninov, Instruments and Experimental Techniques, no. 4, July-Aug. 1960, pp. 548-554.
- Analysis of the Precision of Reading a Double-Crystal Spectrometer, by V. V. Schmidt, Instruments and Experimental Techniques, no. 4, July-Aug. 1960, pp. 555-559.
- A Fast Neutron Time-Of-Flight Spectrometer, by E. A. Zharebin and E. A. Tamanov, Instruments and Experimental Techniques, no. 4, July-Aug. 1960, 560-565.
- Measurement of the Thickness of Thin Coatings on Thick Substrates, by V. Ya. Dudarev, Instruments and Experimental Techniques, no. 4, July-Aug. 1960, pp. 646-649.
- An Apparatus for Low-Temperature Testing with Transported Liquid Helium, by A. B. Fradkov, Instruments and Experimental Techniques, no. 4, July-Aug. 1960, pp. 650-653.
- Effect of Antenna Radiation Angles Upon HF Radio Signals Propagated Over Long Distances, by W. F. Utlaut, J. Res. National Bur. Standards (D. Radio Propagation), vol. 65, no. 2, March-April 1961, pp. 167-174.
- Graphical Determination of Radio Ray Bending in an Exponential Atmosphere, by C. F. Pappas, L. E. Vogler and P. L. Rice, J. Res. National Bur. Standards (D. Radio Propagation), vol. 65, no. 2, March-April 1961, pp. 175-180.
- Some Methods of Detecting Fluctuating Signals in Two-Channel Systems, by Iu. B. Chernyak, Radio Engng. and Elect. (transl. of Radiotekhnika i Elektronika), vol. 4, no. 12, 1959, pp. 22-35.
- The Accuracy of Measuring the Parameters of Oscillations Distorted by Low-Intensity Gaussian Noise, by B. A. Dubinskii, Radio Engng. and Elect. (transl. of Radiotekhnika i Elektronika), vol. 4, no. 12, 1959, pp. 36-46.
- The Dependence of Irregular Ionospheric Radiowave Refraction on the Zenith Angle, by Iu. L. Kokurin, Radio Engng. and Elect. (transl. of Radiotekhnika i Elektronika), vol. 4, no. 12, 1959, pp. 47-53.
- The Application of Chaplygin's Method for the Solution of Some Non-linear Problems of Radio Engineering, by V. I. Kaganov, Radio Engng. and Elect. (transl. of Radiotekhnika i Elektronika), vol. 4, no. 12, 1959, pp. 54-58.
- Interferometric Instrument for the Rapid Measurement of Small Diameters, by Douglas H. Blackburn, Rev. Sci. Instruments, vol. 32, no. 2, Feb. 1961, pp. 137-139.
- Piezoelectric Probe for Plasma Research, by Martin O. Stern and Edward N. Dacus, Rev. Sci. Instruments, vol. 32, no. 2, Feb. 1961, pp. 140-143.
- The Recording of Pressure Step Functions of Low Amplitude by Means of a Composite-Dielectric Capacitance Transducer Placed in a Parallel-T Network, by K. Posel, Witwaterstrand Univ., Dept. Mech. Engng. Rep. 1/61, Jan. 1961, 43 pp.
- Low-Speed Time-Multiplexing with Magnetic Latching Relays, by John F. Meyer, Calif. Inst. Tech., Jet Propulsion Lab. Tech. Rep. 32-54, Feb. 1961, 22 pp.
- A Formula for Radio Ray Refraction in an Exponential Atmosphere, by G. D. Thayer, J. Res. National Bur. Standards (D. Radio Propagation), vol. 65, no. 2, March-April 1961, pp. 181-182.
- Mass Spectrometer for the Isotopic Analysis of Lithium, by R. G. Ridley and D. E. P. Silver, J. Sci. Instruments, vol. 38, no. 2, Feb. 1961, pp. 47-50.
- Recording Integrator for Gas Chromatography, by A. P. H. Jennings, J. Sci. Instruments, vol. 38, no. 2, Feb. 1961, pp. 55-58.
- Simple Mercury Expansion Regulator for Control of Air Temperature to  $^{\circ}0.02$  deg. c, by K. L. Butcher and M. J. Byrne, J. Sci. Instruments, vol. 38, no. 2, Feb. 1961, p. 59.
- Experiments Using Ultra-Fast Pulse Techniques, by G. Goldring, Nuclear Instruments and Methods, vol. 11, no. 1, Jan. 1961 (Proc. Second Accelerator Conference, Amsterdam, Oct. 1960), pp. 29-38.
- The Application of Ray Tracing Methods to Radio Signals from Satellites, by I. N. Capon, Proc. Physical Soc., London, vol. 77, no. 494, Feb. 1, 1961, pp. 337-345.
- Optimum Information Transmission Through a Channel with Unknown Parameters, by R. L. Dobrushin, Radio Engng. and Elect. (transl. of Radiotekhnika i Elektronika), vol. 4, no. 12, 1959, pp. 1-8.
- Theory of Detecting the Useful Signal in the Background of Gaussian Noise and an Arbitrary Number of Interfering Signals with Random Amplitudes and Initial Phases, by Ia. D. Shirman, Radio Engng. and Elect. (transl. of Radiotekhnika i Elektronika), vol. 4, no. 12, 1959, pp. 9-21.
- A Liquid-Helium-Cooled Coaxial Termination, by C. T. Stelzried, Calif. Inst. Tech., Jet Propulsion Lab. Tech. Release 34-224, Jan. 1961, 7 pp.
- Technology Reports, vol. 10, nos. 414-445, Oct. 1960, Osaka Univ., Faculty of Engng., pp. 545-903.
- Measurement of Gaseous Discharge Plasma with Microwave Interferometer (I), by Uichi Kubo and Yoshio Inuishi, pp. 565-578.
- An Ideal Identification Device for Complex Signals, by L. F. Borodin, Radio Engng. (transl. of Radiotekhnika i Elektronika), vol. 15, no. 8, 1960, pp. 60-74.
- The Numerical Solution of Differential Equations Governing the Reflexion of Long Radio Waves from the Ionosphere, IV, by D. W. Barron, Proc. Royal Soc., London, (series A, Math Phys. Sci.), vol. 260, no. 1302, March 7, 1961, pp. 393-408.
- Measurement of Surface Temperatures by Infrared Cinematography, by Nicole Louisnard, Recherche Aéronautique, no. 80, Jan.-Feb. 1960, pp. 29-36. (In French)
- Study of Methods of Dynamic Calibration of Pressure Pickups, by J. Cholatnamy, Recherche Aéronautique, no. 80, Jan.-Feb. 1960, pp. 37-46. (In French)
- The Transmission of Discrete Signals by Means of Phase Difference Modulation, by N. B. Bobrov, Telecommunications (transl. of Elektrosvyaz'), no. 6, 1960, pp. 599-608.
- Calculation of Noise in the Channels of a Radio-Relay Line on the Introduction of Pre-Distortions, by E. L. Gerenrot, Telecommunications (transl. of Elektrosvyaz'),



no. 6, 1960, pp. 637-643.

**On the Density of Recording of Electric Impulses on a Ferro-Magnetic Medium**, by V. G. Makurochkin, *Telecommunications* (transl. of *Elektrosvyaz'*), no. 6, 1960, pp. 644-653.

**Distant Tropospheric Propagation of Ultra-Short Waves**, by A. I. Kalinin, *Telecommunications* (transl. of *Elektrosvyaz'*), no. 6, 1960, pp. 654-670.

**Parameters of an Air Communication Line at High Frequencies**, by V. V. Roditi, *Telecommunications* (transl. of *Elektrosvyaz'*), no. 6, 1960, pp. 678-683.

**Rocket and Satellite Instrumentation**, by B. G. Pressey, *Nature*, London, vol. 188, no. 4747, Oct. 22, 1960, pp. 265-266.

**A Gold-Silicon Surface-Barrier Proton Range Telescope**, by R. Takaki, M. Perkins, and A. Tuzzolino, *IRE Trans. Nuclear Sci.*, vol. NS-8, no. 1, Jan. 1961, pp. 64-72.

**Use of Moon or Satellite Relays for Global Communications**, by L. P. Yeh, *Communication and Elect.*, no. 51, Nov. 1960, pp. 607-615; *Elect. Engng.*, vol. 79, no. 12, Dec. 1960, pp. 1043-1048.

**A Narrow-Bandwidth Video-Tape Recorder for Use in Tiroso Satellite**, by J. A. Zenel, *J. Soc. Motion Picture & Telev. Engrs.*, vol. 69, no. 11, Nov. 1960, pp. 818.

**Radioelectric Whistling Through the Earth's Magnetic Field**, by R. Gendrin, *Comptes Rendus Hebd. des Seances de L'acad. Sci.*, France, vol. 251, no. 9, Aug. 29, 1960, pp. 732-733.

**Mechanization of a Pole Beacon Telemetering Encoder**, by W. E. Arens, *Jet Propulsion Lab., Calif. Inst. Tech., Section Rep.* 334-1, Nov. 14, 1960.

**Description and Evaluation of Angular Encoding Systems Utilized by Goldstone Tracking Antennas**, by M. Perlman, *Calif. Inst. of Tech., Jet Propulsion Lab.*, TM 33-25, Nov. 30, 1960.

**System Capabilities and Development Schedule of the Deep Space Instrumentation Facility**, by J. R. Hall, *Calif. Inst. of Tech. Jet Propulsion Lab.*, TM 33-27, Feb. 13, 1961.

**The Goldstone Station Communications and Tracking System for Project Echo**, by R. Stevens and W. K. Victor, eds., *Calif. Inst. Tech., Jet Propulsion Lab.*, TR 32-59, Dec. 1, 1960.

**VHF Radio Propagation Data for Cedar Rapids-Sterling, Anchorage-Barrow, and Fargo-Churchill Test Paths, April 1951 Through June 1958**, by G. R. Sugar and K. W. Sullivan, *National Bur. Standards, Boulder Labs., Boulder, Colo. Tech. Note* 79, Sept. 1, 1960. (OTS/PB 161,580)

**A Theoretical Study of Sporadic-E Structure in the Light of Radio Measurements**, by K. Tao, *National Bur. Standards, Tech. Note* 87, Jan. 1961. (OTS/PB 161,588)

**Errors of Prediction of a Satellite Orbit Due to Noise in Doppler Observations**, by C. J. Cohen and W. A. Kemper, *Nav. Weapons Lab., Computation and Analysis Lab.*, Dahlgren, Va., NWL-R-1723, Jan. 11, 1961.

**Optimum Stress Design of a Rotating Wire Antenna**, by R. H. Frick, *Rand Corp.* RM-2640-ARPA, Sept. 27, 1960.

**Modulations Imposed on a Radio Signal by Satellite Motions**, by A. T. Waterman, *Stanford Univ., Systems Tech. Lab., Rep.* 758-1, Aug. 29, 1958.

**Television Earth Satellites—USSR** (Nauchno-Tekhnicheskiye Obshchestva SSSR, No. 6, 1960), by V. Litvinenko, *U. S. Dept. of Commerce, Off. Tech. Services, Washington, D. C.*, OTS-60-31,720, Aug. 22, 1960. (JPRS:3749)

## BAHAMAS CONFERENCES

announces its first

### CONFERENCE on MEDICAL and BIOLOGICAL PROBLEMS in SPACE FLIGHT

NOVEMBER 19th to 24th 1961  
in NASSAU in the BAHAMAS

For further particulars, hotel reservations  
and registration

Write: Irvin M. Wechsler,  
Executive Director,  
P. O. Box 1454  
Nassau, Bahamas.

(11¢ postage required)

**Bulletin of Artificial Earth Satellite Optical Tracking Stations** (transl. from *Byulleten Stantsiy Opticheskogo Nabludeniya Iskusstvennyye Sputniki Zemli*, SSSR, no. 8, 1959), by Ye Z. Gindin, *U. S. Dept. of Commerce, Off. Tech. Services, Washington, D. C.*, OTS-60-41,044, July 27, 1960. (JPRS:5146)

**A Mobile Chart of Calculating an Optical Fence**, by V. N. Ivanov. Graphical Method for Calculating Satellite Visibility, by I. A. Klimishin.

**Determination of the Height of an Artificial Satellite from a Single Observation of its Crossing the Meridian Perpendicularly**, by L. A. Urasin.

**Determination of the Height of an Artificial Satellite from an Observation of Its Crossing the Earth's Shadow**, by L. A. Urasin.

**A Simple Method for Predicting Periods of Satellite Visibility at Observation Stations**, by A. G. Sukhanov.

**Determination of the Satellite's Height From Its Entry in the Earth's Shadow**, by V. M. Kondratenko and G. N. Kondratenko.

**Diminishing of the Satellite's Brightness as it Enters the Earth's Shadow**, by B. A. Firago.

**Satellite Observations at the Khar'kov Station**, by V. I. Yezerskiy, V. Kh. Pluzhnikov and E. F. Chaykovskiy.

**Range, Declination, and Doppler-Shift Calculations for an Interplanetary Radar**, by M. LaLonde, *Cornell Univ., Center for Radiophysics and Space Res., Res. Rep.* RS 10, June 30, 1960.

**Long-Focus Cameras for Determining Coordinates of Faint Artificial Earth Satellites**, by M. K. Abele, *Soviet Astronomy AJ*, vol. 4, no. 1, July-Aug. 1960, pp. 134-139.

**Satellite Coverages**, by B. H. Gundel, *Astronaut. Sci. Rev.*, vol. 2, no. 4, Oct.-Dec. 1960, pp. 19-23.

**Geometric Aspects of Satellite Communication**, by F. W. Sindén and W. L. Mammel, *IRE Trans. on Space Elect. and Telemetry*, vol. SET-6, no. 3-4, Sept.-Dec. 1960, pp. 146-157.

**Communication to Space Vehicles**, by H. W. Cooper, *Westinghouse Engr.*, vol. 20, no. 6, Nov. 1960, pp. 179-184.

**A Possible Long-Range Communications Link Between Ground and Low-Orbiting Satellites**, by M. S. Macraakis, *J. Atmospheric Terrestrial Phys.*, vol. 19, no. 3-4, Dec. 1960, pp. 260-271.

**The Courier Communications Satellite**, by R. Kasper, *Rensselaer Engr.*, vol. 14, no. 2, Jan. 1961, pp. 26-27, 29.

**A Method for Interpreting the Doppler Curves of Artificial Satellites**, by G. Boudouris, *J. Brit. Inst. Radio Engrs.*, vol. 20, no. 12, Dec. 1960, pp. 933-935.

**Doppler Navigation and Tracking**, by B. R. Gardner, *IRE Proc.*, vol. 48, no. 12, Dec. 1960, pp. 2016-2017.

**The Pioneer I, Explorer VI and Pioneer V High-Sensitivity Transistorized Search Coil Magnetometer**, by D. L. Judge, M. G. McLeod and A. R. Sims, *IRE Trans. on Space Elect. and Telemetry*, vol. SET-6, no. 3-4, Sept.-Dec. 1960, pp. 114-121.

**Effect of Tracking Accuracy Require-**

ments on Design of Minitrack Satellite Tracking System, by J. H. Berbert, *IRE Trans. on Instrumentation*, vol. 1-9, no. 2, Sept. 1960, pp. 84-88.

Parametric Amplifier for Space Problem Tracking, by C. F. Brett, *Electronics*, vol. 34, no. 4, Jan. 27, 1961, pp. 41-45.

Volume Density of Radio Echoes from Meteor Trails, by N. Carrara, P. F. Checcacci and L. Ronchi, *Proc. IRE*, vol. 48, no. 12, Dec. 1960, pp. 2031-2032.

The Relation of the Satellite Ionization Phenomenon to the Radiation Belts, by J. D. Kraus and R. C. Higgy, *Proc. IRE*, vol. 48, no. 12, Dec. 1960, pp. 2027-2028.

The Influence of Sunspot Number on Transmitter Power Requirements for HF Ionospheric Circuits, by F. T. Koide, *Proc. IRE*, vol. 48, no. 12, Dec. 1960, pp. 2033-2035.

An Equipment for Processing Time-Multiplexed Telemetry Data, by D. J. McLaughlan and T. T. Walters, *I. Brit. Interplanetary Soc.*, vol. 18, no. 1, Jan.-Feb. 1961, pp. 33-35.

Application of Spectroscopic Temperature Measuring Methods to Definition of a Plasma Arc Flame, by Robert G. Nagler, *Calif. Inst. Tech., Jet Propulsion Lab., Tech. Rep.* 32-66, Jan. 1961, 7 pp.

## Atmospheric and Space Physics

Effect of an Electrical Field on Electron Velocity Distribution in a Molecular Plasma (Ionosphere), by A. V. Gurevich, *The Johns Hopkins Univ., Appl. Physics Lab. TG 230-TG 230-T204* (Transl. Series), Dec. 1960, 19 pp. (transl. from *Izvestia Vsesikh Uchebnykh Zavedenii Radiofizika*, vol. 2, no. 3, 1959, pp. 355-369.)

A Radiative Equilibrium Algorithm for Semi-Infinite Atmospheres, by Jean I. F. King, *Air Force Cambridge Res. Center, Geophysics Res. Directorate*, GRD TN-60-603, 1958, 17 pp.

American Vacuum Society, Transactions of the Sixth National Symposium on Vacuum Technology, Philadelphia, Oct. 1959 (includes cumulative index of 1954-1959 Symposia), C. Robert Meissner, ed.

An Ultra-High Vacuum Chamber for Space Simulation, by John C. Simons, Jr., pp. 48-54.

Pressure Simulation of Outer Space, by D. J. Santeler, pp. 129-133.

Ionospheric Motions Observed with High-Frequency Back-Scatter Sounders, by Lowell H. Tveten, *J. Res. National Bur. Standards* (D. Radio Propagation), vol. 65, no. 2, March-April 1961, pp. 115-128.

Relationship Between Red Auroral Arcs and Ionospheric Recombination, by G. A. M. King and F. E. Roach, *J. Res. National Bur. Standards* (D. Radio Propagation), vol. 65, no. 2, March-April 1961, pp. 129-136.

Free-Balloon Borne Meteorological Refractometer, by Jon F. Theisen and Earl E. Gossard, *J. Res. National Bur. Standards* (D. Radio Propagation), vol. 65, no. 2, March-April 1961, pp. 149-154.

Nuclear Reactions in Stars, by T. G. Cowling, *Proc. Royal Soc., London*, (series A, *Math. Phys. Sci.*), vol. 260, no. 1301, Feb. 21, 1961, pp. 170-198.

Investigation of the Ionosphere and of the Interplanetary Gas with the Aid of Artificial Satellites and Space Rockets, by Ya. L. Al'pert, *Soviet Phys. Uspekhi*, vol. 3, no. 4, Jan.-Feb. 1961, pp. 479-503.

Present Status of the Question of the Origin of Cosmic Rays, by V. L. Ginzburg and S. I. Syrovat-Skii, *Soviet Phys. Uspekhi*, vol. 3, no. 4, Jan.-Feb. 1961, pp. 504-541.

Some Evidence of Hydromagnetic Waves in the Earth's Magnetic Field, by Masahisa Sugiura, *Phys. Rev. Letters*, vol. 6, no. 6, Mar. 15, 1961, pp. 255-256.

Cosmic-Ray Flare of November 20, 1960, by Richard T. Hansen, *Phys. Rev. Letters*, vol. 6, no. 6, March 15, 1961, pp. 260-261.

Singularities of the Cosmological Solutions of Gravitational Equations, by I. M. Khalatnikov, E. M. Lifshitz and V. V. Sudakov, *Phys. Rev. Letters*, vol. 6, no. 6, March 15, 1961, pp. 311-312.

Determination of the Balmer Decrement in Auroral Spectra, by F. K. Shiskaya, *Soviet Astronomy AJ*, vol. 4, no. 1, July-Aug. 1960, pp. 178-179.

Emission Spectrum of the Aurora at College, Alaska, by L. Herman, *Annales de Geophysique*, France, vol. 16, no. 3, July-Sept. 1960, pp. 304-318.

The Influence of the Chromosphere on Solar Limb Darkening, by B. E. J. Pagel, *Astrophysical J.*, vol. 132, no. 3, Nov. 1960, pp. 790-800.

The Nature of the Grains in the Tails of Comets 1956h and 1957d, by W. Liller, *Astrophysical J.*, vol. 132, no. 3, Nov. 1960, pp. 867-882.

The Form of Cometary Envelopes, by L. S. Marochnik, *Soviet Astronomy AJ*, vol. 4, no. 3, Nov.-Dec. 1960, pp. 480-484.

A Note on the Analysis of Seven Years Visual Observations of the Aurora From New Zealand and Campbell Island, by M. Gadsden and M. N. Gadsden, *Annales de Geophysique*, France, vol. 16, no. 3, July-Sept. 1960, pp. 414-418.

The Modern State of the Problem of Determining the Origin of Cosmic Rays, by V. L. Ginzburg, and S. I. Syrovatskii, *Uspekhi Fizicheskikh Nauk, USSR*, vol. 71, no. 3, July 1960, pp. 411-469. (Abstracted in *Phys. Express*, vol. 3, no. 3, Nov. 1960, p. 3.)

The Sudden Increase in the Photon Component of Cosmic Radiation on May 4, 1960, by S. Standil, R. P. Bukata and F. K. Chin, *Canadian J. Phys.*, vol. 39, no. 1, Jan. 1961, pp. 229-230.

Observational Tests in Cosmology, by F. Hoyle, *Proc. Phys. Soc., London*, part I, vol. 77, no. 493, Jan. 1, 1961, pp. 1-16.

Interpretation of Cosmology, by J. A. Bastin, *Nature*, London, vol. 188, no. 4754, Dec. 10, 1960, pp. 923-924.

Determination of the Earth's Albedo, by E. K. Dzhasybekova, V. M. Kazachevskii and A. V. Kharitonov, *Soviet Astronomy AJ*, vol. 4, July-Aug. 1960, pp. 125-128.

Ionosphere Direct Measurement Satellite (Explorer VIII) *Nat. Acad. Science, IGY Bull.*, no. 42, Dec. 1960, pp. 10-13.

The Diurnal Sunlit Component of F2 Layer Ionization During the First Half of the Day, by A. I. Likhachev, *Soviet Astronomy AJ*, vol. 4, no. 1, July-Aug. 1960, pp. 129-133.

Measurement of the Electron Concentration in the Ionosphere According to the Rotation of the Polarization Plane of Radio Waves Emitted From Rockets, by K. I. Gringauz and V. A. Rudakov, *Doklady Akademii Nauk SSSR*, vol. 132, no. 6, June 1960, pp. 1311-1313. (In Russian, abstracted in *Phys. Express*, vol. 3, no. 3, Nov. 1960, pp. 29-30.)

Some Characteristics of the Signal Received from 1958  $\delta$ , by F. de Mendonca, O. G. Villard Jr., and O. K. Garriot, *Proc.*

*IRE*, vol. 48, no. 12, Dec. 1960, pp. 2028-2030.

Magnetic Field of Jupiter, by C. H. Barrow, *Nature*, London, vol. 188, no. 4754, Dec. 10, 1960, pp. 924-925.

Types of Irregular Geomagnetic Disturbances and the Mechanisms of Interaction of a Solar Corpuscular Stream with the Outer Atmosphere, by M. S. Bobrov, *Soviet Astronomy AJ*, vol. 4, no. 3, Nov.-Dec. 1960, pp. 392-404.

The Relation Between the Delay Time of Geomagnetic Disturbances and the Relative Sunspot Number, by O. N. Mitropol'skaya, *Soviet Astronomy AJ*, vol. 4, no. 1, July-Aug. 1960, pp. 60-63.

Some Comments on Pochtarev's Paper "The Earth's Magnetic Field in Relation to Other Geophysical Phenomena and to the Geological Structure of the Earth's Crust," by P. N. Kropotkin, *Acad. of Sci., USSR, Bull. Geophys. Series*, no. 6, Jan. 1961, pp. 606-607. (In Russian)

On One Attempt to Explain World Magnetic Anomalies, by Yu D. Kalinin, *Acad. of Sci., USSR, Bull. Geophys. Series*, no. 6, Jan. 1961, pp. 603-705. (In Russian)

On the Possibility of Determining the Magnetic Field Intensity in the External Corona for Propagation of Polarized Radioemission from a Discrete Source, by V. L. Ginzburg, *Izvestiya Vysishikh Uchebnykh Zavedenii Radiofizika, USSR*, vol. 3, no. 2, March-April 1960, pp. 341-342. (Abstracted in *Phys. Express*, vol. 3, no. 3, Nov. 1960, pp. 30-31.)

Some Remarks on the Dust and Haze Formation on Mars, by N. P. Barabashov and V. I. Garazha, *Soviet Astronomy AJ*, vol. 4, no. 3, Nov.-Dec. 1960, pp. 473-479.

Findings from Mercury's Transit, by J. Ashbrook, *Sky and Telescope*, vol. 21, no. 1, Jan. 1961, pp. 16-20.

Scandium 45 as the Reaction Product of Cosmic Rays in Iron Meteorites, II, by H. Wanke, *Zeitschrift für Naturforschung*, vol. 15A, no. 11, Nov. 1960, pp. 953-964. (In German)

Sodium 22 in the Meteorite Breitscheid, by E. Wilcsek and H. Wande, *Zeitschrift für Naturforschung*, vol. 15A, no. 11, Nov. 1960, pp. 1004-1007. (In German)

Formation of an Ionized Meteor Trail, by V. P. Dokuchaev, *Soviet Astronomy AJ*, vol. 4, no. 1, July-Aug. 1960, pp. 106-109.

The Theory of Ionization in Meteor Trails I. Kinetics of the Variation of Ionization Parameters for Meteoroids Heated by Motion in the Earth's Atmosphere, by A. M. Furman, *Soviet Astronomy AJ*, vol. 4, no. 3, Nov.-Dec. 1960, pp. 489-497.

Radar-Echo Observations of Meteors Using Two Receivers of Different Sensitivity, by L. A. Katasev, V. N. Korpusov and A. D. Orlyanskii, *Soviet Astronomy AJ*, vol. 4, no. 1, July-Aug. 1960, pp. 110-113.

Observations of Simulated Meteors, by Richard E. McCrosky, *Smithsonian Inst. Astrophys. Observatory*, (Smithsonian Contributions Astrophys., vol. 5, no. 4, 1961, pp. 29-37).

Orbital Elements of Meteors, by Gerald S. Hawkins and Richard B. Southworth, *Smithsonian Inst., Astrophys. Observatory* (Smithsonian Contributions Astrophys., vol. 4, no. 3, 1961, pp. 85-95)

Precision Orbits of 413 Photographic Meteors, by Luigi G. Jacchia and Fred L. Whipple, *Smithsonian Inst., Astrophys. Observatory* (Smithsonian Contributions Astrophys., vol. 4, no. 4, 1961, pp. 97-129).

Third Annual Conference on Aviation

and Astronautics, Tel-Aviv and Haifa, Israel, Inst. Tech. Dept. Aeron. Engng. (Reprint from Bull. Research Council of Israel, vol. 9C, no. 1-2, Feb. 1961) Feb. 1961, 121 pp.

Structure, Variations and Measurements of the Earth's Ionosphere and Exosphere, by C. Altman, pp. 29-48.  
On Extragalactic Cosmic Rays, by H. Kasha, p. 120.

Applied Probability (Proceedings of Symposia in Applied Mathematics, Vol. 7) McGraw-Hill Book Co., N. Y., for the Amer. Math. Soc., 1961.

Stochastic Processes of Astronomical Interest, by Guido Munch, pp. 51-66.

Proceedings of the Frontiers of Science and Engineering Symposium, Los Angeles, Sept. 1959, Cosponsored by the Inst. of Aeronaut. Sci. and the Univ. of Calif., Inst. of the Aeronaut. Sci., N. Y., 132 pp.

Space Environment, by Sydney Chapman, pp. 6-15.

Astromechanics, by Samuel Herrick, pp. 16-29.

Average Variants of a Semirestricted Planar Problem of Three Bodies, by N. D. Moiseyev, ARS JOURNAL, pp. 393-398, vol. 31, no. 3, March 1961.

Sputtering Effects on the Moon's Surface, by G. K. Wehner, ARS JOURNAL, vol. 31, no. 3, March 1961, pp. 438-439.

Interpolation Average Variants of the Canonical Problem of Celestial Mechanics, by N. D. Moiseyev, ARS JOURNAL, vol. 31, no. 3, March 1961, pp. 387-389.

Complete Averaging of Canonical Problem of Celestial Mechanics with Several Intermediate Elements, by N. D. Moiseyev, ARS JOURNAL, vol. 31, no. 3, March 1961, pp. 390-392.

Cosmic Rays and Outer Space, by S. N. Vernov, ARS JOURNAL, vol. 31, no. 3, March 1961, pp. 399-408.

Man-Made Heating and Ionization of the Upper Atmosphere, by P. A. Clavier, J. Appl. Phys., vol. 32, no. 4, April 1961, pp. 570-577.

Measurement of the Temperature in the Upper Atmosphere to 150 km in a Rocket Experiment, by J. E. Blamont, T. M. Donahue and M. L. Lory, Phys. Rev. Lett., vol. 6, no. 8, April 15, 1961, p. 403.

Electron Clouds: A General Survey, by F. F. Marmo, J. Pressman and L. M. Aschenbrand, Planetary and Space Sci., vol. 3, Feb. 1961, pp. 139-157.

The Use of Modulated Atomic-Beam Techniques for the Study of Space Flight Problems, by G. S. Hollister, R. T. Brackmann and W. L. Fite, Planetary and Space Sci., vol. 3, Feb. 1961, pp. 162-168.

Excitation of the Auroral Green Line in Nitrogen Afterglows, by R. A. Young and K. A. Clark, Planetary and Space Sci., vol. 3, Feb. 1961, pp. 169-174.

Rate of Recombination of Atomic Oxygen Through Flash Spectroscopy in the Vacuum Ultraviolet, by J. Golden and A. L. Myerson, Planetary and Space Sci., vol. 3, Feb. 1961, pp. 175-186.

Molecular Studies with a Lozier Electron Impact Apparatus, by M. Fineman and A. Petrocelli, Planetary and Space Sci., vol. 3, Feb. 1961, pp. 187-194.

Atom Concentration Measurements Using Electron Paramagnetic Resonance, by A. F. Hildebrandt, C. A. Barth and F. B. Booth, Planetary and Space Sci., vol. 3, Feb. 1961, pp. 194-203.

Gravitational Waves in General Relativity, V. An Exact Spherical Wave, by L. Marder, Royal Soc., London, Proc., vol. A-261, no. 1304, April 1961, pp.

91-96.

Ionization Fronts in Interstellar Gas: The Structure of Ionization Fronts, by W. I. Axford, Roy. Soc., London, Phil. Trans. A, Math. Phys. Sci., no. 1029, vol. 253, Feb. 9, 1961, pp. 301-333.

Ionization Fronts in Interstellar Gas and the Expansion of HII Regions, by F. A. Goldsworthy, Royal Soc., London, Phil. Trans. A, Math. Phys. Sci., no. 1028, vol. 253, Feb. 9, 1961, pp. 277-300.

Communication Concerning Scientific Works in the Field of Geomagnetism and Aeronomy During 1957-1959, NASA Tech. Trans. F-60, (transl. of report compiled by the Geomagnetism and Aeronomy Section of the Committee on Geodesy and Geophysics of the USSR Academy of Sciences), March 1961, 91 pp.

Discussions of Solar Proton Events and Manned Space Flight, by Kinsey A. Anderson and Carl E. Fichtel, NASA Tech. Note D-671, March 1961, 11 pp.

Analysis of Gravitational and Geometric Aspects of Geodetic Utilization of Satellites, by William M. Kaula, NASA Tech. Note D-572, March 1961, 38 pp.

Physical and Orbital Behavior of Comets, by Roy E. Squires and David B. Beard, Astrophys. J., vol. 133, no. 2, March 1961, pp. 657-667.

Interplanetary Gas, IV, Neutral Hydrogen in a Model Solar Corona, by John C. Brandt, Astrophys. J., vol. 133, no. 2, March 1961, pp. 688-700.

Interplanetary Gas, III, A Hydrodynamic Model of the Corona, by Joseph W. Chamberlain, Astrophys. J., vol. 133, no. 2, March 1961, pp. 675-687.

Distinction Between the Electromagnetic Constants of Tiktites and Libyan Desert Glass and Their Effect on Lunar Surface Theory, by A. Olte and K. M. Siegel, Astrophys. J., vol. 133, no. 2, March 1961, pp. 706-717.

Ultra-Violet Observations from Satellites, by J. Ring, Brit. Interplanetary Soc., J., vol. 18, no. 1, Jan.-Feb. 1961, pp. 17-19.

Analysis of a Type of Rough-Trial Meteor Echo, by B. A. McIntosh, Canadian J. Phys., vol. 39, no. 3, March 1961, pp. 437-444.

Determining the Acceleration Due to Gravity at the Location of the VNIIM (All-Union Scientific Research Institute of Meteorology), by K. N. Egorov and A. I. Martsinyak, Measurement Techniques (transl. of Izmeritel'naya Tekhnika) no. 8, Aug. 1960, p. 656.

## Human Factors and Bio-Astronautics

Proceeding of the Frontiers of Science and Engineering Symposium, Los Angeles, Sept. 1959, Cosponsored by the Inst. of the Aeronaut. Sci. and the Univ. of Calif. Inst. of the Aeronaut. Sci., N. Y., 132 pp.

Biomedicine, by A. H. Schwichtenberg, pp. 30-37.

Nuclear Flight; the United States Air Force Programs for Atomic Jets, Missiles and Rockets, Kenneth F. Gantz, ed., Duell, Sloan and Pearce, N. Y., 1960, 216 pp.

Radiobiological Aspects of Aircraft; Nuclear Propulsion, by John E. Pickering and Gerrit L. Hekhuis, pp. 167-171.

Human Factors of Nuclear-Powered Aircraft, by Charles A. Dempsey, pp. 172-181.

# AERO-DYNAMICIST

## CAREER APPOINTMENT

The Applied Physics Laboratory of the Johns Hopkins University offers an attractive career appointment to a man with a B.S. degree in aeronautical engineering, an aerodynamics major or strong academic background in mathematics and physics. In addition, the respondent will benefit from some practical experience in the areas indicated below.

The man we seek will conduct wind tunnel tests—and analyze the data—on drag, stability, control, special flow characteristics, etc., for all of APL's missile programs. He will analyze flight test data to verify or revise wind tunnel on theoretical predictions and explain flight anomalies that may be attributable to aerodynamic behavior. He will also assist in planning flights of test vehicles to secure aerodynamic information and check out air frames.

Our modern laboratory is located an equal distance between Washington, D.C. and Baltimore—offering you a choice of country, suburban or city living.

All qualified applicants will receive consideration for employment without regard to race, creed, color or national origin.

For additional details about this position or other interesting career opportunities, direct your inquiry to: Professional Staff Appointments

The Applied Physics Laboratory  
The Johns Hopkins University

8673 Georgia Avenue, Silver Spring, Md.



Public Hazards from Nuclear Aircraft, by B. P. Leonard, Jr., pp. 189-194.

The Interdependence of Manned Spacecraft Design and Radiation Shielding, by L. J. Barbieri and S. Lampert, *Aero/Space Engng.*, vol. 20, no. 4, April 1961.

Space Man vs. Space Machine, by A. R. Hibbs, *Aero/Space Engng.*, vol. 20, no. 4, April 1961, pp. 20-21, 58-60.

Cosmic Rays, Nuclear Reactors and Manned Space Systems, by David Reitz, *Aero/Space Engng.*, vol. 20, no. 4, April 1961, pp. 28-29, 77-94, 96, 59 refs.

## Propellants and Combustion

Thermal Bond Stresses in Case-Bonded Visco-Elastic Propellant Disks, by Bernard W. Shaffer and Myron Levitsky, *New York Univ. College of Engng. Res. Div.*, Feb. 1961, 23 pp.

A Research Study to Advance the State-of-the-Art of Solid Propellant Grain Design, *Thiokol Chem. Corp., Elkton Div.*, E 217-60, Interim Summary Rep., Jan. 1961, 173 pp.

Experimental Investigation of Flame Stabilization in a Deflected Jet, *Calif. Inst. Tech., Jet Propulsion Lab. Rep.* 30-5, Sept. 1959, 60 pp.

Modification of the Burning Rates of Ammonium Perchlorate Solid Propellants by Particle Size Control, by Karl E. Bastress, *Princeton Univ. Dept. Aeron. Engng., Rep.* 536, Jan. 1961, 55 pp. (Thesis, Ph.D.)

Ignition of Hydrogen-Oxygen Rocket Combustor with Chlorine Trifluoride and Triethylaluminum, by John W. Gregory and David M. Straight, *NASA Tech. Note D-684*, April 1961, 24 pp.

Third Annual Conference on Aviation and Astronautics, Tel-Aviv and Haifa, Israel, Inst. of Tech., Dept. of Aeron. Engng. (reprint from *Bull. Research Council of Israel*, vol. 9C, no. 1-2, Feb. 1961), Feb. 1961, 121 pp.

The Effect of Nitromethane Additions on the Combustion of Various Fuels under Spheroidal Conditions, by L. Gross-Gronowski, pp. 29-38.

An Approximate Method of Solid Propellant Internal Star Grain Calculation, by A. Yaron and R. Corlett, p. 119.

Advance in Chemical Physics, v, III, L. Prigogine, ed., Interscience Publisher, N. Y., 1961, 372 pp.

Propagation of Flames and Detonations, by J. O. Hirschfelder and C. F. Curtiss, pp. 59-129, 27 refs.

Electron Diffraction in Gases and Molecular Structure, by O. Bastiansen and P. N. Skancke, pp. 323-362, 81 refs.

High Speed Testing, Vol. 1. A Plastechnic Equipment Corporation, Symposium held at Boston, Mass., Dec. 8, 1958, Interscience Publishers, N. Y., 1960, 112 pp.

High Speed Testing of Composite Solid Rocket Fuels, by Harry D. Brettschneider, pp. 41-53.

Institute of the Aeronautical Sciences, Proceedings of the Frontiers of Science and Engineering Symposium, Los Angeles, Sept. 1959, Cosponsored by the Inst. of the Aeronaut. Sci. and the Univ. of Calif., Inst. of the Aeronaut. Sci., N. Y., 132 pp.

Free Radicals, by James W. Moyer, pp. 38-43.

Cryogenics, by John R. Pellam, pp. 53-60.

A Capacitance Densitometer for Determination of the Transient Densities of Cryogenic Liquids, by A. Harry Sharbaugh and Maxwell W. Lippitt Jr., *ARS JOURNAL*, vol. 31, no. 3, March 1961, pp. 294-296.

Stressing Owing to Internal Pressure in Solid Propellant Rocket Grains, by Howard B. Wilson, Jr., *ARS JOURNAL*, vol. 31, no. 3, March 1961, pp. 309-317.

Calculation of C\* for Highly Dissociated Propellant Combustion Products, by L. J. Gordon, *ARS JOURNAL*, vol. 31, no. 3, March 1961, pp. 374-375.

Investigation of Basic Characteristics of Combustion of a Homogeneous Mixture of an Open Turbulent Stream, by E. A. Petrov and A. V. Talantov, *ARS JOURNAL*, vol. 31, no. 3, March 1961, pp. 408-413.

On the Properties of the Motion of Certain Ideal Gases Following an Explosion at a Point, by N. N. Kutchina, *Appl. Math. Mech. (PMM)*, vol. 24, no. 3, 1960, pp. 735-744.

Photothermoelastic Analysis of Bonded Propellant Grains, by I. M. Daniel and A. J. Durelli, *Experimental Mech.*, vol. 1, no. 3, March 1961, pp. 97-102.

High-Temperature Kinetics in Turbulent Combustors, by W. D. Weatherford Jr., J. P. Cueller Jr. and R. K. Johnston, *I/EC; Ind. Engng. Chem.*, vol. 53, no. 5, May 1961, pp. 398-402.

Stability of Laminar Flames, by Russell E. Petersen and Howard W. Emmons, *Phys. of Fluids*, vol. 4, no. 4, April 1961, pp. 456-464.

Turbulent Structure of Gaseous Detonation, by Donald R. White, *Phys. of Fluids*, vol. 4, no. 4, April 1961, pp. 465-480.

Two-Reaction Steady Detonations, by Jerome J. Erpenbeck, *Phys. of Fluids*, vol. 4, no. 4, April 1961, pp. 481-492.

Shock Initiation of Detonation in Liquid Explosives, by A. W. Campbell, W. C. Davis, J. B. Ramsay and J. R. Travis, *Phys. of Fluids*, vol. 4, no. 4, April 1961, pp. 511-520.

One-Dimensional Laminar Flame Propagation with an Enthalpy Gradient, by J. Adler and D. B. Spalding, *Royal Soc., London, Proc.* vol. A 261, no. 1304, April 1961, pp. 53-78.

Investigation of the Mixing and Burning Process Between Concentric Streams, by E. Le Grives and P. Sarraz, *Zeitschrift für Flugwissenschaften*, vol. 9, no. 2, Feb. 1961, pp. 46-53. (In German.)

Examination of Pressure Oscillations Induced by Changes in the Burning Rate of Flames, by Rose L. Schalla, *NASA Tech. Note D-764*, April 1961, 14 pp.

Modification of the Burning Rates of Ammonium Perchlorate Solid Propellants by Particle Size Control, by Karl E. Bastress, *Princeton Univ., Dept. Aeron. Engng.*, Jan. 1961, 55 pp. (Thesis, Ph.D.)

Spray Formation and Breakup, and Spray Combustion, by A. E. Fuks, *Sundstrand Machine Tool Co. Sundstrand Turbo Div. Tech. Note 4*, Feb. 1958, 129 pp. (AFOSR TN 58-414) (ASTIA AD 158,217) 42 refs.

Preparation of Dipentaborylmethane by Friedel-Crafts Reaction, by Albert C. Antoine, *NACA Res. Mem.* E58A14a, April 1958, 11 pp. (Declassified by authority of NASA TPA no. 45, May 11, 1961.)

Preliminary Evaluation of Pentaborane in a 1/4-Sector of an Experimental Annular Combustor, by Warner B. Kaufman, Erwin A. Lezberg and Roland Breitwieser, *NACA Res. Mem.* E56B13, May 1957, 18 pp. (Declassified by authority of NASA TPA no. 45, May 11, 1961.)

Initial Performance Investigation of Pentaborane Fuel in Free-Flight Ram-Jet Engine, by John H. Disher and Leonard Rabb, *NACA Res. Mem.* E54D28, Jan. 1957, 32 pp. (Declassified by authority of NASA TPA no. 45, May 11, 1961.)

Preliminary Investigation of the Combustion of Pentaborane and Diborane in a Turbojet Combustor at Simulated Altitude Conditions, by J. B. Gibbs, W. B. Kaufman and J. R. Branstetter, *NACA Res. Mem.* E53B18, Feb. 1957, 26 pp. (Declassified by authority of NASA TPA no. 45, May 11, 1961.)

Methane-Oxygen Flame Structure, IV. Chemical Kinetic Considerations, by A. A. Westenberg and R. M. Fristrom, *J. Phys. Chem.*, vol. 65, no. 4, April 1961, pp. 591-607.

Discontinuity Properties of Laminar Flames, by Tony Maxworthy, *Phys. of Fluids*, vol. 4, no. 5, May 1961, pp. 558-563.

Size Distribution and Velocity of Ethanol Drops in a Rocket Combustor Burning Ethanol and Liquid Oxygen, by Robert D. Igebo, *ARS JOURNAL*, vol. 31, no. 4, April 1961, pp. 540-541.

Kinetics of the Reactions of Active Nitrogen with Oxygen and with Nitric Oxide, by M. A. A. Clyne and B. A. Thrush, *Royal Soc., London, Proc.* vol. A 261, no. 1305, April 1961, pp. 259-273.

## CHANGE-OF-ADDRESS NOTICE

In the event of a change of address, it is necessary to include both your old and new addresses, as well as your membership number and coding, when notifying ARS headquarters, in order to insure prompt service. If you are moving or have moved, send the following form to Membership Dept., American Rocket Society, 500 Fifth Ave., New York 36, N. Y.

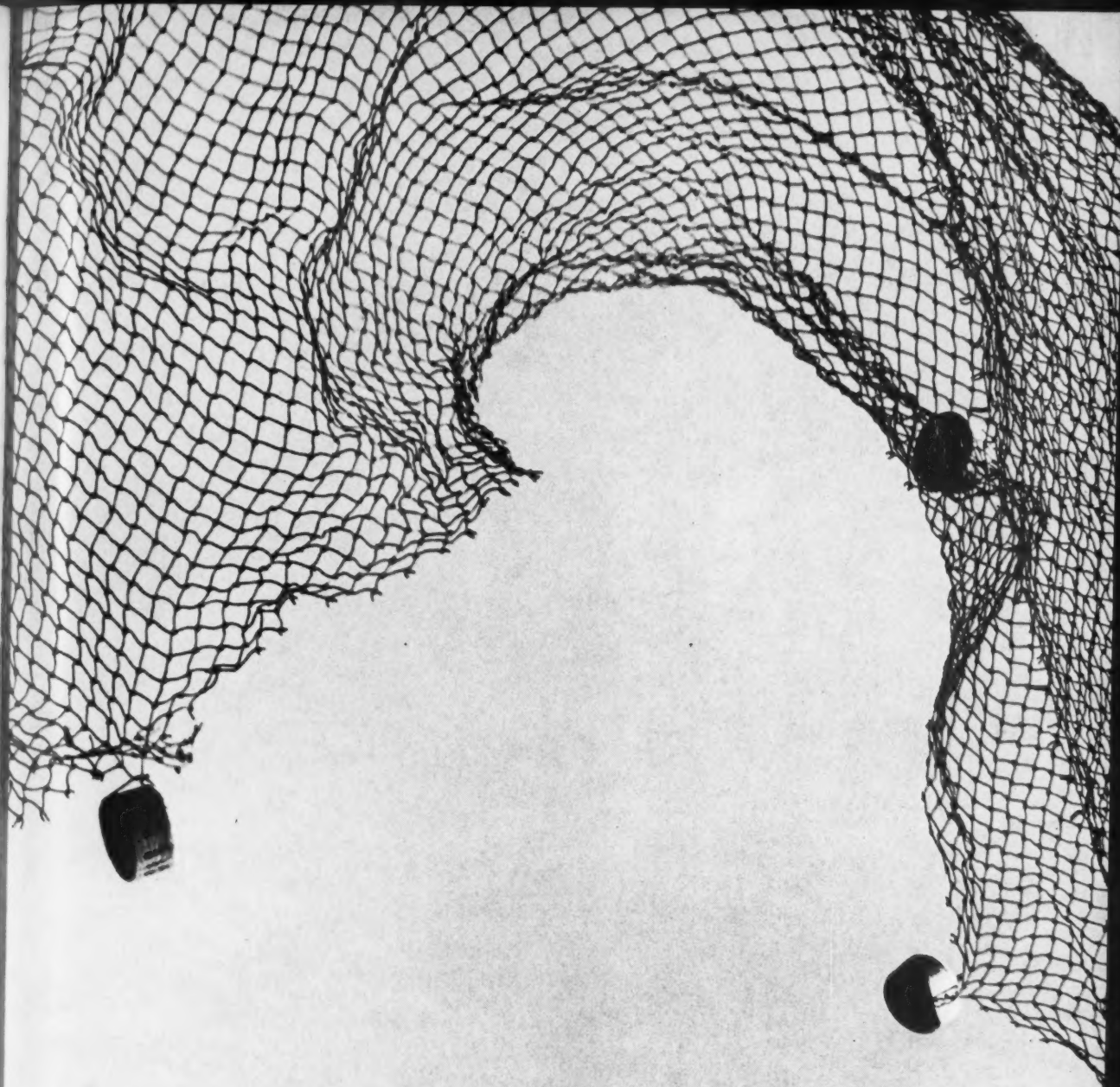
Name \_\_\_\_\_

Membership Card No. \_\_\_\_\_ Coding \_\_\_\_\_

Old Address \_\_\_\_\_

New Address \_\_\_\_\_





## 3-nation net into space

Goldstone, Calif., Woomera, Australia. Krugersdorp, South Africa.

Three different parts of the world thousands of miles from each other. Yet drawn together in a new and unique communications net: the Deep Space Instrumentation Facility.

DSIF is under the technical direction of Cal Tech's Jet Propulsion Laboratory for the National Aeronautics and Space Administration. Staffed and run by the host countries, the tracking stations will have 5-foot-in-diameter antennas, capable of transmitting and receiving. These giant, revolving steel and aluminum saucers are able to send and receive signals hundreds of millions of miles to and from space.

It was at Goldstone that JPL bounced signals off the planet Venus—5-million miles away. This two-month experiment gave us valuable data about the distance and surface of Venus and helped maintain the United States as the leader in planetary radar astronomy.

Communicating with deep space probes is just one function of the three stations of DSIF. Their primary job is tracking all the spacecraft designed by JPL to fly-by, orbit, and land on the moon and planets.

Because the stations provide 360° coverage around the earth, one of the three will always be in contact with each distant spacecraft in flight and after it arrives.

DSIF is an essential participant in the many space projects at JPL. Ranger, Surveyor, Mariner. Some of these spacecraft are imminent. Others are on JPL blackboards. All will bring new technologies, new knowledge of our planets and the topless universes beyond, and a still greater understanding of our own small world.

To carry on these vital projects, we need top scientists and engineers of many different disciplines. We need people who love their work, who want to know, and want to participate in the exploration of other worlds. If you believe you're qualified, then come explore with us. Write today.

### JET PROPULSION LABORATORY

4806 Oak Grove Drive, Pasadena, California

Operated by California Institute of Technology for the National Aeronautics and Space Administration



*All qualified applicants will receive consideration for employment without regard to race, creed, color or national origin.*

## Solid Rockets for Space

Aerojet-General's segmentation principle promises reliable off-the-shelf boosters for space missions. Standardized, transportable segments are stacked and clustered to produce any desired thrust—tailoring the power of the solid motor to meet the requirements of the payload.

*Segmentation is a proven principle.* After several successful segmented firings beginning as early as February, 1960, Aerojet successfully test fired the world's largest solid rocket under an Air Force contract on June 3, 1961—a 55-ton giant producing a half million pounds of thrust. The motor was made of three segments joined together just before firing.

Aerojet's segmented solid rockets provide a rapid, economical response to the challenge of placing large payloads in space.

### SOLID ROCKET PLANT

**CORPORATION**

Sacramento, California

A  
SUBSIDIARY  
OF  
**THE  
GENERAL  
TIRE**  
AND  
RUBBER  
COMPANY



Engineers, scientists—investigate outstanding opportunities at Aerojet

